University of California
Santa Barbara

Investigating the role of grain boundary structure on the thermal and mechanical behavior of nanocrystalline metals

A dissertation submitted in partial satisfaction
of the requirements for the degree

Doctor of Philosophy
in
Materials

by

Glenn Hunter Balbus

Committee in charge:

Professor Daniel S. Gianola, Chair
Professor Tresa M. Pollock
Professor Irene J. Beyerlein
Professor Daniel Kiener

December 2020

The Dissertation of Glenn Hunter Balbus is approved.

Professor Tresa M. Pollock

Professor Irene J. Beyerlein

Professor Daniel Kiener

Professor Daniel S. Gianola, Committee Chair

November 2020

Investigating the role of grain boundary structure on the thermal and mechanical behavior of nanocrystalline metals

by

Glenn Hunter Balbus

For Phee, Herbert, Isabelle, and Jerome

Acknowledgements

This thesis would not be possible without many, many people who have supported me, intellectually or otherwise, for the past four-plus years.

First and foremost, I would like to thank my advisor, Prof. Dan Gianola, for being my mentor through this processes. You have helped me develop professionally as a scientist, researcher, writer, and presenter, and have been incredibly supportive of me personally during my time in Santa Barbara (and in Baltimore, Zurich, and Leoben). Thank you for showing me how to be deeply curious and enthusiastic about science, and for fostering a lively, supportive academic environment.

I would like to thank my committee members, Prof. Tresa M. Pollock, Prof. Irene J. Beyerlein, and Prof. Daniel Kiener for their helpful critiques of my work over the past four years, as well as their support and guidance.

To my lab mates in the Gianola group – Fulin Wang, Jungho Shin, Yolita Eggeler, Rejin Raghavan, Eric Yao, Drew Melchert, Ashley Roach, and Leah Mills – and others – Aidan Taylor, Claire Chisholm, Deryck Stave, Mark Cornish, Patrick Callahan, Jean-Charles Stinville, Marie-Agathe Charpagne, Sean Murray, Collin Holgate, Connie Dong, Mitchell Bordelon, and Sanjeev Kolli – thank you for making the past few years of tedious experiments, dealing with broken instruments, etc., bearable. Thank you for the entertaining and lengthy scientific discussions, and for letting me bounce silly questions and ideas off of you. Thanks for the several impromptu trips to the woods, mountains, and ocean, and for the coffee and beer.

I would like to thank Daniel Kiener, Verena Maier-Kiener, Christoph Gammer, Oli Renk, Marlene Kapp, Markus Alfreider, Andi Bachmaier, Michi Wurmshuber, Barbara Putz, Florian Spieckermann, and all the folks in Leoben who welcomed me with open arms, knowing full well I did not understand a word of German, let alone Styrian. Thank

you for putting up with me, and for making my time in the Alps memorable and productive.

To my fencing family – thank you for always keeping me sane. Nicolas Graziano, thank you for always keeping me on my toes. Ian McCue, thank you for your guidance in so many things. Tim Robinson, thank you for Presidio, for staying late after practice to swap stories, and for encouraging me to coach. Lucas Nichols, Matt Kuiken, Jeff Van Housen, and Theo Funk, thanks for keeping me in shape, driving around to tournaments, and all the bruises. Harriet Eckstein (& Allen Irwin), thank you for being so kind, loving, and supportive (and for the cheese). Oleg Brusilvosky, thank you for always checking in on me, and being a mentor to me for all these years.

None of this would be possible without my parents, Andy and Debbie, and my sister, Skyler. Thank you all for being so supportive of me in everything. Skyler, thank you for always lending me an ear, a couch, and sending me funny tweets. Mom, thank you for always picking up the phone and being my sounding board. Dad, I promise, I don't work on making things invisible... but this probably still won't convince you. Thank you so much, I couldn't have done this without you.

Lastly, to Michelle. Thank you for being the kindest, most supportive, loving human I know. Thank you choosing to do life with me; I love you so much.

Curriculum Vitæ
Glenn Hunter Balbus

Education

2020	Ph.D. in Materials (Expected), University of California, Santa Barbara, CA.
2016	B.S. in Mechanical Engineering, Johns Hopkins University, Baltimore, MD.

Publications

G. H. Balbus, J. Kappacher, D. J. Sprouster, F. Wang, J. Shin, Y. M. Eggeler, T. J. Rupert, J. R. Trelewicz, D. Kiener, V. Maier-Kiener, and D. S. Gianola, "Disordered Interfaces Enable High Temperature Thermal Stability and Strength in a Nanocrystalline Aluminum Alloy," (**Submitted**).

Z. Bai, **G. H. Balbus**, D. S. Gianola, and Y. Fan, "Mapping the Kinetic Evolution of Metastable Grain Boundaries under Non-Equilibrium Processing," *Acta Materialia*, vol. 200, pp. 328-337, Nov. 2020.

F. Wang, **G. H. Balbus**, Y. Su, S. Xu, J. Shin, P. F. Rottmann, J. C. Stinville, L. H. Mills, O. N. Senkov, I. J. Beyerlein, T. M. Pollock, and D. S. Gianola, "Multiplicity of Dislocation Pathways in a Refractory Multi-Principal Element Alloy," *Science*, vol. 370, no. 6512, pp. 95-101, Oct. 2020.

J.C. Stinville, T. Francis, A.T. Polonsky, C.J. Torbet, M.A. Charpagne, Z. Chen, **G.H. Balbus**, F.Bourdin, V. Valle, P.G. Callahan, M.P. Echlin, and T.M. Pollock, "Continuous Digital Image Correlation in the SEM for Time-dependent Mechanisms Measurement," *Experimental Mechanics*, vol. 121, pp. 1-18, Aug. 2020.

G. H. Balbus, F. Wang, and D. S. Gianola, "Suppression of Shear Localization in Nanocrystalline Al-Ni-Ce Via Segregation Engineering," *Acta Materialia*, vol. 188, pp. 63-78, Jan. 2020.

G. H. Balbus, M. P. Echlin, C. M. Grigorian, T. J. Rupert, T. M. Pollock, and D. S. Gianola, "Femtosecond laser rejuvenation of nanocrystalline metals," *Acta Materialia*, vol. 156, pp. 183–195, Sep. 2018.

Abstract

Investigating the role of grain boundary structure on the thermal and mechanical behavior of nanocrystalline metals

by

Glenn Hunter Balbus

Nanocrystalline metals exhibit exceptional mechanical properties, such as high strength and wear resistance, and are actively being investigated for use in high performance structural applications. The ubiquitous use of nanocrystalline alloys in engineering applications is currently limited by two intrinsic material instabilities: rampant, thermally induced grain growth; and catastrophic shear localization during plastic deformation. These instabilities, which originate in the high concentration of grain boundaries and corresponding structural disorder present in nanocrystalline metals, prevent the widespread use of these alloys, especially in mission- or safety-critical applications. However, outstanding questions remain regarding the precise role of grain boundary structure on these instabilities, presenting an exciting opportunity to enable their use.

Using both targeted processing and interface aware alloying strategies, the role of grain boundary structure and chemistry on these instabilities will be explored. Experiments suggest that ultrafast (fs) laser processing provides tunability of the mechanical behavior of nanocrystalline metals by selectively modifying grain boundaries. The degree of tunability is sensitive both to local chemistry and initial relaxation state, suggesting that laser processing increases the energy of the grain boundaries, akin to rejuvenation processing in amorphous metals.

A nanocrystalline aluminum alloy, doped with nickel and cerium, was developed to investigate the chemical and structural effects of multicomponent alloying. The Al-Ni-Ce

alloy exhibits extremely desirable mechanical properties, including high hardness, tunable shear localization behavior, and strength retention at elevated temperature; as well as excellent microstructural stability. The origin of these desirable attributes is explored using *ex-* and *in-situ* diffraction experiments, which suggest the topological disordering of grain boundary regions during processing imparts thermal stability and strength at temperature. These results collectively underscore that grain boundary structure plays a deterministic role in the instabilities associated with nanocrystalline metals, providing novel strategies for alloy design and processing to circumvent these behaviors.

Contents

List of Figures

Page

List of Tables

Page

Chapter 1

Introduction

The development of high strength, polycrystalline metallic materials has enabled technological advances since prehistoric times [1, 2]. Early metallurgical developments, such as alloying copper with arsenic or tin to produce bronze, are not altogether different than the technological advancements that have enabled high performance jet engines in recent years. What differentiates modern day technological developments is our ability to precisely control alloy chemistry and processing, and, hence, the microstructure and properties of materials [3]. Specifically, the ability to control the size, distribution, and orientation of crystalline domains - known as grains - within a material is extremely important for controlling a wide range of properties of metals, including strength and ductility [4–7], high temperature mechanical behavior [3], wear [8], and formability [9].

Materials processing techniques to reduce the grain size are particularly important for producing materials with high strength and wear resistance [4–8]. Nanocrystalline metals, those with grain sizes less than 100 nm, are among the highest strength alloys to date [10]. These materials exhibit a suite of additional desirable properties including good wear resistance [8], fatigue behavior [11,12], radiation tolerance [13], as well as interesting electrical and thermal properties [14–17]. Nanocrystalline metals have received extensive

study since the late 1980s due to the advent of processing techniques such as inert gas atomization, which enabled their fabrication in sufficient volumes for characterization [18]. While the primary interest in nanocrystalline metals originated from their high strength, researchers found that as the grain size approaches the nanoscale, the physical properties of these metals cannot readily be explained by extrapolating our understanding of coarse grained materials.

Due to highly non-equilibrium synthesis methods, large volumes of interfacial material between neighboring grains (e.g. grain boundaries), and unique deformation physics, nanocrystalline metals exhibit instabilities that limit their use in structural applications. Two of the most problematic instabilities present in nanocrystalline metals are their high propensity for (1) shear localization during mechanical loading and (2) thermally induced microstructural coarsening, both of which have been reported extensively in the literature. Our current understanding of these instabilities and our ability to design against them are extremely limited, precluding the development of stable nanocrystalline metals for use in demanding engineering applications.

1.1 Mechanical behavior of nanocrystalline metals

1.1.1 Overview and the Hall-Petch relationship

The mechanical behavior of nanocrystalline metals has been studied extensively over the past thirty years [10, 12, 19]. While much of the early interest in nanocrystalline metals was motivated by the well-known Hall-Petch [4, 6] relationship, which established an inverse relationship between strength and the square root of the grain size (Equation 1.1), it was quickly realized that such a relationship does not hold for materials with

extremely fine grain sizes [20, 21]. The Hall-Petch relationship is:

$$\sigma_y = \sigma_0 + \frac{k}{\sqrt{d}} \tag{1.1}$$

where σ_y is the yield strength, σ_0 is a frictional stress or intrinsic resistance to dislocation motion, k is a material parameter, and d is the grain size. While primarily phenomenological, the classical mechanistic interpretation of the Hall-Petch relationship hinges on the pile-up behavior of dislocations at grain boundaries. Dislocations are extended line defects in a lattice that are responsible for many physical phenomena in crystalline materials, including their mechanical behavior [22]. This traditional explanation of the Hall-Petch relationship suggests that as newly generated dislocations impinge on a grain boundary, they produce a back stress on subsequent dislocations moving towards the grain boundary, hindering their motion. As the grain size decreases, the pile-up spacing becomes smaller and the overall stress required to deform the material increases. While this mechanistic interpretation is frequently invoked, several other mechanistic interpretations of the Hall-Petch relationships invoking dislocation-dislocation interactions have been demonstrated in the literature to correctly predict the Hall-Petch scaling [20].

As grain sizes are reduced to the nanocrystalline regime and the pile-up spacing approaches the grain size, the Hall-Petch relationship fails to accurately predict the increase in strength due to further grain refinement. In metals with grain sizes between 50-100 nm [19], and in some cases even finer grained systems [23], the increase in strength is better approximated by:

$$\sigma_y = \sigma_0 + \frac{k_1}{d} \tag{1.2}$$

where σ_y exhibits a simple inversely proportional relationship with the grain size d. This change in strengthening behavior is an indication of the unique deformation physics

and dislocation behavior within nanocrystalline grains, which is illustrated in Figure 1.1. Legros *et al.* [24] demonstrated that nanocrystalline metals often do not contain grains large enough for a typical Frank-Read dislocation source to be energetically stable. This calculation suggests that the dislocation-back-stress mechanistic explanation of the Hall-Petch relationship likely no longer applies to these materials. Transmission electron microscopy (TEM) investigations on a variety of nanocrystalline metals further corroborate the supposition that residual dislocation content is only stable (and thus, observable) in large grains ($>$ 50 nm) [10]. In-situ deformation experiments provide additional confirmation that dislocations in nanocrystalline metals, while operative, are extremely unstable and move rapidly between nearby grain boundaries [25]. These observations and calculations suggest that the mechanical behavior of nanocrystalline metals cannot be explained using conventional dislocation plasticity in coarse grained materials.

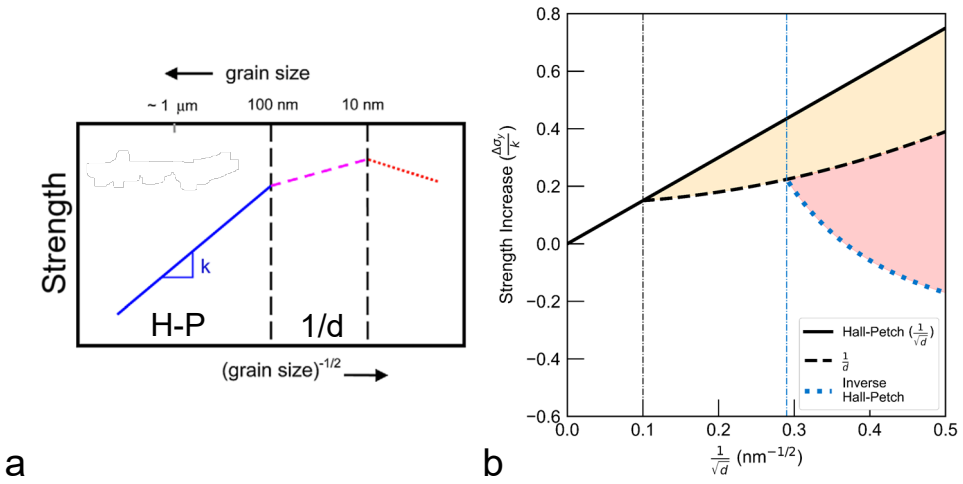

Figure 1.1: Regimes of grain size dependence on strengthening behavior. a, adapted from [10], with permission from Elsevier. b, Normalized increase in strength vs inverse square root of grain size. Yellow shaded area indicates the difference between the Hall-Petch expected strengthening and actual strengthening due to change in deformation mechanisms in nanocrystalline metals. Red shaded area demonstrates the range of properties within the 'inverse Hall Petch' regime, which are extremely sensitive to processing.

1.1.2 Nanocrystalline deformation mechanisms

As traditional dislocation sources are energetically unstable and dislocations cannot be stored in the grain interiors, dislocation-dislocation interactions no longer govern the mechanical behavior of materials with grain sizes in the nanocrystalline regime. In materials with grain sizes too small to store dislocation content, it has been demonstrated using in-situ TEM and molecular dynamics (MD) simulations that the fundamental deformation process is generally governed by the nucleation, propagation, and absorption of dislocations at grain boundaries [25–27]. The transition from conventional dislocation plasticity in coarse grained metals to dislocation-grain boundary plasticity in nanocrystalline metals is shown schematically in Figure 1.2. The transition in underlying deformation physics suggests many of the well-studied phenomena in coarse grained materials are not present in nanocrystalline metals. A prime example of this mechanistic transition is the absence of forest dislocation hardening, which gives rise to pronounced work hardening and macroscopic ductility in coarse grained metals, in nanocrystalline metals [10].

The simple inverse relationship between strength and grain size in Equation 1.2 provides additional mechanistic insight into the transition in deformation behavior from the interactions between dislocations in coarse grained materials and that between dislocations and grain boundaries in nanocrystalline metals. The apparent strengthening caused by reductions of the grain size in the 20 - 50 nm regime can be explained by the behavior of dislocations as they traverse the grain interior during plastic deformation. While dislocation nucleation does play an important role during the deformation of nanocrystalline metals [26], the propagation of dislocations is the thermally activated, rate limiting step [28, 29]. As the dislocation advances, shown schematically in Figure 1.2b, it must effectively 'un-pin' itself along the grain boundary in order to move and accommodate the imposed strain [26]. This behavior is similar to a conventional Orowan

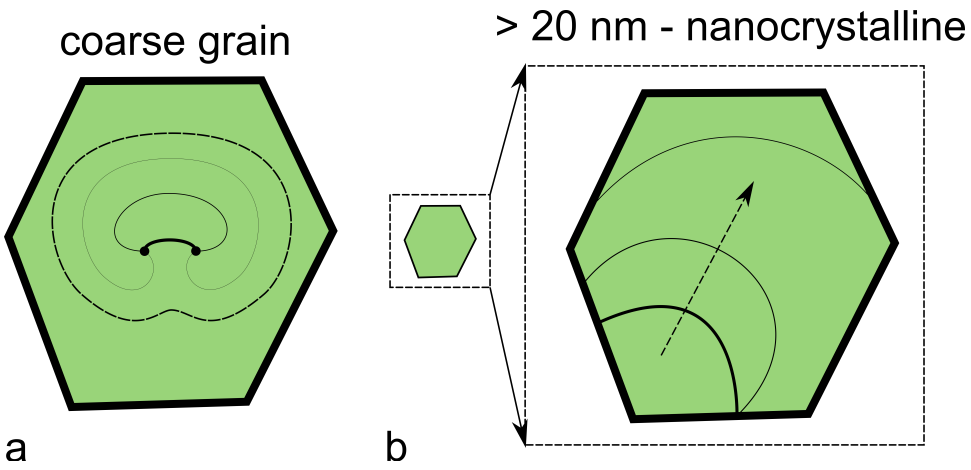

Figure 1.2: Nanocrystalline deformation mechanism schematic. a) Conventional dislocation plasticity in coarse grained material consisting of a Frank-Read source leading to dislocation-dislocation interactions. b) Left, relative scale of nanocrystalline grain relative to coarse grain in a containing Frank-Read source. Right, nanocrystalline dislocation-based deformation, where dislocation segments are pinned at their ends at the grain boundaries. The second dislocation propagation step demonstrates a non-symmetric pinning due to the atomistics of the grain boundary.

bowing stress, which relates the stress required to move a dislocation through an array of unshearable particles to the average spacing of the particles [30]. The Orowan bowing mechanism exhibits a simple inverse relationship between strength and the distance between particles, giving a physical explanation for the relationship between grain size - i.e. the distance between dislocation pinning points - and strength for nanocrystalline metals in this grain size regime [31]. This mechanistic behavior can also explain the prominent role of alloying on the strength of nanocrystalline metals, as varying atomic species at grain boundaries can significantly alter the pinning behavior of dislocations as they propagate across the grain interior [32].

Further reductions in grain size promote the operation of unusual deformation mechanisms, such as grain boundary sliding [33], grain rotation [34], deformation twinning [35], and atomistic shuffling [36,37]. These mechanisms are often grouped into two categories: (1) grain boundary mediated deformation mechanisms, which encompasses all intergran-

ular deformation mechanisms such as grain boundary sliding, rotation, atomistic shuffling, etc., and (2) dislocation mediated deformation mechanisms. This terminology is misleading, as dislocation mediated plasticity in nanocrystalline metals is governed by dislocation-grain boundary interactions. Therefore, it is useful to differentiate deformation mechanisms that involve *intragranular* accommodation (i.e. conventional dislocation plasticity) and those that involve *intergranular* accommodation (sliding, shuffling, etc.) explicitly. Intergranular deformation mechanisms (grain boundary mediated) are operative in nanocrystalline metals where conventional intragranular dislocation plasticity is suppressed and become particularly important in materials with grain sizes of 20 nm or less, given the large volume fraction of interfacial material [38]. Some researchers have even postulated that intergranular deformation mechanisms are responsible for the numerous reports of softening - the so-called 'inverse' Hall-Petch relationship shown in Figure 1.1 - observed when materials in this regime undergo additional reductions in grain size [21, 23, 39].

Mechanistically, many of these intergranular deformation mechanisms involve local atomic shuffling at grain boundaries, a feature researchers have compared to the underlying deformation behavior of amorphous materials [36, 40]. Such localized atomic shuffling is often initiated at smaller strains and requires lower levels of stress to be active compared to dislocation-mediated plasticity [40, 41]. The lower stress level required to trigger these mechanisms is argued to give rise to the softening reported in very fine grained nanocrystalline metals [41]. Deformation involving atomic shuffling at grain boundaries is shown in Figure 1.3, where atomic shuffling was observed immediately after yielding during MD simulations of nanocrystalline Ni deformed under tension [40].

Researchers have suggested that the localized underlying deformation processes give rise to the extreme processing sensitivity observed in nanocrystalline metals [21, 42–44]. The localized atomic rearrangements that underlie these deformation mechanisms can

occur with little thermal or mechanical energy, and may evolve unexpectedly during seemingly 'mild' processing, such as low temperature annealing or mechanical cycling. Macroscopically, deformation involving localized atomic shuffling can be deleterious, often giving rise to early onset strain localization and premature failure [21, 42, 45]. The large volume fraction of grain boundaries, coupled with easily triggered, localized deformation mechanisms allow strain to readily localize and cause catastrophic failure [42,46]. This behavior is known as shear localization or shear banding, and is frequently observed in nanocrystalline metals with grain sizes less than 20 nm [21, 42, 45]. Pillar compression experiments presented in Figure 1.4 demonstrate the significant impact of intergranular deformation mechanisms on shear band formation and premature failure in nanocrystalline materials with very fine grain sizes [42]. This localization behavior can also be understood from a mechanics perspective, where the operation of many deformation mechanisms in concert is necessary to maintain compatibility of the polycrystal. Any individual intergranular deformation mechanism, like grain boundary sliding [33] for instance, acting alone would not allow for compatibility to be satisfied. However, as there are many of these intergranular deformation mechanisms which are both localized and triggered at low levels of stress, once yielding begins in one region of the sample, it can readily propagate in a narrow band, causing premature failure via shear banding. This is in contrast to intragranular dislocation plasticity in conventional metals, which inherently satisfies compatibility and often results in more uniform deformation behavior.

1.1.3 Grain boundary structure and mechanical properties

The atomistic structure of grain boundaries plays an increasingly important role in determining the deformation behavior in nanocrystalline metals when intergranular deformation mechansisms are prominent. This is especially evident in the propensity for

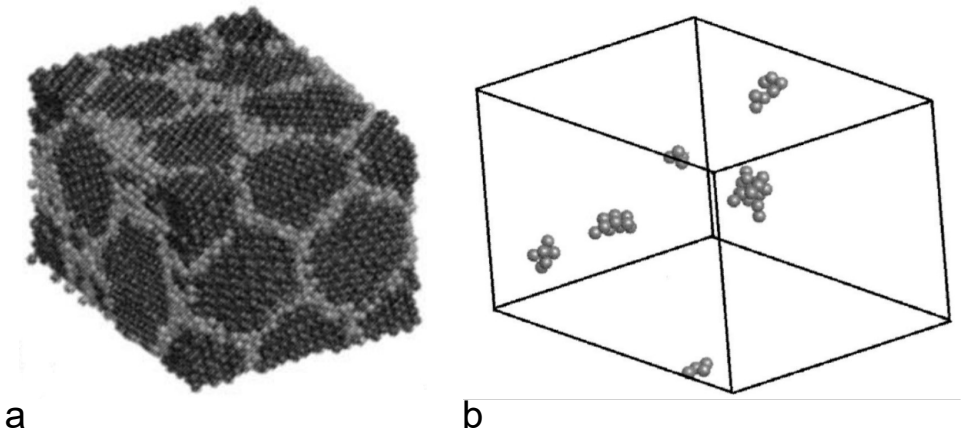

Figure 1.3: Atomic rearrangements observed at grain boundaries during MD simulations of mechanical deformation of a 3 nm average grain size sample of Ni. a, 3 nm average grain size simulation cell. Grain interiors are darker compared with grain boundary regions. b, Localized atomic rearrangements immediately after the onset of macroscopic yield. Reprinted Figures 1 and 3 from [40] with permission by the American Physical Society.

shear localization, which is sensitive to the thermal history and degree of relaxation of the grain boundaries [13, 47–49]. For materials with grain sizes between 20 - 50 nm, imperfections such as steps, kinks, and ledges at grain boundaries can act as stress concentrations, markedly affecting the nucleation and propagation of (partial) dislocations [26]. Experimentally, the evolution of grain boundary defects is argued to give rise to unusual processing effects present in nanocrystalline metals. A prominent example of this is 'relaxation' strengthening: hardening observed after low temperature annealing of nanocrystalline metals with no significant microstructural evolution or chemical enrichment of the boundary [43, 50]. This behavior is shown in Figure 1.5a,b, where the authors compared an as-refined nanocrystalline 316L stainless steel to an annealed condition, and found that the increase in hardness was due to the annihilation of grain boundary defects, rather than chemical enrichment of the boundary [50]. The motion of grain boundary defects, also known as disconnections, has been argued to underpin relax-

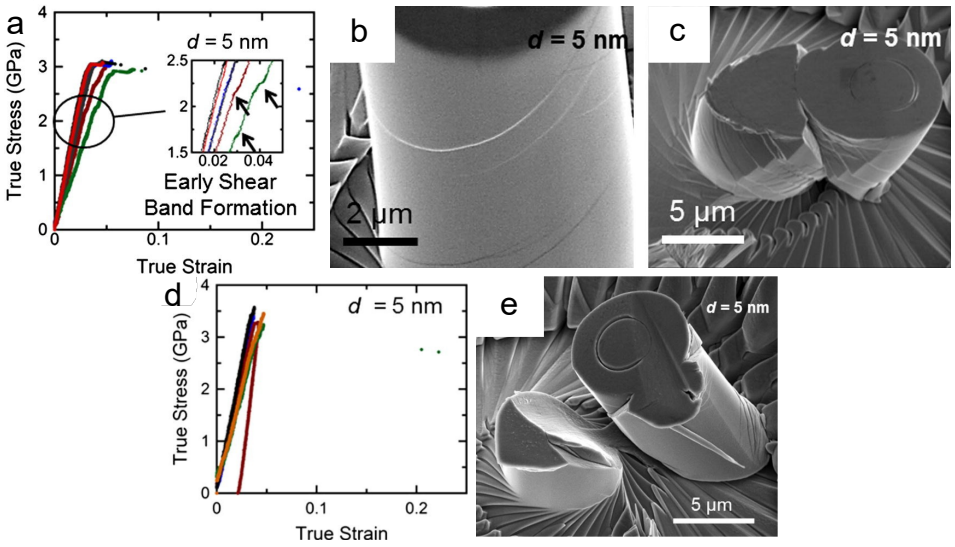

Figure 1.4: Evidence of shear localization in very fine grained nanocrystalline metals, as well as effect of initial grain size. a, Stress strain curves from as-deposited Ni-W samples. b, c, Deformed as-deposited Ni-W pillars with 5 nm average grain demonstrating the formation of several shear bands, also evident in the stress strain curve. d, Stress strain curve from annealed Ni-W pillars with 5 nm average grain size, demonstrating increased strength relative to the as-deposited condition. The annealed samples also exhibit negligible plasticity. e, Annealed, deformed 5 nm grain size pillar. The annealed sample exhibits catastrophic failure after the formation of a single shear band, whereas the as-deposited 5 nm sample exhibits several shear bands prior to failure. Reprinted from [42], with permission from Elsevier.

ation hardening and other unique phenomena in nanocrystalline metals, such as stress-assisted grain growth [51–55]. Disconnections are (bi)crystallographic defects confined to a grain boundary that consist of both dislocation content (b) and step height (h) [54], schematically represented in Figure 1.5c. The role of disconnections on stress-assisted grain growth can be readily seen by the disconnection pair in Figure 1.5c [54]. Under an applied shear stress (positive sense, which would result in the unconstrained black lattice being displaced to the right), the distance between the disconnections would enlarge, effectively increasing the area of white lattice by height h. Researchers demonstrated the importance and ubiquitous presence of disconnections in coarse grained materials as well, whose motion underpins many fundamental behaviors of grain boundaries, such as

grain growth [56], triple point motion [57], and others [54, 58].

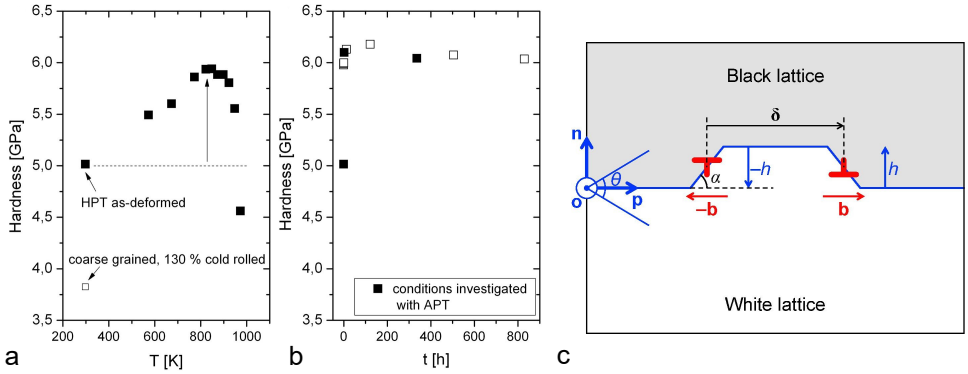

Figure 1.5: a, b, Hardness measured after annealing of a HPT refined nanocrystalline 316L stainless steel reproduced from [50]. c, Schematic of a disconnection pair at a bicrystal interface. Reprinted from [54], with permission from Elsevier.

In nanocrystalline metals with grain sizes below 20 nm, not only do grain boundary defects (i.e. disconnections) play an important role, but the structure of the grain boundary core itself also affects the macroscopic behavior of these materials. In contrast to grain boundaries with discrete disconnections, the atomistic structure of planar, disconnection-free grain boundaries can vary significantly. MD simulations have been used to study the effects of non-equilibrium grain boundary core structures on many physical phenomena, primarily the mechanical behavior [13, 47, 49, 59]. These studies use several approaches to generate a range of planar metastable grain boundary structures with fixed macroscopic degrees of freedom, such as varying the local atomic density of the grain boundary plane [54], displacing one grain relative to another by less than one unit cell [47], or other less intuitive algorithmic approaches [59, 60]. These studies illustrate that high energy, non-equilibrium grain boundary core structures promote intergranular deformation mechanisms, such as uncoordinated atomic shuffling at grain boundaries [61–64] and grain boundary sliding [33]. Researchers have experimentally observed several distinct grain boundary atomistic structures coexisting within a single grain boundary of a coarse grained material [65], reproduced in Figure 1.6 to illustrate

the presence of multiple grain boundary core structures in the absence of disconnection content. This multiplicity of grain boundary core structures has been argued to play a role in diffusional and other macroscopic properties of coarse grained polycrystalline metals as well [66].

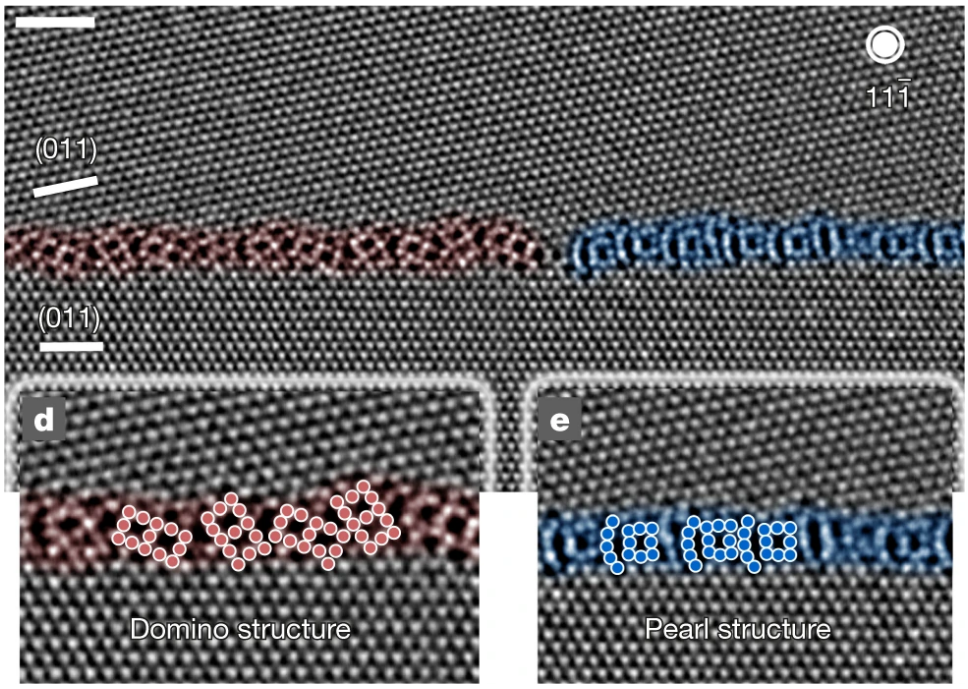

Figure 1.6: High resolution scanning electron microscopy image demonstrating the co-existence of two grain boundary core structures in Cu. The defect separating these two structures can be thought of as an anti-phase boundary line within the grain boundary. Reprinted with permission from Springer Nature [65].

Simulations of nanocrystalline metals with grain sizes below 10 nm have often reported multiple unusual grain boundary structures, however experimental characterization has remained elusive [36, 40, 44]. Nevertheless, grain boundary structure governs mechanical properties in the limit of small grain sizes, where atomistic shuffling [36] and other extremely localized intergranular deformation mechanisms dominate [23]. Extensive work on Ni-, Cu-, and Fe-based nanocrystalline alloys have shown that relaxation processing techniques, such as low temperature annealing and mechanical cycling with amplitudes

well below the global yield stress, isochemically relax grain boundary regions, causing an increase in strength with no modifications to grain size or grain interiors [23,36,43,44,50]. These processes reduce the grain boundary energy in these systems through the structural relaxation of non-equilibrium grain boundaries or the reduction in grain boundary defects [15, 44, 47]. Decreases in grain boundary energy or interfacial defect content increase the activation barrier to initiate plasticity, effectively increasing the strength of these relaxed nanocrystalline metals [67]. This behavior is demonstrated in the pillar compression experiments presented in Figure 1.4a,d, where low temperature annealing increases the yield strength, and in Figure 1.5 where annealing increases the hardness of the 316L sample. Figure 1.4 also demonstrates the significant effects of relaxation processing on deformation morphology. The annealed samples (Figure 1.4d) exhibit fewer operative shear bands compared to the as-deposited material (Figure 1.4b,c), which results in catastrophic failure with negligible plasticity.

The local chemistry of grain boundaries can also dramatically affect the mechanical properties of nanocrystalline alloys. Experiments and MD simulations have demonstrated that the presence of various atomic species at grain boundaries may serve as pinning or de-pinning points, affecting the ability of dislocations to traverse nanocrystalline grains [32, 68]. Rupert [68] demonstrated that this behavior depends strongly on the particular chemical species at the boundary, as well as the exact position of the solute in the grain boundary. Other MD studies have emphasized the effects of chemical segregation on grain boundary energy, which promote overall strength and dislocation-mediated deformation [67,69,70]. Lohmiller *et al.* showed that intragranular deformation mechanisms were promoted over intergranular mechanisms in alloyed systems vs. pure metals [41]. Furthermore, these authors observed that stress assisted grain growth, which occurred in the pure elemental system investigated, was suppressed by alloying. Other studies have noted the same behavior in systems with high concentrations of alloying

additions or impurities, suggesting that the presence of solute atoms at grain boundaries either eliminates grain boundary defects or hinders their motion [23,70–72]. Chemical and structural effects may also occur in concert, wherein solute segregation to grain boundaries has been shown to drive structural transformations at the grain boundary [66, 73]. These grain boundary structural transitions have dramatic effects on the properties of these materials, greatly enhancing ductility and thermal stability of several Cu- and Ni-based nanocrystalline alloys [73–76]. These reports collectively underscore the notion that the local atomic structure at grain boundaries plays a crucial role during the deformation of nanocrystalline metals.

1.2 Similarities to metallic glasses

Sensitivity to thermomechanical history and abundant structural disorder (i.e. low atomic coordination at grain boundaries) in nanocrystalline metals is reminiscent of fully amorphous metals or metallic glasses which are often described as the limit of grain refinement [77, 78]. Metallic glasses are metals lacking long range, periodic atomic structure [79]. Their unique combination of amorphous structure and metallic bonding impart many desirable properties, such as high strength, large elastic limit, low damping [80, 81], and interesting magnetic properties [82, 83]. Many researchers have noted similarities between the thermo-kinetic [84] and mechanical behavior of nanocrystalline metals and metallic glasses [21, 36, 40, 42–44, 77, 78, 85], such as pressure dependent yielding [36] and strong shear localization [42]. Many of these arguments arise from the similarity between the atomic structure of grain boundaries, whose atoms are inherently under-coordinated compared to those residing within the grain interiors, and the atomic structure in the bulk amorphous state. While such comparisons may not hold for the structure of grain boundaries that exhibit special, well ordered configurations [86], even well-ordered grain

boundaries can exhibit many metastable energetic configurations with fixed macroscopic degrees of freedom [47]. This large range in grain boundary energies accessible through micro-degrees of freedom is shown in Figure 1.7b for silicon (Si) [47]. The large degree of metastability of grain boundaries likely underpins the extreme processing sensitivity in nanocrystalline metals. This intrinsic metastability likely also gives rise to the similarities to metallic glasses, which are inherently metastable owing to their amorphous structure.

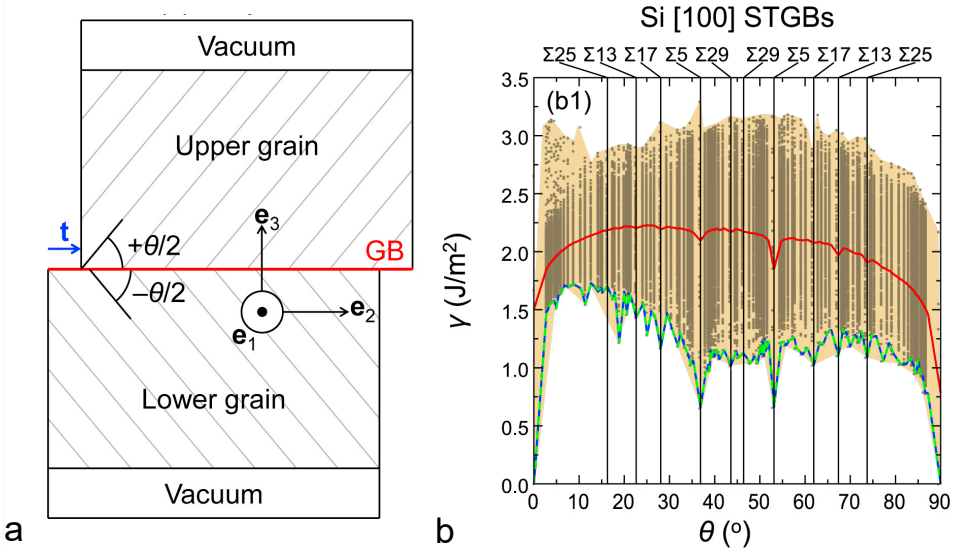

Figure 1.7: Grain boundary metastability observed during bicrystal MD simulations in [47]. a, simulation setup demonstrating micro-degree-of-freedom t - relative displacement of the grain boundary in e_2 direction. b, Simulated grain boundary energies as a function of misorientation. The red curve illustrates the non-equilibrium ensemble averaged grain boundary energy, whereas the blue and green curves are the minimum and equilibrium ensemble averaged grain boundary energies, respectively. The orange shaded region illustrates the broad range of grain boundary energies accessible via micro-degrees-of-freedom. Reprinted from [47], with permission from Elsevier.

Another way to view the apparent similarities between nanocrystalline metals and metallic glasses is to examine the degree of stored enthalpy each material can contain. This is shown in Figure 1.8, which is divided into three sections: coarse grained metals, nanocrystalline metals, and metallic glasses. Coarse grained metals exhibit the smallest

amount of stored enthalpy; it is only attained through severe plastic deformation such as cold rolling which increases the defect content of the alloy and the corresponding stored enthalpy [87]. Coarse graned metals subjected to conventional processing can exhibit stored enthalpies of 1-2% of their melting enthalpies (0.1-1 kJ mol^{-1}). Nanocrystalline metals, due to the high volume of grain boundaries and inherent metastability of these boundaries, exhibit substantially higher stored enthalpies compared to coarse grained metals [47,88,89], with a maximum stored enthalpy of $\approx$ 30-35% of their melting enthalpy (7-10 kJ mol^{-1}). Metallic glasses exhibit the highest degree of stored enthalpy. Due to their highly liquid-like structure, the stored enthalpy of metallic glasses can approach that of their melting enthalpy after extreme processing such as ion irradiation [87,90,91]. The trend present in Figure 1.8 shows that through the introduction of structural disorder, the degree of stored enthalpy available increases concomitantly. This disorder can be manifest in different forms: dislocation based in coarse grained metals, grain boundary related in nanocrystalline metals, or uniformly structural in amorphous metals. Furthermore, in systems with a large degree of stored enthalpy, processing sensitivity becomes much larger, and is directly related to the degree of stored enthalpy. This is evident by the large capacity for stored enthalpy accessible to both nanocrystalline metals and metallic glasses compared to coarse grained metals, as well as the numerous processing routes available to tailor the degree of stored enthalpy. Such processing sensitivity can be viewed as either advantageous for its high tailorability or detrimental due to lack of predictability of material properties.

Despite the numerous similarities between these two material classes, commonalities in the thermomechanical history and processing dependence between nanocrystalline metals and metallic glasses have received little attention. Mechanical properties of metallic glasses show a strong history dependence, where a more relaxed - i.e. a lower energy atomic configuration - glass has a higher yield strength and propensity for shear local-

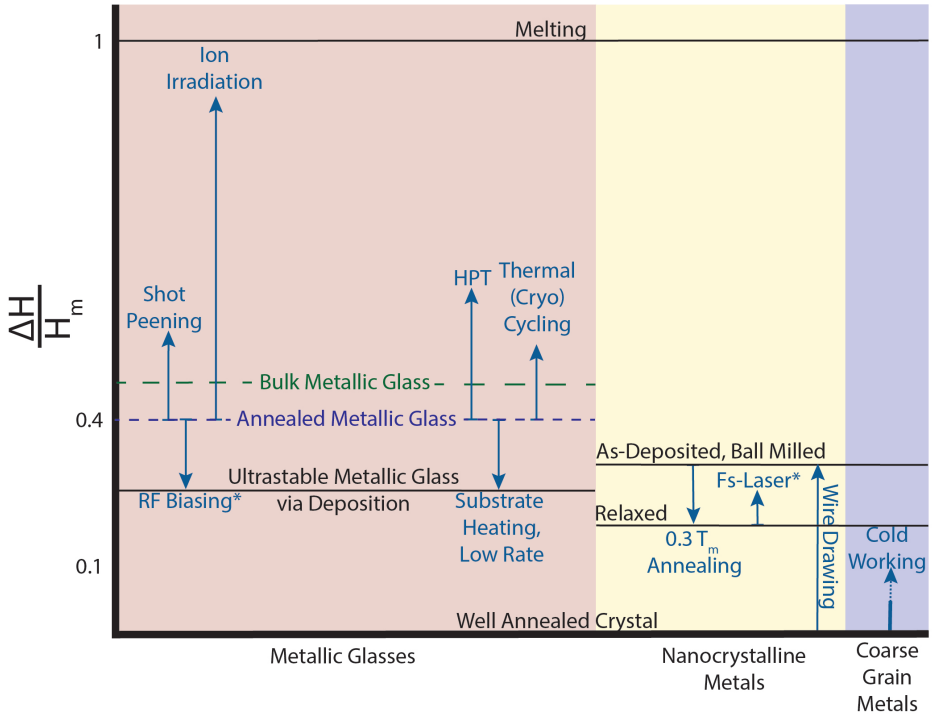

Figure 1.8: Stored enthalpy normalized by the melting enthalpy for metallic glasses, nanocrystalline metals, and coarse grained metals. Calculations were largely based on [87] for metallic glasses and coarse grained metals. Both experimental analyses of excess enthalpy, and estimates based on changes in mechanical properties (see [91]) were used for nanocrystalline excess enthalpies. Baseline values were also estimated by grain boundary volume fractions and corresponding grain boundary enthalpies [15].

ization [92]. Conversely, a more rejuvenated - i.e. higher in energy, more liquid-like - glass exhibits increased ductility with a lower yield strength [93]. Processing routes used to modify the energy of a metallic glass to exploit tunable properties have been studied extensively, notably to facilitate homogeneous plasticity at room temperature [93–98]. Relaxation processing routes are similar to those for nanocrystalline metals - low temperature annealing [92] and cyclic mechanical loading [99] both produce increases in yield stress and modulus of a metallic glass. Rejuvenation processes, largely unique to metallic glasses, include severe plastic deformation [94], and cryogenic cycling [95]. These processing routes induce local dilatational strains, producing structural modifications that

decrease the yield strength and modulus but increase the ductility of the metallic glasses. All of these processing routes are included in Figure 1.8, with arrows corresponding to the directional change in stored enthalpy. Rejuvenation of a metallic glass correlates with increases in free volume, stored enthalpy, and fictive temperature, but can more meaningfully be defined as an increase in energy of the system [87, 93–98]. The scientific understanding of rejuvenation processing and the physical properties of metallic glasses broadly have been greatly aided in recently years by potential-energy-landscape (PEL) analysis. In essence, the PEL is a description of the local energetic configurations of the glass with numerous metastable basins with different total and relative energies owing to the local atomistic structural motifs present in the material. These metastable transitions between motifs exhibit a broad spectrum of activation and relaxation energies which give rise to many of the unusual thermal properties of metallic glasses [100]. PEL analysis has greatly advanced structure-processing-properties relationships in metallic glass, as it enables a compact description of the effects of non-equilibrium processes, such as rapid quenching, annealing, and even mechanical deformation [100–103]. From a practical metallurgical perspective, PEL analysis of metallic glasses has informed processing techniques and enabled rejuvenation processing which has effectively mitigated many mechanical instabilities present in metallic glasses [87].

Rejuvenation processing has broadened applicability of metallic glasses by enabling precise control of mechanical properties via processing - promoting ductility and stable plastic deformation at room temperature in alloys that typically exhibit severe shear band formation and catastrophic failure. Nanocrystalline metals exhibit similar mechanical instabilities that limit their use and have a high degree of processing sensitivity. Therefore, the potential of rejuvenation processing routes to enhance their properties, particularly in mitigating catastrophic shear localization, is tantalizing. Despite these strategies being recently employed for metallic glasses, to date only one processing strat-

egy, which involves femtosecond laser processing and annealing, has been identified that can bi-directionally tailor the state of grain boundaries. This strategy, the the subject of Chapter 3 of this thesis, represents a promising opportunity to enhance the properties of nanocrystalline metals by applying lessons in the metallic glass community.

1.3 Thermal behavior of nanocrystalline metals

While there are numerous similarities between the mechanical behavior of metallic glasses and nanocrystalline metals, the amorphous structure of metallic glasses that enables their unique properties renders them susceptible to crystallization, which severely limits their use in engineering applications. Nanocrystalline metals offer many of the advantages of metallic glasses and can also withstand significantly higher temperatures due to their crystalline domains. Nevertheless, the presence of large interfacial volumes between these crystalline domains can render nanocrystalline metals susceptible to thermal coarsening, but several alloy design strategies have been largely successful in mitigating these thermal instabilities.

1.3.1 Thermodynamics of nanocrystalline metals

Understanding the thermodynamics and kinetics of grain growth and their respective driving forces are essential for mitigating thermal instabilities in nanocrystalline metals. For a closed system, the change in internal energy (dU) at a constant temperature (T), pressure (P), and chemical potential (μ) is a function of the change in entropy (dS), volume (dV), number of atoms (dN), and interfacial area (dA):

$$dU = TdS - PdV + \Sigma\mu_i dN_i + \sigma dA \tag{1.3}$$

This expression assumes a constant interfacial energy (σ). It is also useful to define the change in enthalpy (dH), which is accessible through experimental efforts, and the change in Gibbs free energy (dG) of the system, which provides the thermodynamic driving force under typical experimental conditions:

$$dH = TdS + VdP + \Sigma\mu_i dN_i + \sigma dA \tag{1.4}$$

$$dG = \Sigma\mu_i dN_i + \sigma dA \tag{1.5}$$

By inspection of Equations 1.4 and 1.5, it is clear that a reduction in the interfacial area (A) would produce a decrease in the free energy and enthalpy of the system. This reduction in the free energy provides a thermodynamic driving force for thermally driven grain growth, which is a paramount concern in nanocrystalline metals. Practically, nanocrystalline metals contain a large interfacial area (A) and thus exhibit a large driving force for microstructural coarsening. Such a large driving force for grain growth has rendered many nanocrystalline metals unstable, even at low homologous temperatures. Gertsman *et al.* [104] reported grain growth of nanocrystalline copper prepared through inert gas atomization after storage at room temperature. Similar behavior has been reported in other pure elemental nanocrystalline metals, such as silver and palladium [105, 106].

Alloying pure, elemental nanocrystalline metals with chemical species that exhibit a high enthalpy of segregation is the most common way of limiting microstructural coarsening in nanocrystalline metals. The primary objective of alloying pure nanocrystalline metal is to decrease the grain boundary energy, σ in Equation 1.5, effectively reducing the thermodynamic driving force for coarsening. Weissmuller [107], using similar formulations to that of Gibbs and Cahn [108], derived the following expression for the decrease

in grain boundary energy due to the presence of excess solute at the grain boundary in the dilute limit:

$$\sigma = \sigma^0 - N_\beta(\Delta H^{seg} + RTln(\frac{N_\beta^m}{N^m})) \tag{1.6}$$

where:

$$\Delta H^{seg} = \Delta H^{sol}_{\beta in \alpha} - \Delta H^{sol}_{\beta in GB} \tag{1.7}$$

From Equation 1.6, it is evident that in systems with a positive enthalpy of segregation (ΔH^{seg}), there will be a reduction in the grain boundary energy (σ) through the additions of the solute species (β), and their enrichment of the grain boundary (N_β). The model is schematically illustrated in Figure 1.9. Through the addition of solute (β), which tends to sit at grain boundary sites, the microstructure can be divided into crystalline domains consisting of predominantly α (unshaded regions in c, d) and grain boundary regions consisting of both α and β. This analysis, coupled with semi-empirical Miedma-type [109–112] models for solution enthalpies has enabled the synthesis of numerous nanocrystalline systems which exhibit significantly improved thermal stability, such as Ni-W, W-Ti, Fe-Zr, and others [113–115, 115, 116].

A different approach to stabilizing nanocrystalline metals is to focus on suppressing the kinetics of grain growth. The velocity (v) of a grain boundary driven under thermal excitation is proportional to the grain boundary mobility (M) and the thermodynamic driving force for grain growth, the grain boundary energy (γ or σ) [117]:

$$v \propto M\gamma. \tag{1.8}$$

Equation 1.8 demonstrates that decreasing either the thermodynamic driving force or the mobility of the grain boundary will serve to decrease the velocity of the grain boundary, effectively limiting thermal coarsening. General strategies to suppress the kinetics of grain

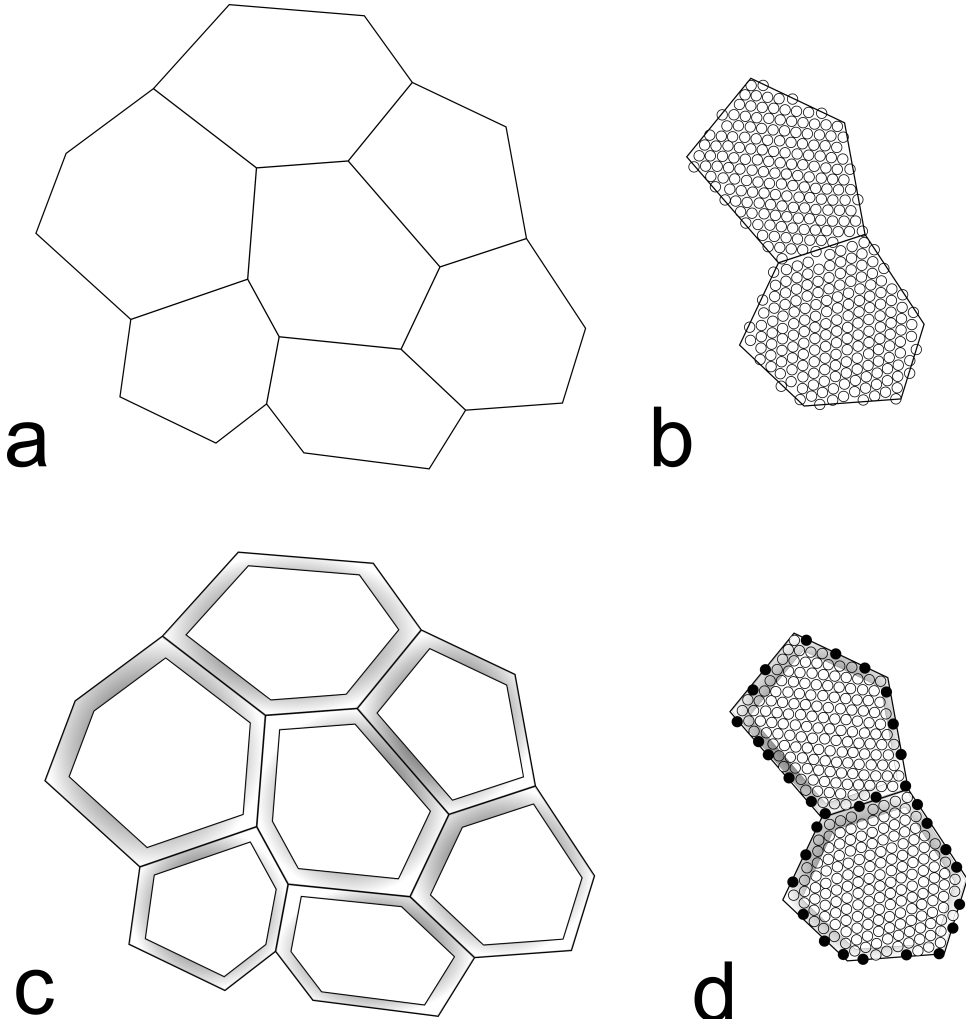

Figure 1.9: Grain boundary segregation model from Weissmuller [107]. a, b macro and microscopic view of pure polycrystalline material. c, d, macro and microscopic view of alloyed polycrystalline material. Gradient filled regions in c, d are used to illustrate the grain boundary regions, which are distinct from the crystalline grain interiors in formulations used in [107]. Black circles in d illustrate solute additions.

growth primarily focus on reducing the grain boundary mobility (M) through alloying to induce clustering or precipitation at the grain boundaries. Unlike thermodynamic reductions in grain boundary energy, reductions in mobility are generally the result of grain boundary pinning, also known as Zener pinning. Zener's model is widely utilized for understanding grain growth processes in coarse grained alloys with dispersoids or

precipitates, which effectively pin the grain boundary as it moves [118–120]. This model does not directly account for the atomistics of grain boundaries. As such, researchers have argued Zener's model is not directly applicable to nanocrystalline metals, but that it serves as a general motivation for kinetic strategies of imparting thermal stability. This approach has been demonstrated in alloys which exhibit phase separation or clustering at grain boundaries, such as immiscible fcc-bcc combinations like Cu-Nb [121, 122], Cu-Ta [123, 124] and Cu-Mo [13, 125] alloys. Nanocrystalline alloys that exhibit such clustering or phase separation are some of the most thermally stable alloys to date and have many desirable properties such as high creep resistance [123].

1.3.2 Atomistic structure of grain boundaries and thermal behavior

Not only does the atomistic structure of grain boundaries dramatically affect the mechanical properties of nanocrystalline metals, grain boundary structure also significantly affects the thermal behavior of nanocrystalline metals. The presence of multiple grain boundary structures [65] is thought to underpin many unusual phenomena in coarse grain materials, such as abnormal grain growth [126] and unusual diffusion behavior [127, 128]. In nanocrystalline metals, the high volume fraction of grain boundaries suggests that the effects of this metastability may exacerbate thermal instabilities, potentially giving rise to the numerous reports of abnormal grain growth in nanocrystalline metals, Ni especially [129–134].

While the multiplicity of grain boundary states may underpin several prominent thermal instabilities in nanocrystalline metals, researchers have demonstrated that through processing and alloy design, the presence of metastable grain boundaries can be beneficial for microstructural stability. Researchers have emphasized the role of amorphous inter-

granular films on thermal stability of several nanocrystalline alloys, primarily Cu-Zr-base systems [73]. These alloys are resistant to coarsening after tens of hours at temperatures near their melting point [75], indicative of the most promising thermal stability exhibited by a nanostructured metal to date. The experimentally observed amorphous structure and impact on thermal stability in a Cu-Zr alloy is presented in Figure 1.10, where the presence of the amorphous intergranular film serves to provide microstructural stability at temperatures near the melting point. Several other alloys have been identified that exhibit amorphous intergranular film formation with controlled processing, such as Cu-Hf and Ni-Zr [125]. Expansion into multicomponent alloying [135] has demonstrated that materials design / alloying strategies [125] to induce amorphous structural motifs at grain boundaries may be broadly applicable across many alloy systems, rather than the limited ones currently identified.

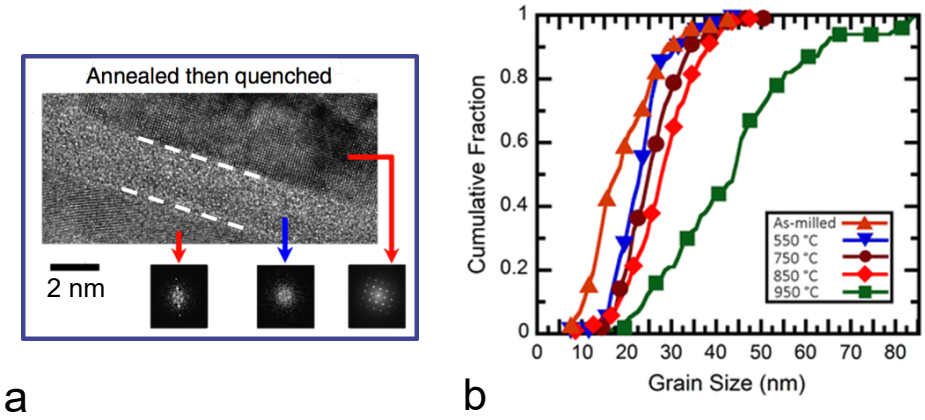

Figure 1.10: a, Experimental observation of amorphous intergranular film in Cu-3Zr from [73]. b, Thermal stability of Cu-3Zr after 1hr annealing times. Reprinted by permission Springer Nature [75].

The underlying thermodynamic argument for the enhanced stability imparted by amorphous intergranular films is the competition between interfacial energies of the crystalline-amorphous interface and the grain boundary energy. In order for an amorphous intergranular film to form, the amorphous-crystalline interface energy must be

less than half of the grain boundary energy [136–139]. A more complete description accounting for the energy of formation of the amorphous content is expressed in Equation 1.9, where the amorphous interfacial state with thickness h, free energy of formation (ΔG_{am}) and corresponding interfacial energies γ_{gb} and γ_{sl} will only form if the inequality is satisfied.

$$\Delta G_{am} \times h < \gamma_{gb} - 2\gamma_{sl} \tag{1.9}$$

This can also be interpreted from a macroscopic perspective, where the presence of the interfacial state has effectively reduced the grain boundary energy, resulting in a reduction in the driving force for coarsening [139]. There may be additional benefits to nanocrystalline metals with amorphous intergranular films, such as sluggish grain boundary diffusion, that also promote thermal stability. While these descriptions of interfacial states at grain boundaries are counter to Gibbsean descriptions of bulk phases, these unusual grain boundary structures play a decisive role in the properties of nanocrystalline metals.

1.4 Outstanding questions

The scientific understanding of the mechanical and thermal behavior of nanocrystalline metals has greatly improved over the past several decades, including detailed thermodynamic and kinetic approaches to imparting thermal stability and experimental efforts to provide mechanistic insight into nanocrystalline deformation behavior. However, the ability to design or tailor nanocrystalline alloys to be thermally stable, resistant to catastrophic shear localization, or, most importantly, ***both***, by targeting grain boundaries remains elusive due to the limited understanding of grain boundary structure-property relationships. Furthermore, the effects of targeted processing and alloying on

grain boundary structure have not been systematically investigated, presenting an exciting opportunity for scientific investigation. The high degree of processing sensitivity, explicit similarities in deformation behavior [21], and the recent promise demonstrated by the incorporation of amorphous interfacial structures on the thermal [140] and mechanical properties [73] of nanocrystalline metals suggest that the understanding of nanocrystalline metals can be greatly improved by the cross-pollination from disparate scientific communities, specifically from the metallic glass community; yet, these commonalities have not been viewed, let alone thoroughly explored, as a potential avenue to address the limitations of nanocrystalline metals.

1.5 Overview & objectives

In this thesis, I will present the results of several experimental efforts exploring selective processing and interface-aware alloying strategies to target grain boundaries, and the effects of these strategies on the mechanical and thermal instabilities in nanocrystalline alloys. These processing routes and alloying strategies were motivated by similar strategies elucidated in the metallic glass literature to improve macroscopic ductility and glass formability. First, I will present results of an investigation into the role of processing - specifically femtosecond laser processing - on mechanical properties of a variety of nanocrystalline alloys in order to demonstrate the potential of non-equilibrium processing to tailor the properties of nanocrystalline metals. Next, I will discuss a novel Al-Ni-Ce nanocrystalline alloy which exhibits remarkable thermal and mechanical properties, owing to the complex chemical and structural evolution of the grain boundaries. This thesis work originated as a natural extension of previous investigations of the Gianola Group focusing on the mechanical behavior of nanocrystalline Al-base alloys performed by Dr. Mo-Rigen He and investigations of metallic glasses performed by Dr. Daniel J. Mag-

agnosc. These previous studies highlighted the sensitivity of nanocrystalline metals to the grain boundary structure, as well as the definitive role metastability plays in the mechanical properties of metallic glasses. Such expertise enabled investigations of both processing effects and multicomponent alloying on grain boundary structure and properties. This work was funded through a National Science Foundation Early-Concept Grant for Exploratory Research (NSF-EAGER) to design more damage tolerant nanocrystalline materials for use in micro-electro-mechanical system (MEMS) applications. I was funded additionally through a National Science Foundation Graduate Research Fellowship Program (NSF GRFP) fellowship.

The structure of this thesis is as follows. Chapter 2 presents experimental methods and approaches for investigating the role of grain boundary structure on properties of nanocrystalline metals, including material synthesis, femtosecond laser experiments, indentation and electron microscopy techniques. Chapter 3 presents results of the femtosecond laser irradiation experiments performed on a variety of nanocrystalline alloys. This chapter also includes a discussion of the underlying physics responsible for the marked change in behavior of the laser irradiated material. Chapter 4 focuses on the mechanical and thermal properties of the nanocrystalline Al-Ni-Ce alloy using ex-situ characterization techniques. Chapter 5 is a detailed discussion on the origin of the enhanced thermal stability of the nanocrystalline Al-Ni-Ce alloy, including Monte-Carlo modeling efforts and *in-situ* electron microscopy experiments. Chapter 6 discusses the elevated temperature mechanical properties of the Al-Ni-Ce alloy measured via elevated temperature indentation. Chapter 6 also includes a discussion of corresponding deformation mechanisms and modeling efforts used to predict the maximum thermal exposure prior to microstructural evolution and mechanical degradation.

1.6 Permissions and attributions

- The work presented in Chapter 3 is the result of a collaboration with Dr. Charlette Grigorian and Professor Timothy Rupert from the University of California, Irvine, Zhitong Bai and Professor Yue Fan at the University of Michigan, and Dr. McLean Echlin, Professor Tresa Pollock, and Professor Daniel Gianola from the University of California Santa Barbara. This chapter was previously published in *Acta Materialia* [141]. Balbus, G. H., Echlin, M. P., Grigorian, C. M., Rupert, T. J., Pollock, T. M., & Gianola, D. S. (2018). Femtosecond laser rejuvenation of nanocrystalline metals. *Acta Materialia*, 156, 183-195. Reproduced with permission of the authors who retain copyright: https://doi.org/10.1016/j.actamat.2018.06.027

- The work presented in Chapter 4 is the result of a collaboration with Dr. Fulin Wang and Professor Daniel Gianola. The chapter was previously published in *Acta Materialia* [142]. Balbus, G. H., Wang, F., & Gianola, D. S. (2020). Suppression of shear localization in nanocrystalline Al-Ni-Ce via segregation engineering. *Acta Materialia*, 188, 63-78. Reproduced with permission of the authors who retain copyright: https://doi.org/10.1016/j.actamat.2020.01.041

- The work presented in Chapters 5 and 6 is the result of a collaboration with Johann Kappacher, Professor Verena Maier-Kiener, and Professor Daniel Kiener from Montanuniversität Leoben (Austria); Dr. David Sprouster and Professor Jason Trelewicz from Stony Brook University; Professor Timothy Rupert from the University of California, Irvine; and Dr. Fulin Wang, Dr. Yolita Eggeler, Dr. Jungho Shin, and Professor Daniel Gianola from the University of California, Santa Barbara. Much of these chapters has been submitted to *Nature Materials*. Balbus, G. H., Kappacher, J., Sprouster, D. J., Wang, F., Shin, J. H., Eggeler, Y. M.,

Rupert, T. J., Trelewicz, J. R., Kiener, D., Maier-Kiener, V., & Gianola, D. S. Disordered Interfaces Enable High Temperature Thermal Stability and Strength in a Nanocrystalline Aluminum Alloy, *Submitted*.

- Additional discussion in Chapter 7 regarding the effects of laser processing on grain boundary structure was the result of a collaboration with Zhitong Bai and Professor Yue Fan at the University of Michigan [143]. Other collaborations briefly discussed here include contributions from Dr. Oliver Renk, Professor Verena Maier-Kiener, and Professor Daniel Kiener from Montanuniversität Leoben (Austria).

Chapter 2

Materials and Methods

Experimental investigations into the structure of grain boundaries, particularly those in nanocrystalline metals, are notoriously challenging. Grain boundaries are spatially confined, largely lack long range periodicity, and are extremely sensitive to processing, all of which hinder many traditional experimental techniques. Furthermore, due to the grain sizes of the materials of interest (5 - 50 nm), isolation, let alone characterization, of a single boundary is challenging. Nevertheless, recent advancements in electron microscopy have greatly expanded our capabilities for characterizing grain boundaries, and the effects of changes in grain boundary structure are evident when probing ensemble properties, as in more conventional experimentation such as mechanical testing and thermal analysis.

In this chapter, several synthesis techniques utilized to produce the nanocrystalline metals that will be reported in this thesis will be discussed, as well as processing techniques utilized to modify grain boundary structures. Next, mechanical and thermal testing techniques utilized to probe ensemble effects of grain boundary metastability will be presented. Finally, structural characterization techniques such as transmission electron microscopy will be briefly outlined, including specific sample preparation techniques for *in-situ* heating experiments.

2.1 Materials synthesis

Nanocrystalline alloys investigated in this thesis were prepared using three synthesis techniques: sputter deposition, high pressure torsion, and ball milling. The majority of samples utilized in this thesis, as well as the only samples prepared at UCSB, were prepared by sputter deposition, which will be discussed first. A brief discussion of high pressure torsion, as well as the comparative advantage of synthesis via severe plastic deformation will follow. Ball milling will not be discussed in great detail, as all samples prepared by ball milling were made by Dr. Charlette Grigorian in Professor Timothy Rupert's group at the University of California, Irvine, but the sample preparation details for materials utilized in this work will be presented.

2.1.1 Sputter deposition

Sputter deposition is a thin film synthesis technique where an energetic gaseous plasma is utilized to eject material from a source, often referred to as the 'target'. The material ejected from the source is then collected, or deposited, onto a substrate. The process by which the plasma removes material from the target is known as sputtering, which lends its name to the synthesis process. Schematically, this process is shown in Figure 2.1.

In order to strike and maintain the plasma used to deposit material, high power magnetrons are utilized to generate large electric potentials and magnetic fields near the target. In the presence of a process gas at low pressure, the large potentials generated across the magnetrons can 'ignite' and maintain a plasma of the process gas. Modern sputter deposition systems use specially designed shielding and plasma geometries to direct the ejected material towards the substrate, resulting in relatively high sputtering yields. Argon was utilized as the process gas for all synthesis in this work, and is typically

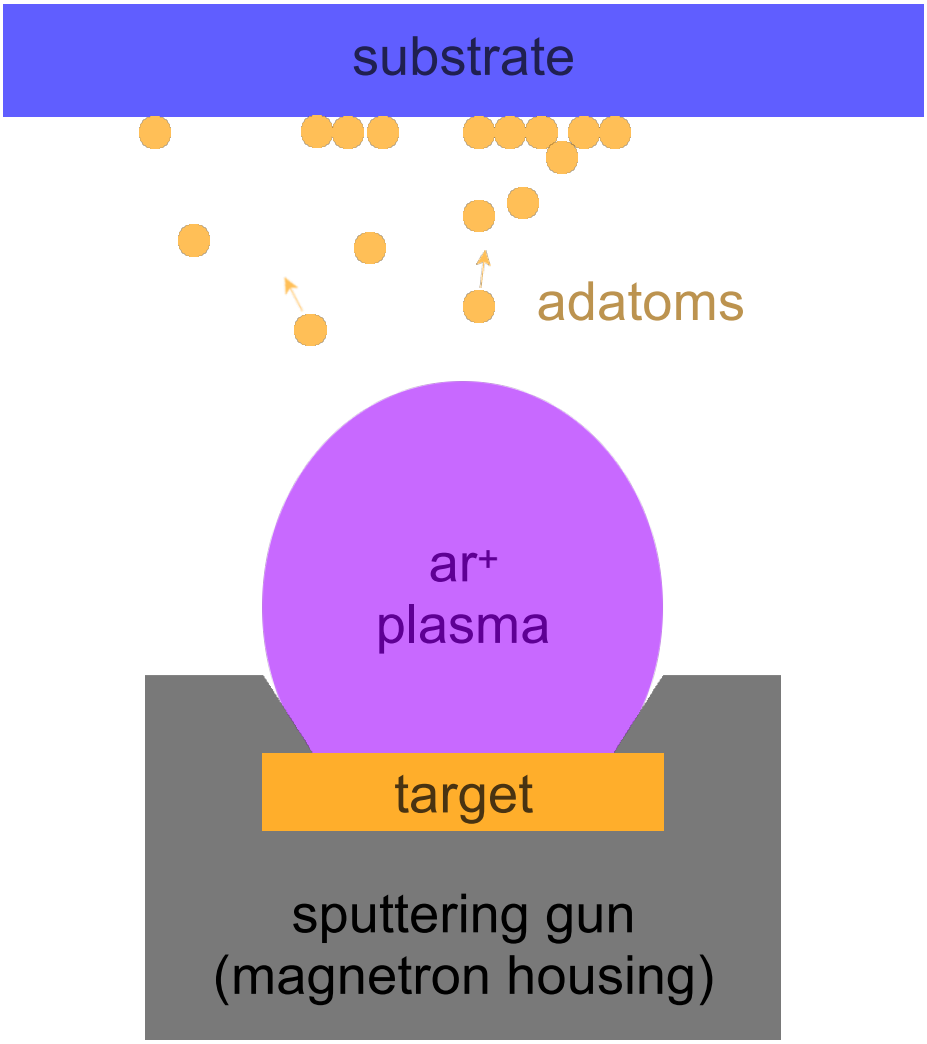

Figure 2.1: Sputter deposition schematic.

used due to its non-reactivity; other process gasses such as nitrogen or oxygen can be used during reactive sputter deposition of nitride or oxide films. For additional information regarding plasma formation, various effects of process gas pressure, substrate temperature, etc. the reader is referred to the textbooks by Ohring [144] and Vossen [145]. Additional detailed instructions on the operation of the AJA sputter chamber located in the Materials Processing Lab at UCSB are included in the Appendix.

Sputter deposited Al-O films utilized in the study presented Chapter 3 were prepared

by Dr. Mo-Rigen He as described in [71, 72] using an Explorer 14 Sputtering system (Denton Vacuum) at Bryn Mawr college.

Al-Ni-Ce sputtered materials were synthesized in an AJA ATC 1800 sputter deposition system. The alloy composition was controlled using confocal DC sputtering from two, 2-inch diameter sputter targets, of pure Al (99.999% purity) and pre-alloyed $Al_{87}Ni_7Ce_6$ (at. %, 99.95% purity) purchased from Angstrom Sciences. Sputtering was performed using a power of 100 W for the pure Al target and 175 W for the alloyed target, resulting in a net deposition rate of 0.27 nm s^{-1}. Base pressures prior to each deposition were below 10^{-7} Torr. All depositions were performed using a processing chamber pressure of 3 mTorr Ti-gettered Ar. To promote a nanocrystalline microstructure, the targets were shuttered every 36 seconds for 5 seconds. This procedure was performed on a variety of substrates and thicknesses for different subsequent experimental investigation. 1 μm thick samples were deposited on Si (100) wafers for mechanical testing, onto soda lime glass wafers for X-ray studies, and on single crystal NaCl wafers for ultrafast calorimetry. Electron transparent (40 nm) samples were deposited onto Cu transmission electron microscopy (TEM) grids with C support films for (S)TEM analysis, as well as onto Protochips Fusion E-chip heating devices with C support films for *in-situ* (S)TEM heating.

2.1.2 High pressure torsion

High pressure torsion (HPT) is a severe plastic deformation technique where material is subjected to large compressive and torsional stresses to induce grain refinement. Several excellent overviews of the science behind dislocation cell formation and grain refinement via HPT, as well as practical limitations, applications, etc. are referenced here [146–148]. Practically, HPT is performed by placing a small (1-2 cm diameter) sample between two large anvils, loading the sample in compression, and then rotating one anvil to induce

torsional stresses on the material. This process is schematically shown in Figure 2.2.

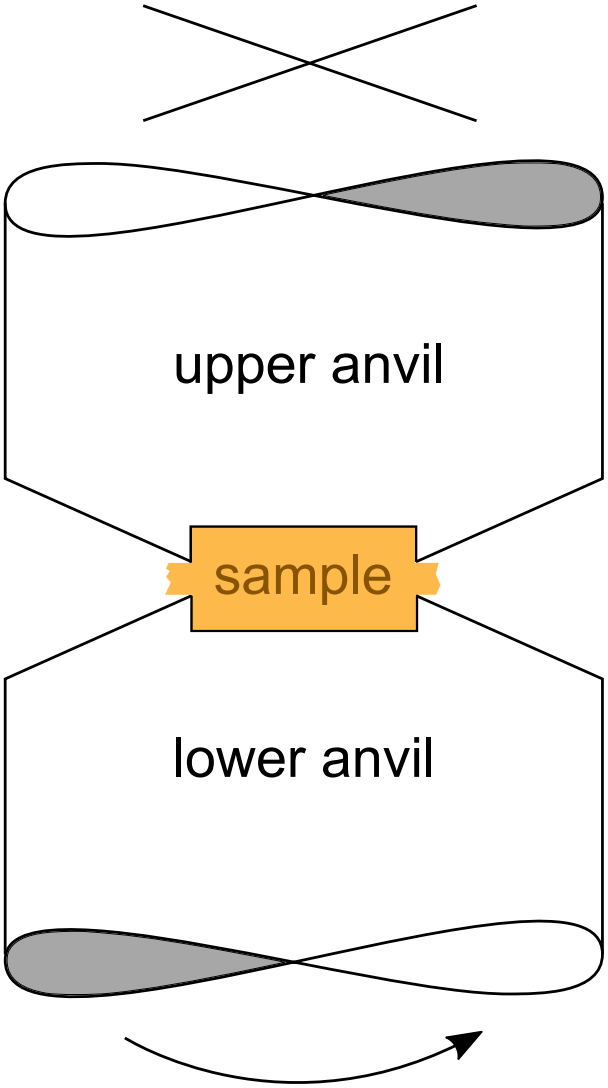

Figure 2.2: HPT Schematic. The arrow signifies the rotation of the lower anvil relative to the upper anvil. Adapted from [149]

HPT is advantageous over other synthesis methods because it does not necessarily introduce impurities into the sample during grain refinement, which can markedly affect the grain refinement process. This enables somewhat independent control of sample chemistry and grain size. Unlike continuous sputter deposition, where the grain size is generally linked to thickness or impurity (dopant) concentration, the sample chem-

istry in HPT is controlled prior to deformation, and the degree of grain refinement is dependent upon the total shear strain imposed during deformation [149, 150]. This enables theoretically independent control of grain size and chemistry. In practice, this is somewhat less straightforward, as the steady state HPT grain size (i.e. the grain size at which additional shear strain will not induce additional changes in grain size) is strongly sensitive to chemistry. Often, the outputs generated by HPT apparatuses are limited, sometimes providing only the rotation and torque. This makes controlling the precise level of grain refinement a priori challenging. Additional complications arise in multiphase alloys, where the dissolution of intermetallic compounds during HPT strongly affects the chemical distribution of the sample. While possible, materials generated with multiphase precursor materials frequently exhibit non-uniform dissolution of precursor phases, resulting in a heterogeneous chemical distribution that can affect the properties of the refined material.

The specific procedures utilized to produce nanocrystalline 316L steel samples utilized in this this are as follows. 6 mm diameter rods of 316L stainless steel were cut into segments with a thickness of 0.8 mm. These disks were then loaded into two tool steel HPT anvils and compressed at 7.2 GPa. While holding this pressure, the lower anvil was rotated 10 turns at 0.2 RPM, resulting in an equivalent strain of 136. Electron microscopy revealed a resultant average grain size of 20 nm. Annealing of this sample was performed at 550 °C for 1 hour under Ti-gettered Ar at ambient pressure. Additional details on high pressure torsion experiments can be found in [151].

2.2 Ball milling details

Nanocrystalline Cu-3 at.%Zr samples were prepared using mechanical ball milling in a SPEX SamplePrep 8000M Mixer/Mill to produce powders with μm-sized particle

diameters and nm-sized grains. Powders were milled for 10 hours using a hardened steel vial and milling media, and stearic acid in the amount of 2 wt.% was added as a process control agent. Annealing treatments were performed at 950 °C in vacuum for one hour to promote Zr diffusion to grain boundaries and allow for the formation of amorphous intergranular films (AIFs). Samples were then either rapidly quenched in water or slowly cooled in air from the annealed state. Rapidly quenching stabilized the microstructure at high temperature, including any AIFs present at grain boundaries. It is important to note that AIFs are not found at every GB throughout the microstructure, and a variety of complexion types and thicknesses are commonly found within a given sample. In [73,75], AIFs as thin as 0.5 nm and as thick as 5.7 nm were observed in a quenched Cu-Zr sample; however, sharp grain boundaries were also present within the same sample.

2.3 Femtosecond laser irradiation

Femtosecond (fs) laser processing, while not necessarily a synthesis method for producing nanocrystalline metals, presents a unique modality to impose large stresses and temperatures in extremely short times. Fs laser-material interactions are fundamentally different from longer pulse or continuous wave laser-material interactions due to the disparity in timescales between electronic excitation (fs) and phonon-electron relaxation (ps). This difference in timescales facilitates a largely athermal, mechanical ablation process, which is useful in mitigating damaged zones during machining [152]. High fluence fs-laser processing has been used extensively for micromachining, enabling serial sectioning and micromechanical sample preparation, as well as other applications where material removal with minimal residual damage is required [153,154]. Many experimental observations and computer simulations have studied the ablation behavior of materials exposed to high fluence fs-laser irradiation [152,155–161]. Fs-laser irradiation can also be

used as a small scale experimental technique to simulate high strain rate shock phenomena in materials. For more detailed explanations on various facets of fs-laser-material interactions, the reader is referred to Refs. [152, 162].

Recent simulations have indicated that grain size affects fs-laser ablation. Fs-laser-material interactions within grain boundary regions are fundamentally different than in bulk crystalline regions due to spatially heterogeneous electron-phonon coupling behavior [158]. While the majority of the investigations into fs-laser-matter interactions have been focused on high fluence ablation behavior, hybrid two-temperature model/molecular-dynamics simulations have indicated that at energies below the ablation threshold, significant tensile and compressive stresses can be induced by the laser [158, 159]. The resulting combination of high stresses, short timescales, largely athermal processing, and potential confinement to grain boundary regions suggests that the fs-laser processing may have the characteristics necessary to induce structural modifications to grain boundaries.

Laser treatments investigated in this thesis were performed using a Clark MXR CPA-2110 Series Ti:Sapphire Ultrashort Pulse Laser with a 1 kHz repetition rate, 780 nm wavelength, and 150 fs pulse width in air (22 °C, 42-70% relative humidity). The output power variability of the laser was less than 1%. The beam was attenuated with a series of neutral density filters and a rotating half-wave plate followed by a p-polarized beam splitter before being focused down by a 500 mm focal length plano-convex lens with a $\frac{1}{e^2}$ radius of 30.8 μm measured as described in [163]. Average laser energies were measured using an Ophir Photonics High Sensitivity Thermal Laser Sensor. All experiments were conducted with an average power in the range of 0-15 mJ, corresponding to fluences of 0-0.5 J cm^{-2}. Ablation thresholds were characterized by performing a series of non-overlapping single pulse arrays at fluences between 0.037 J cm^{-2} and 0.3 J cm^{-2} in increments of 0.015 J cm^{-2}. The onset of ablation was determined by measuring changes in sample height across the irradiated regions using an Asylum MFP-3D

atomic force microscope in tapping mode, following the procedure in [164]. These values and corresponding errors are presented in Table 2.1. To collect sufficient information for subsequent nanomechanical evaluation, areas of ≈ 0.01 mm^2 were irradiated with single pulses by translating the stage 10 μm between subsequent laser pulses, as illustrated in Figure 2.3a-c. Figure 2.3d shows an area that was irradiated with a fluence above the ablation threshold, which is included to demonstrate the process. Figure 2.3e shows an area treated with a fluence below the ablation threshold with no obvious changes to the surface. The fluences reported are the average single pulse fluences measured prior to treatment. Due to the slight overlapping pulse geometry, the reported number of pulses is a lower bound on the effective pulse count experienced by the sample.

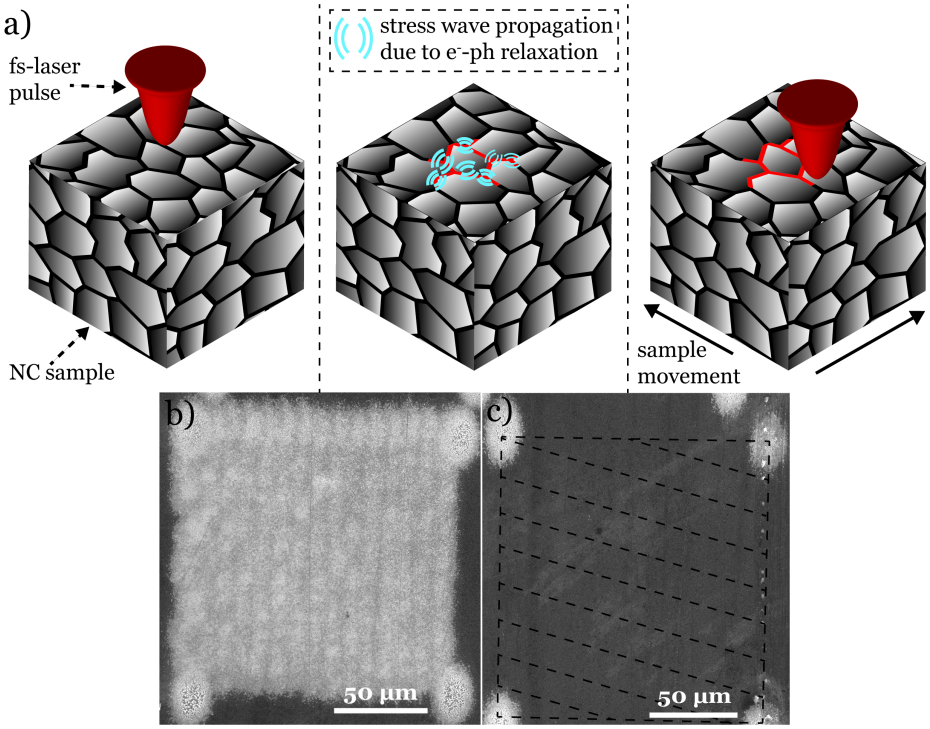

Figure 2.3: a) Schematic showing the fs-laser treatment procedure. A single fs-pulse irradiates the NC sample, which then emits elastic waves. Once this process has completed, the sample is translated and irradiated with a series of pulses until the desired irradiated area is reached. b) SEM image of the Al-4.8 at.%O sample irradiated with a fluence above the ablation threshold. The four lighter areas on the corners of the square are fiducial marks. c) SEM image of the Al-4.8 at.%O sample irradiated with a fluence below the ablation threshold. Dashed lines indicate region that has been irradiated.

Table 2.1: Summary of samples utilized in femtosecond laser studies presented in Chapter 3 - chemistry, average grain size, and optical parameters obtained from literature, as well as non-irradiated indentation hardness and ablation thresholds.

Material	$\boldsymbol{t_{film}}$ **(nm)**	$\boldsymbol{C_{solute}}$ **(at. %)**	$< d >$ **(nm)**	$\mathbf{H}_o$ **(GPa)**	**Ablation Threshold J cm^{-2}**	**Optical Absorption Coefficient** κ	**Optical Penetration Depth** δ **(nm)**
Al-0.8 at.%O	156	0.8 ± 0.1	84	1.5 ± 0.3	0.2 ± 0.02	8.46	7.3
Al-4.8 at.%O	210	4.8 ± 0.5	19	2.3 ± 0.7	0.15 ± 0.02	8.46	7.3
Q-Cu-Zr	*	3 ± 0.1	42	1.5 ± 3.0	0.6 ± 0.33	4.82	13
SC-Cu-Zr	*	3 ± 0.1	43	1.5 ± 3.0	0.7 ± 0.50	4.82	13

* Q-Cu-Zr and SC-Cu-Zr are powder samples prepared by ball milling.

2.4 Mechanical characterization - nanoindentation

To probe the effects of processing (e.g. fs-laser, annealing) and alloying on mechanical properties, indentation, specifically nanoindentation, was utilized. Indentation is a relatively inexpensive, high throughput mechanical testing technique where a hard tip with a known shape is driven into a material. The force and displacement of the tip are measured as it plastically deforms the material, and using contact mechanics [165], the properties of the deformed material can be extracted. Nanoindentation, where the load, displacement, and speed of the tip can be precisely controlled at nm or sub-nm resolution (routine with modern actuators) enables the measurement of site specific mechanical properties, such as hardness and modulus, as well as rate dependent properties (strain rate sensitivity, activation volume). Nanoindentation also enables investigation of both incipient plastic deformation behavior (dislocation activation) and mechanical properties of small volumes of material (such as thin films) [165–169].

All room temperature experiments were performed using a Nanomechanics iMicro system equipped with a 50 mN actuator (Nanomechanics iNano head) and a diamond Berkovich tip. Constant strain rate tests were performed with two testing protocols: the factory standard 'Advanced Dynamic E and H.NMT' and a custom method written by Prof. Dr. Verena Maier-Kiener named 'SRTest.NMT.' While both methods are capable of constant strain rate indentation, the factory standard method does not reach the set strain rate until depths of $\approx$ 100 nm, whereas the custom method reaches the set strain rate at depths as shallow as 5 nm. This is demonstrated in Figure 2.4. Thus for any rate-sensitive measurements where the factory standard method was used, the instantaneous (depth resolved) properties (hardness, modulus) at the instantaneous strain rate were utilized, rather than the set-point strain rate value. These values were also compared with data extracted from larger depths where the strain rate was more stable. For

indentation experiments of fewer than 50 indents, the tip area function of the Berkovich tip was calibrated on a fused silica standard prior to testing. For extremely depth sensitive experiments (e.g. fs-laser irradiation in Ch 3), for experiments with more than 50 indents, or on very hard materials (refractories), the tip area function was calibrated prior to testing and re-measured after testing to ensure that the tip area function had not evolved considerably during the experiment. All data was collected operating the machine using the continuous stiffness method (CSM), where a dynamic oscillation is superimposed during loading to measure hardness and elastic modulus as a function of depth [168]. Measurements on thin films were performed on data collected at depths $< 10\%$ of the film thickness to minimize substrate influence when possible. When not possible, such as for 100-200 nm thick Al-O films, a Saha-Nix [170] approach was utilized and values were extracted from depths of $\approx 30\%$ of the film thickness.

Elevated temperature nanoindentation experiments were performed by Johann Kappacher (Montanuniversität Leoben, Austria) on 1 μm thick samples deposited onto Si using a Nanomechanics InSEM Nanoindenter equipped with a 50 mN load cell. Hardness measurements were performed with a diamond Berkovich tip indenter manufactured by Synton-MDP at an indentation strain rate of 0.1 s^{-1}. The tip area function was calibrated on fused silica before all experiments [168]. Separate samples were utilized for each testing temperature in order to simplify the effects of any complicated heating / testing protocol. These experiments were performed from a unique sample which was heated from room temperature to the specific testing temperature at 10 °C min^{-1}, held at temperature for 2 hours to minimize temperature gradients prior to indentation, tested for $\approx$ 1.5 hours, and then cooled to room temperature at 10 °C min^{-1}. No systematic variation in strength was observed during the 1.5 hour test time. The hardness values were averaged between 180 and 220 nm indentation depth. Room temperature hardness and modulus data for thirteen indents performed on the as-deposited material are pre-

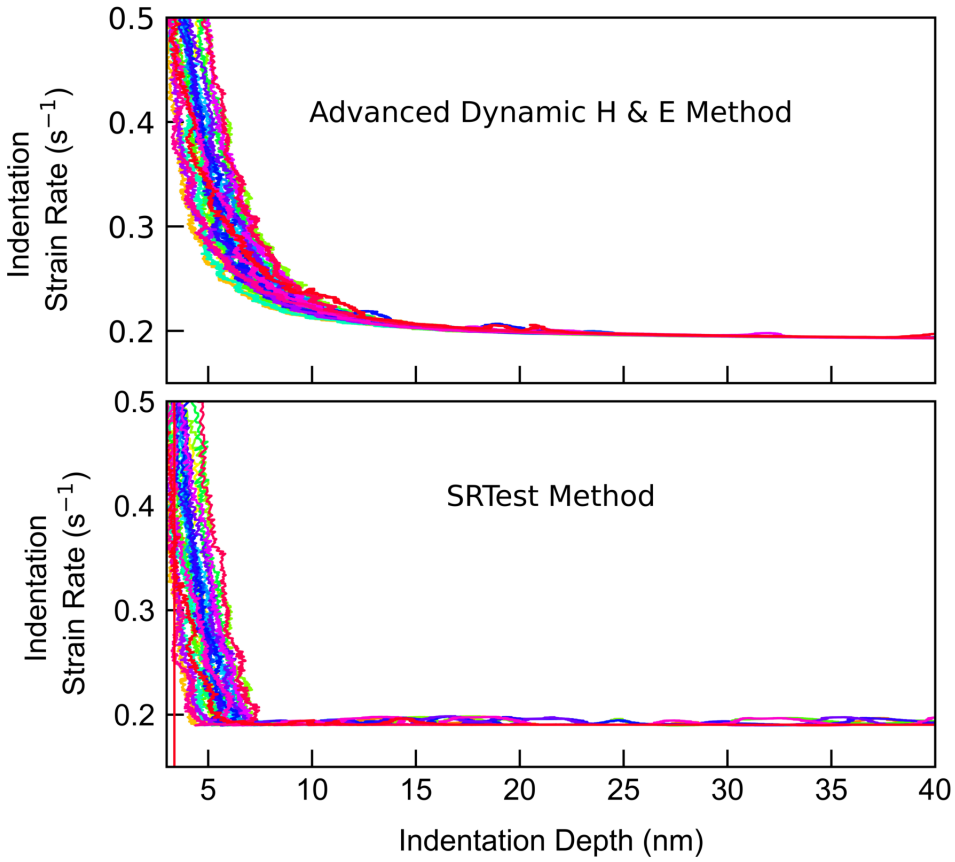

Figure 2.4: Indentation strain rate values during indentation on (100) Si wafer. Top: factory standard 'Advanced Dynamic H & E' method. Bottom: custom 'SRTest' method. It is hard to see from these plots, but the strain rate from the factory method never actually attains the setpoint (it is always off by ≈ 0.01 s^{-1}.)

sented in Figure 2.5, demonstrating the influence of the Si substrate. The modulus data is significantly affected by the substrate, whereas the hardness data is largely substrate insensitive. This can be ascertained as the hardness of single crystal (100) Si exceeds 10 GPa [171], but a significant increase in hardness at large depths is absent in Figure 2.5. Thus, while the hardness data presented is extracted from depths larger than 10% of the film thickness (100 nm), the hardness values are representative of intrinsic material behavior. The depth selected for hardness measurements was chosen to optimize between minimal substrate influence, and was enough penetration to minimize geometrical inac-

curacies, instabilities, and transient behavior of the testing platform. Furthermore, the hardness values are not significantly different than those extracted from an indentation depth of 100, but the stability of the testing platform improves at larger penetration depths at elevated temperature. Strain rate jump tests were performed by reducing the strain rate from 0.1 s^{-1} to 0.01 s^{-1} at a depth of 200 nm, and jumping back to 0.1 s^{-1} at a depth of 350 nm to elucidate the strain rate sensitivities and activation volumes, as described in Ref. [167, 172].

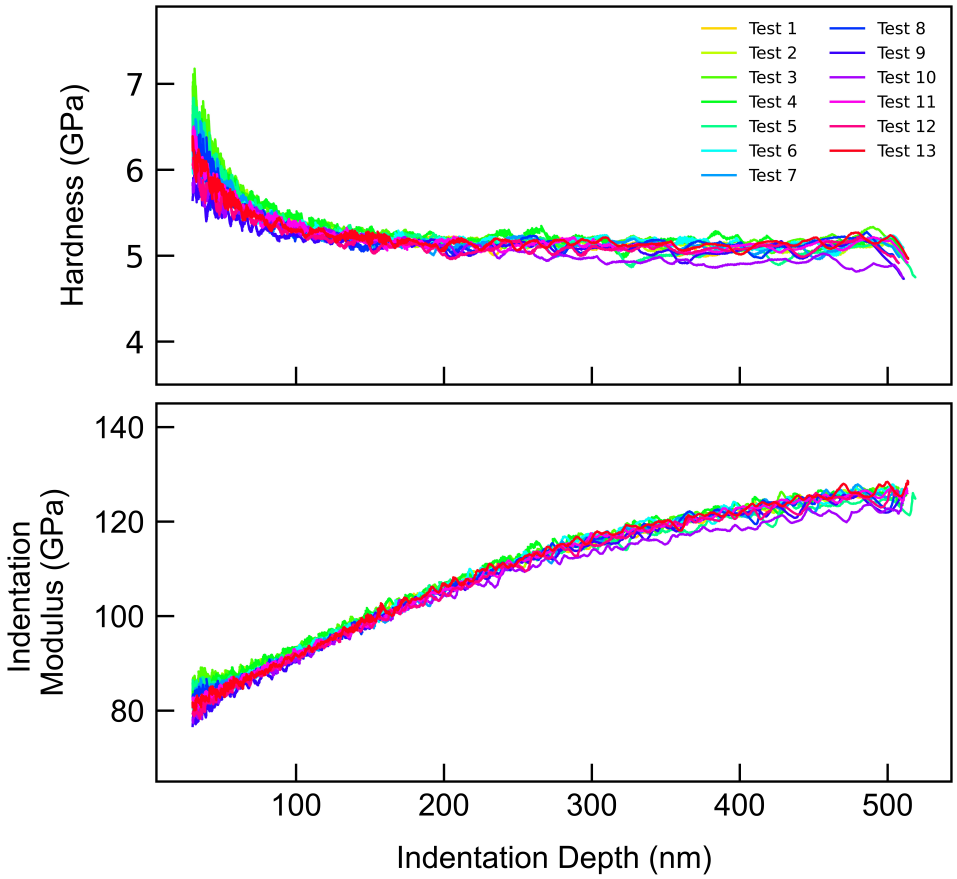

Figure 2.5: Depth resolved indentation hardness and modulus for the as deposited Al-Ni-Ce alloy.

2.5 Thermal characterization

Thermal stability is an outstanding problem plaguing nanocrystalline metals. Thus thermal characterization, through static annealing and various dynamic thermal analysis techniques are necessary to gain insight into the effects of processing and alloying.

Ex-situ annealing studies were performed using either a quartz tube furnace in a Ti-gettered Ar environment ($<10^{-8}$ ppm O_2) to minimize additional oxidation, or in the AJA sputter deposition chamber under ultra high vacuum (10^{-7} Torr). *In-situ* annealing studies in the electron microscope will be discussed in the next section.

Ultrafast or flash differential scanning calorimetry (DSC) was performed using a Mettler Toledo Flash DSC 2+ device. DSC is a thermal analysis technique where two crucibles - one with the sample of interest, another with a known reference material - are heated at the same rate, and the heat flow required to maintain the samples at the same temperature throughout the heating protocol is recorded. The difference between these two heat flow signals exhibits signatures of thermally activated processes that either release (exothermic) or require (endothermic) external thermal energy to maintain the same temperature. From the quantification of these signatures in the differential signal, heat capacity, enthapies of phase transformations, and many other quantitative thermal measurements can be performed. The Flash DSC 1/2+ device relies on a MEMS-based SiN heater that can access heating and cooling rates up to 10^4 K s^{-1} and is capable of detecting thermal signatures from very small masses of material. One limitation of this testing platform is that, unless the samples have a known melting enthalpy and can be melted directly onto the chip (often damaging the sensor), the masses of material are difficult to measure. As such, quantifying the absolute values of exothermic and endothermic events is challenging. However, quantitative information can be extracted by varying the heating rate during DSC runs, and applying the Kissinger analysis [173–175].

By measuring the peak temperature associated with a thermal event at different rates, the activation energy associated with the process can be estimated.

DSC heating runs presented in Chapter 5 were performed under an Ar atmosphere at ambient pressure. Silicone oil was used as a contact medium to ensure adequate thermal contact between the sample and the heater. All heating chips were calibrated prior to testing. After application of silicone oil, the chip was heated and cooled repeatedly to measure the background signal introduced by the silicone oil, as well as uniformly distribute the oil on the heater membrane. 1 μm thick Al-Ni-Ce samples were first floated off from NaCl wafers in steam distilled H_2O, dried, and manipulated onto a glass slide for sectioning. The sample was then cut using a razor blade to fit within the $\approx$ 100 μm diameter heater on the Mettler Toledo UFS heating chip. A single hair brush was used to manipulate the sectioned sample from the glass slide onto the chip. The chip was then loaded into the Flash DSC 2+ device and heated from 25 °C to 425 °C at a set heating rate. A new sample was used for each heating rate, given the irreversibility of the thermal evolution in the Al-Ni-Ce alloy. The same UFS chip was utilized for all of these studies.

2.6 Structural characterization

Three modalities of diffraction experiments were utilized to investigate the structure and deformation morphology of nanocrystalline metals investigated in this work: scanning electron microscopy, transmission electron microscopy, and transmission X-ray diffraction in the synchrotron.

Conventional scanning electron microscopy (SEM) was utilized to investigate the surface morphology of Al-O and Cu-Zr samples after laser processing, as well as after nanoindentation of Al-Ni-Ce samples to study the pile up behavior around and beneath

the indenter. These experiments were performed in a FEI Thermo-Fisher Teneo FE-SEM, Apreo-S FE-SEM, and an Apreo-C FE-SEM. Surface characterization was performed at low accelerating voltages to minimize the interaction volume and increase surface sensitivity. All experiments were performed below 5 kV, with some as low as 2 kV in the Apreo systems.

Transmission electron diffraction experiments in the transmission electron microscope (TEM) and in the SEM (TSEM) were also utilized to study processing and deformation effects on nanocrystalline metals. TSEM experiments were performed on Al-O films to investigate microstructural effects of fs-laser irradiation. These were performed in the Teneo system at 30 kV, 0.4 nA, and using an annularly-segmented scanning transmission electron microscopy detector. Both bright and dark field conventional TEM were used to investigate the microstructure of the Al-Ni-Ce alloys. TEM experiments were performed using either an FEI Technai G2 Sphera TEM (Chapter 4) or FEI Thermo-Fisher Talos (S)TEM (Chapters 4-6). Dark field (DF) TEM was used to generate grain size distributions of the alloy after various thermal exposures, as well as investigate deformation behavior of the alloy. DF TEM experiments were performed with a small (10 μm) objective aperture on various segments of the {111} and {200} diffraction rings. High angle annular dark field (HAADF) scanning transmission electron microscopy (STEM) in the TEM provided insight into chemical evolution of the Al-Ni-Ce alloys during both *ex-* and *in-situ* annealing studies. The STEM modality in the TEM enables simultaneous acquisition of HAADF, annular DF, and BF STEM images, which was beneficial during *in-situ* annealing studies to differentiate the effects of chemical re-ordering (HAADF) and grain orientation evolution (ADF / BF). Electron dispersive x-ray spectroscopy (EDS) is also possible using the SEM and STEM, which provided more quantitative chemical information than the HAADF images alone, which are primarily sensitive to atomic mass (Z) contrast.

In-situ heating experiments on the Al-Ni-Ce alloy were performed using Protochips Fusion e-chip devices. In order to mask off electrical contacts and other portions of the Protochips Fusion chips during sputter deposition, two small cleaved pieces of Si wafers were manually clipped on to the surface of the Protochips Fusion chip so that just the region with the C support film was exposed during deposition. Schematically, this is shown in Figure 2.6. It is necessary to perform depositions from the top-side of the Protochips device, as depositing conductive material on the underside connects the heating elements and disturbs the temperature calibration on the chip. *In-situ* heating experiments were performed while collecting images at 2048 X 2048 resolution using BF, ADF, and HAADF detectors. These experiments were performed at a constant heating and cooling rate of 0.5 °C s^{-1}. The dwell time was calibrated such that each image was acquired over $\approx$ 0.5 s. A custom powershell script was utilized to record timestamps of image acquisition on the computer controlling the Protochips device in order to sync the experiments in post-processing. Samples were heated to a set temperature, held at temperature, and cooled back to room temperature while acquiring STEM images. Before and after each heating segment, selected area diffraction patterns (SADPs), EDS spectra, and conventional BF and DF TEM images were recorded. Set-point temperatures of 100 °C, 200 °C, 325 °C and 380-450°C were chosen in order to compare with *ex-situ* heating experiments. EDS spectral maps of 1000 X 1000 pixels were collected by summing at least 60 individual spectral images collected with a 4 s dwell time per pixel. HAADF-STEM images were simultaneously acquired with EDS spectral maps. Chemical profiles were generated using Velox (Thermo Fisher Scientific) or, in cases where there was not sufficient chemical resolution to investigate pixel-wise data, post-processed in HyperSpy [176] to rebin the data. This interrupted heating profile enabled the acquisition of multiple datasets during evolution of the microstructure to provide insight into both the structural and chemical evolution of the Al-Ni-Ce alloy system.

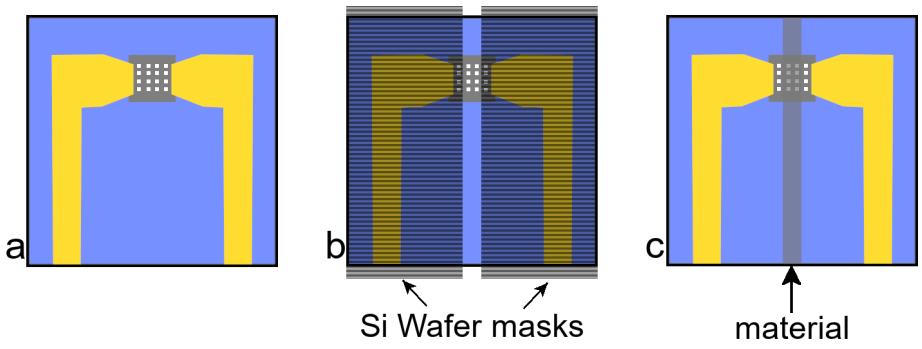

Figure 2.6: Protochips e-chip masking schematic. a, pristine protochip top surface with Au contacts exposed. b, schematic positioning of Si wafer pieces as masks to prevent deposition onto electrical leads / heater. c, after deposition with narrow strip of conductive material not in contact with leads or heating elements.

Transmission x-ray diffraction experiments on Al-Ni-Ce samples were performed by Dr. David Sprouster at the National Synchrotron Light Source-II (Brookhaven National Laboratory, Upton, NY) using beamline 28-IDI. All measurements were performed with an amorphous silicon-based flat panel detector (PerkinElmer) mounted orthogonal to the beam path and centered on the beam. The sample-to-detector distances and tilts of the detector relative to the beam were refined using a Nickel powder standard. The wavelength of the incident x-rays was 0.1666 Å (74.42 keV). 80 patterns were collected for each sample and the two-dimensional images were then averaged together and radially integrated, to obtain the one-dimensional diffraction patterns. The amount of film material in the X-ray beam is minimal (compared to the substrate), and the film signal is <1 % of the total volume in the X-ray beam. In order to eliminate the signal from the substrate, the scattering component from the glass substrate was subtracted from the diffraction patterns. The diffraction patterns collected were corrected for PDF-specific corrections (self-absorption, multiple scattering and Compton scattering) and converted to atomic PDFs, G(r), over a Q-range of 1-20 $Å^{-1}$ using PDFgetX3 [177] software.

Chapter 3

Femtosecond Laser Rejuvenation of Nanocrystalline Metals

In this chapter the effects of sub-ablation-threshold fs-laser irradiation on the mechanical properties of several nanocrystalline alloys are explored. These results suggest a material agnostic reduction in hardness by up to 90% due to sub-ablation-threshold fs-laser irradiation in nanocrystalline metals, without any evidence of microstructural evolution, namely grain coarsening. The magnitude of the softening observed is sensitive to the energetic or structural state of the grain boundaries, as illustrated by two Cu-Zr samples with different thermal histories, and is reversible by annealing at low temperatures. These results suggest that targeted processing can locally modify grain boundary structure, enabling significant tunability in mechanical properties, and potentially mitigating catastrophic shear localization in nanocrystalline metals.

3.1 Femtosecond laser irradiation background

Rejuvenation processing routes, which have been extremely beneficial in improving the room temperature ductility of metallic glasses, has not been reported in nanocrystalline metals. Rejuvenation processing routes for metallic glasses categorically occur quickly and at low temperatures in order to suppress any competing structural relaxation [87]. A previously unexplored processing technique that possesses these characteristics is pulsed ultrafast laser processing. Unlike longer pulse laser-material interaction, which have been used as heat sources for processing both nanocrystalline metals and metallic glasses [178–180], femtosecond (fs) pulse laser-material interactions are fundamentally different due to the difference in timescales between electronic excitation (fs) and phonon-electron relaxation (ps) [181]. This difference in timescales facilitates a largely athermal, mechanical ablation process, which is useful in mitigating damaged zones during machining [152]. High fluence fs-laser processing has been used extensively for micromachining, enabling serial sectioning and micromechanical sample preparation, as well as other applications where material removal with minimal residual damage is required [153, 154]. Many experimental observations and computer simulations have studied the ablation behavior of materials exposed to high fluence fs-laser irradiation [152,155–161]. Recent work has highlighted the effects of grain boundaries on fs-laser irradiation due to the spatially heterogeneous electron-phonon coupling behavior due to structural disorder [158], as well as the significant tensile and compressive stresses that can be induced at low energies [158, 159]. The resulting combination of high stresses, short timescales, largely athermal processing, and potential confinement to grain boundary regions suggests that the fs-laser processing may have the characteristics necessary for rejuvenation of grain boundaries, analogous to processing developed by the metallic glass community.

We hypothesize that the stresses generated by the fs-laser at energies below the ablation threshold may be used to modify the mechanical behavior of nanocrystalline metals via short-range atomic rearrangements at grain boundaries, where when incurred due to thermal and mechanical cycling have been shown to cause dramatic shifts in mechanical properties with negligible microstructural evolution. In this chapter, several measurements demonstrating the influence of sub-ablation threshold femtosecond laser pulses on location-specific properties of nanocrystalline Al-O and Cu-Zr, materials selected to explore a range of different grain boundary chemical and structural states, will be reported. These results suggest that sub-ablation femtosecond laser pulses cause a dramatic and recoverable reduction in hardness accompanied by negligible changes in grain size, reminiscent of rejuvenation processes in metallic glasses.

3.2 Sample selection for fs-laser processing

Samples were deliberately selected to give insight into the effects of grain size, chemistry, and grain boundary energy state on sub-ablation threshold fs-laser treatments. The two nanocrystalline Al samples demonstrate the effect of grain size and solute concentration. The grain size of these samples can be controlled during deposition by varying the amount of O incorporated during sputter deposition, which serves to pin grain boundaries. This behavior and the effect of O impurities on the mechanical behavior of Al films has been shown extensively in Ref. [71]. Bright field (BF) TEM images of both as-deposited Nanocrystalline Al samples are shown in Figure 3.1a, b. Comparison between the Cu-Zr samples enables us to explore the effects of the initial grain boundary state on fs-laser treatments for a fixed grain size, as both quenched (Q-Cu-Zr) and slowly cooled (SC-Cu-Zr) Cu-Zr samples have the same chemistry and grain size. Comparing the effects of sub-ablation threshold fs-laser irradiation on these alloys to the Al samples provides

insight across material systems. Due to the two sample preparations for the Cu-Zr alloy - quenching and slowly cooling from high temperature - the samples possess different initial grain boundary states. The quenched sample possesses an amorphous intergranular film (AIF), which is a metastable, non-equilibrium grain boundary structure at room temperature where the laser treatments are performed. AIFs are at equilibrium at elevated temperature and form in these alloys due to the propensity for Zr to segregate to grain boundaries, which reduces the energetic penalty for the formation of an amorphous film. The amorphous structure is thought to form at grain boundaries due to the interfacial energy and the locally high concentration of Zr in Cu, which exhibits good glass formability [73]. BF and high resolution TEM (HRTEM) images of the quenched sample are shown in Figure 3.1c, e, where the presence of this amorphous region is demonstrated by the mottled region outlined in the image. Slowly cooling the samples resulted in atomistically sharp grain boundaries, as shown in the BF and HRTEM images in Figure 3.1d,f. Any treatment used to modify the structure of the boundary would be expected to be sensitive to the initial energetic configuration, and thus manifest in different mechanical responses.

3.3 Hardness variations

We first begin by investigating the effects of grain size in the nanocrystalline Al samples on the hardness measured before and after fs-laser irradiation. Figure 3.2a shows the hardness of the coarsest grained Al-0.8 at.%O sample (average grain size of 80 nm) irradiated by the fs-laser at various sub-ablation fluences, and indicates no significant variation in the hardness. Deviations from the initial hardness are observed after the onset of ablation, and the variability in these measurements also increases at high laser energies. The ablation threshold of the Al-0.8 at.%O sample occurred at a fluence of 0.2

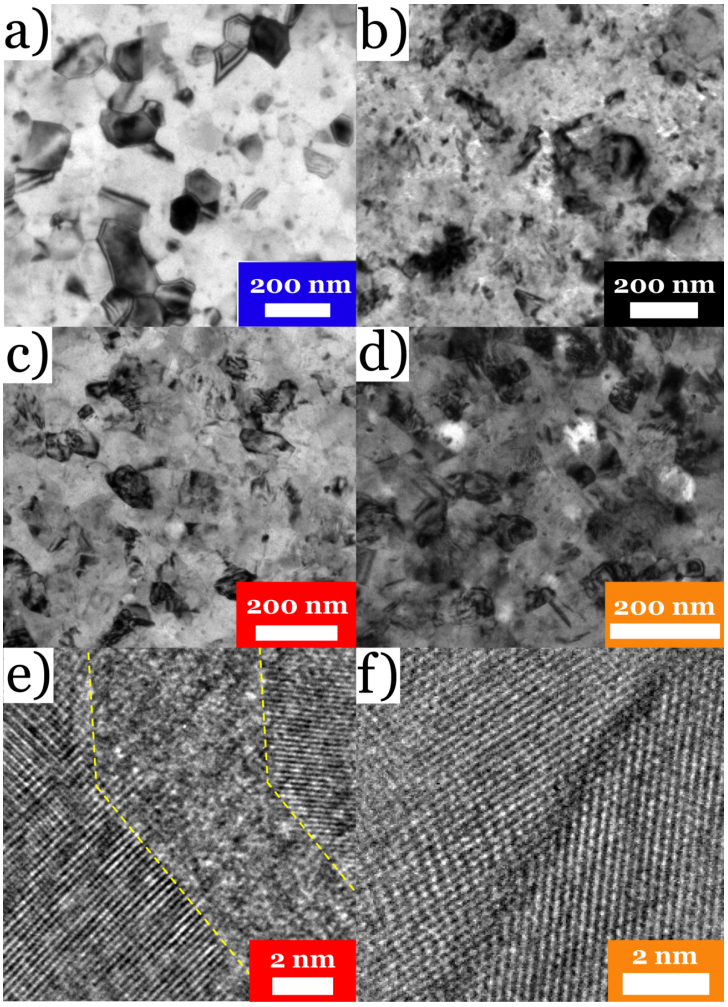

Figure 3.1: TEM images of all samples utilized in this study. a) BF image of Al-0.8 at.%O sample. Corresponding data plotted in blue. b) BF image of Al-4.8 at.%O sample. Corresponding data plotted in black. c) BF TEM image of Q-Cu-Zr, corresponding data plotted in red. d) BF TEM image of SC-Cu-Zr, corresponding data plotted in orange. e) HRTEM image of Q-Cu-Zr, amorphous region indicated by dashed yellow lines. f) HRTEM image of SC-Cu-Zr. No amorphous region is present at the grain boundary shown.

$\pm$ 0.02 J cm^{-2}. This agrees well with literature values for fs-laser ablation of Al, which range from 0.1-0.19 J cm^{-2}, suggesting that dilute amounts of oxygen incorporation do not dramatically affect the ablation threshold compared to pure Al [158, 182]. Figure 3.2b shows the hardness of the Al-4.8 at.%O sample after similar laser treatments, where

a dramatic decrease in hardness of up to 80% ($\approx$ 2 GPa) is observed at energies nearing the ablation threshold. The hardness of the Al-4.8 at.%O monotonically decreases with increasing laser fluence. The inset shows several representative load-displacement curves from the untreated and 0.066 J cm^{-2} treated region, where the peak load is significantly lower for the fs-laser irradiated sample. The ablation threshold was measured at 0.15 $\pm$ 0.02 J cm^{-2}, 25% lower than the Al-0.8 at.%O sample. While decoupling the effects of impurity incorporation and grain size are difficult for these samples, this result suggests that either the reduction in grain size or increased O content, or some combination thereof, determines the material susceptibility to fs-laser-induced changes in hardness and ablation behavior.

The influence of grain boundary state on the mechanical response of samples subjected to sub-ablation-threshold fs-laser irradiation was investigated in the Q- and SC-Cu-Zr samples. These samples have nominally identical chemistries and grain sizes, but with different grain boundary structures. Figure 3.2c shows the effects of fs-laser irradiation on the Q-Cu-Zr sample possessing AIFs, which manifests as up to a $\approx$ 60% ($\approx$ 1.6 GPa) maximum reduction in hardness, and Figure 3.2d shows the fs-laser effects on the SC-Cu-Zr sample, which exhibits up to a $\approx$ 80% ($\approx$ 2.5 GPa) decrease in hardness. In all cases, the reduction in hardness monotonically increases with fluence up to a saturation value near the ablation threshold. Hardness values in Figure 3.2c, d were extracted from depths of 40 $\pm$ 5 nm in order to capture the near-surface effects of the laser. Both Q-Cu-Zr and SC-Cu-Zr have similar initial hardness values, which is consistent with previous investigations of these materials [73] that report a 10% difference in yield strengths between the two samples. An analysis of the changes in hardness as a function of depth will be presented in the following section. The ablation thresholds of the Q-Cu-Zr and SC-Cu-Zr samples were 0.33 $\pm$ 0.02 J cm^{-2} and 0.5 $\pm$ 0.02 J cm^{-2}, respectively (Table 2.1). This difference in ablation thresholds will be discussed further, as, unlike the

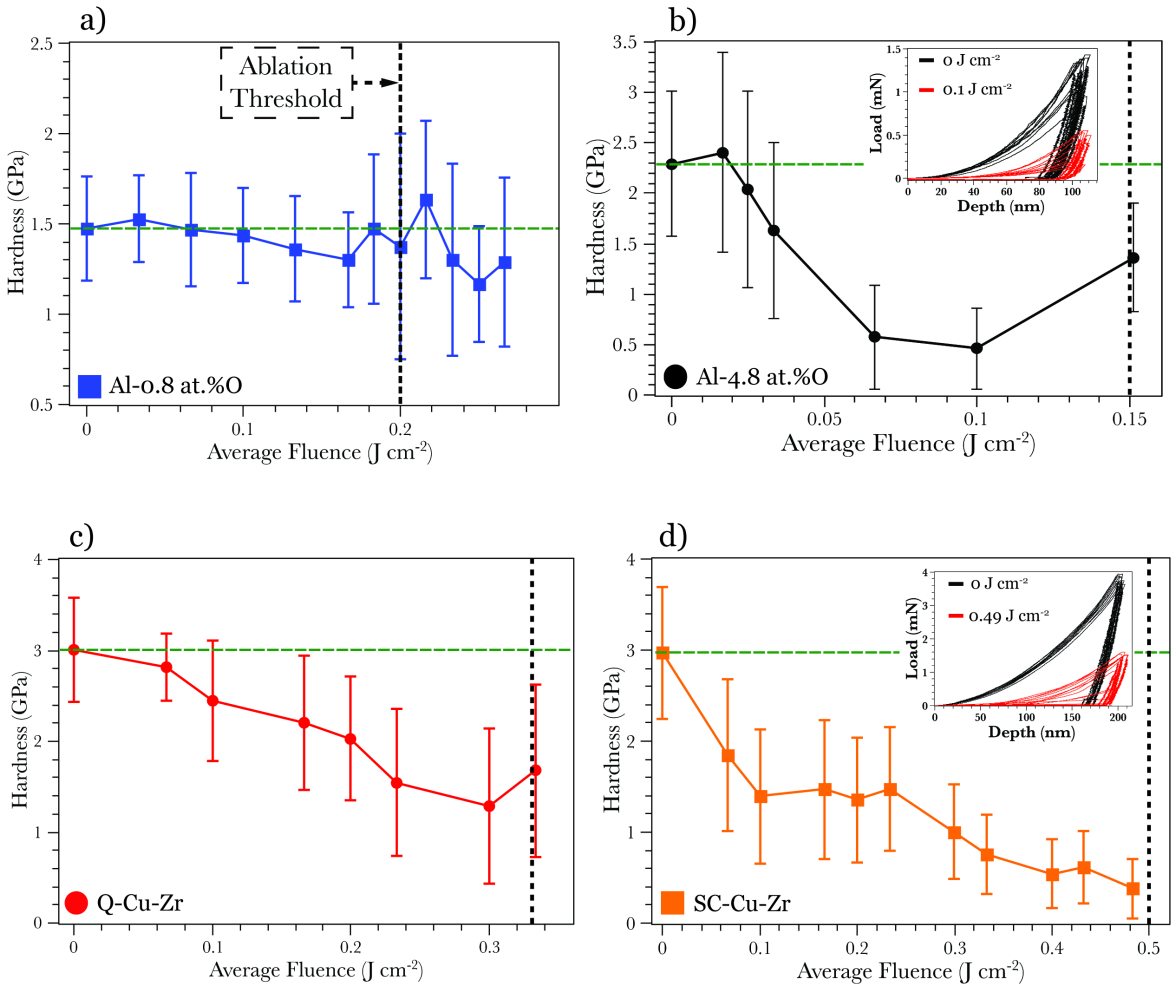

Figure 3.2: Hardness measured by nanoindentation as a function of laser fluence for all samples. The green horizontal dashed line is the mean hardness of the non-irradiated sample, and the ablation threshold is denoted by the vertical dashed line. a) Al-0.8 at.%O, b) Al-4.8 at.%O, and several representative load-displacement curves for the untreated and 0.066 J cm^{-2} treated regions. c) Q-Cu-Zr. d) SC-Cu-Zr, and several representative load-displacement curves for the untreated and 0.495 J cm^{-2} treated regions. All data plotted in b-d are at energies below the ablation threshold (vertical dashed line) for each material.

Al-O samples, these samples have nominally the same grain size and chemistry, so any difference in their ablation behavior is only due to the different grain boundary structures present in the different samples.

3.4 Depth dependence

To better characterize the intrinsic bounds of the laser induced change in hardness, we frame our results in terms of the geometries of each sample. The two features of the geometry in question are (i) the microstructure - grain size and grain boundary thickness - and (ii) the optical penetration depth of the laser. To do this, we investigate the depth dependence for all samples, with a focus on the Cu-Zr samples, as their bulk form simplifies the interpretation compared to the nanocrystalline Al films on substrates. The laser predominantly interacts with the material in the optical penetration depth for 780 nm wavelength light, which can be calculated using $\delta = \frac{1}{\alpha} = \frac{\lambda}{4\pi\kappa}$, where δ is the optical penetration (or skin) depth, α is the optical absorption coefficient, λ is the wavelength of irradiation and κ is the extinction coefficient. Appropriate parameters are located in Table 2.1. κ for the Cu-Zr samples was calculated using a rule of mixtures, $\kappa_{AB} = \chi_A\kappa_A + \chi_B\kappa_B$ where κ_A and κ_B are the extinction coefficients of the pure metals from Refs. [183–185], and χ_A and χ_B are the compositional ratios of A and B, respectively.

While the stress state resulting from fs-laser-matter interactions is complex and not strictly confined to this skin depth, we expect the largest effect in this region. Simulations predict a lower ablation threshold for certain amorphous Cu-Zr compositions compared to their crystalline counterparts [159], and also a lower ablation threshold for nanocrystalline Al compared to single crystalline Al [158], so we posit that the total grain boundary 'volume' influenced by the laser will be important in understanding the resultant mechanical deformation. By assuming an average grain size, shape, grain boundary thickness, and approximate plastic zone, we calculate several quantities of interest - (i) an approximate volume of material probed via indentation, (ii) the volume of grain boundary regions probed, (iii) the volume of probed materials and grain boundaries that are within the optical skin depth, as well as (iv) the volume fraction of 'affected' grain bound-

aries, defined as the ratio of the volume of boundaries within the optical skin depth of the plastic zone to the volume of boundaries probed in the plastic zone of the indenter. For the following calculations, we assume cuboidal grains with side lengths equal to the average grain size and a constant grain boundary thickness for each material. For the Cu-Zr samples, TEM measurements of grain boundary thicknesses from [73] of 3 nm for the AIFs in Q-Cu-Zr and 0.5 nm for the ordered grain boundaries in SC-Cu-Zr are used. As previously mentioned, a range of AIF thicknesses exists within any given sample. For reference, a typical distribution of AIF thicknesses for this sample is presented in Ref. [73], and AIF thicknesses of roughly 3 nm were most commonly observed. We assumed a grain boundary thickness of 0.5 nm for both Al samples, consistent with other measurements of grain boundary thickness in the literature [186–188]. Schematically this is shown in Figure 3.3, where the gray regions depict grain interiors and black regions grain boundaries. The plastic zone size probed during indentation was assumed to be a hemisphere with radius $r = 1.9a$ where a is the contact radius of the tip at the prescribed depth [189]. Additionally, to compare different samples and analyze intrinsic material effects, we normalize the hardness as follows:

$$\frac{\Delta H}{H} = \frac{H(\phi) - H(\phi = 0)}{H(\phi = 0)} \tag{3.1}$$

where $H(\phi)$ is the hardness of the material exposed to single pulse fs-laser pulses at fluence ϕ. Figure 3.4 shows the normalized change in hardness as a function of the volume fraction of affected boundaries for all samples. The data in Figure 3.4 was extracted from regions with the largest change in hardness in Figure 3.2 - 0.178 J cm^{-2} for the Al-0.8 at.%O, 0.1 J cm^{-2} for Al-4.8 at.%O, 0.3 J cm^{-2} for Q-Cu-Zr, and 0.49 J cm^{-2} for SC-Cu-Zr. Figure 3.4 indicates that, when normalized by the geometric constraints of the samples, the observed softening appears to saturate at a threshold level of affected grain

boundary volume fraction of $\approx$ 5 X 10^{-5}. We investigated this behavior at all sub-ablation fluences using the same analysis, and, for a given sample, the salient feature is that the saturation threshold is constant, despite the different magnitudes of softening. The relative magnitudes of the softening between samples also depend on the initial reference state of each sample. The Al-0.8 at.%O exhibits an insignificant change in hardness at all depths and sub-ablation fluences, whereas the Al-4.8 at.%O and SC-Cu-Zr exhibit significant softening behavior. The Q-Cu-Zr shows a smaller magnitude of softening, but exhibits similar trends compared to the Al-4.8 at.%O and SC-Cu-Zr samples.

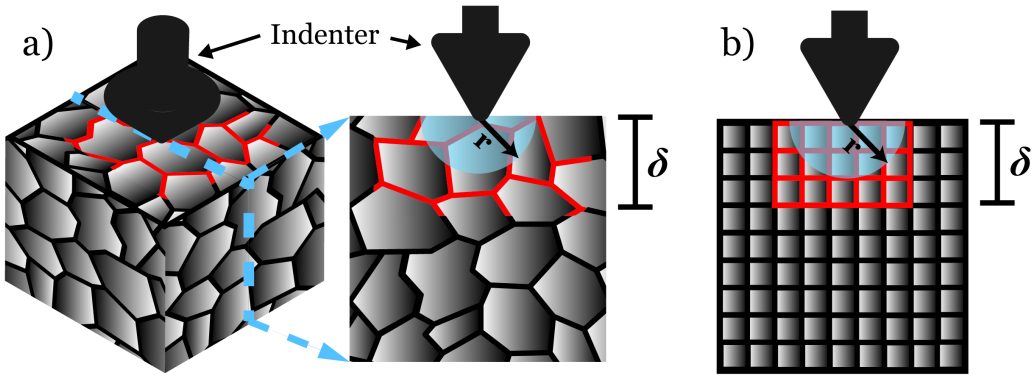

Figure 3.3: a) Schematic showing nanocrystalline sample being mechanically deformed with an indenter and corresponding vertical cross-section. The red region indicates part of the sample that has been irradiated with the laser. The light blue shaded hemispherical region with radius r is the approximate plastic zone of the indenter, and δ is the optical penetration depth of the laser. b) shows the approximate geometry used to calculate a volume fraction of grain boundaries affected and probed.

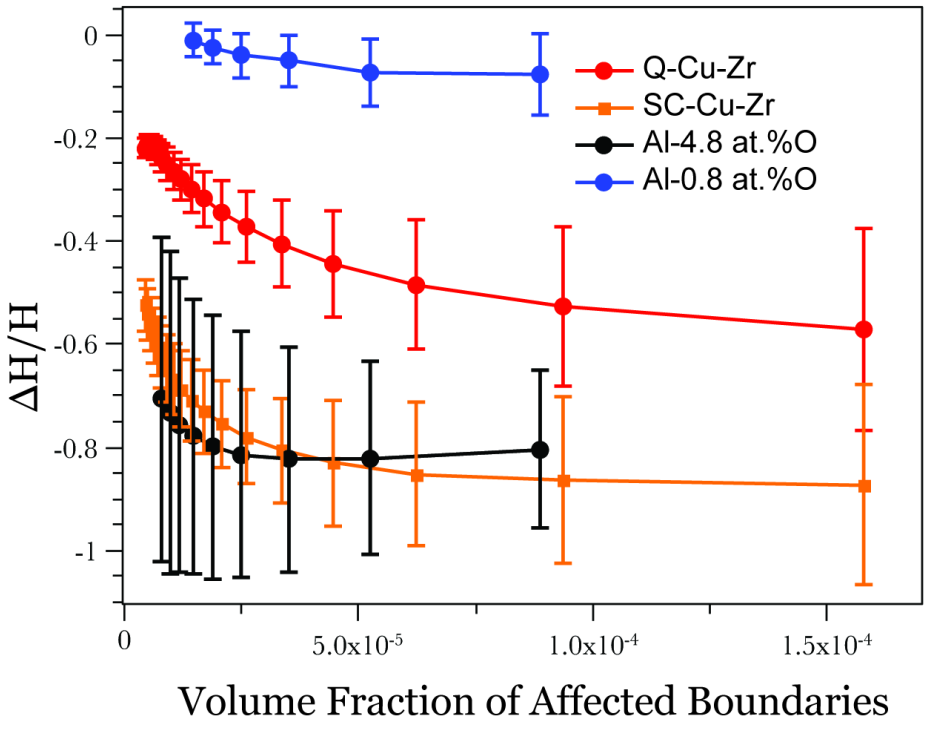

Figure 3.4: Normalized change in hardness as a function of volume fraction of affected grain boundaries for all samples. Data presented here was extracted from indentation measurements from regions with the largest change in hardness in Figure 3.2 - 0.178 J cm^{-2} for the Al-0.8 at.%O, 0.1 J cm^{-2} for Al-4.8 at.%O, 0.3 J cm^{-2} for Q-Cu-Zr, and 0.49 J cm^{-2} for SC-Cu-Zr. Hardness reduction for the Al-4.8 at.%O, SC-Cu-Zr, and Q-Cu-Zr saturate near a volume fraction of $\approx$ 5x10^{-5}. The saturation behavior suggests that the effects of the laser are spatially constrained to surface grain boundary regions, and there is an intrinsic upper bound on the change in hardness associated with the fs-laser treatments. Similarities in the magnitudes of the normalized change in hardness for the Al-4.8 at.%O and SC-Cu-Zr suggest both samples are low energy reference configurations.

3.5 Discussion

3.5.1 Influence of grain boundaries

Our results presented thus far have indicated that (i) sub-ablation threshold fs-laser irradiation causes dramatic (up to 80%) reductions in hardness in the nanocrystalline alloys (Al-4.8 at.%O, Q- and SC-Cu-Zr) with very fine grain size ($<$ 50 nm), (ii) negligible

changes in hardness of larger grain nanocrystalline sample (Al-0.8 at.%O), and (iii) a strong dependence on the geometry of the samples and fs-laser-material interaction. To better understand these results, we begin by discussing the sample with the largest grain size, where laser-material interactions are largely in the grain interiors.

Figure 3.2b indicates no significant change in hardness of the Al-0.8 at.%O sample with increasing laser fluence. What differentiates this sample from the others in this study is the larger grain size and smaller concentration of alloying additions (see Table 2.1). Performing the same geometric analysis as above, the Al-4.8 at.%O possesses a grain boundary volume fraction of $\approx 7.5\%$, whereas the Al-0.8 at.%O has a grain boundary volume fraction of $\approx 2\%$. The calculated optical penetration depth for both of these samples is 7.3 nm, suggesting a smaller 'affected' volume of grain boundary for the Al-0.8 at.%O samples. Compared to the other samples, particularly the Al-4.8 at.%O, which exhibit a large decrease in hardness, the absence of any change in hardness in the Al-0.8 at.%O is noteworthy because it suggests that (i) the fs-laser interactions that cause softening in the other samples occur predominantly at grain boundaries, that (ii) vacancy or Frenkel pair formation within the grain interior is not responsible for the changes in mechanical properties of the other samples, and that (iii) residual stresses and dislocation activity induced by the laser are not responsible for the softening in other samples. Each of these mechanisms will be discussed in detail below.

Due to the relatively large grain size of this sample (80 nm, primarily due to the smaller amount of oxygen that decorates grain boundaries [72,190]), and the smaller volume of grain boundaries both affected by the fs-laser and probed during indentation, the absence of a dramatic change in hardness in this sample indicates that grain boundaries are responsible for the softening observed in other samples. This suggestion is further corroborated by the results of molecular dynamics (MD) simulations [158] indicating that energy deposition caused by the laser occurs differently due to the presence of grain

boundaries, due to locally different electron-phonon (e-ph) coupling behavior. This will be discussed further in Section 3.5.4.

Iyer *et al.* [191] showed using density functional theory (DFT) that the formation enthalpy of point defects such as monovacancies, self-interstitials, and Frenkel pairs is dramatically reduced under high hydrostatic tensile stresses. The authors in Ref. [191] suggest that fs-laser ablation via void coalescence and spallation may be facilitated by point defect formation under the large hydrostatic stresses induced by the fs-laser. The DFT calculations suggest that the critical hydrostatic tensile stress for vacancy formation is 9 GPa in Al. Atomistic simulations from Gill-Comeau and Lewis [158] suggest that, while the maximum pressure induced by the fs-laser may reach values of close to 9 GPa prior to the onset of ablation in nanocrystalline Al, the maximum tension is much lower, below 3 GPa. This, coupled with the lack of change in hardness of the Al-0.8 at.%O sample as compared to the Al-4.8 at.%O sample, suggests that the change in mechanical properties is unrelated to point defect formation within the grain interiors due to tensile hydrostatic stresses. In contrast, local atomic displacements and defects may be induced at higher energy sites, such as grain boundaries or triple points, at lower tensile hydrostatic stresses experienced during sub-ablation fs-laser irradiation. Taken as a whole, it is evident in this relatively large-grained sample that any lattice defects introduced by the laser interactions play a negligible role in controlling hardness.

Nanoindentation measurements of hardness are quite sensitive to residual stresses [192]. The presence of tensile residual stresses due to fs-laser irradiation have not been documented in the literature, however compressive residual stresses have been observed during ablation [162]. Samples under a biaxial tensile residual stress show a strong softening behavior in nanoindentation [192]. However, due to the absence of any change in mechanical response of the Al-0.8 at.%O sample, the injection of residual stresses into this material from sub-ablation threshold fs-laser treatments is not a viable explanation

for the observed softening.

3.5.2 Potential softening mechanisms

To explain the laser-mediated observed softening effect in the Al-4.8 at.%O and Cu-Zr samples, we hypothesize four potential mechanisms that could cause the observed decrease in hardness: (i) grain growth, (ii) nucleation and coalescence of porosity, (iii) (de)segregation of solute atoms, and (iv) grain boundary rejuvenation - subtle atomic rearrangements at boundaries akin to rejuvenation in amorphous alloys.

Fs-laser ablation is thought to be caused by mechanical spallation rather than melting or evaporation, which occur too slowly and with too large of a damaged zone to be responsible for ultrafast laser ablation [152]. However, thermal effects are present and should not be ignored, especially at low fluences and high pulse numbers [193, 194]. Due to the propensity for grain growth of nanocrystalline metals both due to thermal loads and stress, coarsening may be responsible for the observed softening seen in Figure 3.2. To examine any coarsening due to fs-laser treatments, TSEM [195] was performed on the Al-4.8 at.%O sample. Figure 3.5a shows the microstructure of the as-deposited Al-4.8 at.%O. Figure 3.5b shows the microstructure of the 0.066 J cm^{-2} laser treated Al-4.8 at.%O. No obvious grain growth is seen in these images, certainly not corresponding to the magnitude predicted by a simple Hall-Petch analysis [4, 196–198]. Based on this analysis and the TSEM images, we conclude that softening due exclusively to grain growth is not a reasonable explanation for the observed behavior.

Figure 3.5c shows a high angle annular dark field (HAADF) TSEM image of the 0.066 J cm^{-2} laser treated Al-4.8 at.%O. HAADF is sensitive to local chemistry and mass-thickness product of the sample [199], so porosity would manifest as dark regions in the image. Figure 3.5c indicates no obvious porosity due to fs-laser irradiation. While

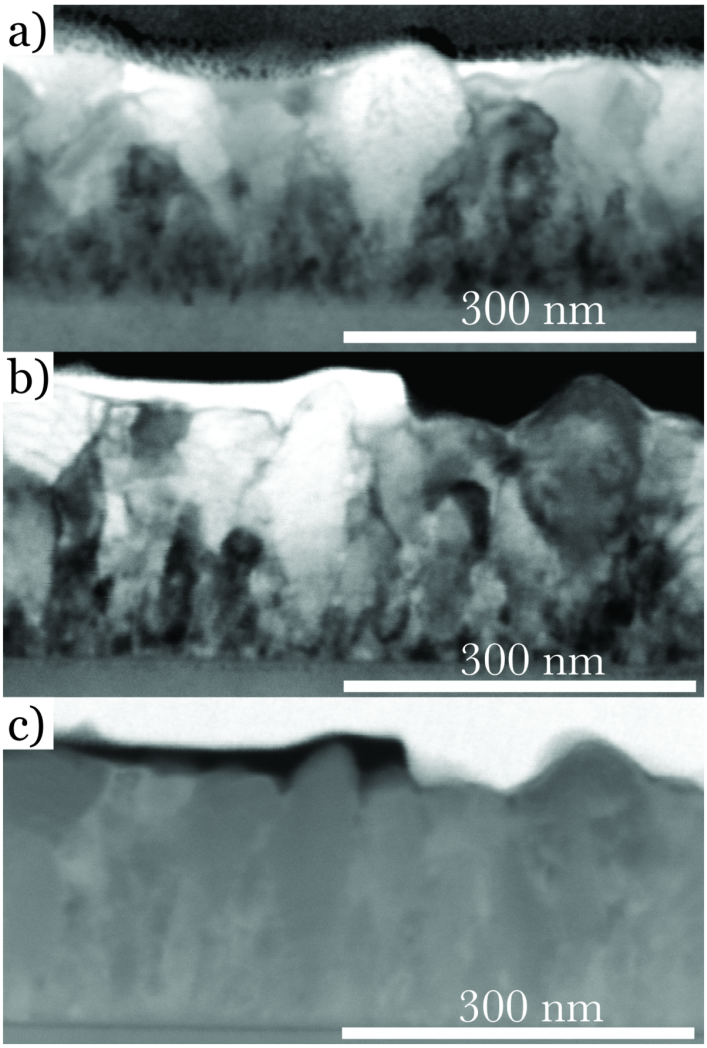

Figure 3.5: a) BF TSEM image of a cross section of the untreated Al-4.8 at.%O sample. b) BF TSEM image of a cross section of the 0.066 J cm^{-2} treated Al-4.8 at.%O sample, the fluence that corresponds to the maximum change in hardness observed in this sample. C) HAADF TSEM image of a cross section of the 0.066 J cm^{-2} treated Al-4.8 at.%O sample. The fs-laser irradiation direction is from the top.

simulations [160] indicate that subsurface porosity generation is possible during femtosecond laser ablation under some conditions, we see no evidence of this occurring here. Figure 3.5c contains slight differences in intensity within the sample, predominantly due to different grain orientations and concentration of O at grain boundaries, which has been previously investigated in these samples by atom probe tomography [71, 190]. These ob-

servations suggest that evolution of porosity is not the dominant mechanism behind the observed softening.

Much of the strength and stability of these nanocrystalline alloys can be attributed to solute (O for the Al-4.8 at.%O, and Zr for the Cu-Zr samples) located at the grain boundaries that serves to stabilize the nanostructure and mediate intergranular deformation mechanisms. Recent work by Hu *et al.* [23] indicated that annealing-induced grain boundary segregation of Mo in nanocrystalline Ni-Mo alloys resulted in increases in hardness of several GPa for all samples tested with only moderate increases in grain size. The most dramatic change shown in [23] was for the highest Mo concentration studied (Ni-21.5 at.% Mo), which underwent a 128% increase in hardness from $\approx$ 4.9 GPa to 11.2 GPa. Thus, the mechanical properties of this system can be tied to the grain boundary structure and solute excess. If the grain boundary structure were to be modified by forcing some solute atoms into the interior of the grain, i.e. desegregation, this could manifest as softening. For this to be a measurable effect, it requires that the structure not relax to its initial state prior to indentation - i.e. a solute atom displaced by the laser could not segregate back to the grain boundary at room temperature. Looking at the Al-4.8 at.%O sample, we see that this diffusion time is far too short to produce a measurable effect.

While diffusion coefficients of O in Al are difficult to measure experimentally, we expect the diffusivity to be generally faster than that of Oxygen in α-Al_2O_3, which we will use as a lower bound. At room temperature, we calculated a lower bound diffusion coefficient of $D_o = 4.29$ cm^2 s^{-1} using the model proposed in Ref. [200]. Assuming a diffusion depth of $x \approx \sqrt{4D_o t}$, and an average grain size of 20 nm, the time needed for the solute to diffuse back to a grain boundary would be $t \approx \frac{x^2}{4D_o} \approx \frac{(20nm)^2}{4D_o} < 2 \times 10^{-13} s$, which implies that any interstitial O displaced as a result of fs-laser irradiation would have diffused to the grain boundary in the time between the laser treatment and indentation.

Hence, we conclude that this type of chemical effect is not responsible for the softening we measure.

3.5.3 Rejuvenation

We thus hypothesize that the observed softening caused by the fs-laser is mechanistically rooted in the high local stresses at grain boundaries produced by the fs-laser, which induce short-range atomic rearrangements that serve to decrease the apparent hardness. We adopt the term rejuvenation to echo similar descriptions utilized in the metallic glass community, where rejuvenation processes have been shown to elicit dramatic softening measured by a decrease in hardness and modulus, as well as the potential for tensile ductility [87]. Rejuvenation in the metallic glass community has been described as an increase in the overall energy of the system by occupying higher-energy metastable structural states [87]. This mechanism concentrated at grain boundary regions is predicated on the existence of a multiplicity of inherent metastable structural configurations, as recently suggested by Refs. [47, 201]. This process is akin to rejuvenation processes employed by the metallic glass community, which induces softening and suppresses catastrophic shear localization. The effect of rejuvenation processes in metallic glasses depend upon the initial energy state, and are also completely recoverable through subsequent relaxation treatments such as low temperature annealing [87,94]. Drawing these parallels to fs-laser irradiation of nanocrystalline metals, we explore the effects of the initial energy state between the SC-Cu-Zr and Q-Cu-Zr samples, as well as the effects of low temperature annealing performed on the SC-Cu-Zr and Al-4.8 at.%O.

3.5.4 Initial energy state

Figure 3.4 allows us to compare the effects of fs-laser treatments on two samples with the same chemistry but different initial energy states - the Cu-Zr alloy samples. The Q-Cu-Zr sample with amorphous boundaries represents a high-energy, non-equilibrium initial state, whereas the SC-Cu-Zr samples exhibit grain boundary structures closer to equilibrium. Since rejuvenation processes raise the energy of the system, driving it further from equilibrium, we expect that the Q-Cu-Zr sample will have a smaller magnitude change than the SC-Cu-Zr subject to any rejuvenation process. Simulations of amorphous solids have shown the presence of distinct solid-like and liquid-like atomic structures, and that the relative fraction of solid-like and liquid-like environments can be tailored through various processing, such as different cooling rates [90]. The higher energy states of the solid will exhibit more liquid-like environments, and when the material is composed of completely liquid-like structures, it is effectively a supercooled liquid. In our case, the fs pulses of energy are being utilized to drive the system energetically uphill, and a large volume fraction of initially liquid-like structures may drive the system toward an earlier onset of ablation. Figure 3.4 indicates that the Q-Cu-Zr exhibits a smaller magnitude of the saturation $\Delta H/H$ than the SC-Cu-Zr. Furthermore, the ablation threshold of the SC-Cu-Zr sample is approximately 50% higher than the Q-Cu-Zr. Both of these observations are in line with the supposition that sub-ablation threshold fs-laser treatments can be understood as a rejuvenation process, and can also be reconciled by considering the physics of the fs-laser-material interactions. Namely, these interactions rely on the disparity between electronic excitation, which occurs in fs, and phononic relaxation, which occurs in ps. Thus, in materials with heterogeneous atomic structures, there may be heterogeneous relaxation behavior due to locally different electron-phonon (e-ph) coupling. In the Cu-Zr alloys, this plays a significant role. It has

been shown in MD simulations that disordered $CuZr_2$ has an e-ph collision rate that is over an order of magnitude larger than pure Cu, and an e-ph coupling factor double that of pure Cu at low temperatures [159]. This difference in e-ph coupling times in amorphous and crystalline Cu-Zr may lead to locally higher energy deposition in regions with the stronger e-ph coupling and shorter e-ph coupling time. The role of grain boundaries on e-ph coupling times and strength is debated in the literature [158, 202, 203]. Gill-Comeau and Lewis [158] performed MD simulations of fs-laser ablation for nanocrystalline Al, accounting for the effects of grain boundaries on e-ph coupling, and found that nanocrystalline Al has an earlier onset of ablation than single crystal Al, in general agreement with our experimental results here. We suggest that, similar to the analysis performed by [158], grain boundary regions have characteristically larger e-ph coupling factors and shorter equilibration times. This implies that the fs-laser affords the unique ability to locally deposit energy at grain boundary regions. As a consequence, the higher volume fraction of amorphous material localized at grain boundary regions in the Q-Cu-Zr sample would exhibit an earlier onset of ablation, as there is a faster and more dramatic electronic relaxation process occurring in this material. The SC-Cu-Zr sample has a smaller volume of disordered material, and would be expected to have a higher ablation threshold - in agreement with our observations.

The smaller magnitude $\Delta H/H$ in the Q-Cu-Zr can be reconciled as follows: if we envisage that the laser causes small structural changes in the grain boundaries that drive them further from equilibrium, the sample with a relaxed (more equilibrium) grain boundary structure will be able to access more metastable, high-energy configurations, compared to an initially non-equilibrium, high energy grain boundary structure. In other words, occupying a deeper position in the basin of the energy landscape provides ample room for moving energetically uphill. This broader range of metastable states implies a larger $\Delta H/H$. This also follows logically from an e-ph relaxation perspective

- small atomic rearrangements in the amorphous region where the majority of the e-ph equilibration occurs would not necessarily lead to drastic differences in mechanical behavior, as the formation of a shear band is suppressed at these length scales [204]. Thus, prior to the onset of ablation, a smaller change in hardness is expected in the Q-Cu-Zr sample than the SC-Cu-Zr. This is seen in Figure 3.4, where the Q-Cu-Zr undergoes a 57% reduction in hardness, whereas the SC-Cu-Zr undergoes an 87% reduction.

Figure 3.4 also shows the normalized change in hardness for the Al samples. Interestingly, the grain boundary volume dependence and normalized change in hardness of the Al-4.8 at.%O and SC-Cu-Zr are quite similar in this plot. This can be ascribed to both samples containing initially relaxed, low energy grain boundary configurations. The Al-4.8 at.%O, despite its fine grain size, is stabilized by the high solute concentration, evidenced by the apparent mechanical stability of this sample [71]. A similar interpretation for the SC-Cu-Zr can be inferred owing to its thermal history and the tendency for Zr segregation to grain boundaries.

3.5.5 Relaxation annealing

Annealing experiments were performed on the irradiated Al-4.8 at.%O and SC-Cu-Zr samples to determine if the observed decrease in hardness is recoverable. Since AIFs are only in equilibrium at very high temperature and are kinetically frozen in at room temperature, an annealing treatment would likely remove any AIFs present. Therefore, we do not anneal the Q-Cu-Zr sample here. All heat treatments were performed in a quartz tube furnace in an Ar environment ($< 10^{-8}$ ppm O_2) to minimize additional oxidation. The Al-4.8 at.%O film was annealed for 90 min at 205 °C. The SC-Cu-Zr sample was annealed for annealed for 120 min at 350 °C. Temperatures were chosen to be ≈ 0.5 T_m, slightly higher than other relaxation heat treatments reported for nanocrystalline met-

als [23, 43, 44, 205]. Relaxation annealing temperatures are chosen to be low enough to preclude grain growth, but high enough to allow short-range diffusive atomic rearrangements, predominantly at grain boundaries where the structural disorder and diffusivities are much higher. The higher temperature range was selected due to the apparent thermal stability of these samples, owing to the high propensity for solute segregation in these material systems [73, 75, 190]. To ensure that the microstructure does not undergo coarsening during this annealing treatment, TEM investigations of grain size were conducted. The average grain size of the Al-4.8 at.%O after annealing was 22 ± 9 nm, and the average grain size of the SC-Cu-Zr after annealing was 44 ± 16 nm. We note no significant coarsening of the microstructure or recrystallization after annealing at these modest temperatures.

Indentation tests were performed on the same regions before and after annealing to elucidate any changes in mechanical properties caused by the heat treatment. Figure 3.6a,b show the hardness measurements of the Al-4.8 at.%O and SC-Cu-Zr samples conducted before and after relaxation annealing, with the duration and homologous temperatures of the heat treatment indicated in each plot. The green horizontal dashed line indicates the mean initial, non-irradiated hardness measured for each of the two samples. Annealing returned the hardness of the Al-4.8 at.%O to 2.44 GPa, compared to a hardness of 0.57 GPa after irradiation, and the SC-Cu-Zr to 2.87 GPa, compared to a hardness of 0.77 GPa after irradiation. These results indicate that the effect caused by the fs-laser treatments is fully reversible upon annealing, and the initial mechanical properties of the samples are recovered. By recovering the same hardness value as the initial non-irradiated samples, we can conclude that the initial energy state of both the Al-4.8 at.%O and SC-Cu-Zr samples is relatively low, and any effects induced by the fs-laser can be reversed through boundary-mediated mechanisms operative at low temperatures. Figure 3.6c shows the modulus data for the SC-Cu-Zr sample, indicating that the fs-laser

induces small changes in modulus. It appears that the two areas probed after annealing have statistically insignificant changes in modulus. The recoverability of the mechanical response after low temperature annealing further proves that grain growth and evolution of porosity are not responsible for the change in mechanical properties, as the temperatures for this annealing treatment were not high enough to remove porosity or coarsen the grains. Further kinetic studies are necessary to fully characterize this relaxation process and identify activation energies associated with the rate-limiting mechanisms.

3.5.6 Mechanisms of nanocrystalline fs-laser mediated rejuvenation

We hypothesize that several mechanisms may be operative in eliciting rejuvenation, but they are all predicated on the physical underpinning of local atomic shuffling leading to metastable grain boundary configurations. This phenomenon can be represented in a number of ways - accessing various micro degrees of freedom at grain boundaries [47], civilian or military shuffling modes at grain boundaries [33], grain boundary structural transitions [66, 206], modification of disconnection densities [55], or shear transformation zone (STZ)-like activity [36, 40, 42]. Han *et al.* [47] show using MD simulations that a bicrystal can exhibit many metastable grain boundary structures for a given misorientation. The high stresses involved during fs-laser processes may be sufficient to modify the structure of grain boundaries, as suggested by Iyer *et al.* [191]. While Ref. [191] focuses on point defect formation, they argue that at grain boundaries or other high-energy sites, the critical stress needed to form a vacancy or Frenkel pair may decrease to be energetically favorable from stresses induced by the fs-laser. The presence of these defects along a grain boundary may change the atomic structure of the boundary to a higher energy configuration. Similarly, the high stresses may enable other shuffling modes at grain

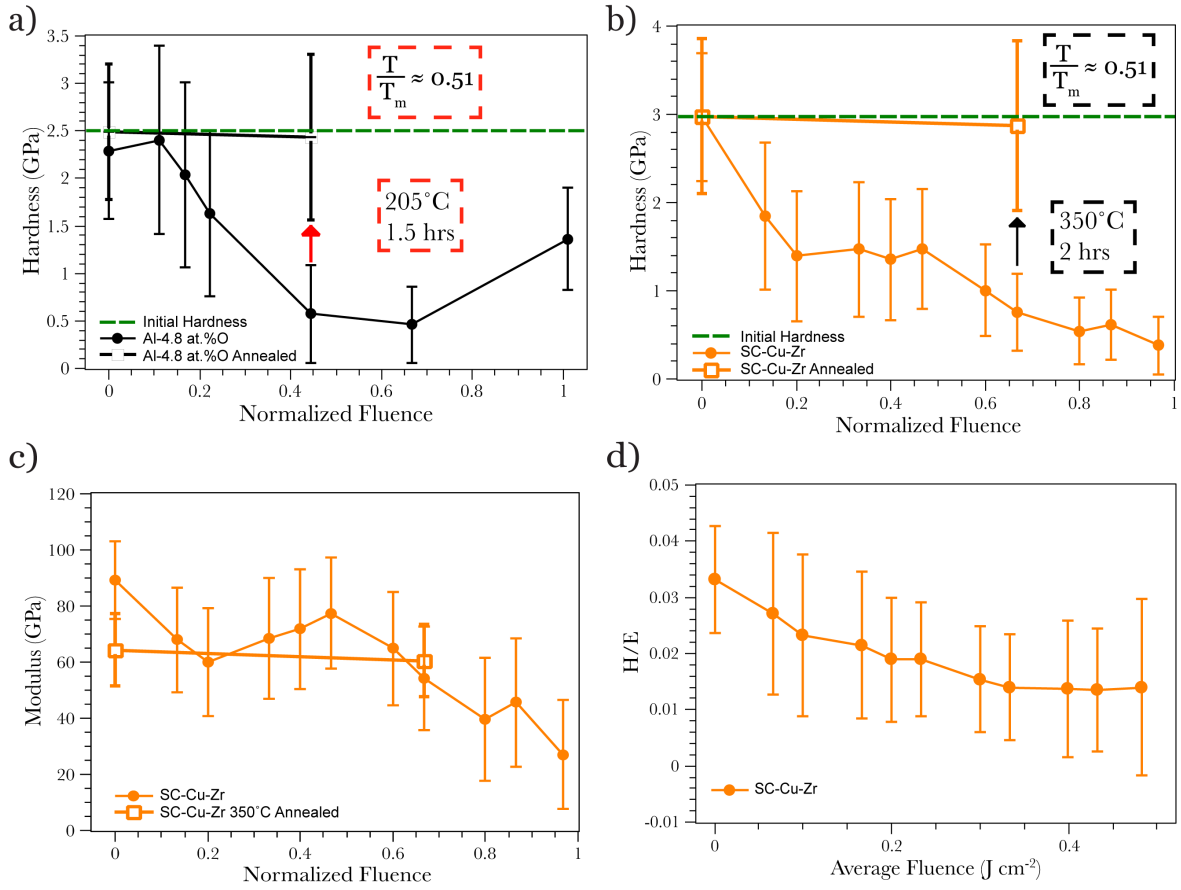

Figure 3.6: Effects of recovery annealing heat treatments on the Al-4.8 at.%O and the SC-Cu-Zr samples. a) Hardness as a function of the normalized fluence for the Al-4.8 at.%O sample. Normalized fluence is the measured fluence divided by the ablation threshold for each material. Filled black circles indicate the material prior to annealing, and the open black squares are the measurements conducted after annealing at 205 °C for 1.5 hours. b) Hardness as a function of normalized fluence for the SC-Cu-Zr sample annealed at 350 °C for 2 hours. Initial measurements prior to annealing are indicated by filled in orange circles, whereas measurements performed after annealing are shown as open orange squares. c) Shows the measured modulus for the SC-Cu-Zr sample annealed at 350 °C for 2 hours as a function of normalized fluence, and d) shows the ratio of the hardness to the modulus as a function of average fluence for the same sample.

boundaries [33], which also enable the formation of high-energy grain boundary structures. The presence of metastable grain boundary structures has been shown to affect the operative deformation mechanisms, favoring grain boundary sliding, void formation and intergranular cracking [13]. STZ-like activity at grain boundary regions of nanocrystalline

metals has been reported for materials with small grain sizes [36, 40, 42, 46], where STZs can coalesce to form a catastrophic shear band. Recent results showing that the size of correlated regions participating in STZ-like rearrangements is of the order of the particle diameter (atomic size) [207] lends credence to the idea that rearrangements can occur even in spatially constrained grain boundary regions. Activation of STZ-like mechanisms during deformation would significantly decrease the strength of a material, as evidenced by the softening behavior of nanocrystalline metals commonly observed at very fine grain sizes [36]. Given the subtlety of the structural changes occurring at the atomic scale at grain boundaries, advanced characterization methods will be needed to elucidate the differences in atomic configurations responsible for the changes in mechanical behavior.

3.6 Generality and applicability to other alloys

3.6.1 Grain boundary molecular dynamics simulations

In order to investigate the atomistic details of grain boundary rejuvenation and provide insight into the experimental results above, Bai *et al.* [143] performed MD simulations on metastable grain boundaries in Cu to investigate their energetic evolution. While greater detail is provided in Ref. [143], the basic premise of these simulations was to investigate the structural evolution of grain boundaries subject to various thermal exposures, including isothermal holds and rapid heating/cooling. By mapping out the evolution of these metastable grain boundary structures subject to various thermal profiles, a broadly applicable potential-energy-landscape (PEL) description of grain boundaries can be elucidated, presenting a physics-based, fundamental description of grain boundary evolution, including a description of events that occur during fs-laser irradiation.

Many grain boundary structures were instantiated by locally perturbing an ideal grain

boundary, as shown in Figure 3.7. These boundaries were then subjected to isothermal annealing at various temperatures, results of which are also presented in Figure 3.7. The energetic evolution of these grain boundaries is sensitive to both the temperature of the isothermal hold and the initial energetic state, meaning that thermal exposures can either induce a decrease in grain boundary energy - relaxation or ageing - or an increase in energy - rejuvenation - depending on their initial energy or the temperature during annealing.

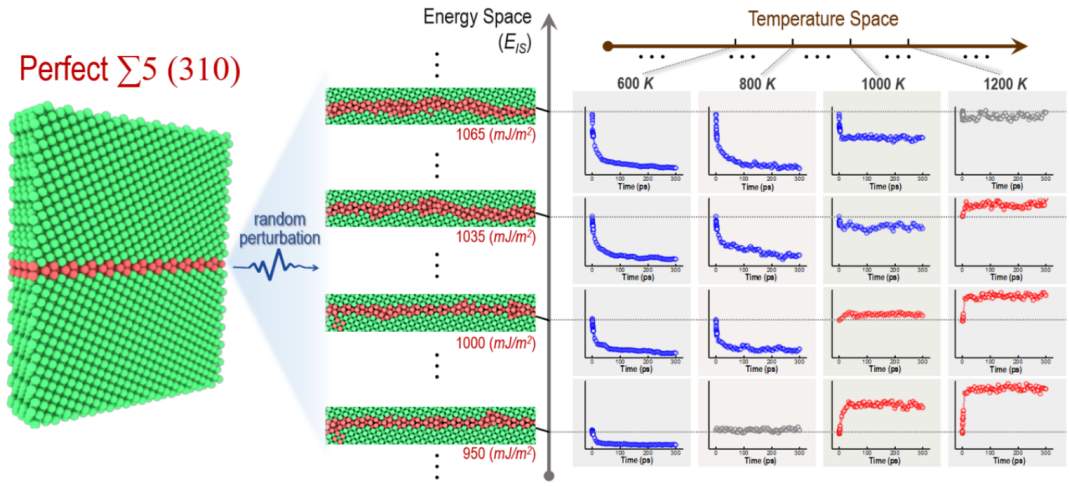

Figure 3.7: (Left) A multiplicity of metastable Σ5 (310) GBs. (Right) Energtic evolution during isothermal annealing at various temperatures from 0 K to 1300 K.

Coupling the direct outputs from these heating simulations, which include the grain boundary energy and structure, with activation-relaxation-techniques that provide the activation and relaxation energy spectra for the grain boundaries, a map of grain boundary energetic evolution was produced (Figure 3.8a). This map also includes the physics-based PEL-type description of the grain boundary evolution, with the relaxation - rejuvenation crossover denoted by the yellow points. The yellow dashed line reflects the simulated relaxation - rejuvenation crossover point, demonstrating excellent agreement. Additional MD heating simulations performed on a relaxed grain boundary (shown in

Figure 3.8b) demonstrate the validity of the PEL description. The heating experiments, which were truncated at several temperatures in the rejuvenation regime (blue arrows), demonstrate the energetic hysteresis of the grain boundaries. At temperatures above the crossover, the energy of the grain boundary continues to increase even during cooling; however, after cooling below the crossover, the energy of the grain boundary decreases.

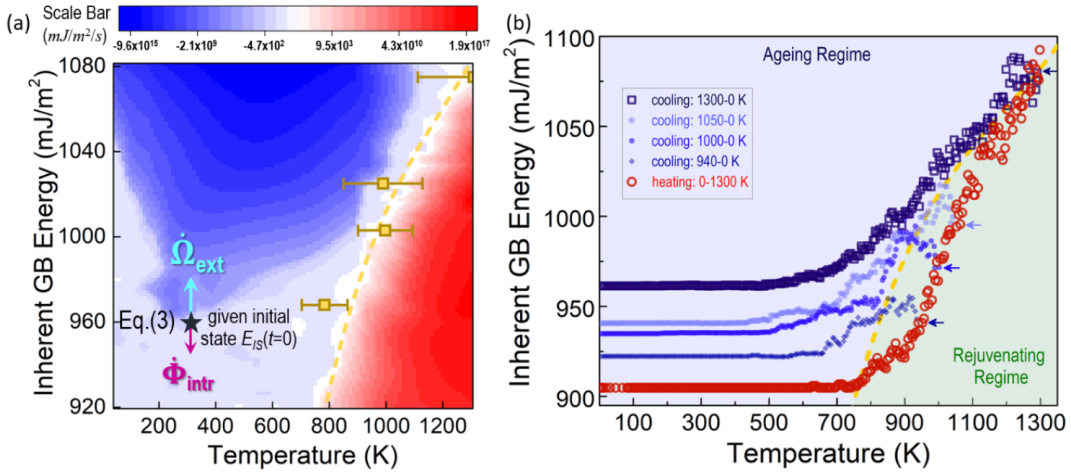

Figure 3.8: (a) Map of GB's energetic variation rate in energy-temperature space. In the blue regime $(\frac{\partial E_i s}{\partial t})|_T < 0$, and the system exhibits an ageing behavior; while in the red regime the energy derivative is positive, and the system exhibits rejuvenation. The ageing/rejuvenating crossover boundary is marked by the dashed yellow curve. The open yellow squares with error bars are the theoretically calculated steady state solutions. (b) MD validations on GB's metastability evolution under fast heating-cooling cycles at the rate of 10 K ps^{-1}. The anomalous peaks in the truncated thermal cycles (i.e. heating/cooling switching at intermediate temperatures of 940 K, 1000 K, and 1050 K marked in the plot) overlap well with the dashed yellow curve extracted from (a), suggesting the validity of the obtained ageing/rejuvenating mechanism map.

These simulations present additional corroboration of the rejuvenation of grain boundaries, and the potent similarities between nanocrystalline metals and metallic glasses. Given the well established link between grain boundary energy and strength in nanocrystalline metals [67], this description of the energetic evolution of grain boundaries is extremely informative for developing the scientific understanding of the strength of materials which exhibit predominantly intergranular plasticity, as well as processing-properties

relationships for these materials. The results also lend credence to the origin of fs-laser effects hyptothesized above, as an energetic pulse at a fixed temperature (or a rapid heating and cooling cycle) may increase the energy of the grain boundaries, reducing the strength (hardness) of the material.

3.6.2 Applicability to other alloys

Additional experiments on HPT refined, nanocrystalline 316L steel samples and sputter deposited Al-Ni-Ce samples were performed to investigate the generality of fs-laser rejuvenation across nanocrystalline alloys, specifically multicomponent alloys. Figure 3.9a-b) presents the reduction in hardness manifest in both as-deposited and relaxed conditions for the Al-Ni-Ce and 316L alloys, respectively. For further comparison, the normalized hardness data for all alloys subjected to fs-laser processing are presented in Figure 3.9c. These data, in conjunction with the previous investigations on other Al and Cu alloys, as well as detailed atomistic simulations, suggest that the reduction in hardness during rejuvenation processing (fs-laser irradiation) is an inherent property of grain boundaries, and thus material agnostic. Samples with higher energy grain boundaries exhibit suppressed ablation thresholds and smaller reductions in hardness for both binary and chemically complex nanocrystalline materials. This behavior is quite apparent in the chemically complex 316L steel. In the as-deformed state, this material undergoes a mild decrease in hardness as a result of laser rejuvenation. By relaxing the material by annealing it at 550 °C for 1 hour prior to laser irradiation, the material subsequently exhibits a nearly 90% decrease in the normalized hardness owing to laser rejuvenation, strongly implicating the importance of the initial GB state.

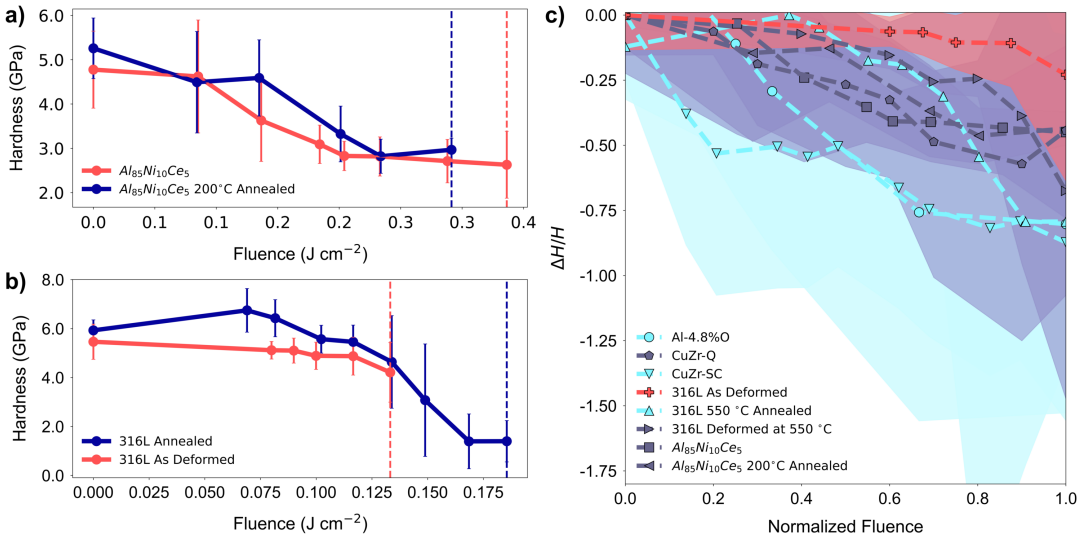

Figure 3.9: a) Hardness vs fluence for as-deposited Al-Ni-Ce and 200 °C annealed Al-Ni-Ce nanocrystalline alloys. b) Hardness vs fluence for as-refined and 550 °C annealed 316L samples. The red curves represent higher energy samples while the blue curves represent lower energy samples. c) Normalized change in hardness as a function of normalized laser fluence for all materials investigated.

3.7 Conclusions

The mechanical measurements and characterization of nanocrystalline Al-O and Cu-Zr alloys subject to sub-ablation threshold fs-laser treatments presented in this chapter suggest the following conclusions. Nanoindentation measurements indicate that sub-ablation-threshold fs-laser treatments cause a significant decrease in hardness in nanocrystalline metals with grain sizes finer than 50 nm. The induced softening can be ascribed to the fs-laser interaction with grain boundary regions, due to structural and chemical heterogeneities. Coarsening, porosity, and segregation effects can be ruled out as causes for the softening. The reduction in hardness is depth dependent, and consistent across samples normalized for grain boundary volume. The magnitude of softening caused by the fs-length laser pulses is dependent upon the initial energetic state of the material - samples with non-equilibrium grain boundary structures had a smaller magni-

tude softening prior to ablation, whereas samples near equilibrium had large tunability in hardness. The softening induced by the fs-laser is fully recoverable upon annealing at low temperatures, suggesting that atomic motion at grain boundary regions (operative at such low temperatures) is responsible for both the softening and relaxation. The fs-laser treatment evidently concentrates its deposition of energy in grain boundary regions possessing disorder, with minimal impact to the crystalline grain interiors.

The simulation work performed by Bai *et al.* [143] provided further insight into the fundamental underpinnings of grain boundary rejuvenation, motivating additional studies on highly alloyed systems (316L steel, Al-Ni-Ce). These studies indicate the broad applicability of 'rejuvenation' processing across alloy systems. The simulations themselves suggest that PEL analysis is readily applicable to grain boundaries, presenting a new outlook for processing of nanocrystalline metals.

This chapter suggests that the similarities between nanocrystalline metals and amorphous alloys are vast, and that our understanding of mechanical behavior of nanocrystalline metals may be greatly informed by the metallic glass community. The application of processing strategies across disciplines, such as fs-laser processing, and material classes can be useful in broadening the tunability and functionality of nanocrystalline materials. The premise of structural rejuvenation of nanocrystalline metals and its impact on properties such as ductility and damage tolerance is a promising area for future research.

Chapter 4

Effects of Alloying on Deformation Behavior of Nanocrystalline Al-Ni-Ce

Rejuvenation processing, while promising for modifying the grain boundary state and concomitant deformation behavior of nanocrystalline metals without altering their chemistry, is only one avenue for tailoring the behavior of nanocrystalline metals. Alloying to improve microstructural stability has been studied extensively and can greatly impact the grain boundary structure in nanocrystalline alloys. In this chapter, the effects of targeted alloying on the grain boundary structure, and corresponding mechanical properties of a nanocrystalline Al alloy are discussed. The Al alloy investigated exhibits many desirable properties, such as a very small grain size (7.6 nm), high hardness (exceeding 4.6 GPa) and thermal stability (up to 0.7 T_m) due to the chemical segregation behavior of Ni and Ce alloying additions. This alloy also exhibits strong sensitivity to thermomechanical processing, where relaxation annealing induces a dramatic increase in hardness and transition in deformation behavior.

4.1 Al-Ni-Ce alloy design

While binary nanocrystalline alloys have been studied extensively, the role of alloying in multicomponent systems is not as well characterized. Recent work from Xing *et al.* [208] demonstrates that the synergistic behavior of alloying additions in ternary and higher order alloys can deviate significantly from the anticipated pairwise interactions, giving rise to unexpected microstructural stability. As such, given the limited selection of binary alloying additions for Al-base alloys, as well as the potential for myriad grain boundary structural motifs with a variety of atomic species, designing a ternary Al-based nanocrystalline alloy that exhibits a strong propensity for co-segregation of alloying additions to grain boundaries may provide a unique opportunity to probe these phenomena, as well as develop an Al alloy with exceptional properties.

Multicomponent nanostructured Al alloys have been reported in studies of partially crystallized amorphous alloys, which exhibit desirable properties such as high strength and low density [82, 209–212]. In amorphous Al-based alloys, combinations of transition (TM) and rare earth (RE) metals are frequently used as alloying additions to increase the complexity of crystallization products, thereby increasing the glass formability of these systems [82]. Al-TM-RE alloys have high strength and a variety of unique microstructures [82, 213]. While the Al-TM-RE alloy space is broad, the Al-Ni-RE ternary system has been characterized, and appears promising. Multiphase Al-Ni-RE crystalline alloys exhibit desirable solidification microstructure formed during casting, as well as their thermomechanical properties owing to thermally stable nanoscale precipitates [209]. Various RE elements have been studied in these systems, but Ce is promising for a variety of reasons. Binary Al-Ce alloys are being investigated as promising alloys for additive manufacturing due to the high thermal stability, as well as relative abundance of Ce from various RE production [214]. The thermal and mechanical behavior of amorphous Al-

Ni-Ce alloys have been characterized quite extensively [82, 210, 213, 215–218], and exhibit thermal behavior that is desirable for a nanocrystalline system. After annealing at low temperatures, Al-Ni-Ce amorphous alloys first crystallize through the nucleation of FCC-Al particles in an amorphous matrix [216]. Then, due to the negligible solubility of Ce and Ni in FCC-Al, these elements are rejected into the amorphous material surrounding the FCC-Al nuclei. This strong propensity for elemental segregation of Ni and Ce away from crystalline Al suggests that these may be suitable alloying additions for a nanocrystalline Al alloy. These attributes suggest that a single phase nanocrystalline Al-Ni-Ce based alloy may exhibit both enhanced thermal and mechanical stability due to the strong tendency for Ni and Ce to segregate during low temperature annealing, as well as the potential for the formation of amorphous intergranular films due to the overall glass formability of this alloy space [125, 219].

4.2 Al-Ni-Ce vs. pure Al: microstructure and properties

High angle annular dark field (HAADF) STEM micrographs from the thin as-deposited $Al_{85}Ni_{10}Ce_5$ samples shown in Figure 4.1a demonstrate the extremely fine microstructure produced during the interrupted sputtering of such a highly alloyed Al-based system. Conversely, the bright field STEM micrograph of the pure Al (Figure 4.1b) exhibits a much larger grain size. Using dark field (DF) TEM for the $Al_{85}Ni_{10}Ce_5$ and annular dark field STEM for the pure Al, grain size distributions were measured (Figure 4.1c). Average grain sizes of 28 $\pm$ 11 nm for the pure Al sample and 7.6 $\pm$ 2 nm for the $Al_{85}Ni_{10}Ce_5$ were measured. As the thin specimens are only $\approx$ 40 nm thick, the grain size of the pure Al sample is slightly larger than half of the film thickness - a common

observation for sputtered films at relatively high homologous temperatures [144]. The HAADF micrograph of the as-deposited $Al_{85}Ni_{10}Ce_5$ exhibits relatively uniform contrast with small domains outlined in regions of higher contrast, presumably Al enriched in Ni and Ce given the atomic number contrast [220]. The size of domains observed in the HAADF image correspond to the grain size measured from DF TEM imaging. Due to the negligible solubility of either Ni or Ce in Al [210, 211], and the high homologous temperature of Al at room temperature, moderate segregation of these elements to grain boundaries in the as-deposited microstructure is expected.

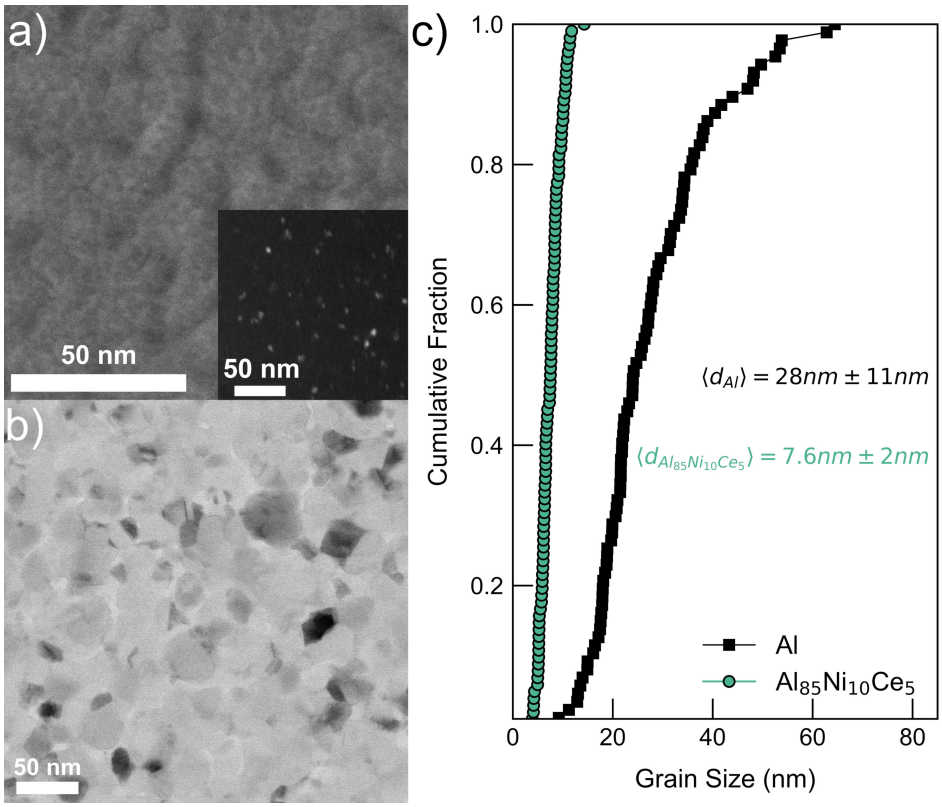

Figure 4.1: STEM micrographs and corresponding grain size distributions of thin samples on C-TEM grids. a) HAADF STEM image of the as-deposited $Al_{85}Ni_{10}Ce_5$, b) BF STEM image of the Al sample, and c) grain size statistics generated from DF TEM images of the $Al_{85}Ni_{10}Ce_5$, and annular DF STEM images of the Al. The inset in a) is a corresponding DF image of the as-deposited $Al_{85}Ni_{10}Ce_5$.

Selected area diffraction (SAD) patterns taken with a 10 μm diameter aperture

(Figure 4.2a-b) demonstrate a single-phase FCC structure for both the pure Al and $Al_{85}Ni_{10}Ce_5$. The SAD pattern from the pure Al exhibits several distinct spots resulting from diffraction of individual grains, rather than a continuous ring, due to the larger grain size (see Figure 4.1c). Given the high glass formability of this alloy, the absence of a typical amorphous halo in the diffraction pattern of the $Al_{85}Ni_{10}Ce_5$ is surprising. To further analyze any structural differences between pure Al and $Al_{85}Ni_{10}Ce_5$, the radially integrated intensity of the diffraction patterns is shown Figure 4.2c. We observe only a small broadening of the {111} peak in the $Al_{85}Ni_{10}Ce_5$ sample and presence of higher order planes in the diffraction pattern, suggesting that the sample is predominantly crystalline. Further examination of Figure 4.2c indicates a small shift in the peak locations in the $Al_{85}Ni_{10}Ce_5$ compared to the pure Al. Using Gaussian peak fitting of the {111} peak location, we measure a lattice parameter of 4.065 Å for the $Al_{85}Ni_{10}Ce_5$ sample, corresponding to a $\approx 0.5\%$ lattice expansion compared to pure Al (dashed lines in Figure 4.2d). This suggests the formation of a non-equilibrium, supersaturated solution of Ni and Ce in a nanocrystalline Al microstructure - a feature often reported in alloys prepared via sputter deposition [14, 144].

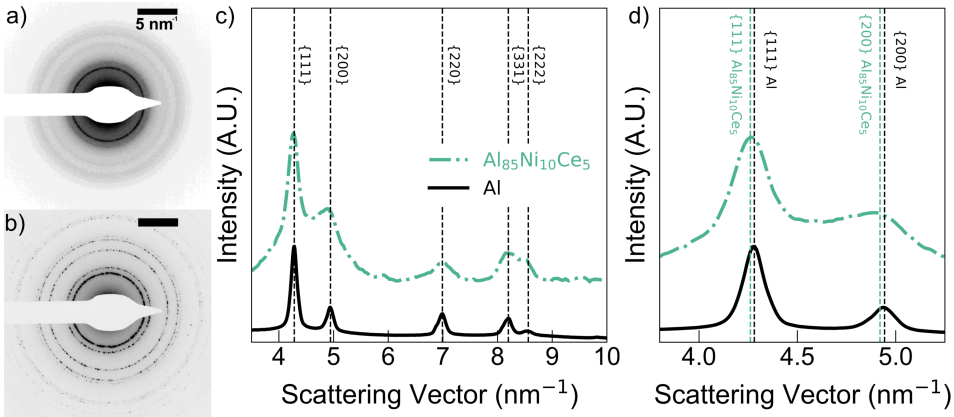

Figure 4.2: a-b) Diffraction patterns taken from the thin $Al_{85}Ni_{10}Ce_5$ and Al samples. c-d) corresponding integrated azimuthal intensity.

While these results are indicative of the behavior of the 40 nm thick films, we do not

observe significant differences between these and the 1 μm thick $Al_{85}Ni_{10}Ce_5$ films. As will be discussed in Section 4.3.2, the average grain size and composition measured from the cross-sectional TEM observations of the thick $Al_{85}Ni_{10}Ce_5$ films are nearly identical to those measured in Figure 4.1. Similar studies on nanocrystalline Al alloys [71,72] have also demonstrated that, while there may be a slight difference in the grain aspect ratio of thicker films compared to plan view TEM samples, the microstructures are otherwise comparable. As such, we posit that observations made on thin $Al_{85}Ni_{10}Ce_5$ specimens can be extended to that of the thick films.

The mechanical properties of thick samples (both pure Al and $Al_{85}Ni_{10}Ce_5$) deposited onto Si (100) wafers were measured by nanoindentation. Figure 4.3 shows representative indentation morphologies observed in the SEM, along with load-displacement data from 20 indentations performed on each of these samples. These experiments were performed at an indentation strain rate of 0.1 s^{-1} to a fixed depth of 500 nm. The indented $Al_{85}Ni_{10}Ce_5$ shown in Figure 4.3a exhibits profuse shear band formation both in the pileup region as well as beneath the indenter. This behavior during indentation experiments, often observed of amorphous metals, is rarely observed in crystalline materials. The presence of these shear bands in the indented $Al_{85}Ni_{10}Ce_5$ will be discussed in great detail in Section 5.1. The hardness values of the pure Al and the $Al_{85}Ni_{10}Ce_5$ are 0.99 $\pm$ 0.19 GPa and 4.67 $\pm$ 0.24 GPa, respectively. These values were extracted from a depth of 100 nm to minimize any influence from the substrate. While residual stresses can affect the mechanical properties measured during indentation [192], these differences arise due to contact area discrepancies, and disappear when the contact area is corrected. Using the final contact area measured in the SEM (Figure 4.3a), we note an error of less than 0.5% between the hardness reported in Figure 4.3c using the CSM technique and the hardness calculated using the final load and contact area measured in SEM. It is clear from Figure 4.3b that the pure Al film is quite rough, and the average grain size

in the pure Al thick films is likely larger than reported in Figure 4.1. The surface roughness is consistent with other observations of sputtered Al films, particularly those sputtered at high rates [71, 72, 144]. The large grain size is likely due to the absence of any alloying elements or impurities which would serve to pin the grain boundaries and preserve the small grain size during deposition of the pure Al. For pure metals, the grain size is typically dependent upon the thickness of the film, which explains the apparent discrepancy [144]. This behavior is not observed in systems with alloying additions to stabilize the grain size, such as the $Al_{85}Ni_{10}Ce_5$ (see additional observations in Section 4.3.2).

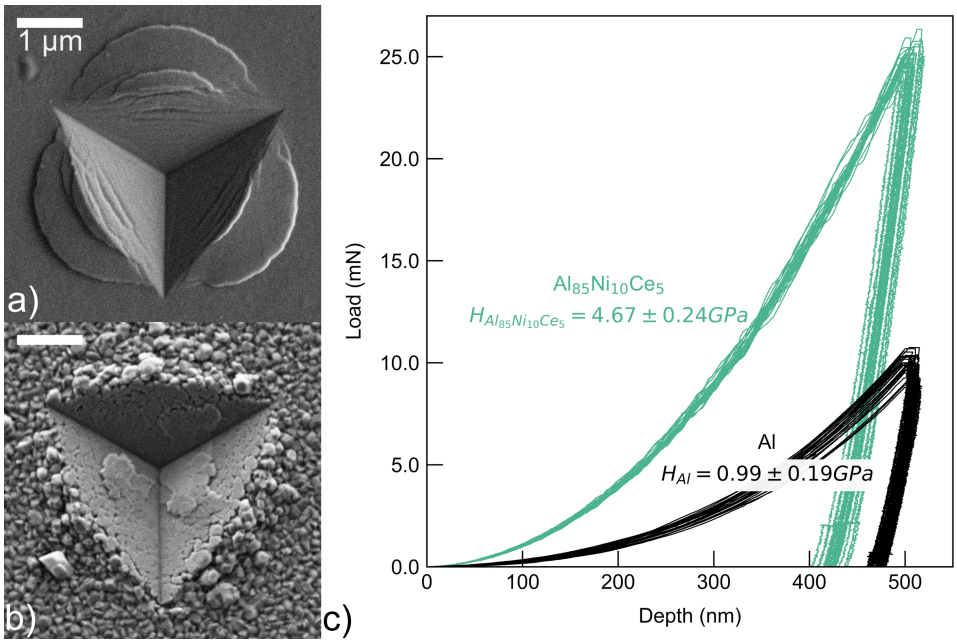

Figure 4.3: Indentation morphology observed in SEM of thick a) as-deposited $Al_{85}Ni_{10}Ce_5$ and b) Al samples, along with corresponding load-depth curves c).

4.3 Annealing effects

4.3.1 Microstructural evolution and mechanical properties

In order to study the effects of annealing on the nanocrystalline $Al_{85}Ni_{10}Ce_5$, particularly the tendency for co-segregation of Ni and Ce to grain boundaries and the subsequent mechanical behavior, both the thick and thin samples were subjected to isochronal-isothermal annealing at 200 °C, 325 °C, and 380 °C. The microstructures of the thin annealed samples are presented in Figure 4.4. Micrographs of the as-deposited sample and those annealed at 200 °C and 325 °C (Figure 4.4 a-c) were acquired using HAADF STEM imaging, whereas the sample annealed to 380 °C (Figure 4.4d) was imaged using conventional bright field TEM. It is clear from the microstructural images in Figure 4.4a-c that annealing up to 325 °C induces strong chemical segregation with negligible grain coarsening. This segregation behavior is consistent with the literature on amorphous Al-Ni-Ce alloys, where diffusion of Ni and Ce away from FCC-Al nuclei precedes second phase precipitation [210, 211]. At temperatures above 380 °C, intermetallic phases such as Al_3Ni and $Al_{11}Ce_3$ [218] begin to precipitate out and the microstructure coarsens rapidly to form the eutectic microstructure observed in Figure 4.4d.

Mechanical properties of the thick samples subjected to identical annealing procedures were probed using nanoindentation. These indentation experiments were performed at strain rates varying from 0.01 s^{-1} to 1.00 s^{-1}. Indentation hardness and modulus values, extracted from 100 nm depths for all samples and strain rates tested, are presented in Figure 4.5. We observe that at temperatures below 380 °C, there is an increase in both hardness (ΔH = 0.95 GPa) and modulus (ΔE = 20 GPa). At 380 °C, the hardness begins to decrease, concomitant with the microstructural coarsening observed in Figure 4.4d. Figure 4.6 shows the hardness as a function of nominal indentation strain rate, along with corresponding activation volume ($\nu = 3\sqrt{3}\frac{\partial \log \dot{\epsilon}}{\partial H}$) and strain rate

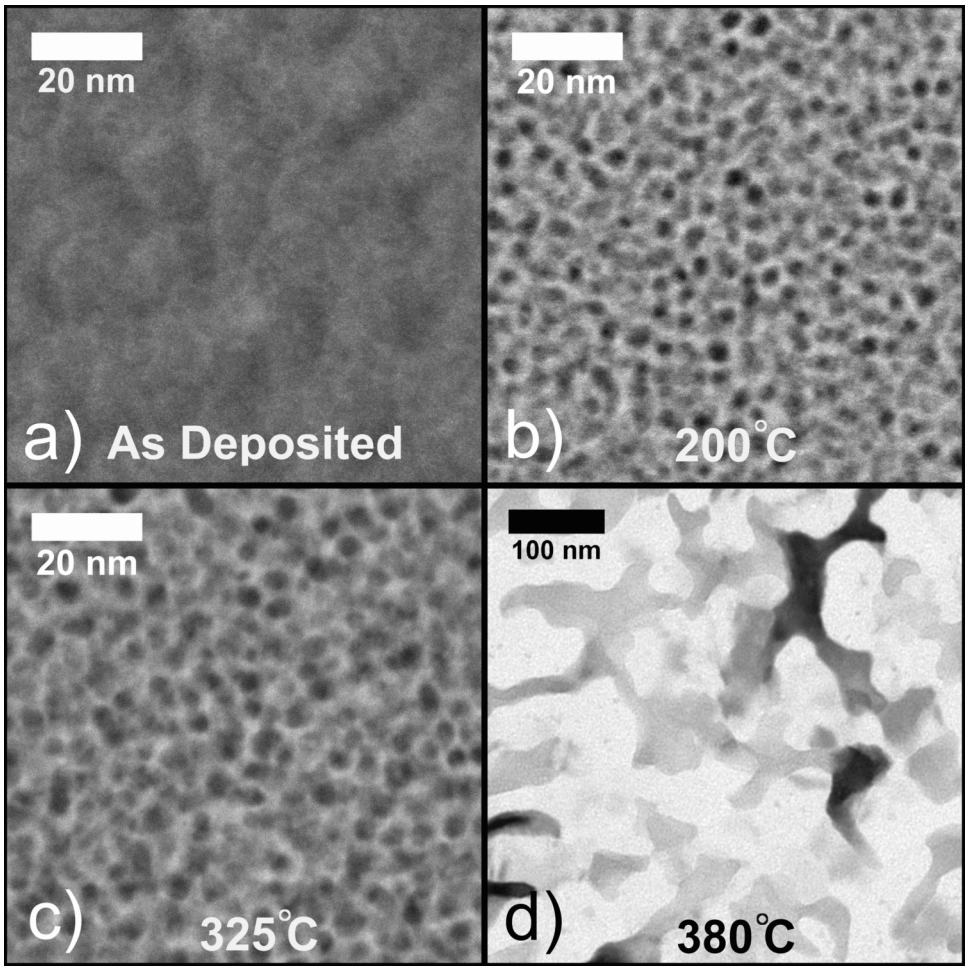

Figure 4.4: Microstructure of the thin samples on C-TEM grids in the a) as-deposited state, and subjected to annealing at b) 200 °C, c) 325 °C and d) 380 °C. a-c) are HAADF STEM images, whereas d) is a BF TEM image.

sensitivity exponent ($m = \frac{\partial \log H}{\partial \log \dot{\epsilon}}$) for each annealing temperature. The m values and activation volumes were calculated as described by Maier *et al.* [172]. Values for ultra-fine grained Al, nanocrystalline Ni, and nanocrystalline 316L steel are included as a reference [221, 222]. While inertial effects are quite important at high indentation strain rates, we noticed an insignificant ($< 5\%$) change when comparing either the activation volume or m values calculated from only the slowest strain rates (< 0.1 s^{-1}) to those calculated over the entire range measured.

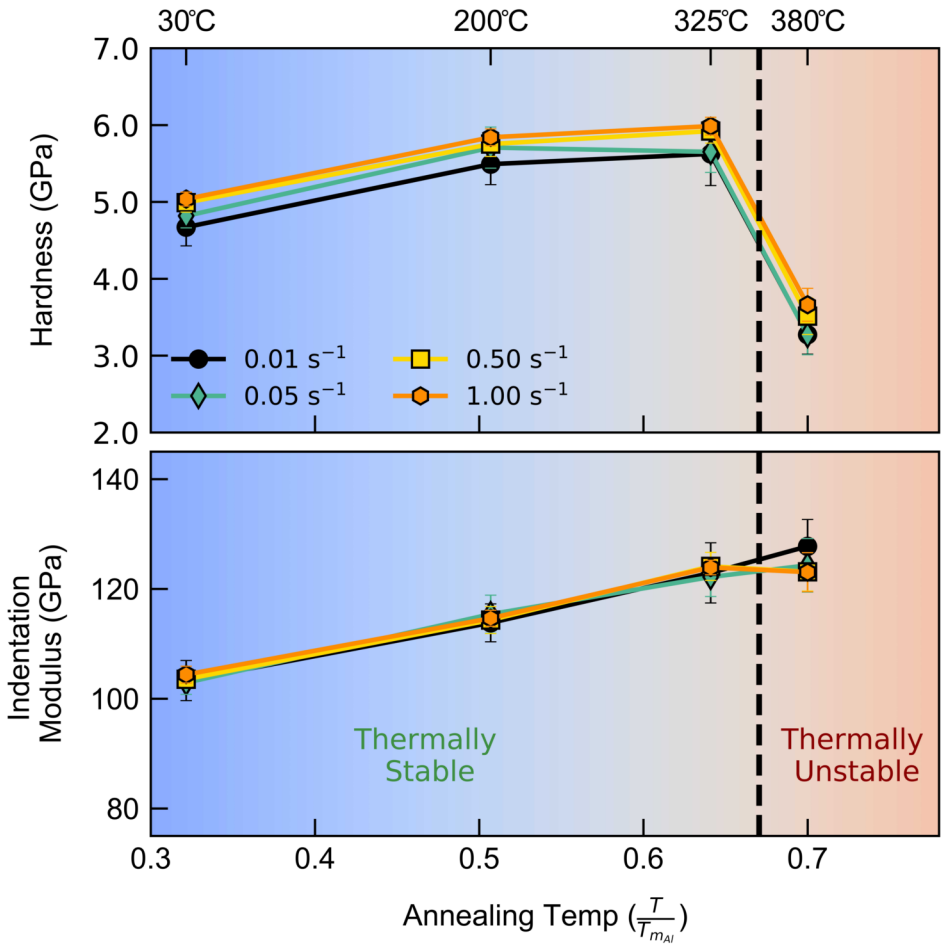

Figure 4.5: Indentation hardness and modulus measured after various isochronal-isothermal annealing, at various nominal indentation strain rates.

The microstructural evolution observed in Figure 4.4 is consistent with the change in hardness observed in Figure 4.5 (as noted above), as well as the strain rate sensitivity behavior in Figure 4.6. Prior to the onset of microstructural coarsening (i.e. at annealing temperature below 380 °C), we observe an increase in hardness of $\approx$ 1 GPa along with strong chemical segregation, a phenomena termed segregation hardening [23, 188, 219]. The activation volumes in Figure 4.6b of $\approx$ 8 b^3, prior to the onset of coarsening, suggest that intergranular deformation mechanisms are operative. While we do observe an increase in the strain rate sensitivity exponent after the onset of coarsening, the val-

ues of both m and ν after coarsening are still in the intergranular deformation regime ($\nu = 5 - 50b^3$, $m = 0.01 - 0.1$). This is consistent with the microstructural evolution presented in Figure 4.4, as the microstructure retains a nanoscale eutectic structure after precipitation. These values are also consistent with reports of rapidly solidified or cast alloys with similar compositions [209, 213].

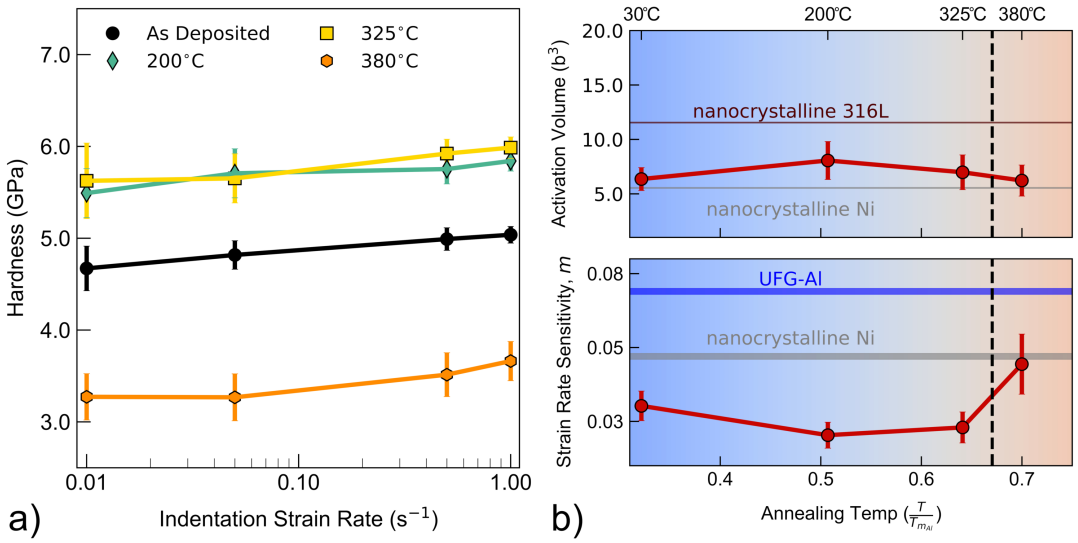

Figure 4.6: a) Indentation hardness as a function of nominal indentation strain rate plotted for each different annealing temperature. b) Strain rate sensitivity exponent m and corresponding activation volume extracted from the data presented in a). Error bars in b) correspond to 95% confidence intervals. Data for UFG Al, nanocrystalline Ni, and nanocrystalline 316L are from Refs. [221, 222]

The microstructures in Figure 4.4 suggest that a spatially extended grain boundary region develops as a result of chemical segregation. Using HAADF images acquired using identical camera settings (Figure 4.4) and applying identical image thresholding the minimum distances between neighboring grains was measured for at least 50 grains in each annealing condition. Corresponding distributions of the widths of the spatially extended grain boundary regions for samples annealed at 200 °C and 325 °C are presented in Figure 4.7. The widths of the as-deposited sample were difficult to resolve given the uniform contrast of the image, and were all quite thin (< 0.5 nm), so a vertical dashed

line at 0.5 nm is included as an upper bound for the widths of the grain boundaries in the as-deposited condition. While the detailed TEM procedures established by [126] are necessary for identifying specific types of grain boundary structures, establishing an appropriate diffraction condition for samples with many grains through the thickness was not possible for these samples. Nevertheless, the analysis presented in Figure 4.7 indicates that both the 200 °C and 325 °C annealed samples have a mean grain boundary width of 1.0 nm and standard deviation of 0.4 nm, suggesting a transition from an ordered grain boundary in the as-deposited condition to an amorphous intergranular film after annealing. A nano-beam electron diffraction pattern of the 325 °C annealed sample taken with a 10 nm diameter probe size is included as an inset in Figure 4.7 to better elucidate the local structure [223]. The probe size utilized when collecting this diffraction pattern is larger than the maximum grain size, thus the diffraction pattern contains information both from the inter- and intragranular regions. The diffraction pattern shown in Figure 4.7 exhibits both prominent crystalline peaks and an amorphous halo - suggestive of the formation of an amorphous intergranular film after annealing. This amorphous halo is unlikely to arise due to surface oxides or carbonaceous layers, all of which manifest at smaller reciprocal space vectors and would thus be obscured by the beam-stop [217]. Surprisingly, these amorphous intergranular films are expected to be in equilibrium at high temperature and require fast quenching to be preserved at room temperature [140]. It appears that in this system, either due to spatial confinement or the good glass formability of the Ni and Ce enriched zone, the critical cooling rates are lower in this alloy.

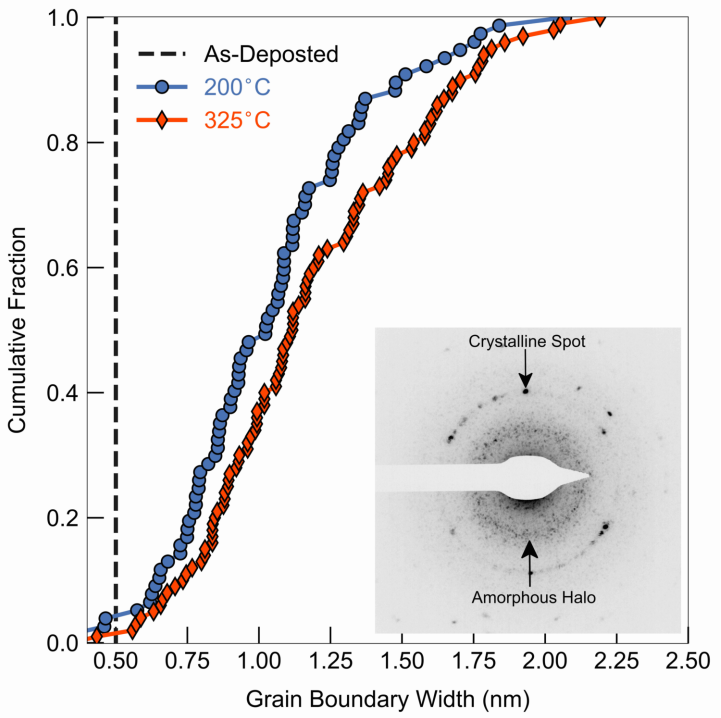

Figure 4.7: Distribution of grain boundary widths measured from micrographs of the 200 °C and 325 °C annealed samples in Figure 5. The vertical dashed line indicates the maximum grain boundary width measured for the as-deposited condition. The inset is a nano-beam diffraction pattern generated from the 325 °C sample, showing indications of a crystalline and amorphous structure.

4.3.2 Indentation deformation microstructure

To better understand the hardening observed prior to coarsening, particularly its effect on the deformation morphology, SEM micrographs of representative indentations from samples annealed up to 325 °C are presented in Figure 4.8. The as-deposited $Al_{85}Ni_{10}Ce_5$ exhibits profuse shear localization both under the indenter and in the pileup region (Figure 4.3a, Figure 4.8a). Figure 4.8b shows the indentation morphology after annealing at 200 °C for 1 hour, where the shear localization in the pileup region has diminished quite substantially, but distinct semi-circular shear offsets are still present. After annealing at 325 °C for 1 hour (Figure 4.8c), shear localization in the pileup region is minimal and almost completely eliminated, which occurs alongside increasing hardness

(Figure 4.5).

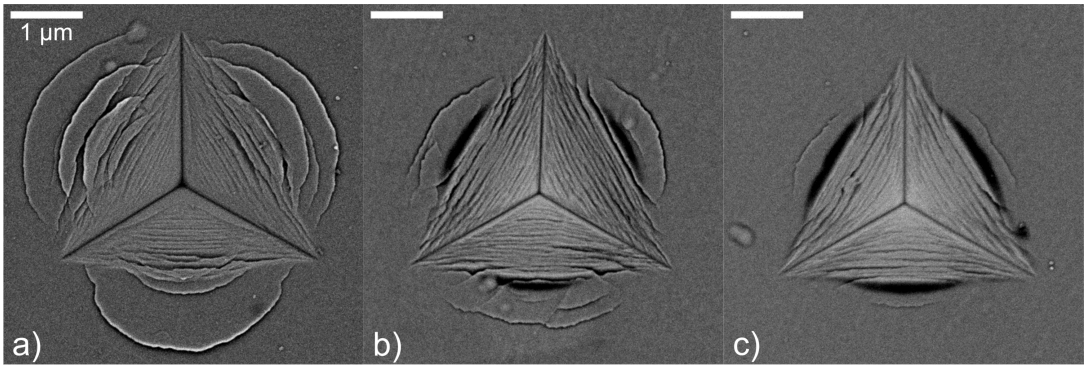

Figure 4.8: Indentation morphologies of $Al_{85}Ni_{10}Ce_5$ samples in the a) as-deposited, b) 200 °C and c) 325 °C annealed state.

To fully characterize the transition in deformation morphology observed in Figure 4.8 due to annealing, including any induced grain growth or rotation, TEM lamella were extracted from the as-deposited and 200 °C annealed sample, as shown in the inset in Figure 4.9a. Figure 4.9a shows a bright field (BF) TEM image of the representative microstructure of the as-deposited film far away from the indent. The development of a slight elongation of the grains in the growth direction of the film (up in Figure 4.9a) is observed. Figure 4.9b shows a BF TEM image from under the indent of the as-deposited $Al_{85}Ni_{10}Ce_5$, showing several regions of dark contrast emanating out from beneath the indenter. These are regions where many grains have rotated into a diffraction condition that would not be illuminated in BF imaging. No obvious grain coarsening under the indent was observed in any of these regions, in contrast to other reports [140].

BF TEM images of the lamella extracted from underneath an indent in the 200 °C annealed sample are shown in Figure 4.9d. The undeformed microstructure of the 200 °C annealed sample (Figure 4.9c) exhibits the same grain size and morphology (i.e. slight elongation in the growth direction) as the undeformed, as-deposited film (Figure 4.9a). The deformed microstructure of the 200 °C annealed sample (Figure 4.9d) exhibits two

faint dark regions underneath the indenter where grains have rotated. However, the dark regions in the 200 °C annealed sample (Figure 4.9d) are oriented differently from those in the as-deposited material (Figure 4.9b). The regions in the 200 °C annealed sample (Figure 4.9d) are nearly perpendicular to those observed in the as-deposited sample (Figure 4.9b), which align normal to the surface of the indent. This localized reorientation will be discussed in detail in Section 4.4.3.

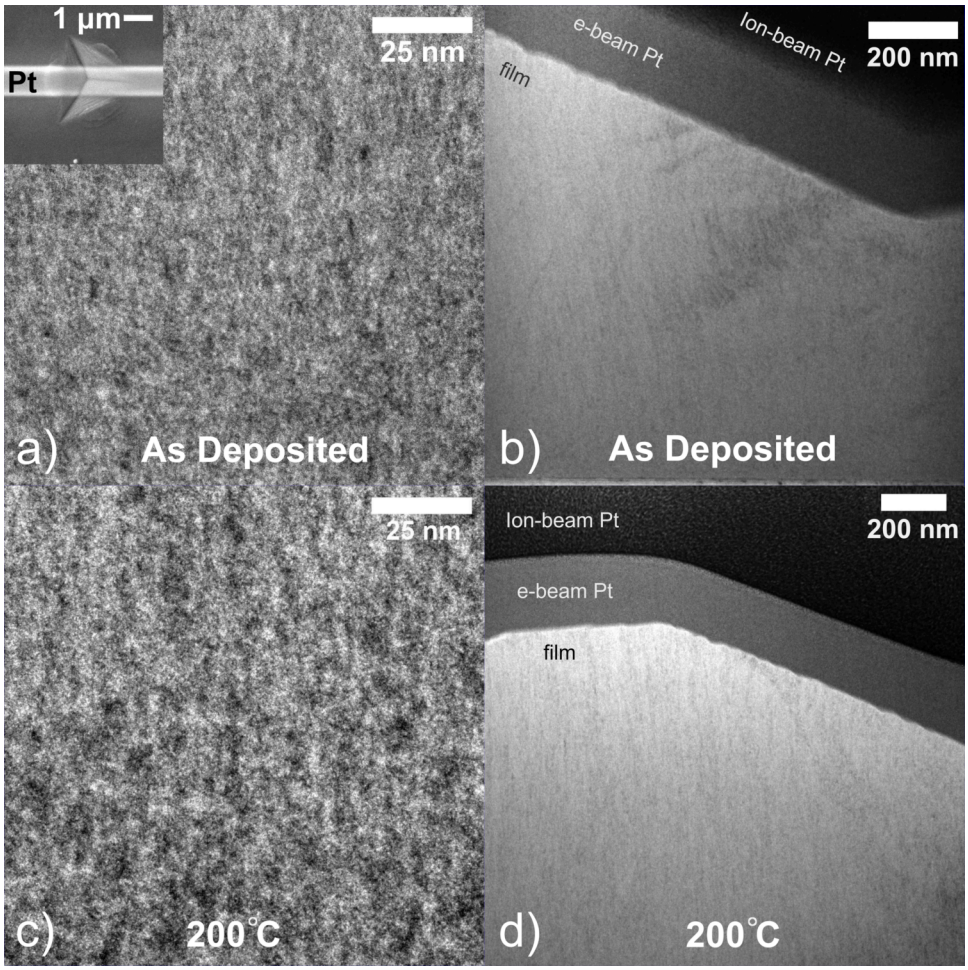

Figure 4.9: BF TEM micrographs of TEM lamella extracted from near an indent in the a)-b) as-deposited $Al_{85}Ni_{10}Ce_5$ and c)-d) the 200 °C annealed $Al_{85}Ni_{10}Ce_5$. a) and c) were acquired far away from the indentation, whereas b) and d) are directly beneath the indent. The inset in a) shows the geometry for extraction of the lamella, where the bright horizontal region is the Pt layer deposited to minimize Ga+ damage during sample preparation in the FIB.

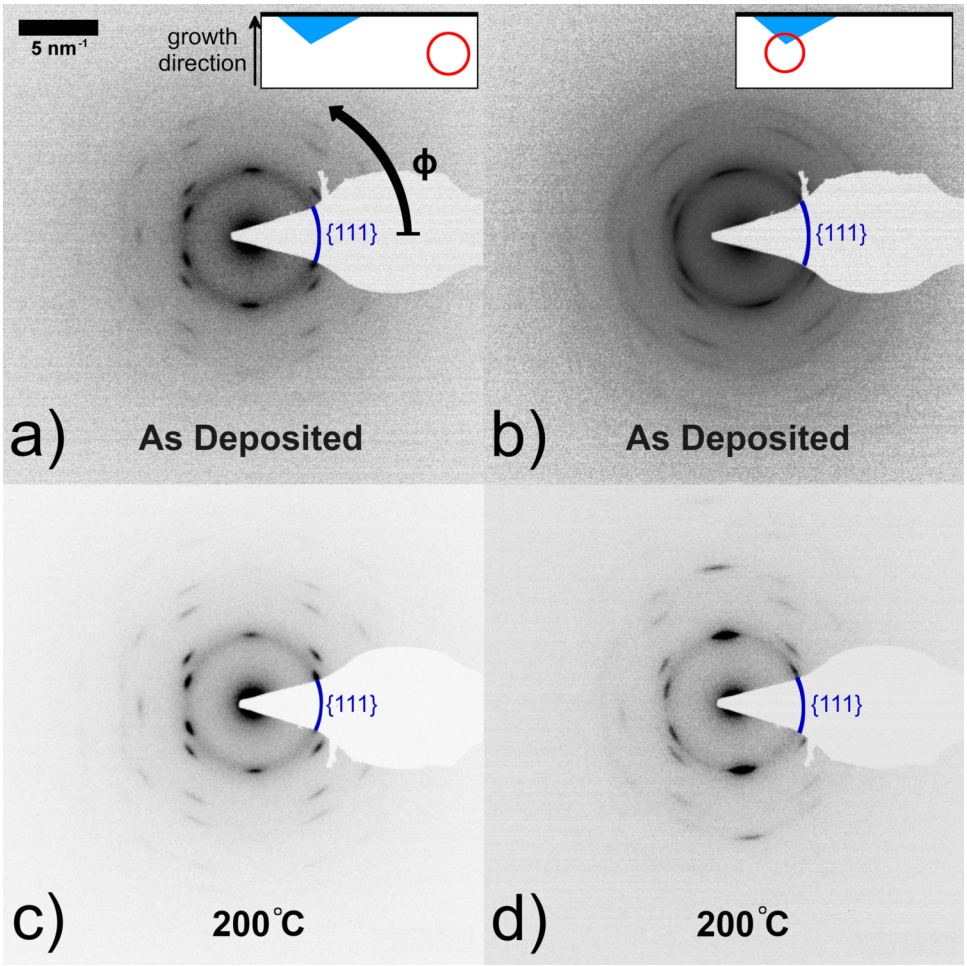

Figure 4.10: Diffraction patterns taken from different selected area regions in the FIB prepared samples. a-b) were taken from the as-deposited sample: a) was taken away from the indent, b) was taken from beneath the indent, schematically represented in the inset by the red circle. c-d) were taken from the 200 °C sample: c) away from the indent, d) beneath the indent. The black arrow is used to indicate the origin and positive direction for the azimuthal projections in Figure 4.11.

Diffraction patterns of these samples were taken from two regions - far away from the indent to characterize the texture in the undeformed sputtered films, and beneath the indent (Figure 4.10). The selected area is schematically represented in the insets in Figure 4.10a and b. The undeformed as-deposited and 200 °C annealed samples exhibit six distinct spots originating from diffraction of {111} planes (Figure 4.10a and c). This texture corresponds to a predominant {111} texture in the growth direction

of the film, which is consistent with sputtering fiber texture reported in the literature for other FCC metals [144]. We observe little difference between the two undeformed microstructures, which is consistent with the thermal behavior of the thin samples (Figure 4.4a-b). However, there is a clear difference between the diffraction patterns of the as-deposited and 200 °C deformed material (Figure 4.10b and d). Both the as-deposited (Figure 4.10b) and 200 °C annealed (Figure 4.10d) diffraction patterns show clear grain rotation as a result of the deformation induced by the indenter, yet the specifics of the rotation clearly differ between the two samples. The 200 °C annealed diffraction pattern (Figure 4.10d) appears to have undergone a rigid rotation - i.e. a majority of grains in the 200 °C annealed samples giving rise to the diffraction pattern in Figure 4.10c have rotated by a fixed amount. Conversely, the as-deposited material (Figure 4.10b) exhibits significant streaking of the diffraction spots, indicating that many grains remain in their initial orientation after deformation, while others rotate to a similar degree (or more) than those in the 200 °C annealed material. To further illustrate this rotation and streaking, the normalized intensity of the {111} diffraction ring is plotted as a function of azimuthal angle (ϕ) for each diffraction pattern in Figure 4.11. The intensity of each azimuthal projection was normalized using the maximum value for ease of comparison. Using Gaussian peak fitting, we measure an average rotation of 7.75 ° for the as-deposited $Al_{85}Ni_{10}Ce_5$ and 5.6 ° for the annealed $Al_{85}Ni_{10}Ce_5$ due to the indentation. Using the first and last peaks in (Figure 4.11, $\phi \approx 80° - 90°, 260° - 270°$), we measure an average peak broadening due to the deformation imposed by indentation of approximately 40 ° for the as-deposited sample, and negligible broadening (< 3 °) for the annealed $Al_{85}Ni_{10}Ce_5$, suggesting both a larger magnitude and broader distribution of grain rotation in the as-deposited $Al_{85}Ni_{10}Ce_5$.

Traditional DF images illuminating the regions where grain reorientation is most extreme are presented in Figure 4.12. These images were collected by placing the objective

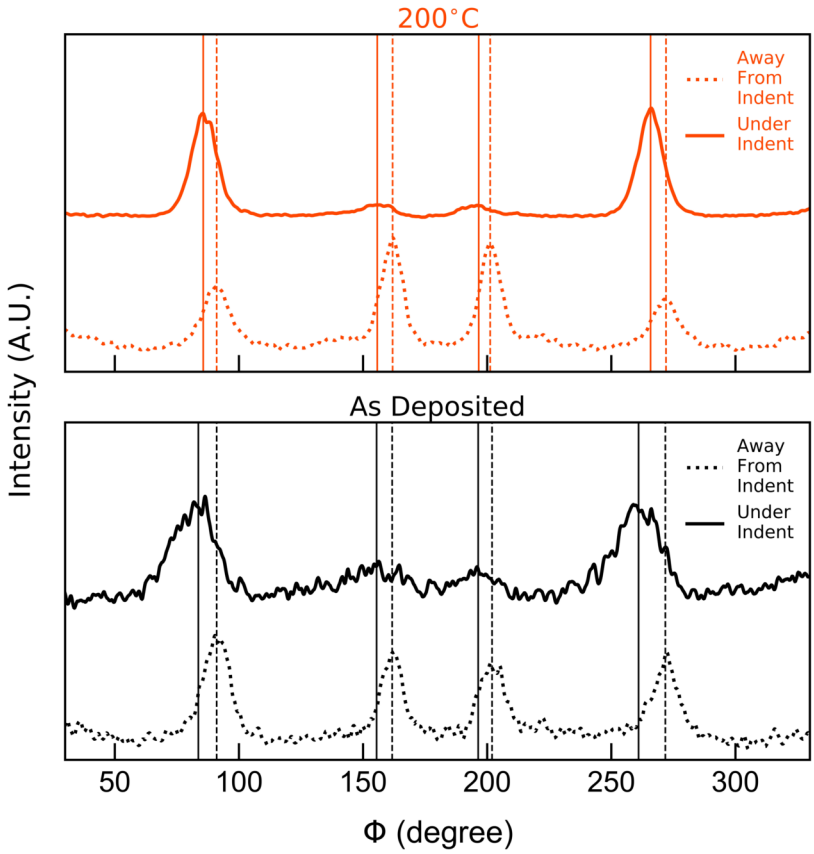

Figure 4.11: Azimuthal projected intensities from the {111} diffraction ring from each of the FIB prepared samples. The intensities were normalized by their maximum and vertically offset for ease of interpretation. Vertical lines represent the peaks identified using a Gaussian peak fitting algorithm.

aperture over the {111} and {200} diffraction rings near $\phi = 100° - 140°$, schematically shown in the inset in Figure 4.12a. The placement of the objective aperture was chosen such that regions that had undergone the most grain rotation would be illuminated. The azimuthal region between 100 ° - 140 ° is ideal for this analysis, as it does not include grains with the predominant undeformed texture. This can be seen in Figure 4.11, where this region is between the two most prominent peaks for the intensities measured away from the indent. Figure 4.12 illustrates that the largest degree of grain rotation is lo-

calized in small regions for both the as deposited (Figure 4.12a) and 200 °C annealed samples. These regions correspond to the aforementioned dark regions in the bright field images (Figure 4.9d,b). However, aside from the surface that deforms quite severely due to the contact with the indenter in both cases, the morphology of these regions beneath the contact surface differs dramatically between the two samples. Figure 4.12a shows that the regions with the largest grain rotation extend nearly perpendicularly from the surface of the indent in the as-deposited material, whereas regions in the annealed material that exhibit the greatest degree of rotation (Figure 4.12b) propagate vertically down from the surface of the indent. The details of this behavior will be discussed in detail in Section 4.4.2.

4.4 Discussion

Our results presented above indicate that the single-phase FCC nanocrystalline $Al_{85}Ni_{10}Ce_5$ prepared by sputter deposition exhibits a 7.6 nm average grain size, excellent mechanical properties (hardness $>$ 4.6 GPa) and good thermal stability (up to 0.7 T_m). Indentation experiments suggest that the hardness increases after annealing up to 325 °C while shear localization, as evinced by shear offsets in the pileup region of indentation experiments, is suppressed due to the formation of a Ni and Ce rich, amorphous grain boundary region. The objective of this discussion is to identify the mechanistic origins of this transition in deformation behavior.

4.4.1 Suppression of shear localization

The indent morphologies of the as-deposited $Al_{85}Ni_{10}Ce_5$ samples presented in Figure 4.3a exhibit profuse shear band formation in the pileup region, a feature often observed during indentation of amorphous metals [224, 225]. Vaidyanathan *et al.* modeled the

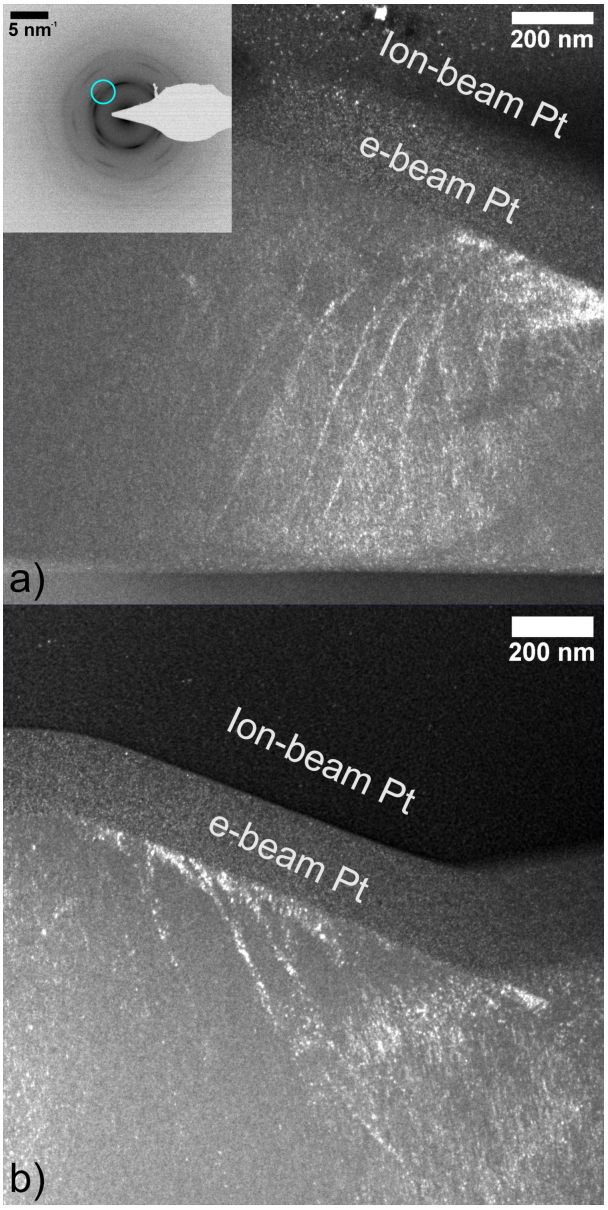

Figure 4.12: DF TEM images from the a) as-deposited and b) 200 °C annealed sample. The objective aperture placement is shown schematically in the inset in a) by the cyan circle, covering the {111} and {200} diffraction rings, in the regions between the peaks owing to the initial texture.

stress state around a Berkovich indentation using finite element simulations [225]. They demonstrated that the circular pattern between corners of the Berkovich indenter corresponds to regions with the highest von Mises stress, thus the regions where shear band

initiation would take place. This observation, in conjunction with existing macroscopic experiments on metallic glasses which demonstrate localized elastic-perfectly-plastic or shear softening behavior [226], explains why numerous shear offsets in such a circular pattern are often observed during indentation of metallic glasses. Nanocrystalline metals have similarly poor strain-hardening behavior and localized plasticity [227], but only rarely are such shear offsets observed. Several researchers observed shear localization in the pileup region during indentation of nanocrystalline Ni-W with grain sizes <15 nm, concomitant with clear displacement bursts during loading, suggesting that the shear offsets are due to the discrete nature of plasticity in materials with such fine grain sizes [21, 43, 45, 140].

Annealing the as-deposited $Al_{85}Ni_{10}Ce_5$ samples below 380 °C, prior to the onset of precipitation and coarsening, both increases the hardness dramatically (Figure 4.5) and suppresses obvious shear localization evident in the pileup region (Figure 4.8, Section 4.3). This observation is markedly different from the behavior of nanocrystalline metals reported in the literature. Rupert *et al.* [43] performed annealing experiments on nanocrystalline Ni-W and observed similar magnitude increases in hardness due to annealing, but that the propensity for shear localization increased markedly. Additional pillar compression experiments suggest that this behavior occurs despite the activation of stress-assisted coarsening, which has been suggested to enhance plastic flow of nanocrystalline metals [42, 53, 140]. Several of these works note that this increased propensity for shear localization due to annealing is quite similar to that of metallic glasses [42, 43].

Processing routes can have a large impact on the shear localization behavior of metallic glasses. Most notably, nearly complete suppression of shear localization during indentation of metallic glasses has been observed for glasses driven to more rejuvenated, or liquid-like states [95, 228, 229]. Meng *et al.* [228] observed suppression of strong shear localization during indentation of a Zr-based metallic glass subjected to high pressure

torsion (HPT). These authors report that the HPT process drives the structure of the material to a softer, more rejuvenated state, where there are many atomic sites where localized atomic rearrangements can occur. The more homogeneous distribution of these sites where atomic rearrangements can more easily occur manifests as a decrease in macroscopically observed shear localization. These authors (and others [229]) observe that the mechanical properties of the glass scale linearly with the degree of stored enthalpy - where a harder glass exhibits a smaller stored enthalpy, implying a relaxed, lower energy state.

Annealing may relax non-equilibrium grain boundaries through the elimination of grain-boundary defects, limiting preferential sites where plasticity can initiate [42, 43]. The argument follows that, similar to metallic glasses, nanocrystalline metals with a more uniform distribution of non-equilibrium boundaries may lead to a more homogeneous deformation morphology without obvious shear localization. However, while nanocrystalline metals with such a uniform distribution of non-equilibrium boundaries may deform more homogeneously, their deformation behavior is still undesirable. Such non-equilibrium boundaries are much more susceptible to deform via grain boundary sliding and atomic shuffling mechanisms, rather than dislocation-mediated plasticity. Grain boundary sliding and atomic shuffling are triggered at much lower levels of stress - suggesting a similar trade-off between strength and deformation morphology akin to that observed in metallic glasses. While this relationship - i.e. a more relaxed nanocrystalline metal is harder and exhibits a larger propensity for localization - has been observed in all previous studies [42, 43, 85, 140], it is counter to what we observe in the nanocrystalline $Al_{85}Ni_{10}Ce_5$ (see Figure 4.5 and Figure 4.8). Brink and Albe [85] observed similar behavior to that observed in Ni-W alloys [42, 43], where the degree of grain boundary relaxation is critical for predicting catastrophic shear localization in systems with a grain size < 10 nm. They also suggest that the maximum strength of a nanocrystalline metal occurs when the grain boundary state is well relaxed - the same condition where local-

ization is most prominent. Again, our results suggest the opposite behavior: annealing the nanocrystalline $Al_{85}Ni_{10}Ce_5$ samples at low temperatures, presumably relaxing the material, not only induces increases in hardness and modulus, but the propensity for localization decreases, suggesting a fundamental difference between the $Al_{85}Ni_{10}Ce_5$ and materials investigated in previous studies.

4.4.2 Deformation mechanisms and texture

The strain rate sensitivity analysis presented in Figure 4.6b, where no significant change in activation volume is observed due to annealing, allows us to conclude that intergranular deformation mechanisms are responsible for accommodating deformation in these alloys irrespective of the extent of chemical segregation. This is unsurprising given the microstructures presented in Figure 4.4, which all exhibit a truly nanocrystalline microstructure despite annealing up to 0.7 T_m. There are numerous intergranular deformation mechanisms operative in nanocrystalline metals, encompassing behavior ranging from atomic shuffling at grain boundaries [40], to grain rotation [34], sliding [33], and the slip of (partial) dislocations as they traverse grain interiors [26]. While many of these mechanisms are potentially deleterious due to their tendency for localization [46], many of the more exotic deformation mechanisms, such as sliding and rotation, can be suppressed through grain boundary relaxation and chemical segregation to grain boundaries, favoring predominantly intragranular dislocation-mediated plasticity [41, 49, 69, 72, 230]. Such a mechanistic transition is unlikely to manifest in strain rate sensitivity measurements, as these mechanisms are all expected to exhibit activation volumes in the range of 3 - 10 b^3 [172, 231], which are difficult to isolate given the uncertainty of our measurements. However, subtle differences in deformation behavior are evident through textural analysis.

Detailed work from Lohmiller *et al.* [41] investigating the deformation of nanocrystalline Pd through *in-situ* synchrotron XRD experiments concluded that intergranular deformation mechanisms, such as atomic shuffling and grain boundary shear and slip, do not cause the formation of a particular crystallographic texture. This is in contrast to intragranular dislocation mediated plasticity, which cause the formation of various crystallographic textures in both coarse grained FCC materials [232] and in highly segregated nanocrystalline metals [140, 233]. Texture evolution in nanocrystalline metals has been broadly discussed by Weissmüller *et al.* [234] and others [235, 236], who suggest that deformation accommodated by intergranular rotation and sliding may randomize pre-existing texture, whereas deformation accommodated by intragranular dislocation-mediated plasticity would favor crystallographic orientations where slip is easiest.

The diffraction patterns presented in Figure 4.10 and Figure 4.11, as well as the DF images in Figure 4.12, suggest that the transition in deformation morphology observed in the $Al_{85}Ni_{10}Ce_5$ with annealing is due to a suppression of localized grain rotation and more homogenous dislocation-based plasticity. As mentioned in Section 4.3.2, when comparing Figure 4.10c to Figure 4.10d, it is evident that the majority of the grains in the annealed sample have undergone a rather uniform rotation of 5.6 °, accommodating the imposed deformation without randomizing the texture. In the as-deposited condition (Figure 4.10a-b), there is both significant grain rotation and randomization of the texture due to deformation. The initial texture formed during deposition favors {111} planes oriented with their normal along the growth direction, so the re-orientation of these grains to accommodate slip on {111} $\langle 1\bar{1}0 \rangle$ directions is necessary for dislocation plasticity to participate in the deformation. The texture observed in the deformed material exhibits the same symmetry as the undeformed material with a 5.6 ° rotation. This is indicative of intragranular dislocation-mediated deformation [41,233–236] in the annealed $Al_{85}Ni_{10}Ce_5$, suggesting there is a mechanistic difference between the deformation of the as-deposited

and annealed samples.

4.4.3 Evolution of deformation microstructure

The DF TEM images Figure 4.12 highlight the differences due to annealing in the location of grains which undergo significant plasticity during indentation. While there is a great deal of plastic deformation at the surface in contact with the indenter, we focus our attention on the deformation occurring beneath the contact surface where we can more directly compare our observations to existing models of Berkovich indentation. Finite element modeling of Berkovich indentation has shown that during elastic loading, iso-stress contours of the resolved shear stress are oriented roughly normal to the surface of the indent [237]. The DF image presented in Figure 4.12a of the as-deposited material beneath the indent shows obvious grain rotation and localization in regions emanating in similar orientations (i.e. normal from the indent surface), suggesting that grains within these regions have rotated after reaching a critical flow stress. The corresponding diffraction pattern in Figure 4.10b (and corresponding section of Figure 4.11) exhibits delocalization and streaking of the peaks in the {111} diffraction ring. Due to the placement of the objective aperture (see inset in Figure 4.12a), the grains that have given rise to the intensity in the image are those that have undergone the most significant rotation, specifically those responsible for the streaking of the secondary peak in Figure 4.11 ($\phi = 150^\circ - 180^\circ$). Furthermore, according to the modeling work of Min *et al.* [238] the regions that exhibit severe grain rotation in the as-deposited $Al_{85}Ni_{10}Ce_5$ extend past contours of appreciable plastic strain predicted by the model. The excellent agreement of the spatial pattern of grain rotation with iso-stress contours [237], rather than plastic strain contours [238], suggests that the deformation in the as-deposited $Al_{85}Ni_{10}Ce_5$ is primarily facilitated by intergranular deformation mechanisms such as atomic shuffling,

grain rotation, and sliding, rather than intragranular dislocation-mediated deformation, ultimately leading to softening and strain localization after initiation at a critical stress.

Iso-contours of accumulated plastic strain from finite element modeling [238] agree quite well with the illuminated regions in the annealed $Al_{85}Ni_{10}Ce_5$ (Figure 4.12b). In the annealed $Al_{85}Ni_{10}Ce_5$, grain rotation is most prominent in regions with the largest accumulated plastic strain, further suggesting that the annealed sample exhibits predominantly dislocation based plasticity. This preference for intragranular dislocation plasticity over non-dislocation based intergranular deformation mechanisms gives rise to the transition in deformation morphology from strong localization in the as-deposited state to homogeneous deformation in the annealed condition. However, a key question remains: why does the segregation of Ni and Ce to grain boundaries and the formation of an amorphous intergranular region induce a transition from intergranular to intragranular deformation and suppress shear localization?

4.4.4 Enhanced mechanical properties of nanocrystalline Al-Ni-Ce

To better understand the role of the Ni and Ce rich grain boundary, we turn our focus to the mechanical properties of the $Al_{85}Ni_{10}Ce_5$ samples which exhibit ultrahigh hardness. The mechanical behavior of rapidly solidified amorphous Al-Ni-Ce alloys with similar compositions reported by Inoue *et al.* [82, 211] exhibit hardness values ranging from 2.6 - 4.7 GPa subject to various annealing procedures. The materials explored in that study with highest hardness are generally brittle and contain a large density of both crystalline Al and intermetallic phases [211]. The mechanical behavior of other binary nanocrystalline Al based alloys have been reported in the literature, but hardness measurements exceeding 2 GPa are mainly observed in alloys with two-phase microstructures

with a large density of brittle intermetallic compounds [239]. Recently, nanocrystalline Al-Mg alloys have been prepared using mechanical alloying that exhibit hardness values exceeding 4.5 GPa after annealing due to strong grain boundary segregation [230]. Thus, the high hardness of the as deposited $Al_{85}Ni_{10}Ce_5$ of 4.67 $\pm$ 0.24 GPa is quite remarkable, and the exceptionally high hardness of 5.62 $\pm$ 0.41 GPa in the 325 °C annealed condition stands apart from other Al alloys (Figure 4.5).

A traditional Hall-Petch [4, 6] analysis is insufficient for predicting the mechanical behavior of the as-deposited $Al_{85}Ni_{10}Ce_5$ due to the small grain size and complex chemical environment at the grain boundaries. Utilizing Hall-Petch coefficients from [198], the grain size reported in Figure 4.1, a Tabor factor of 3 [197], and even including a term for solid solution strengthening [240], we calculate an expected hardness of 1.55 GPa, significantly lower than what is measured. Thus, the remainder of the hardening must be linked to the role of grain boundary chemistry in mediating dislocations nucleation and propagation.

The change in mechanical response due to the formation of a Ni and Ce rich amorphous intergranular film formed during annealing can be reconciled by the elastic contrast between the grain interior and the grain boundary. From the existing studies of Al-Ni-Ce amorphous alloys [210], along with the HAADF images in Figure 4.4, it is clear that annealing drives strong chemical segregation of Ni and Ce to the grain boundaries. This is expected to energetically relax the grain boundaries as well as mechanically stiffen them, making them less prone to sliding or localized atomic shuffling [13, 49, 69]. Simulations of grain boundaries in nominally pure systems have demonstrated that grain boundaries themselves exhibit lower moduli than their crystalline counterparts [241, 242]. The small increase in modulus in Figure 4.5 at temperatures below 0.7 T_m is indicative of such a segregation/relaxation induced stiffening of the grain boundaries. Furthermore, grain boundary stiffness has been shown to substantially affect the behavior of intra-

granular dislocations [243]. Fundamentally, this can be understood from an image force perspective, where an elastically stiff, Ni and Ce rich extended grain boundary would exert a repulsive force on any intragranular dislocations, in addition to providing strong dislocation pinning.

In order to understand the enhancement in mechanical properties due to the formation and evolution of the spatially extended, amorphous grain boundary (Figure 4.13a), we propose the following model, shown schematically in Figure 4.13b. Using the grain boundary widths measured in Figure 4.7 and assuming cuboidal grains with an average grain size of that presented in Figure 4.1, we estimate a volume fraction of grain boundary content in the samples of approximately 36%. Using this volume fraction, in combination with the moduli measured experimentally using indentation (Figure 4.5), we can estimate the modulus evolution of the grain boundary region. Assuming that the modulus is partitioned such that that the grain interiors upon annealing are pure Al with a Young's modulus of 69 GPa [244], and can be described using a Voigt-type rule of mixtures [245], we estimate grain boundary moduli of approximately 200 GPa for the annealed samples. This estimated modulus is high due to the extremely low modulus of the grain interiors, but is quite similar to that of pure Ni [246], thus we view this as an upper bound for the stiffness of the grain boundary. Using the image force analysis of Öveçoğlu *et al.* [247], we can calculate the force on a screw dislocation within the Al grain as a function of distance from the neighboring Ni-Ce rich grain boundaries (shown schematically with an edge dislocation in Figure 4.13b). This model suggests that there is an equilibrium distance of a dislocation several burgers vectors from the adjacent Ni/Ce layers (3.4 b for the 200 °C sample and 3.9 b for the 325 °C sample), and a rapidly increasing repulsive force for a dislocation closer to the adjacent layers. The image force construction breaks down when the distance of the screw dislocation to the interface is very small. Therefore, to estimate the maximum repulsive force on the dislocation, we choose a distance of 1.5 b

away from the interface to calculate the maximum resistance for dislocation propagation. The repulsive force on a dislocation at a distance of 1.5 b from the interface, normalized by the image force $f = \frac{\mu b^2}{2\pi D}$, where μ is the shear modulus, D is the average grain size, and b is the burgers vector, is -1.99 in the 200 °C sample and -2.43 for the 325 °C sample. The corresponding far field stress required to overcome this barrier is 296 MPa for the 200 °C and 362 MPa for the 325 °C. Incorporating this increased resistance to dislocation motion due to the spatially extended, stiffer grain boundary region, we predict that the increase in hardness is $dH = 3 \times d\sigma_y$ of 888 MPa for 200 °C or 1.08 GPa for 325 °C. The measured changes in hardness for these samples compared to the as-deposited material are 820 MPa (200 °C) and 950 MPa (325 °C), which are in excellent agreement with the model prediction. Schematically, the effects of the amorphous intergranular film are shown in Figure 4.13c, where a dislocation traversing the grain must overcome the barrier for nucleation (τ_n) the barrier due to pinning forces at the grain boundary (τ_{pin}), as well as the image forces from the stiff grain boundary region (τ_{gb}) in order to move under the applied stress (τ).

The image force analysis above suggests that the formation of a stiff, amorphous intergranular film, in contrast with a compliant grain interior rationalizes the enhanced hardness of the annealed $Al_{85}Ni_{10}Ce_5$. Additional implications on the mechanical response due to the presence of an amorphous intergranular film include the suppression of shear localization. Pan and Rupert [248] simulated dislocation-grain-boundary interactions in Cu-Zr with amorphous grain boundaries, and observed that the presence of an amorphous grain boundary enables the absorption of several dislocations prior to failure. The simulations also indicate that the von Mises stress in neighboring grains is nearly unaffected by the absorption of dislocations at the amorphous grain boundary, whereas the absorption of a dislocation at an atomically sharp grain boundary leads to high stresses and crack formation. Given this behavior in simulations, the formation of a Ni-Ce rich

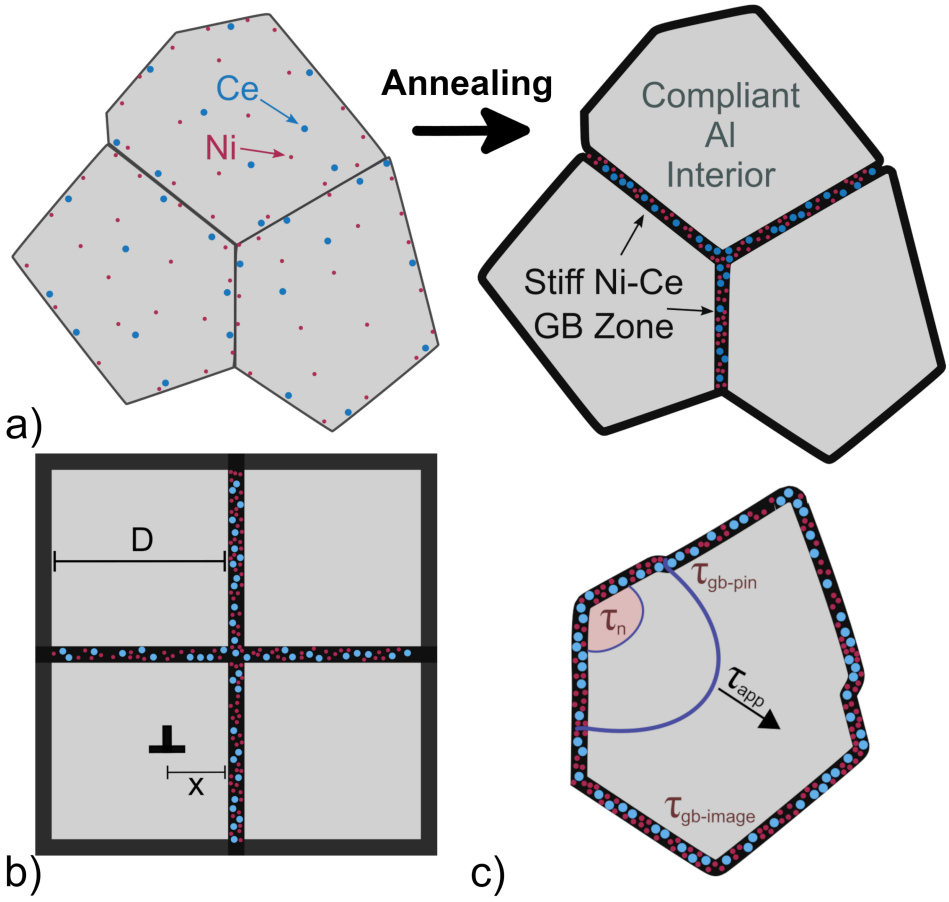

Figure 4.13: Schematic demonstrating a) the formation of a Ni and Ce rich amorphous grain boundary during annealing, b) the model proposed in Section 5.4 with a dislocation embedded in an Al grain of length D and distance X from the grain boundary, and c) the ability of the annealed $Al_{85}Ni_{10}Ce_5$ to accommodate dislocations at the amorphous grain boundaries without transmitting or nucleating new dislocations in neighboring grains.

amorphous intergranular film may be responsible for the suppression of long-range localization. In conjunction with the suppression of intergranular deformation mechanisms in favor of intragranular dislocation plasticity, the tendency for a grain boundary to absorb several dislocations prior to initiating plasticity in neighboring grains would prevent the formation of a percolating path necessary for localization. Pan and Rupert [248] demonstrated that for a 1 nm thick amorphous grain boundary, at least two dislocations can be accommodated prior to crack formation. Given the large shear strain induced by a single

dislocation traversing a 7.6 nm grain ($b/D \approx 4.63\%$ [41]) for the $Al_{85}Ni_{10}Ce_5$, it is possible for the amorphous grain boundaries present in the annealed $Al_{85}Ni_{10}Ce_5$ to accommodate the deformation without affecting neighboring grains. Furthermore, despite the thickness of the amorphous grain boundaries present in the $Al_{85}Ni_{10}Ce_5$ remaining relatively constant due to annealing above 200 °C (Figure 4.7), the segregation-driven increase in stiffness of the grain boundary likely provides additional screening of dislocations that impinge on the grain boundaries [243]. Such screening would further inhibit long range localization, promoting both high strength and homogeneous plastic flow. Thus, the role of such a stiff Ni-Ce rich amorphous intergranular film serves three primary purposes: (1) to impede the intragranular motion of a dislocation providing increased strength, (2) to serve as a strong obstacle for intergranular dislocation transmission, and (3) to provide additional accommodation of impinging dislocations at the grain boundary, all of which assist in mitigating the propensity for localization.

4.5 Conclusions

In this chapter, we discussed the mechanical behavior of a single-phase FCC nanocrystalline Al-Ni-Ce alloy prepared by sputter deposition followed by systematic annealing to drive segregation to grain boundaries. The detailed indentation analysis and electron microscopy investigations of the deformed material allow us to draw the following conclusions.

The $Al_{85}Ni_{10}Ce_5$ sample exhibits many desirable properties, such as a very small grain size (7.6 nm), high hardness (exceeding 4.6 GPa) and thermal stability (up to 0.7 T_m). Indentation morphologies indicate that shear localization, as evinced by shear offsets in the pileup region of indentation experiments, is prominent in the as-deposited state and suppressed due to low temperature annealing. This reduction in shear localization

occurs concomitantly with increases in hardness and modulus. DF TEM analysis of the as-deposited and 200 °C annealed material indicate that the degree of grain rotation, as well as the spatial distribution of regions which have undergone significant plasticity are different, despite identical loading conditions during indentation, suggesting a transition in the operative deformation mechanism. This transition in grain rotation behavior and suppression of obvious shear localization coincides with the formation of amorphous content in the material, likely in the form of an amorphous intergranular film. Image force analysis indicates that the presence of such a stiff intergranular film in contrast with a compliant grain interior is responsible for the increases in strength observed during low temperature annealing, as well as preventing long range localization by promoting uniform intragranular dislocation plasticity over intergranular deformation processes.

These observations suggest that the relationship between mechanical behavior, including strength, propensity for shear localization, and deformation morphology in nanocrystalline alloys may be more complex than the literature would suggest. Specifically, understanding the intricacies of grain boundaries and the evolution of the grain boundary atomistic structure are crucial for predicting the behavior of interface-dominated materials such as nanocrystalline metals with grain sizes below 10 nm.

Chapter 5

Thermal Stability of Nanocrystalline Al-Ni-Ce

In the preceding chapter, the room temperature mechanical properties of an alloyed Al-Ni-Ce nanocrystalline alloy were investigated, indicating an unusual transition in deformation behavior due to the strong propensity for chemical segregation to grain boundaries during processing (annealing). This chapter presents a detailed study using ultrafast calorimetry, *in-situ* transmission electron microscopy (TEM) heating, and X-ray total scattering to uncover the link between the structural evolution of the fully continuous AIFs and thermal stability of the Al-Ni-Ce alloy. Exposure to intermediate temperatures drives chemical segregation and structural evolution of AIFs in the Al-Ni-Ce alloy, enhancing the mechanical properties (demonstrated in Chapter 4) and delaying precipitation of intermetallic phases to higher temperatures. This collective behavior renders the microstructure stable above 64% of its melting point, providing microstructural stability exceeding that in many 'stable' nanocrystalline alloys.

5.1 Elucidation of thermal stability in nanocrystalline Al-Ni-Ce

Our alloy design strategy is premised on the use of chemical complexity and the propensity of multiple interface-segregating species in a multicomponent alloy system [135]. We selected the Al-Ni-Ce ternary system owing to the synergistic co-segregating tendencies of Ni and Ce [142], which will be discussed in greater detail in Section 5.3, and the resulting chemical and structural grain boundary configuration that satisfies the classical criteria for glass formability [79] and AIF formation [125]. We first examine the evolution of microstructure and its role in the thermal stability of nanocrystalline Al-Ni-Ce. *Ex-situ* annealing experiments performed at 200 °C - 380 °C (0.5 - 0.7 T_m), (Figure 5.1a-d) indicate that the sputter deposited Al-Ni-Ce alloy does not exhibit grain growth at temperatures of $\approx$ 325 °C (0.64 T_m) for one hour. High angle annular dark field (HAADF) images in Figure 5.1b,c suggest that grain boundary regions are enriched in Ni and Ce at temperatures between 200 °C - 325 °C, consistent with chemical partitioning in devitrified Al-Ni-Ce alloys [210]. After annealing at 380 °C, the intermetallic phases Al_3Ni and $Al_{11}Ce_3$ precipitate (Figure 5.1d), allowing the remaining Al microstructure to coarsen. Figure 5.1e presents a normalized change in mean grain size extracted from samples presented in Figure 5.1a-d alongside several thermally stable nanocrystalline alloys from the literature [75, 249–254], demonstrating the remarkable stability of the Al-Ni-Ce alloy (additional data provided in Figure 5.3). The alloys included in Figure 5.1e are representative of several classes of nanocrystalline alloys: pure metals, 'stable' alloys, and amorphous intergranular film (AIF)-containing alloys. Pure metals exhibit the least resistance to coarsening, experiencing significant grain growth at 0.2 - 0.3 T_m. 'Thermally stable' alloys exhibit markedly higher thermal stability, pushing up to 0.4 - 0.5 T_m prior to significant coarsening. These alloys include the highest performing

nanocrystalline alloys to-date, including W-Ti [113], Cu-Ta [123, 249], and Ni-W [250]. At the highest homologous temperatures are AIF-containing alloys, specifically a Cu-Zr nanocrystalline alloy and the Al-Ni-Ce alloy [73, 75]. These AIF containing alloys exhibit the highest thermal stability of a nanocrystalline metal to date. The full grain size distributions (Figure 5.2) exhibit a narrow spread that does not markedly evolve during annealing prior to intermetallic precipitation. Abnormal grain growth, which has been reported in nanocrystalline alloy systems containing heterogeneous grain boundary segregation [255], can thus be eliminated as a potential instability mechanism.

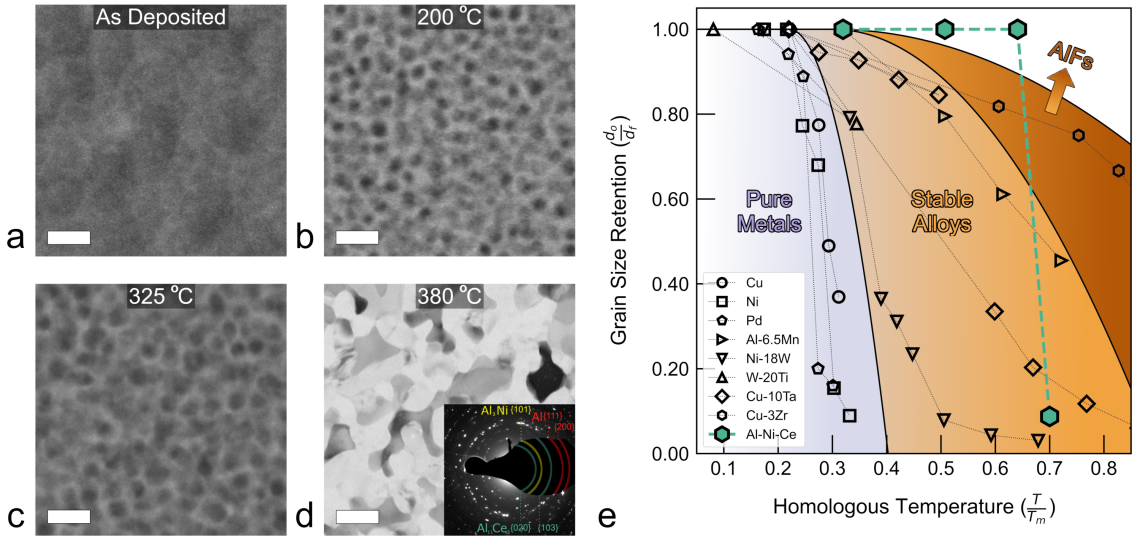

Figure 5.1: *Ex-situ* thermal stability analysis. **a-d**, HAADF (**a-c**) and BF (**d**) micrographs of samples annealed for one hour at temperatures of 100 °C, 200 °C, 325 °C, and 380 °C. Scale bars are 10 nm in **a-c** and 100 nm in **d**. **b-c** exhibit chemical segregation of high mass elements (Ni, Ce) to grain boundaries (bright), resulting in Al rich grain interiors (dark); **d**, provides evidence of intermetallic precipitation and grain growth. Inset is a diffraction pattern shown the presence of Al_3Ni (yellow {101}), $Al_{11}Ce_3$ (green {020} and {103}) and Al (red, {111} and {200}). **e**, Grain size retention for several thermally stable nanocrystalline alloys, alongside the Al-Ni-Ce alloy, as a function of homologous temperature. Data from [75, 249–254].

The thermal envelope of microstructural stability and underlying thermal signatures associated with chemical redistribution and intermetallic precipitation were quantified

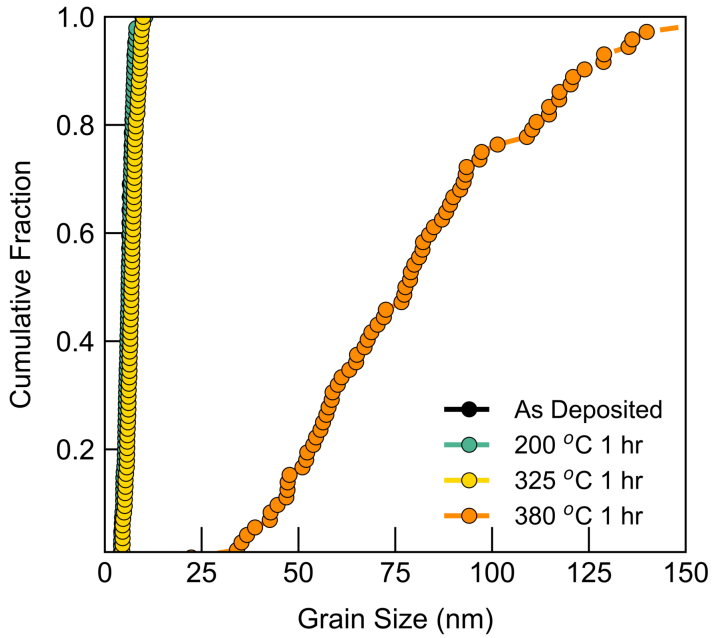

Figure 5.2: Cumulative grain size distributions measured from dark field TEM experiments of *ex-situ* annealed Al-Ni-Ce alloy samples.

using ultrafast differential scanning calorimetry (DSC). Heat flow traces (Figure 5.4a) demonstrate the presence of two exothermic events, labeled T_{gb} and T_{precip}. The event labeled as T_{gb} occurs at temperatures that coincide with chemical enrichment of grain boundaries in Ni and Ce (Figure 5.1b,c), while the second exothermic event (T_{precip}) occurs at temperatures above 325 °C and is ascribed to the nucleation and growth of intermetallics. Qualitatively, the heat flow traces in Figure 5.4a indicate that the precipitation event (T_{precip}) is not strongly dependent upon heating rate, unlike the low temperature exothermic event (T_{gb}). Kissinger analysis (Figure 5.4b) suggests activation energies of 116 kJ/mol and 413 kJ/mol for the exothermic events at T_{gb} and T_{precip}, respectively. The activation energy of 116 kJ/mol is consistent with diffusive activity of Al, Ni, or Ce in an FCC-Al matrix [260, 261], whereas the precipitation activation energy (413 kJ/mol) is uncharacteristically large. Typical values for intermetallic precipitation in Al-Ni-Ce glasses are $\approx$ 200 kJ/mol [262], less than half the value we measure. The

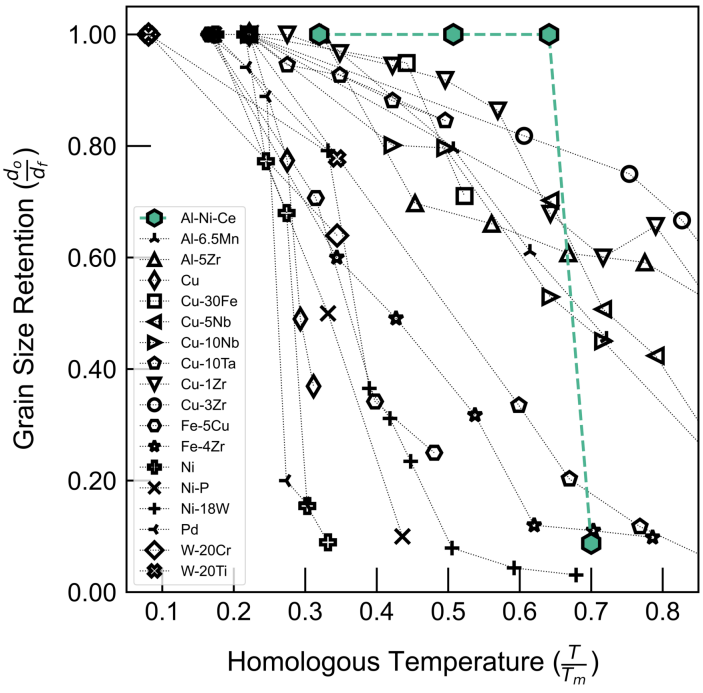

Figure 5.3: Grain size retention vs homologous temperatures for many nanocrystalline alloys. Data from References [75, 113, 114, 121, 196, 249–254, 256–259].

precipitation activation energy we measure is also larger than those in all ternary amorphous Al-transition metal-rare earth alloys [216, 262] and is comparable to higher order amorphous Al-alloys such as AlNiYCoLa [263], whose large activation energy originates in the formation and evolution of several intermetallics with multiple crystal structures.

In-situ TEM heating experiments (Figure 5.5) provide direct visualization of the structural evolution during thermal exposure of the Al-Ni-Ce alloy. The evolution at temperatures below 325 °C is characterized by Ni and Ce grain boundary enrichment and subtle evolution of the Al grains. Individual heating segments to temperatures below 150 °C indicate little microstructural activity, consistent with the absence of thermal events in the calorimetric signal. At temperatures above 150 °C, instances of grain reorientation occur and become more numerous at temperatures approaching 325 °C (Figure 5.5a, b). The reorientation events are evident in the diffraction patterns, where more

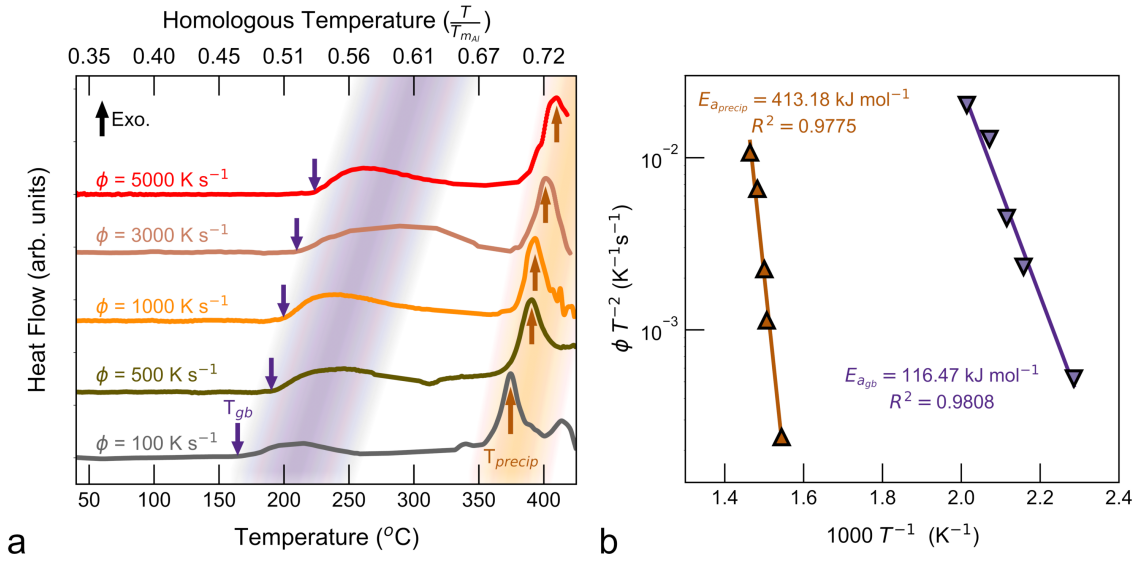

Figure 5.4: Ex-situ differential scanning calorimetry. **a** DSC heat flows with arrows noting onset and peak temperatures of the low (T_{gb}) and high (T_{precip}) temperature exothermic events, respectively. **b**, Kissinger analysis of the two primary exothermic events noted in **a**.

intense and discrete spots after annealing at 325 °C signify fewer unique grain orientations in the imaged area (Figure 5.5d). The presence of more intense diffraction spots often implies grain growth, however grain size distributions measured during the *in-situ* heating experiments (Figure 5.6) indicate no significant grain growth. After heating to 450 °C, the HAADF snapshots (Figure 5.5c) show significant grain growth alongside the nucleation of $Al_{11}Ce_3$ and Al_3Ni precipitates (Figures 5.5d, 5.7) during the second exothermic event detected in the heat flow trace (Figure 5.5e). The negligible mutual solubility of alloying additions in the intermetallic phases suggests that the chemical distribution prior to intermetallic precipitation severely hinders the precipitation kinetics. Furthermore, the role of confinement in the form of both size effects, which suppress the crystallization of nanoscale amorphous alloys [264], and strain energy penalties associated with intermetallic precipitation within the sub-nm-scale AIFs [265] may complicate intermetallic precipitation in the Al-Ni-Ce alloy, giving rise to the high activation energy

of precipitation. These observations, in conjunction with the calorimetric analysis, suggest a co-dependent thermal stability behavior wherein the presence of the AIF stabilizes the microstructure, and the subsequent AIF evolution limits the precipitation of $Al_{11}Ce_3$ and Al_3Ni intermetallics, giving rise to the exceptional high temperature stability of the alloy.

5.2 Amorphous intergranular films underlie thermal stability

The structural evolution of the AIFs that occurs during annealing below 325 °C improves the low-temperature hardness of the alloy [142] while simultaneously impacting the phase decomposition, as evidenced by the high activation energy for intermetallic precipitation (Figure 5.4b). To elucidate the structural signatures underpinning the thermal stability, synchrotron X-ray scattering experiments were performed on the as-deposited and 200 °C annealed material. The total scattering patterns (Figure 5.8a) and resulting pair distribution function (PDF) analysis (Figure 5.9) provides crucial insight on short- and medium-range ordering motifs through the detection of diffuse scattering signals that are usually overwhelmed by the Bragg scattering features. Specifically, the total scattering intensity (Figure 5.8a) exhibits contributions from the amorphous phase (the AIFs) corresponding to the peaks near 1.5 and 2.6 $Å^{-1}$. These peaks become less prominent upon annealing, whereas crystalline features at 4.4 and 6.8 $Å^{-1}$ become more pronounced after annealing. As we do not observe significant grain growth or the nucleation of new grains in Figure 5.1b,c as well as in the *in-situ* TEM experiments (Figure 5.5a-c), nor in previous work [142], we ascribe this evolution in intensity primarily to the structural evolution within the AIF regions.

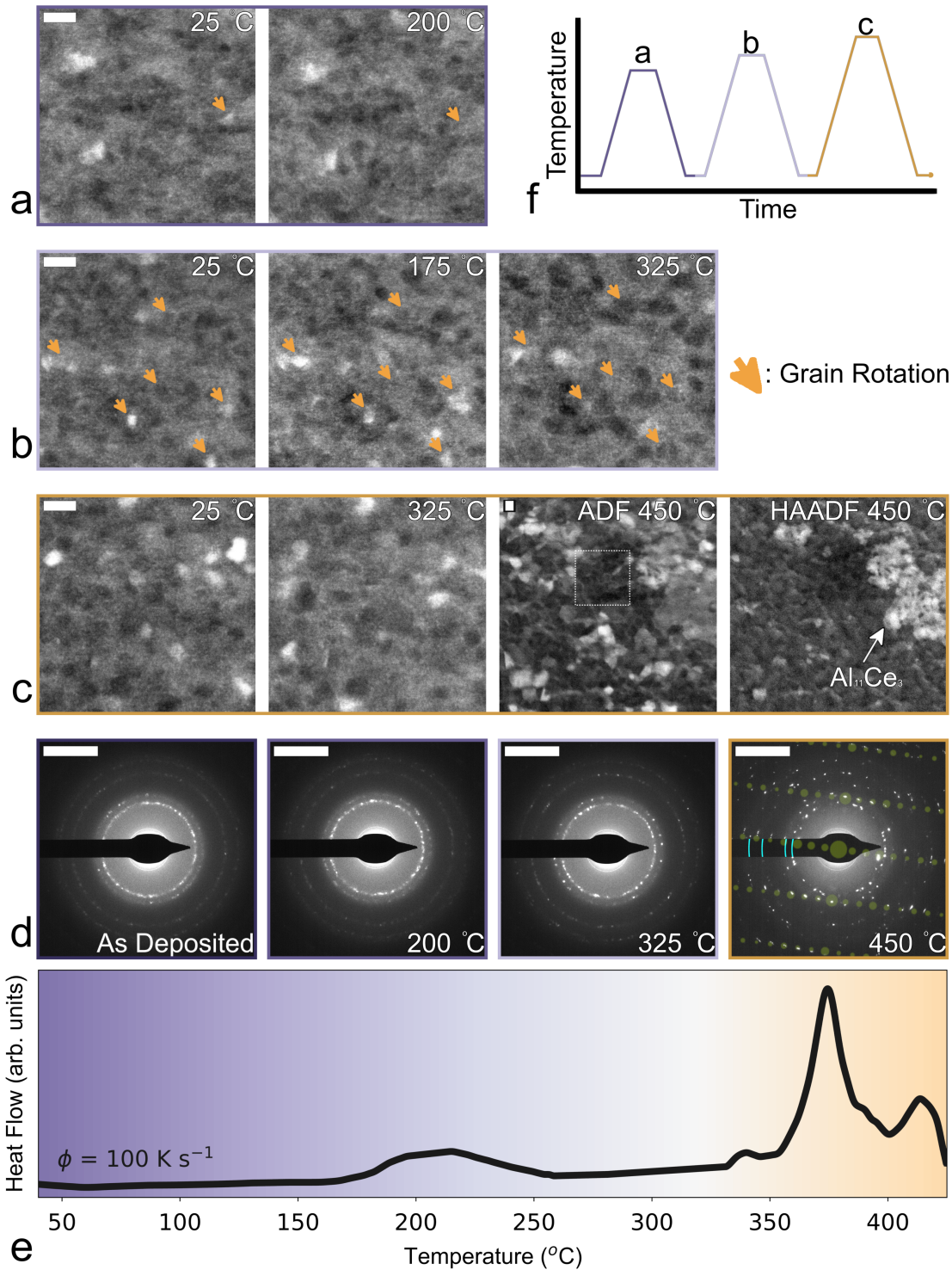
a
25 °C
200 °C
f
Temperature
a
b
c
Time
b
25 °C
175 °C
325 °C
: Grain Rotation
c
25 °C
325 °C
ADF 450 °C
HAADF 450 °C
Al11Ce3
d
As Deposited
200 °C
325 °C
450 °C
e
Heat Flow (arb. units)
ϕ = 100 K s−1
50
100
150
200
250
300
350
400
Temperature (°C)

Figure 5.5: *In-situ* TEM heating experiments. **a-c**, Annular dark field (ADF) STEM micrographs collected during separate heating segments up to 200 °C, 325 °C, and 450 °C. Instances of grain reorientation are noted by orange arrows. Scale bars are 10 nm. **c** also contains a HAADF STEM micrograph collected during final heating sequence up to 450 °C. Dashed region in 450 °C ADF micrograph is the original area imaged at 25 - 325 °C. **d**, Selected area diffraction patterns collected at room temperature after heating to temperature noted. Scale bars are 5 nm^{-1}. Slight evolution in the diffraction patterns is evident at 325 °C, corresponding to reorientation events noted by arrows in **b**. Simulated electron diffraction pattern of a [011] zone axis of α- $Al_{11}Ce_3$ is overlaid in green for comparison to 450 °C diffraction pattern collected from intermetallics in **c**. {111}, {200}, {220} and {311} Al diffraction rings are noted in blue along the beam-stop. **e**, DSC heat flow curve from *ex-situ* analysis for comparison of thermal signatures to direct observations. **f**, Schematic of experimental heating profile.

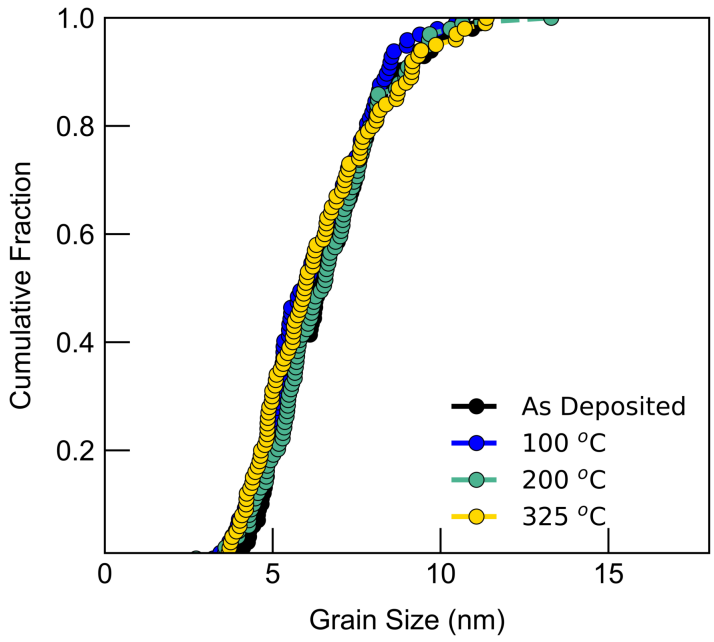

Figure 5.6: Grain size cumulative area distributions derived from conventional dark field TEM images during in-situ heating experiments.

We further examine the evolution of the amorphous grain boundary regions using the total structure factor in Figure 5.8b, which was calculated directly from the background corrected XRD patterns using PDFGetX3 [177]. Two peaks in Figure 5.8b originate from the amorphous content of the material: the feature labeled 'Pre-peak' at 1.5 $Å^{-1}$ and an-

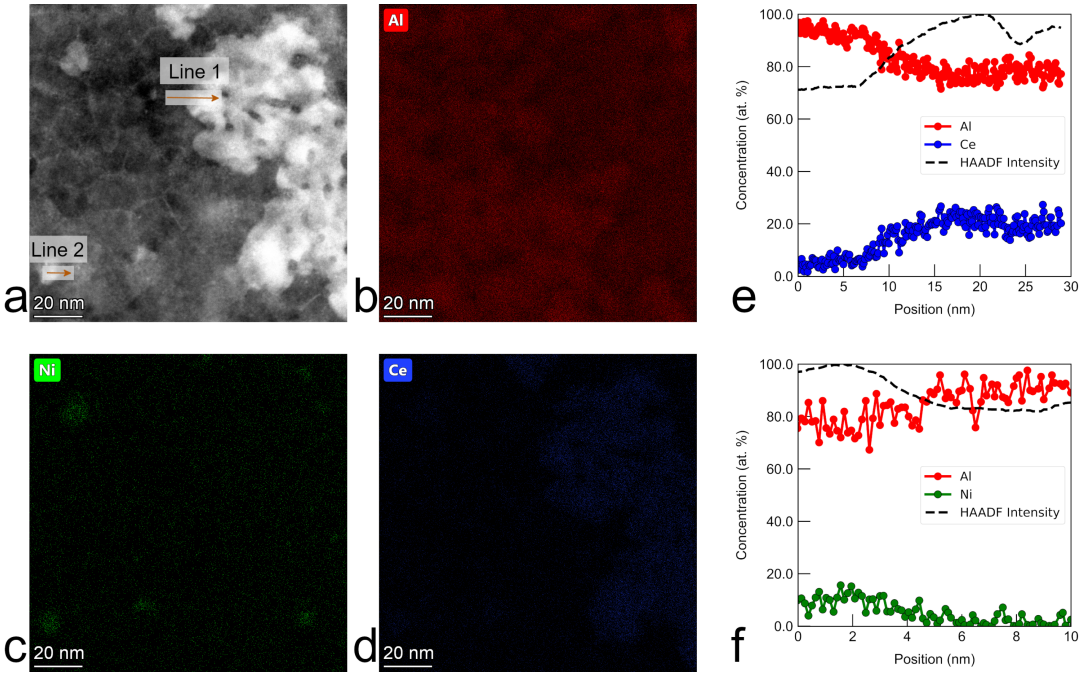

Figure 5.7: EDS map and quantification of Al-Ni-Ce alloy heated in-situ to 450 °C. **a**, HAADF image. Color elemental maps of **b**, Al **c**, Ni and **d**, Ce. Presence of Ni (Al_3Ni) and Ce ($Al_{11}Ce_3$) rich precipitates can be seen in **c**, **d**. **e**, Elemental line profiles of Line 1 crossing into the $Al_{11}Ce_3$ precipitate. **f**, Elemental line profiles of Line 2 beginning in an Al_3Ni precipitate.

other at 2.8 $Å^{-1}$. As the feature at 2.8 $Å^{-1}$ does not evolve significantly with annealing, we will focus our discussion on the feature at 1.5 $Å^{-1}$. Pre-peaks, subtle yet distinguishable features in diffraction experiments of amorphous materials [266], have been observed via neutron and X-ray diffraction experiments of many Al-based liquid and amorphous alloys [267, 268]. These features arise from the medium-range order of solute additions, which take on a quasi-periodic arrangement due to strong pairwise atomic interactions and the packing motifs of polyhedral clusters [262, 267–269]. We observe a significant reduction in the pre-peak present in the structure factor (Figure 5.8b) of the nanocrystalline Al-Ni-Ce alloy after annealing. This reduction in pre-peak magnitude is indicative of a destabilization of the regular packing of solute-centered polyhedra within the AIFs, which has important implications for thermal stability. Structural rearrangements that

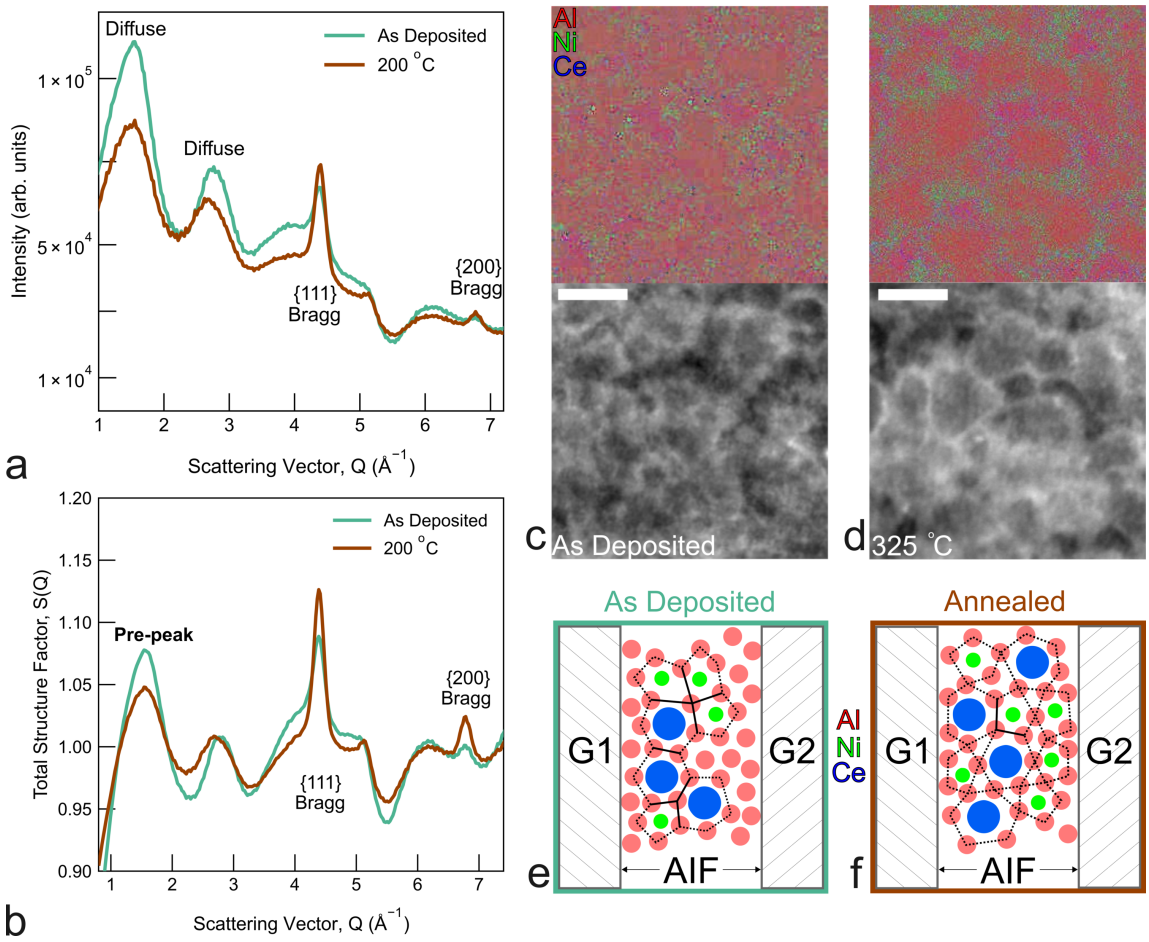

Figure 5.8: **a**, Background subtracted, radially integrated total scattering patterns for thin film X-ray experiments. Two types of features are noted: 'diffuse' features from the amorphous structure and 'Bragg' features from crystalline domains. **b**, Total structure factors derived for the as deposited and annealed (200 °C, 1 hour) sample. The large pre-peak at ≈ 1.5 Å^{-1} and Bragg peaks at {111} and {200} {hkl}s are noted. **c**, **d**, HAADF-STEM and electron dispersive X-ray spectroscopy (EDS) maps of the as-deposited (**c**) and heated (**d**, 325 °C, *in-situ*) Al-Ni-Ce sample. Scale bars are 10 nm. The EDS maps are color coded: Al is red, Ce is blue, and Ni is yellow. The color intensity corresponds to the local concentration in atomic percent, scaled to the minimum and maximum values. Separate grayscale maps are provided in Figures S.7-8 The range of compositions reflected in the color intensities in c are [94, 95] % Al, [3.5, 4.1] % Ni and [1.32, 1.35] % Ce, and for **d** [94, 97] % Al, [0, 6.3] % Ni and [0, 3.4] % Ce, respectively. **e**, **f**, Schematic evolution of solute-centered polyhedral packing within the AlF between two neighboring grains (G1 and G2, hatched) in the as-deposited and annealed states. Dashed lines indicate solute-centered polyhedra, which exhibit more vertex sharing with annealing. Edge sharing faces are noted by solid lines.

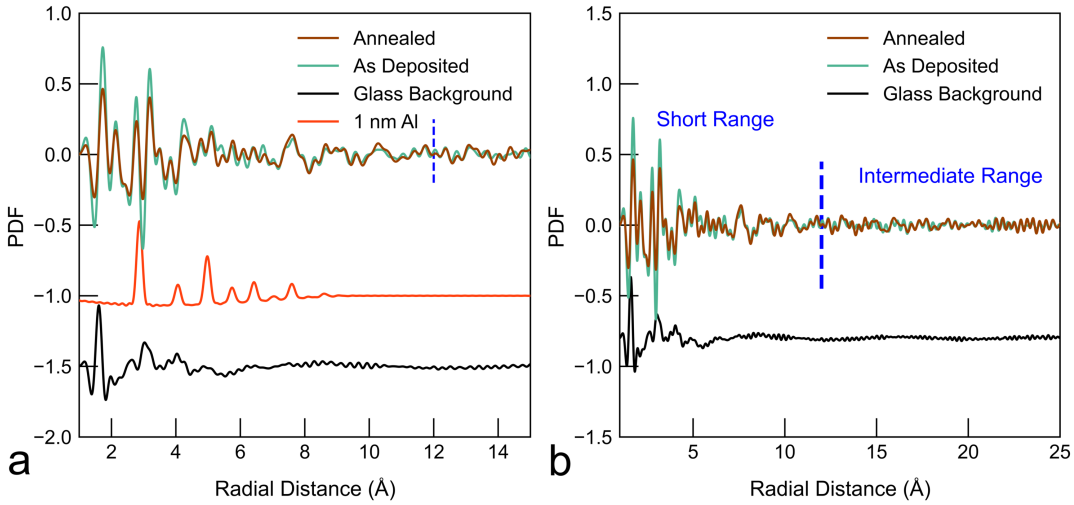

Figure 5.9: **a**, Atomic PDFs showing short-range atomic correlations in as deposited and annealed specimens. Comparisons to a 1 nm FCC Al model and glass substrate PDFs are included for reference. **b**, Evidence of long range ripples at distances > 1.2 nm potentially indicating some longer-range structural motifs within the amorphous phase.

reduce the connectivity of solute-centered atomic clusters giving rise to the pre-peak also effectively minimize structural precursors to the equilibrium crystalline phases, resulting in enhanced thermal stability [270, 271]. The structural evolution evident in Figure 5.8b occurs concomitantly with the chemical enrichment of the AIF in Ni and Ce (Figures 5.1b,c, 5.8c,d, 5.10, 5.11). This increase in local Ni and Ce concentration from $Al_{94.6}Ni_{4.1}Ce_{1.3}$ to $Al_{86.6}Ni_{10}Ce_{3.4}$ (Figures 5.8c,d, 5.12, 5.13) inhibits the regular packing of solute-centered polyhedra, consistent with increasing thermal stability in amorphous alloys with increasing concentrations of Ni and Ce [270].[1] This is depicted schematically in Figure 5.8e,f, where the solute centered polygons exhibit more edge-sharing in the as-deposited case and more vertex-sharing with higher Ni and Ce concentrations. The reduction in structural motifs that provide favorable templating with the equilibrium $Al_{11}Ce_3$ and Al_3Ni phase, the chemically challenging precipitation process, as well as

[1]Figures 5.12 and 5.13 were rebinned Figures 5.10 and 5.11 to 250 X 250 pixels (4x reduction) using HyperSpy [176]. The pixel-wise EDS spectra were summed in order to generate spectra with sufficient intensity for accurate elemental quantification.

potential strain energy penalties [265] and size effects [264], all underlie the microstructural stability of the Al-Ni-Ce alloy. Interestingly, the intrinsic stability owing to the formation of AIFs and its evolution to suppress precipitation act in a co-dependent way; the thermodynamic stabilization mechanism evidently begets the kinetic ones.

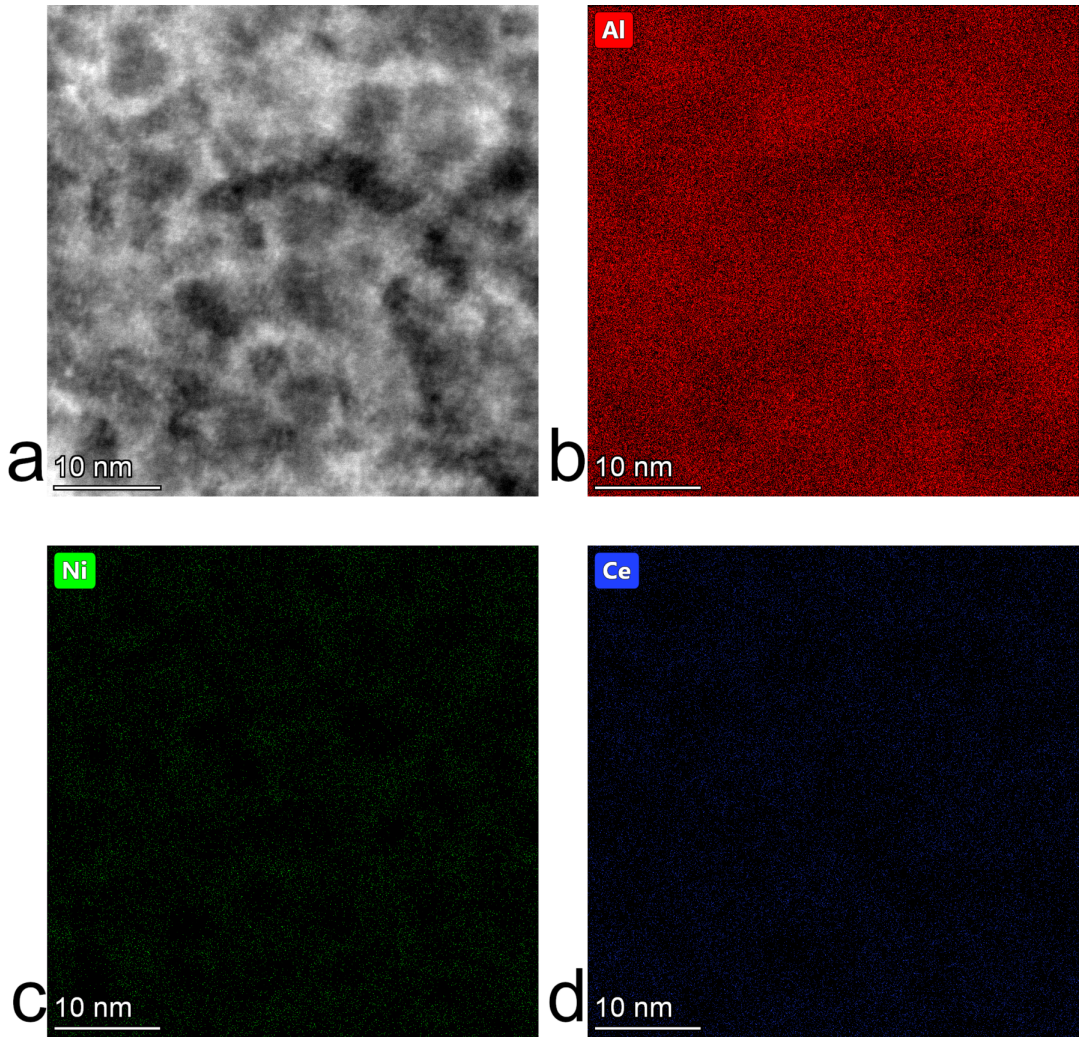

Figure 5.10: EDS map of as-deposited Al-Ni-Ce alloy. **a**, HAADF image. Color elemental maps of **b**, Al **c**, Ni and **d**, Ce.

Our detailed thermal analysis and characterization of the Al-Ni-Ce samples collectively point to an emergent thermal stability. Annealing at temperatures below 325 °C induces three phenomena that occur in concert: 1) chemical enrichment of the amor-

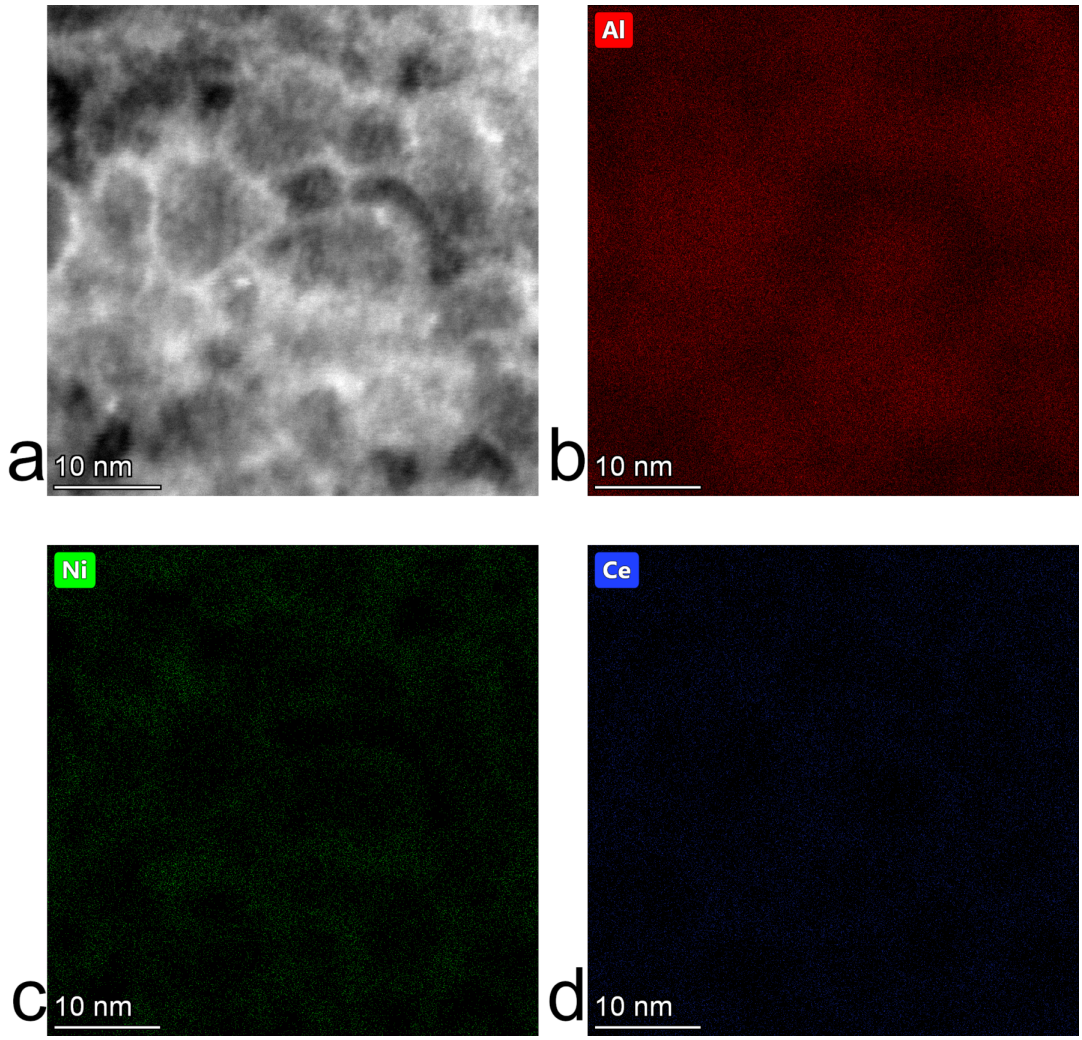

Figure 5.11: EDS map of Al-Ni-Ce alloy heated in-situ to 325 °C. **a**, HAADF image. Color elemental maps of **b**, Al **c**, Ni and **d**, Ce. Chemical redistribution of Ni and Ce to grain boundaries is qualitatively demonstrated in **c, d**, compared to Figure 5.10**c, d**.

phous grain boundaries in Ni and Ce, 2) Al grain reorientation, and 3) a reduction in the medium-range structural order of the AIFs. All three phenomena are fundamentally mediated by diffusive activities, in good agreement with the low temperature activation energy obtained from calorimetric analysis. The chemical enrichment of the grain boundaries, evident in the HAADF micrographs and EDS measurements, is consistent with previous investigations of amorphous alloys due to the negligible solubility of Ni and

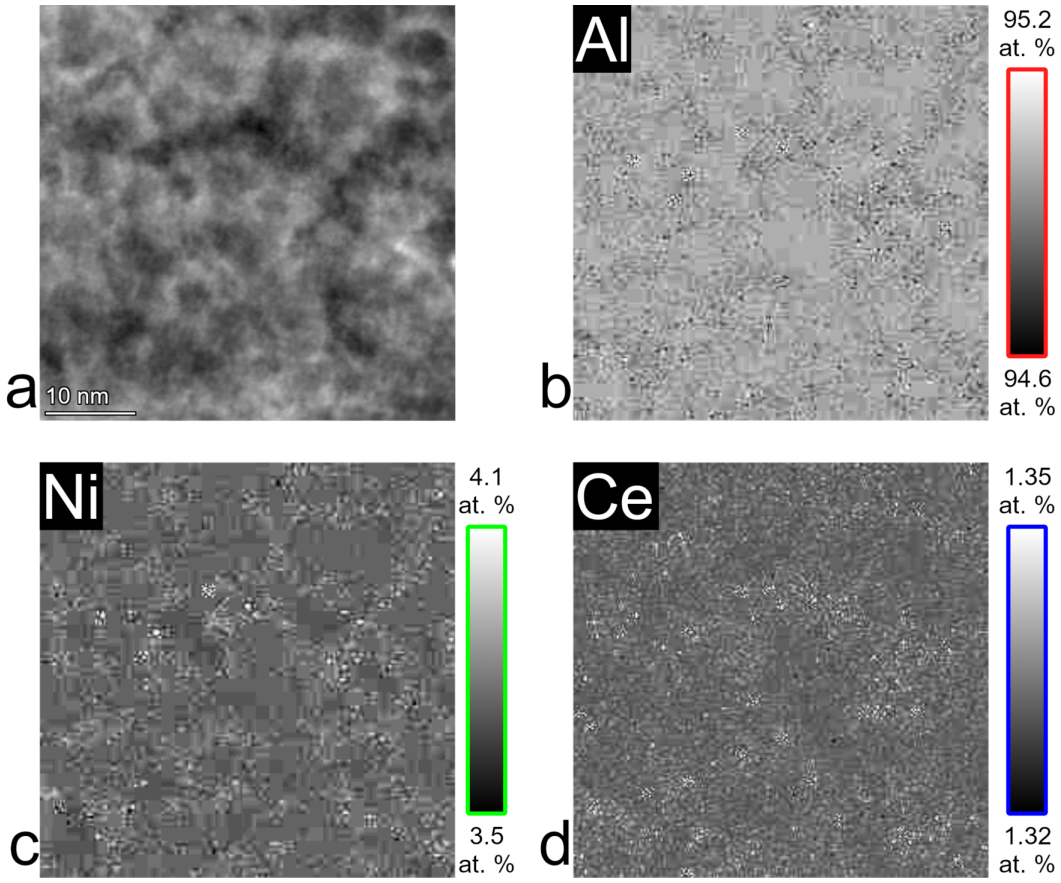

Figure 5.12: As deposited EDS map post-processed in HyperSpy with reduced binning. **a**, HAADF-STEM rebinned image. **b**, Al atomic quantification; **c**. Ni atomic quantification; **d**, Ce atomic quantification.

Ce in Al [210]. Grain reorientation occurs as a result of diffusive events [27], potentially minimizing the surface or grain boundary energy. The signatures from the X-ray total scattering analysis suggest the increase in Ni and Ce in the AIFs causes a destabilization of Ni- and Ce-centered, polyhedral, medium-range order in the amorphous regions of the material, complicating intermetallic precipitation. These concerted effects enhance the thermal stability of the microstructure by stabilizing the AIFs and concomitantly improve the mechanical properties and deformation behavior of the alloy [142].

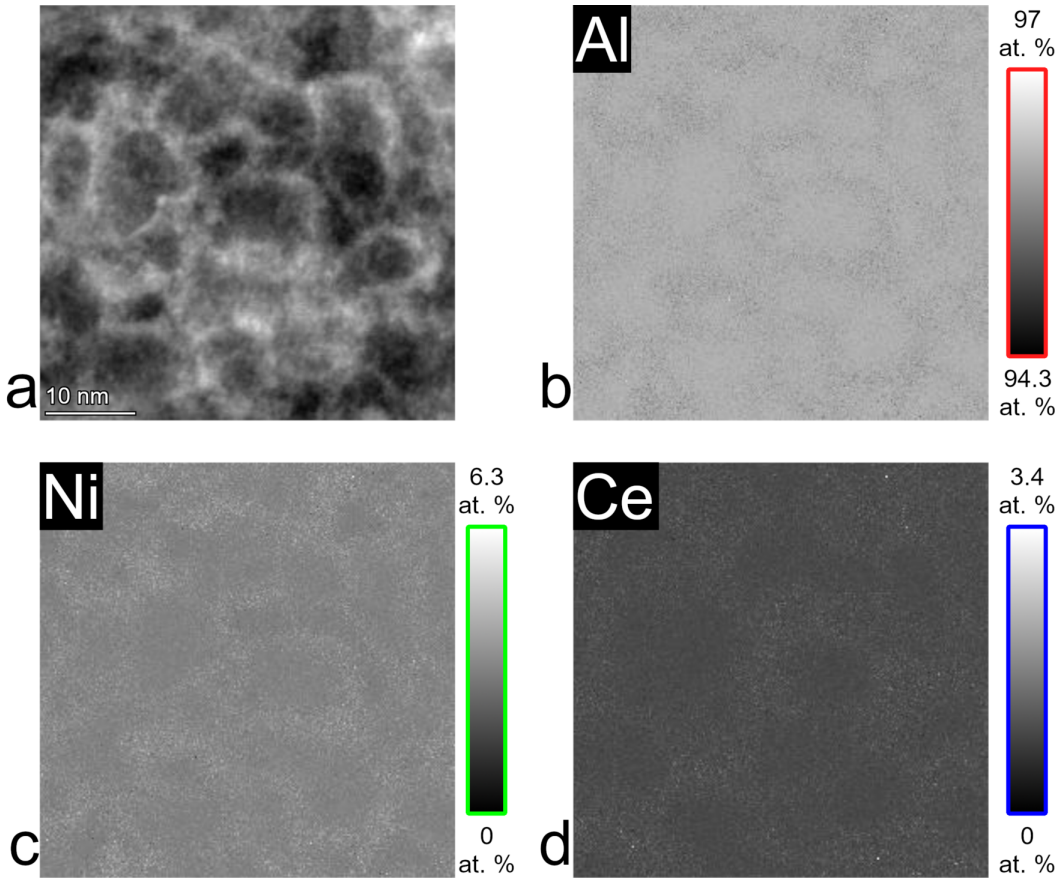

Figure 5.13: 325 °C in-situ annealed EDS map post-processed in HyperSpy with reduced binning. **a**, HAADF-STEM rebinned image. **b**, Al atomic quantification; **c**. Ni atomic quantification; **d**, Ce atomic quantification.

5.3 Nanocrystalline monte carlo simulations

Researchers have recently demonstrated the use of lattice-based Monte Carlo simulations for studying the effects of alloying in nanocrystalline metals [272]. These methods are computationally inexpensive (specifically when compared with simulated annealing or hybrid Monte Carlo molecular dynamics simulations), presenting a simplistic tool for understanding performance of nanocrystalline alloys. The 'nanocrystalline Monte Carlo' (NCMC) methods utilize a modified Ising model to distinguish between grain boundaries and grain interiors, as well as atomic species, all of which have unique bond energies

that can be estimated using bulk thermodynamic quantities. These methods utilize regular solution parameters, which have also been utilized to demonstrate nanometer-scale equilibrium grain sizes in certain binary alloys, or discrete pairwise bond energies [188]. Investigations of mutlicomponent nanocrystalline alloys specifically can benefit from such simulations, as the effects of alloying additions to these systems is often more complex than in binary alloys [208,273,274]. Additional complexity can also be added in to NCMC procedures, such as the incorporation of intermetallic precipitation or ordering (in cases where the phases of interest are orderings on the host lattice) [275].

5.3.1 NCMC simulation procedure

The basic procedure for performing these simulations is as follows. First, a simulation cell of a spatially extended lattice is created. For the simulations in this work, an FCC lattice was used, but the method is applicable to BCC/HCP lattices as well. Next, a microstructure is overlaid by assigning grain ids to sections of the lattice. This may be done using Voronoi tessellation, or manually in case of special geometries (bicrystals, triple points, etc.). The lattice is then decorated with different atomic species by assigning different sites with different chemical ids to be used in calculating the total energy (i.e. different species exhibit different bond energies). The simulation then proceeds by performing Monte Carlo steps (swaps) until some stoppage criterion is met. In conventional Monte Carlo simulations, reaching a constant chemical potential is frequently used as a stoppage criterion, however this cannot be used here, as the overall composition of the system is not changing. As such, these simulations are generally run for a large number of steps, and the total energy of the system should reach a constant value, suggesting equilibrium. Two types of swaps are performed in these simulations: atomic swaps and grain boundary swaps. At each Monte Carlo step, two atoms with different species ids

are selected and switched. Following the metropolis algorithm, the swap is accepted if either the change in energy of the system is negative ($\Delta E < 0$) or with a probability of $P = \exp \frac{-\Delta E}{kT}$ where k is the Boltzmann constant and T is the temperature (i.e. a Boltzmann distribution). NCMC simulations in the literature perform grain boundary swaps by randomly selecting an atom and changing its grain id either to match that of an adjacent grain (resulting in grain growth) or by assigning it a new grain id (resulting in grain nucleation) [208, 272].

The bond energies used in these simulations are quite simplistic. For like elements, the bond energies were estimated from the cohesive energy of the pure elements (E_{coh}), shown in Equation 5.1 where z is the coordination number and subscripts refer to the type of bonding (i.e. aa, ab, bb, etc.) [276]:

$$E_{coh} = zE_{aa} \tag{5.1}$$

The mixing enthalpies of binary alloys were used to calculate the pairwise bond energies between unlike elemental species (Equation 5.2):

$$\Delta H_{mix} = z(E_{ab} - \frac{E_{aa} + E_{bb}}{2}) \tag{5.2}$$

The grain boundary bond energies for pure elements was calculated assuming a grain boundary energy of 0.2 J cm^{-2} (for Al) combined with Equation 5.3, where γ is the grain boundary energy, t is a grain boundary thickness (0.5 nm), and Ω is the atomic volume:

$$\gamma_a = \frac{zt(E^{gb}_{aa} - E^{c}_{aa})}{2\Omega_a} \tag{5.3}$$

The grain boundary energies for unlike elemental species were calculated using estimates

of the segregation enthalpies from [219, 277, 278], and Equation 5.4 from [279]:

$$\Delta H_{seg} = \frac{z}{2}(2E^c_{ab} - E^c_{aa} + E^{gb}_{aa} - E^{gb}_{ab} - \frac{E^c_{aa} + E^c_{bb}}{2}). \tag{5.4}$$

5.3.2 Bi-crystal studies

For the purposes of studying the Al-Ni-Ce alloy, modified NCMC simulations were performed on bi-crystal geometries to study the anticipated segregation behavior of the Ni and Ce in an Al matrix. Such a simulation does not incorporate the amorphous structure of the grain boundaries, but is useful in interpreting one aspect of the chemical segregation observed experimentally. The simulations were performed by creating a cell with dimensions 20 X 20 X 5 (FCC unit cells) initialized such that a planar grain boundary is created with its normal in the +y direction. The cell is then randomly decorated with Ni and Ce solute atoms. The composition used in these simulations was $Al_{97}Ni_2Ce_1$. A 2D projection of this initialization is shown in Figure 5.14. In order to investigate the segregation behavior of Ni and Ce, the grain boundary geometry was fixed, and periodic boundary conditions were used, effectively creating a layered structure with two grain boundaries. No grain boundary swaps were allowed during this simulation. The system was then equilibrated at several temperatures over $>$ 6,000,000 Monte Carlo steps.

In order to confirm equilibration of the system, the total change in energy of the system was computed at every successful atomic swap. The changes in energy during simulations performed at several temperatures are shown in Figure 5.15. It appears that equilibrium is reached in all elevated temperature ($>$ 0 K) simulations. The variability in the higher temperature curves in Figure 5.15 diminishes after more successful Monte Carlo swaps. At 0 K, conventional metropolis Monte Carlo simulations may result in metastable equilibrium states, as the simulation only allows energetically favorable swaps.

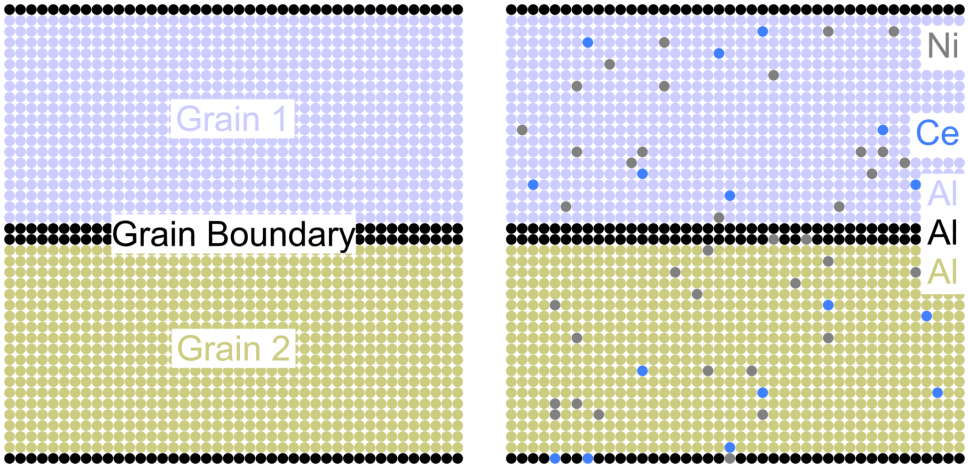

Figure 5.14: 2D projection of bi-crystal Monte Carlo initialization.

This may cause the system to become trapped and not necessarily sample the most energetically favorable condition. That being said, the total reduction in energy for simulations performed at 0 K after > 6,000,000 total Monte Carlo steps is generally lower than those attained at elevated temperatures.

2D equilibrated snapshots, as well as grain boundary enrichment factor as a function of temperature of the binaries - $Al_{98}Ce_2$ and $Al_{98}Ni_2$ - and ternary - $Al_{97}Ni_2Ce_1$ - are shown in Figure 5.16. Grain boundary enrichment factor (β) is the ratio of the local grain boundary composition (χ_a^{gb}) to the total concentration in the alloy (χ_a), as shown in Equation 5.5:

$$\beta = \frac{\chi_a^{gb}}{\chi_a} \tag{5.5}$$

While the enthalpies of segregation of Ce in Al reported in Ref. [219] are slightly positive, experimental evidence of Al-Ce alloys and Ref. [277] suggest that Ce exhibits a strong propensity for segregation away from Al. As such, the simulation was performed with a negative enthalpy of segregation for Ce in Al (-20 kJ/mol). Ni, on the other hand, exhibits a slightly positive enthalpy of segregation in Al, so a small, positive value

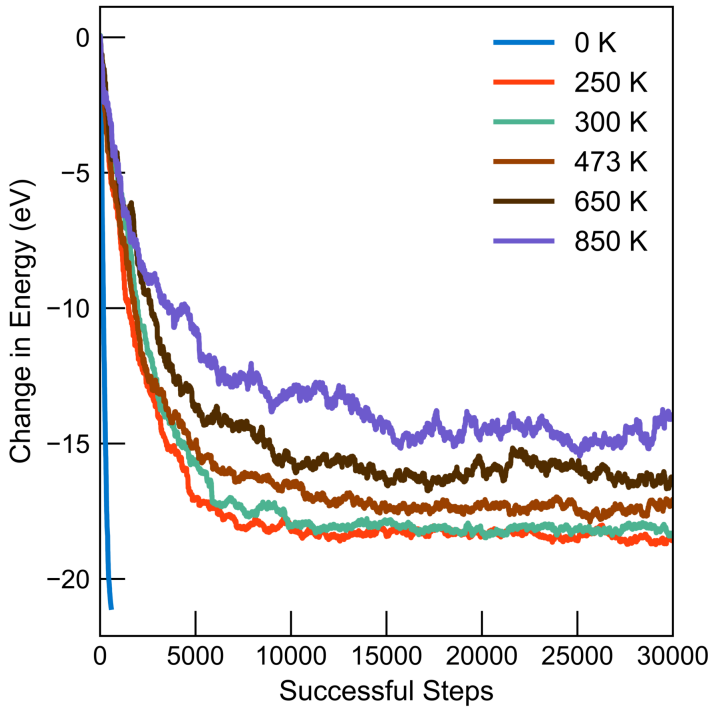

Figure 5.15: Net change in energy of simulation cell as a function of successful Monte Carlo steps in $Al_{97}Ni_2Ce_1$.

was used in the simulation (5 kJ/mol). In the binary cases, this results in clear grain boundary enrichment of Ce, and grain boundary depletion of Ni, evident both in the 2D slices and in the grain boundary excess measurements. The pairwise interaction between Ni and Ce is attractive, so an enthalpy of segregation of Ni in Ce of -25kJ/mol was used. This value is more negative than the estimate in Ref. [219], but agrees with the experimentally observed segregation behavior and negative mixing enthalpies [210, 278]. These bond energies result in in Ce and Ni enrichment of grain boundaries in the ternary alloy at low temperatures. At high temperatures in the ternary alloy, the grain boundary enrichment of Ni decreases, but remains greater than 1 for all simulations performed, highlighting the import of ternary alloying in this system (i.e. including both Ni and Ce, as opposed to just Ni or Ce). Lastly, the temperature at which Ce depletion begins is shifted to higher temperatures in the ternary case.

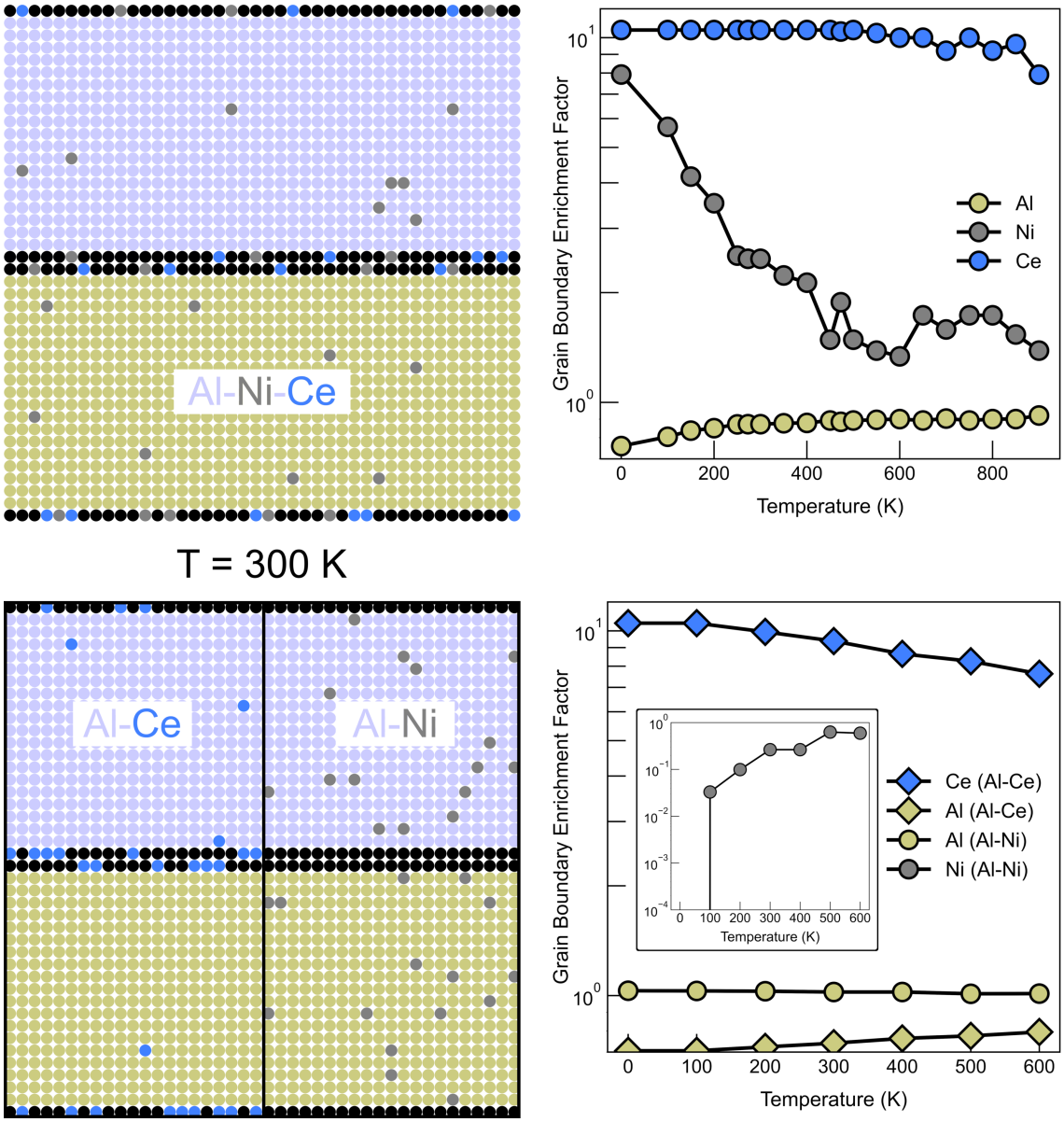

Figure 5.16: Equilibrated 2D snapshots of ternary $Al_{97}Ni_2Ce_1$ (top left) and binary $Al_{98}Ni_2$ and $Al_{98}Ce_2$ (bottom left) at 300K. The ternary system shows enrichment of the grain boundary in both Ni and Ce, whereas only the binary Al-Ce exhibits grain boundary enrichment. This is quantitatively shown in the grain boundary enrichment figures on the right.

5.4 Conclusions

These results underscore the role of multicomponent alloying and amorphous intergranular film evolution via chemical enrichment on the thermal stability of nanocrystalline alloys. The experimental investigation into the thermal stability of the nanocrystalline Al-Ni-Ce alloy suggest that the reduction in the short range order of the AIF during low temperature annealing due to solute enrichment reduces the propensity for intermetallic precipitation by reducing the amorphous structural motifs similar to those in the equilibrium crystalline phases. This structural evolution within the AIF stabilizes the nanocrystalline microstructure against grain growth up to high homologous temperatures. The detailed chemical evolution studied using EDS mapping during *in-situ* heating experiments suggests that the structural evolution is caused by chemical enrichment of the grain boundaries in Ni and Ce, which have been supported by computationally inexpensive NCMC simulations. This study not only provides great insight into the structural origins of thermal stability in AIF-containing nanocrystalline alloys, but also may be utilized to identify novel multicomponent nanocrystalline systems which exhibit exceptional thermal stability.

Chapter 6

Elevated Temperature Mechanical Properties of Nanocrystalline Al-Ni-Ce

In the preceding chapter, experimental investigations into the origins of thermal stability in an AIF-containing Al-Ni-Ce nanocrystalline alloy demonstrated that the evolution of the atomistic structure of the amorphous content of the alloy give rise to the promising microstructural stability. However, outstanding questions remain regarding the mechanical integrity of AIF-containing alloys at elevated temperature. In this chapter, high temperature nanoindentation will be utilized to demonstrate the excellent elevated temperature strength of the nanocrystalline Al-Ni-Ce alloy. These results suggest that the nanocrystalline Al-Ni-Ce alloy not only exhibits thermal stability exceeding that of many thermally stable nanocrystalline alloys, but exhibits high temperature mechanical properties that outperform all current state-of-the-art Al alloys. Activation parameter analysis of the temperature dependent strength suggests that, prior to second phase precipitation, the weak temperature dependence can be ascribed to shear-transformation-zone based

grain boundary plasticity within the AIFs. After intermetallic precipitation, the alloy exhibits a stronger temperature dependence similar to that of precipitation strengthened Al alloys. By combining these results with calorimetric modeling from the previous chapter, a model for anticipating the transition between strength regimes after various thermal exposures is proposed.

6.1 Elevated temperature mechanical properties

The room and elevated temperature mechanical properties of the Al-Ni-Ce alloy measured by high temperature nanoindentation. These data were converted to strength values assuming a Tabor factor of 3 (i.e. $\sigma = \frac{H}{3}$) [20, 97, 197]. This Tabor factor is large given the high hardness to modulus ratio [280], resulting in lower reported strength values, but was used to account for any potential pressure sensitivity of the alloy [40]. Figure 6.1 presents an estimate of the room temperature specific strength of the Al-Ni-Ce alloy. The density was calculated using the composition of the alloy determined by EDS ($Al_{94.9}Ni_{3.8}Ce_{1.3}$), and the elemental densities for constituent elemental metals. Figure 6.1 demonstrates the high strength, low density, and extremely small grain size of the Al-Ni-Ce alloy relative to many Al-based alloys. The properties of conventional Ti-6Al-4V and Mg AZ31B, both high specific strength alloys utilized in aerospace applications, are included here as well to demonstrate the exceptional properties of the Al-Ni-Ce alloy.

The temperature-dependent properties (Figure 6.2) of the as-deposited Al-Ni-Ce alloy demonstrate that while several nanostructured Al alloys exhibit comparable room temperature strength, our alloy exhibits higher strength at elevated temperatures compared to all previously reported nanostructured and high performance conventional Al alloys [283, 290–293]. The strength decreases from 1650 MPa at room temperature in the as-deposited state to 1350 MPa at 250 °C. After heating to 250 °C and cooling back down,

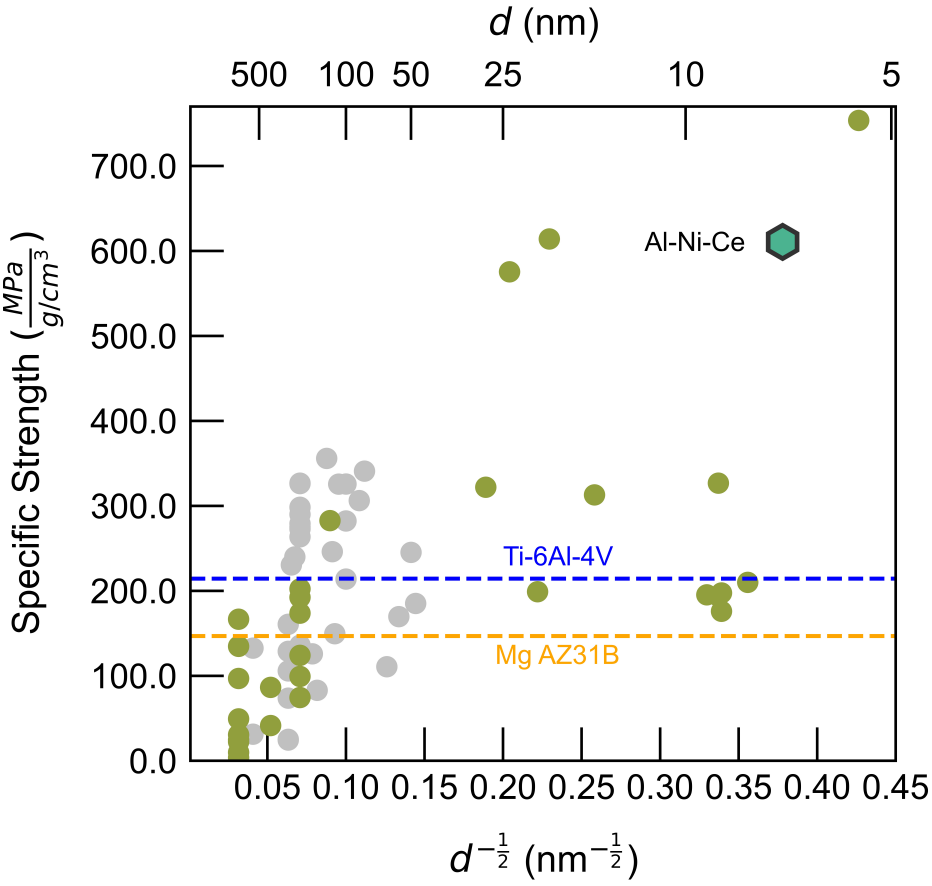

Figure 6.1: Estimated specific strength of Al alloys as a function of grain size. High specific strength alloys Ti-6Al-4V and Mg AZ31B are included for comparison. Data measured by indentation is colored in green. Data from references [230, 239, 281–289]

the room temperature strength of the alloy attains a maximum of 1800 MPa, providing additional corroboration of a grain boundary relaxation process. The strength drops considerably at temperatures above 300 °C due to significant microstructural evolution and intermetallic precipitation, evident in the room temperature hardness measurements performed after heating (Figure 6.2, hatched marker). At 325 °C the strength was measured to be 230 MPa - a large reduction relative to the room temperature performance of the alloy, but still considerably higher than many precipitation-strengthened Al-alloys, including high-performance Ce-containing cast Al-alloys [292, 293].

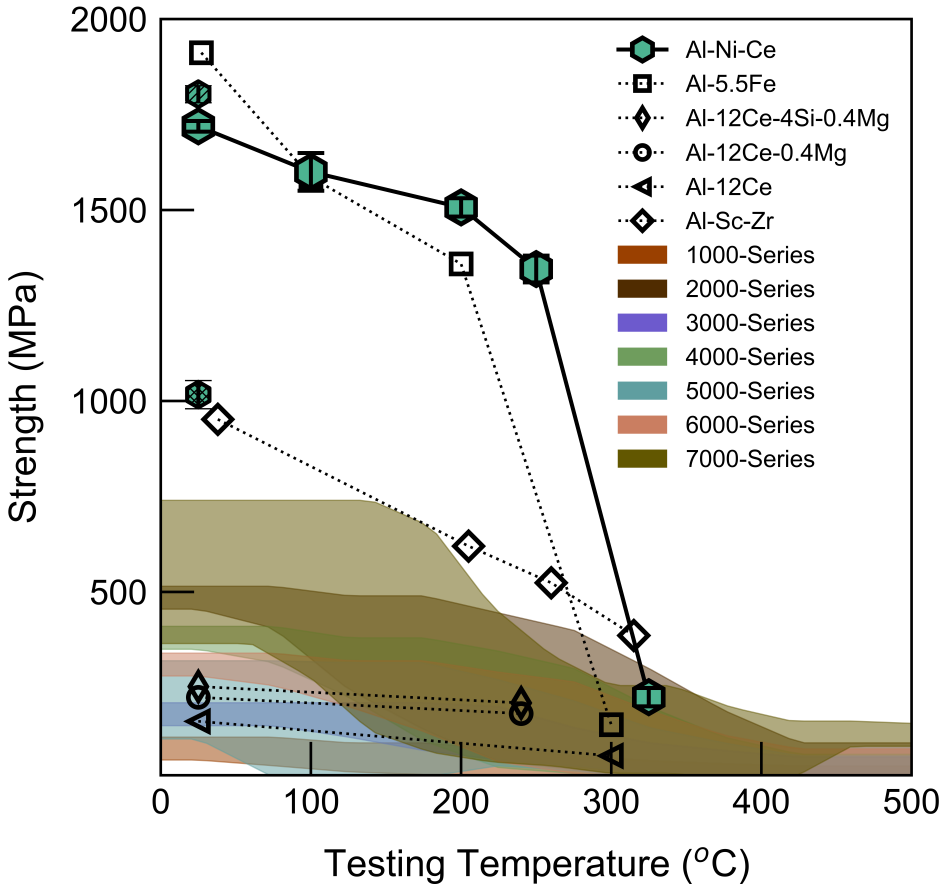

Figure 6.2: Elevated temperature mechanical properties of the Al-Ni-Ce alloy, alongside conventional (1XXX-7XXX series) alloys, Sc and Ce containing alloys, and other high performance Al-alloys (data from [283, 290–293]). Error bars for the Al-Ni-Ce sample are within the marker. The maximum room temperature strength was recorded after heating to 250 °C is noted by the single hatched hexagonal marker. The room temperature strength after heating to 325 °C is noted by the cross hatched hexagonal marker.

6.2 Activation parameter analysis

Despite these impressive elevated temperature mechanical properties, the mechanistic origin underpinning the temperature-dependent strength of the alloy is not obvious. While all metallic alloys exhibit temperature-dependent strength, we seek to unravel the competing roles of the amorphous and crystalline domains on this temperature dependence in our AlF-containing nanocrystalline alloy. In order to isolate these effects, we

first consider the role of the amorphous phase on the strength. Bulk amorphous metals exhibit a near universal temperature-dependent yield strength [294], presented below:

$$\frac{\tau}{G} = (0.036 \pm 0.002) - (0.016 \pm 0.002) \times \frac{T}{T_g}^{\frac{2}{3}} \tag{6.1}$$

where τ is the shear yield stress, G is the shear modulus, T is the temperature and T_g is the glass transition temperature. The relationship in Equation 6.1 was derived using shear transformation zone (STZ) theory, and numerical parameters for the critical shear strain necessary to initiate plasticity were fit with a large body of data on numerous metallic glasses. The temperature dependent yield strength according to this universal yield description in amorphous alloys using a shear modulus of 29 GPa and a glass transition temperature of 220 °C [212, 295] for the Al-Ni-Ce alloy are presented in Figure 6.3. While the absolute strength predicted by the universal yield description in amorphous alloys does not suffice in predicting the properties of the Al-Ni-Ce alloy (Figure 6.3), the temperature dependence is quite similar, suggestive of a similar underlying deformation process.

One promising attribute of elevated temperature indentation testing is the ability to derive activation parameters from both the rate and temperature sensitivity of the measured properties, which provide insight into the mechanistic underpinning of the mechanical behavior. Several analysis techniques exist for extraction of these parameters from testing, such as those explored in Refs. [296–298]. However, given the substrate influence on the indentation modulus (Figure 2.5), several of these techniques are unsuitable for the present data. Nevertheless, using a phenomenological, power law description for the 'steady state' yield strength [296], σ_s, we can extract activation parameters as

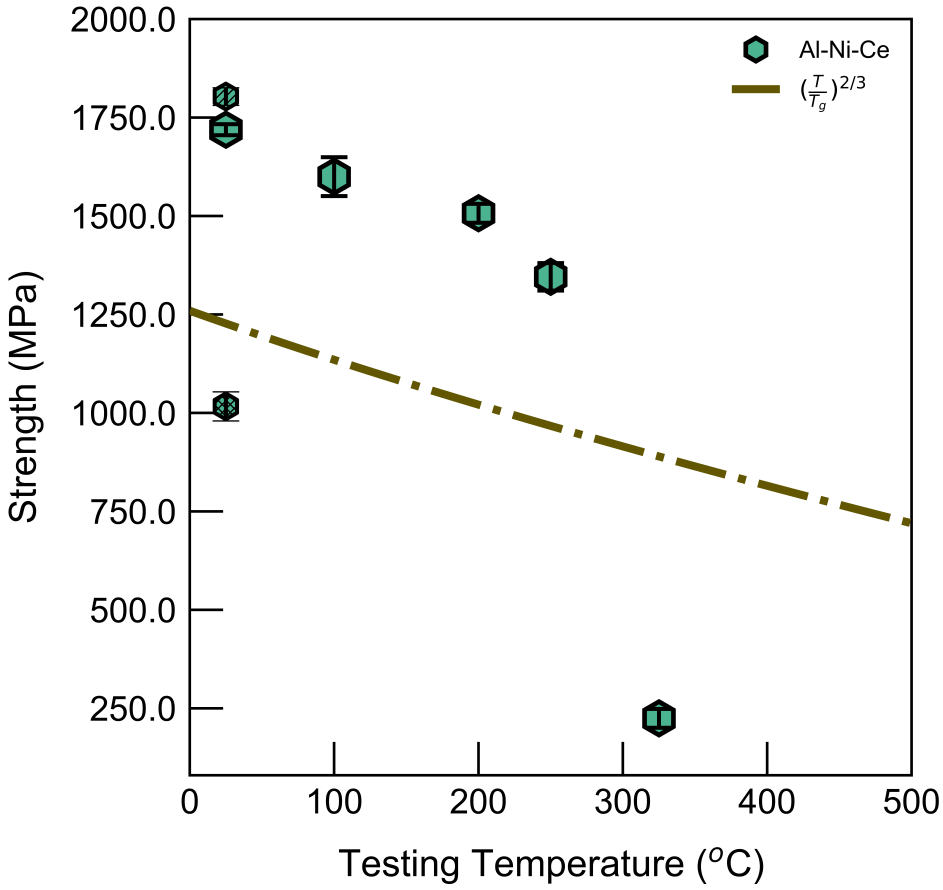

Figure 6.3: Elevated temperature strength of Al-Ni-Ce alloy with universal strength dependence derived for bulk metallic glasses from Ref. [294].

follows:

$$\sigma_s = K\dot{\epsilon}^m \tag{6.2}$$

where K is a pre-exponential factor, $\dot{\epsilon}$ is the strain rate and m is the rate sensitivity. Next, we assume that the strain rate is governed by a thermally activated mechanism such that:

$$\dot{\epsilon} = B \exp \frac{-\Delta G^*}{kT} \tag{6.3}$$

$$\sigma_s = K' \exp \frac{-m\Delta G^*}{kT} \tag{6.4}$$

where B, K' are constants, k is the Boltzmann constant, and ΔG^* is the apparent activation enthalpy. From this description, we can calculate the apparent activation energy by obtaining the slope of $ln(\sigma_s)$ vs $\frac{m}{T}$, which yields an activation enthalpy of 12.7 kJ mol^{-1} or 0.13 eV for the AIF regime, and an activation enthalpy of 120 kJ mol^{-1} or 1.24 eV for the intermetallic regime. Strain rate sensitivity values were measured during indentation jump tests performed at each testing temperature. The activation volumes measured during jump tests at room temperature prior to microstructural coarsening are unusually high and were not used for activation parameter analysis; rather, activation volumes of 8 b^3, consistent with AIF-containing elevated temperature measurements as well as those reported in Ref. [142], were utilized for the room temperature activation volume when performing activation parameter analysis. All data measured (and utilized in these calculations) are presented in Table 6.1. Corresponding fits to data are presented in Figure 6.4.

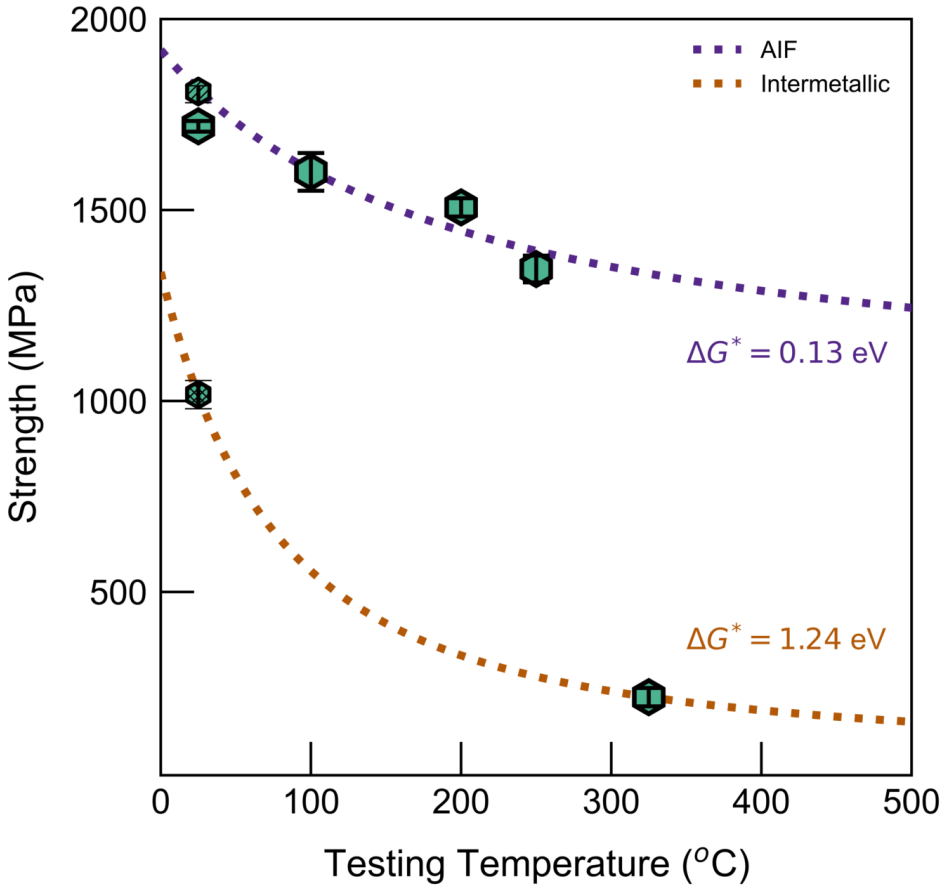

Figure 6.4: Mechanical properties of the Al-Ni-Ce alloy, along with corresponding fits from activation parameter analysis.

Table 6.1: Summary of elevated temperature indentation testing - testing temperature, previous thermal exposure, hardness, and rate sensitivity measurements.

Test Temperature (°C)	**Previous Exposure (°C)**	**H_o (GPa)**	**Activation Volume (b^3)**	**Strain Rate Sensitivity, m**
25	25	5.16 ± 0.04	123 ± 54*	0.0023 ± 0.0007
25	200	5.43 ± 0.07	181 ± 84*	0.0016 ± 0.0008
25	250	5.42 ± 0.06	207 ± 119*	0.0015 ± 0.0007
25	325	3.05 ± 0.11	11 ± 1	0.0373 ± 0.0026
100	25	4.81 ± 0.15	32 ± 21	0.0140 ± 0.0060
200	25	4.52 ± 0.07	10 ± 2	0.0501 ± 0.0091
250	25	4.04 ± 0.11	6 ± 1	0.1000 ± 0.0150
325	25	0.67 ± 0.07	31 ± 2	0.1390 ± 0.0076

* All activation parameter calculations were performed using a room temp (25 °C) activation volume of 8 b^3 from Ref. [142]. The origin of the large room temperature activation volume data measured in the Al-Ni-Ce alloy during jump testing is actively being investigated.

Focusing on the AIF regime, we can estimate the Helmholtz activation energy as described in Ref. [62] through the addition of the mechanical work as follows:

$$\Delta F = \Delta G^* + \Delta W \Delta W = \nu_{act}\sigma = \nu_{act}\frac{H}{3} \tag{6.5}$$

where ν_{act} is the activation volume, σ is the stress, and H is the hardness. This calculation results in a Helmholtz energy between 0.9 and 1.35 eV, which agrees excellently with that for STZ activity in a monolithic Al-based glass [299] and grain boundary atomistic shuffling in nanocrystalline metals [62]. While estimating STZ volume using such analysis is the subject of fervent debate, and may not provide physically meaningful information, using the formulation presented in Ref. [62], the STZ-size can be estimated by dividing the activation volume by the critical shear strain to initiate plasticity, assumed to be 0.2. This results in an estimated STZ volume for the Al-Ni-Ce alloy is between 0.7 and 1.1 nm^3, or 43-67 atoms. The reader is encouraged to compare these values with the grain boundary thickness distributions presented in Chapter 4, Figure 4.7, as well as the size of the domains measured from synchrotron experiments, Figure 5.9.

These observations suggest that the rate limiting feature of the mechanical behavior of the AIF-containing Al-Ni-Ce alloy regime is STZ activity in the AIF-grain boundary regions, consistent with previous studies of crystalline-amorphous nanolaminates [300]. Other researchers have noted that such STZ-like grain boundary deformation displays a temperature dependence similar to that of the universal yield criterion for metallic glasses [62], which agrees well with Figures 6.3 and 6.4. Although this precise deformation mechanism has been argued to underpin the deleterious shear localization behavior in nanocrystalline metals at low temperatures [62, 233], STZ-like rate limiting deformation mechanisms provide intrinsic high temperature strength retention in our ternary alloy, suggesting that AIFs not only enhance microstructural stability and damage tolerance,

but enable high temperature strength.

6.3 Predicting the transition in deformation behavior

The dramatic reduction in strength at 325 °C is due intermetallic precipitation, eliminating the AIFs and enabling microstructural coarsening. This is evident not only in the reduction in room temperature strength collected after heating to 325 °C, but also in the activation analysis for these data. This analysis suggests a Gibbs activation enthalpy of 1.24 eV for the precipitation regime (shown in Figure 6.5), identical to dislocation-mediated behavior in UFG Al [298]. We use this mechanistic insight, combined with the kinetic parameters obtained from our calorimetry, to next predict the transition between the AIF-controlled and precipitation regimes, which is essential in designing materials for critical applications. Given the origin of this transition is rooted in intermetallic precipitation, we can apply the Kissinger analysis (Figure 5.4b) to estimate the transition temperature of mechanical properties due to precipitation. Since this method provides a relationship for peak temperature during non-isothermal conditions, it serves as a conservative estimate of this transition by calculating the peak temperatures for precipitation with an equivalent heating rate of the total thermal exposure per 1 °C. For instance, for a 30 min exposure, the equivalent heating rate would be $\frac{1°C}{30min} \approx 5.54 \times 10^{-4} \frac{°C}{s}$, corresponding to an estimated peak or transition temperature of 288 °C, in excellent agreement with the experimental data. Additional estimated transition temperatures are included in 6.5 for 2 and 1000 hours at temperature. These estimates are quite conservative - Figure 5.1**c** demonstrates microstructural stability for 1 hour at 325 °C, while the calorimetric model predicts stability for less than 10 minutes - but are useful for applications where

retention of strength at temperature is critical. Such a simplistic model may also enable high-throughput screening of future novel alloys with the primary objective of increasing the precipitation peak temperature, enabling nanocrystalline alloy development for even higher temperature applications.

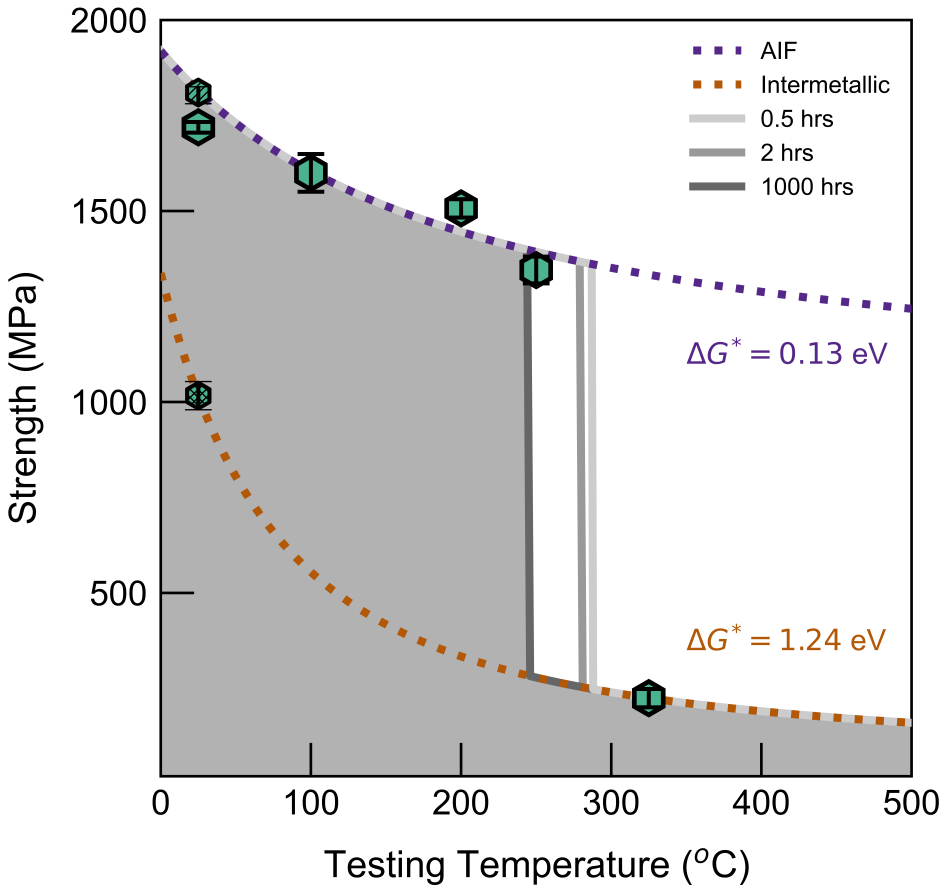

Figure 6.5: Projected transition temperatures for various time exposures from calorimetric modeling, alongside strength and activation parameter analysis above.

6.4 Conclusions

In this chapter, we have discussed the high temperature mechanical behavior of the Al-Ni-Ce alloy. Elevated temperature indentation measurements suggest the Al-Ni-Ce

alloy exhibits strength retention that outperforms all high performance Al-alloys to date below 300 °C and absolute strengths comparable with high performance alloys at higher temperatures, despite precipitation of intermetallic phases and coarsening of the microstructure. Analysis of these high temperature data suggest grain boundary mediated STZ-like activity dominates the mechanical behavior prior to intermetallic precipitation, manifest in a weaker temperature dependence on strength than conventional Al-alloys. Finally, calorimetric analysis is able to provide a conservative estimation of the transition temperature between AIF-controlled and precipitation-controlled mechanical properties. These results not only demonstrate the scientific origin of the exceptional properties of this Al-Ni-Ce alloy, but also provide insight into alloy design strategies that embrace the presence of atomic disorder, ultimately leading to alloys with exceptional high temperature performance.

Chapter 7

Conclusions and Perspective

This thesis has presented several experimental studies investigating the role of grain boundary structure in controlling the properties of nanocrystalline metals. First, in Chapter 3, the effects of non-equilibrium processing, namely femtosecond-laser irradiation, on the strength of several nanocrystalline alloys was presented. Much of the motivation for this investigation was the recent advancements in processing techniques available for tailoring the properties of metallic glasses, such as HPT, cryogenic cycling, and controlled thermal exposures, all of which enable isochemical control over the strength and ductility of amorphous metals. Nanocrystalline metals, while arguably similar to metallic glasses, have not been subjected to non-equilibrium processing in order to tailor their properties, likely due to the limited processing routes available to selectively target grain boundaries. The use of the femtosecond laser to induce a highly non-equilibrium state at grain boundary regions is the first example of such targeted processing. Femtosecond-laser irradiated nanocrystalline metals demonstrated a significant decrease in hardness, dependent upon the structural and energetic state of the boundary. Al-O, 316L stainless steel and slowly cooled Cu-Zr exhibited the largest decreases in hardness, ranging from 70-90% normalized reductions. Quenched Cu-Zr, Al-Ni-Ce, and as-deformed 316L

stainless steel exhibit a smaller reduction due to their initial high-energy grain boundary structures. All reductions in hardness were reversible through relaxation processing, suggesting that femtosecond-laser irradiation induces structural rearrangements at grain boundaries resulting in driving the grain boundary state further from equilibrium. Combined with detailed atomistic simulations, these results suggest that rejuvenation is an inherent property of grain boundaries, irrespective of the specific alloy in question. The results presented in Chapter 3 suggest that such processing routes may be extremely beneficial in controlling site-specific properties of a nanocrystalline metal by directly affecting the local structure and increasing the energetic state of the grain boundaries.

Chapters 4-6 present experimental investigations of a nanocrystalline Al-base alloy with Ni and Ce alloying additions. These results highlight the importance of grain boundary state on the room temperature strength, deformation morphology, and deformation physics (Chapter 4); thermal stability (Chapter 5); and elevated temperature mechanical behavior (Chapter 6). The multicomponent alloy chemistry and highly non-equilibrium synthesis technique (sputtering) utilized to prepare the Al-Ni-Ce alloy allows for investigations into the structural evolution from high energy grain boundary states in the as-deposited condition to more relaxed grain boundaries after annealing. This evolution is evident in the mechanical behavior, including increased strength (4.6 - 5.4 GPa), suppression of strong shear localization during indentation, and concomitant transitions in deformation mechanism from intergranular to intragranular plasticity at room temperature.

The thermal behavior of the alloy also demonstrates the impact of the grain boundary evolution. Calorimetric studies of the Al-Ni-Ce alloy performed at a variety of fast heating rates confirm the presence of two exothermic events, indicative of grain boundary chemical enrichment (and relaxation) and intermetallic precipitation. Heating rate analysis demonstrates that the grain boundary enrichment event occurs via diffusion of

alloying additions within the crystalline domains, whereas the intermetallic precipitation event is much more difficult than any other reported precipitation reaction in amorphous Al alloys.

The investigations into the Al-Ni-Ce alloy also emphasize the importance of amorphous intergranular films on mechanical and thermal behavior of the alloy. While there are numerous metastable grain boundary core structures that do not include spatially extended amorphous zones, amorphous intergranular films have been shown to dramatically increase the thermal stability of several nanocrystalline alloys, and are extremely promising from an alloy design perspective. The amorphous intergranular films in the Al-Ni-Ce alloy demonstrably enhance the microstructural stability compared to a pure Al alloy, evidenced by the extremely fine grain size of the alloy at room temperature vs the micrometer-size grains in the pure Al sample prepared identically. Furthermore, the Al-Ni-Ce alloy exhibits thermal stability that exceeds many 'thermally stable' nanocrystalline alloys, owing to the amorphous grain boundaries akin to Cu-Zr, Ni-Zr and Cu-Zr-Hf alloys in the literature. The presence of amorphous intergranular films seemingly increases the difficulty for intermetallic precipitation and reduces Al diffusion between neighboring grains, both of which prevent microstructural evolution during *in-situ* annealing studies. Structural characterization of the amorphous content of the alloy via X-ray diffraction suggests that the medium-range atomistic order, which exhibits similar symmetries to the intermetallic equilibrium structure in the as-deposited condition, becomes less ordered during annealing due to the enrichment in Ni and Ce. This structural and chemical evolution prevents easy crystallization into the equilibrium intermetallic phases after thermal exposures below the precipitation temperature, and is manifest in mechanical properties as well, such as the increase in modulus observed during room temperature indentation, transition in deformation morphology, and exceptional high temperature strength.

Overall, these studies suggest that grain boundary engineering accessed via targeted processing or alloying to modify the local grain boundary structure is a promising new avenue for controlling the properties of nanocrystalline metals. Both targeted processing and alloying have been shown to alter the metastable state of the grain boundaries in nanocrystalline metals, affecting their polycrystalline, ensemble behavior. This is manifest in controlled changes in strength and thermal evolution, however additional work is needed to precisely quantify the relative importance of competing structural and chemical effects. Alloying effects on grain boundary structure appear more potent - the structural analysis of grain boundaries in the Al-Ni-Ce alloy highlight the important of multicomponent alloying strategies to mitigate thermal stability and impart resistance to shear localization, both of which have direct applicability for designing next generation Al (or other) alloys with exceptional strength and elevated temperature performance. Compared with processing effects, which, on their own, appear to only affect the mechanical response by modifying the grain boundary structure, alloying is seemingly more important for producing high performance nanocrystalline metals. Nevertheless, nonequilibrium rejuvenation processing is a nascent and promising approach for modifying grain boundaries, and as such, may prove to be more effective in creating nanocrystalline components with greater functionality moving forward. Investigations into novel processing routes that selectively target grain boundaries, as well as the effects of these processing routes in alloyed systems, are less likely to succeed than alloying studies alone, but may enable precise control of the deformation behavior in nanocrystalline metals, enhancing both scientific and industrial interest in nanocrystalline metals.

7.1 Recommendations for further study

While targeted processing routes and alloying may enable production of nanocrystalline metals with desirable properties, enabling their use in practical engineering applications, the investigations in this thesis present several avenues for future research to better understand these phenomena, broadening their applicability to real engineering materials. Suggestions are outlined below.

7.1.1 Processing effects

The results presented in Chapter 3, including the detailed modeling work performed by Bai *et al.* [143], suggest that the femtosecond laser processing produces non-equilibrium grain boundaries, which serve to decrease the strength of nanocrystalline metals. Recently, efforts combining detailed electron microscopy, atom probe tomography, and atomistic simulations have been used to observe non-equilibrium grain boundary structures in bi-crystals of Cu [65], triple points [301] and grain boundaries in Si [302]. While such efforts are challenging in nanocrystalline metals, due to the large number of small grains which complicate experimental efforts to isolate a single grain boundary, the effects of non-equilibrium processing on grain boundaries in a coarser grained material may prove insight into the underlying behavior during femtosecond laser irradiation. To study this, I suggest the following experimental and computational plan:

- Sputter deposit 1-2 micrometer thick Cu films onto (0001) or $(0\bar{1}01)$ Sapphire wafers near 200 °C, akin to the molecular beam epitaxy method presented in [65, 301–304], which encourages a semi-epitaxial, coarse grained, <111> or <110> growth direction texture in the copper.

- Perform coarse EBSD scans of the microstructure to identify high symmetry, planar grain boundaries.
- Lift out TEM lamella of grain boundary and characterize near surface atomistic structure of grain boundary using high resolution HAADF STEM.
- Expose nearby region of the same grain boundary with a sub-ablation femtosecond laser pulse.
- Extract TEM lamella of exposed boundary and characterize structure identical to previous sample to observe any structural modifications.

These experiments can be coupled with MD heating simulations similar to [143] to identify likely metastable grain boundary structural motifs of Cu grain boundaries in MD simulations. Multislice TEM simulations [305] can be performed on the resulting simulated grain boundary structures to compare with experimentally observed atomistic structures.

Other researchers [42] have suggested that a larger volume fraction of non-equilibrium grain boundaries may enhance the overall ductility and prevent catastrophic failure via significant shear band formation, at the expense of strength. While such behavior is evident in amorphous metals, and indirectly in Ref. [42], it is still not clear if the presence of metastable grain boundaries improves tensile ductility or other mechanical properties such as fatigue or wear. Until bulk nanocrystalline samples can be synthesized, likely by powder-metallurgy routes, tribology experiments may be simple ways to elucidate the role of metastable grain boundaries on the wear behavior:

- Perform spherical indent scratch testing on both pristine and femtosecond irradiated regions.

- If any measurable differences are observed, further characteristics of the wear behavior may prove interesting, such as depth dependence, plowing behavior with different tip geometries, or microscopy investigations into microstructural evolution beneath the wear track.

While other researchers have suggested the relaxation state of the grain boundary significantly affect the wear behavior [306], and that well-relaxed, stable grain boundary structures provide enhanced wear behavior [307], femtosecond laser processing enables direct assessment of the differences between alloying and metastable grain boundary structure on properties.

Lastly, cryogenic cycling has been observed as a promising rejuvenation processing route for metallic glasses [95]. While initial exploratory efforts into the effect of cryogenic cycling on HPT refined 316L stainless steel samples proved unsuccessful Figure 7.1, exploring the effects of cryogenic cycling on the tensile ductility of free-standing Al-Ni-Ce films with amorphous grain boundaries may behave differently. As the effects of cryogenic cycling appear more prominent in La-based glasses, the high Ce content in grain boundary regions in these samples may prove amenable to structural evolution due to cryogenic cycling than grain boundaries in the austenitic stainless steel used in initial experiments. Quick screening can be performed using hardness testing of films on Si substrates, followed by *in-situ* tension testing of freestanding films.

7.1.2 Alloying effects

The results presented in Chapters 4-6 emphasize the importance of alloying to alter grain boundary structural motifs, and the concomitant effects on properties of nanocrystalline metals. Substantial efforts are currently underway to develop novel nanocrystalline alloys with amorphous intergranular films to improve their thermal stability relative to

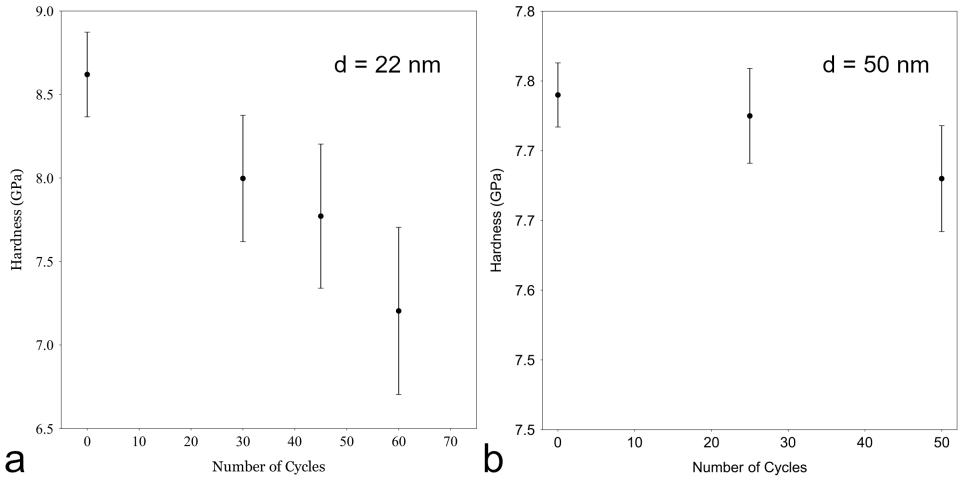

Figure 7.1: a, Hardness of 20 nm 316L stainless steel prepared by HPT as a function of cryogenic cycles. b, Hardness of 50 nm 316L stainless steel prepared by HPT vs cryogenic cycling. Cycling was performed by dunking the sample in liquid N_2 for 1 minute, removing it and allowing the sample to cool in contact with a brass heat sink for 1 minute. It appears there is a strong grain size effect in these samples, although further experiments are needed to verify.

the Al-Ni-Ce alloy, so I will outline a few ideas for experiments to elucidate the fundamental behavior of nanocrystalline metals with amorphous grain boundaries and the role of local chemistry, rather than alloying strategies to further enhance the properties of known nanocrystalline metals with amorphous grain boundaries. While simulations have demonstrated the role of amorphous grain boundaries in enhancing ductility of Cu-Zr alloys by increasing the dislocation absorption capacity of grain boundaries [248], experimental observations of such fundamental dislocation-level phenomena has not been reported in the literature. To assess this, the following experimental plan is proposed:

- Akin to previous experimental plan, and those performed by [304], Cu pseudo-epitaxy films sputtered on Sapphire can be prepared, with a subsequent deposition of 10-20 nm of Zr, Hf, or alloyed Zr-Hf. The combination of Zr and Hf may be beneficial for producing thick amorphous films for diffraction-based structural characterization [135].

- Films can be annealed to induce Zr/Hf diffusion to grain boundaries in Cu, followed by rapid quenching [73], and initial TEM liftout and characterization of grain boundaries to ensure the presence of amorphous intergranular films.

- *In-situ* deformation TEM samples can then be prepared by FIB, and deformed such that individual dislocations can be observed interacting with the amorphous grain boundary. If possible, these experiments can be coupled with high resolution imaging [304] and nanobeam diffraction [308–310] to elucidate structural evolution within the amorphous intergranular film.

7.1.3 Combined processing and alloying

In isolation, either alloying or processing are likely insufficient to produce nanocrystalline metals with a wide variety of tailorable properties; combined alloying and processing may prove effective in producing nanocrystalline metals with both exceptional and tailorable properties.

The sequence of events leading to the formation of amorphous grain boundaries has not been experimentally observed. Unlike the detailed atomistic / high resolution microscopy investigation proposed to investigate the formation of unusual grain boundary structures due to laser irradiation, the *in-situ* heating experiments performed on the Al-Ni-Ce alloy in Chapter 5 are likely quite amenable to observations of grain boundary amorphization in alloys with slightly larger grain sizes than the Al-Ni-Ce material. As such in-situ heating experiments performed on sputter deposited Cu-Zr or Cu-Zr-Hf nanocrystalline alloys, which exhibit substantially larger grain sizes than the Al-Ni-Ce material when deposited [125], may yield insight into this phenomena.

- Electron transparent (20-40 nm) thick Cu-Zr films can be sputtered onto a Protochips heating platform chip.

- After initial microscope setup and selection of grain boundaries in appropriate diffraction conditions to view evolution of the grains and the boundary, long EDS scans can be performed to study the as-deposited chemical distribution.

- Samples can then be heated quickly to 925 °C while imaging. According to [73, 75,125,135], amorphous intergranular films should form at this temperature, which should be captured during the experiment.

- After holding at elevated temperature for several minutes for adequate imaging, the sample can be quenched down to room temperature. The grain boundary structure can then be characterized at room temperature, including additional long EDS scans.

- Additional thermal exposures can be performed to watch the dissolution of the amorphous film at moderate temperatures [73], the effect of quench rate, as well as *in-situ* observations of grain growth (provided sufficient microscope time).

- Further additional experiments performed with Cu-Zr bi-crystalline samples as in previous suggested studies manipulated onto Protochips heating platform can also be performed to simplify any complications owing to the nanocrystalline microstructure, and provide atomistic insight into this behavior.

Investigations of the effect of fs-laser irradiation on Cu-Zr and Al-Ni-Ce alloys presented in Chapter 3 suggest that the extent of the reduction in hardness of these materials is smaller due to their initially non-equilibrium grain boundary structure, however the overall effect of fs-laser irradiation on deformation morphology is still unclear. The profuse shear banding behavior in the as-deposited Al-Ni-Ce alloy presents an opportunity to quickly investigate the effect of fs-laser irradiation on deformation morphology. Preliminary investigations demonstrate a significant change in shear band morphology after

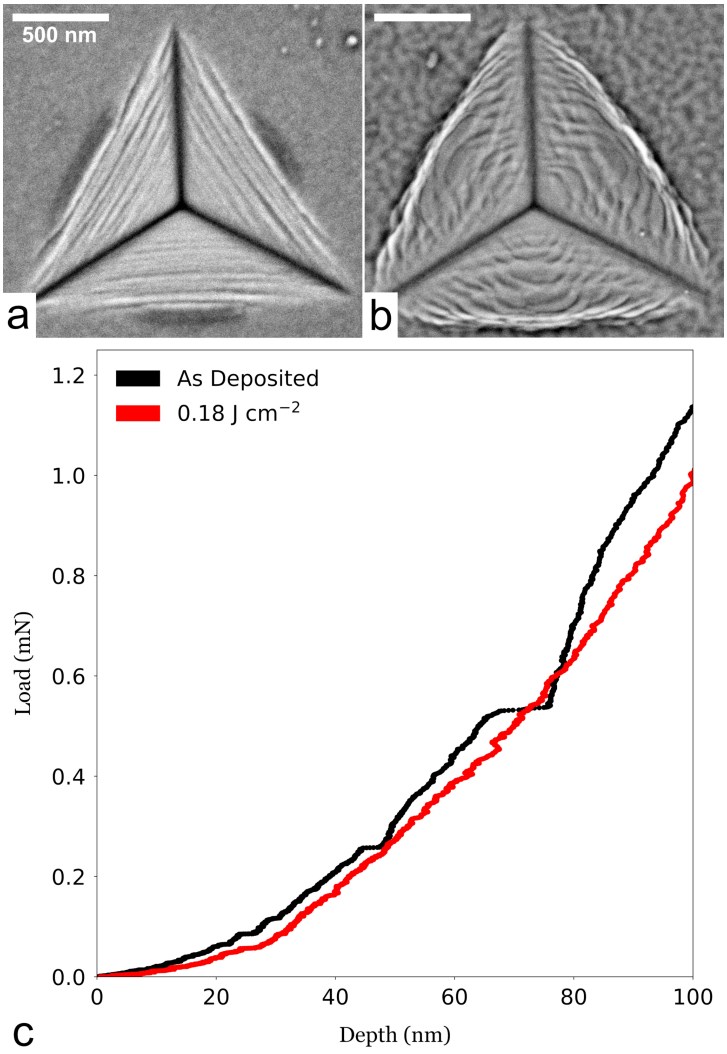

Figure 7.2: Morphological evolution of as deposited Al-Ni-Ce shear localization behavior after laser irradiation. a, unirradiated sample containing profuse shear bands beneath the indenter. b, 0.19 J cm^{-2} irradiated sample exhibiting a strange deformation morphology. c, load displacement curves demonstrating an apparent reduction in localization events after laser irradiation, indicated by constant load, 'pop-in' events.

laser irradiation Figures 7.2 and 7.3, which may have implications for the deformation behavior during more conventional loading - namely ductility. *In-situ* tension tests performed in the SEM on freestanding samples in the as-deposited, 200 °C annealed, and fs-laser irradiated states would provide insight into the effects of both annealing and fs-laser irradiation on macroscopic ductility. Finally, X-ray synchrotron studies elucidat-

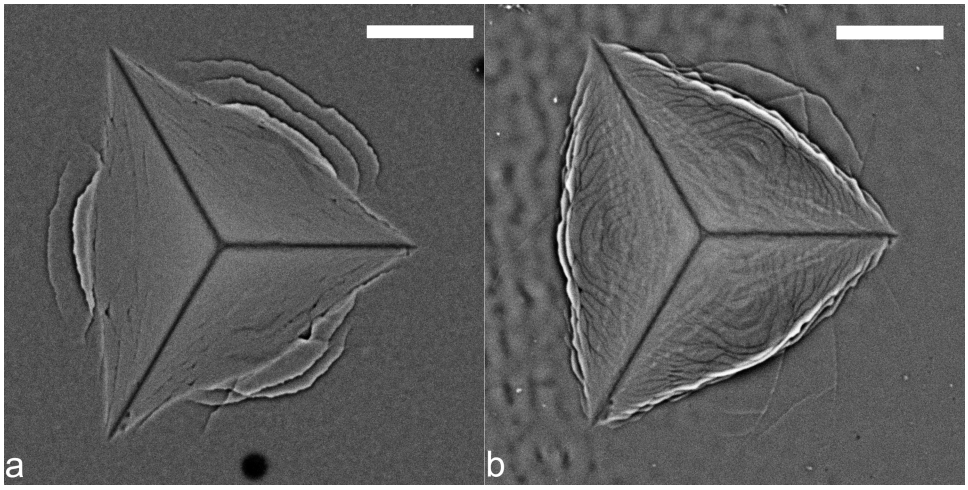

Figure 7.3: Morphological evolution of 200 °C annealed Al-Ni-Ce alloy a, before fs-laser irradiation and b, after 0.23 J cm^{-2} fs-laser irradiation. Scale bars are 1 μm.

ing the structural evolution of the amorphous grain boundaries after fs-laser irradiation, similar to the experiments presented in Chapter 5, would provide both macroscopic property level effects (i.e. changes in strength and ductility) and atomistic insight into grain boundary modification. The insight gleaned from these and other suggested experiments would greatly enhance our detailed understanding of the importance of grain boundary metastability on important mechanical properties, and nuances associated with combined alloying and processing of nanocrystalline metals.

Appendix A

Appendix

A.1 AJA Sputtering System Manual

Below is a brief guide to basic operation of the AJA sputter deposition system in the materials processing lab (MPL) at UCSB. Additional information can be found in the documentation on the flash drive hooked to the sputter chamber, by calling AJA directly, or by asking other members of the Gianola group (Ashley Roach & Dr. Jungho Shin).

1. Overview

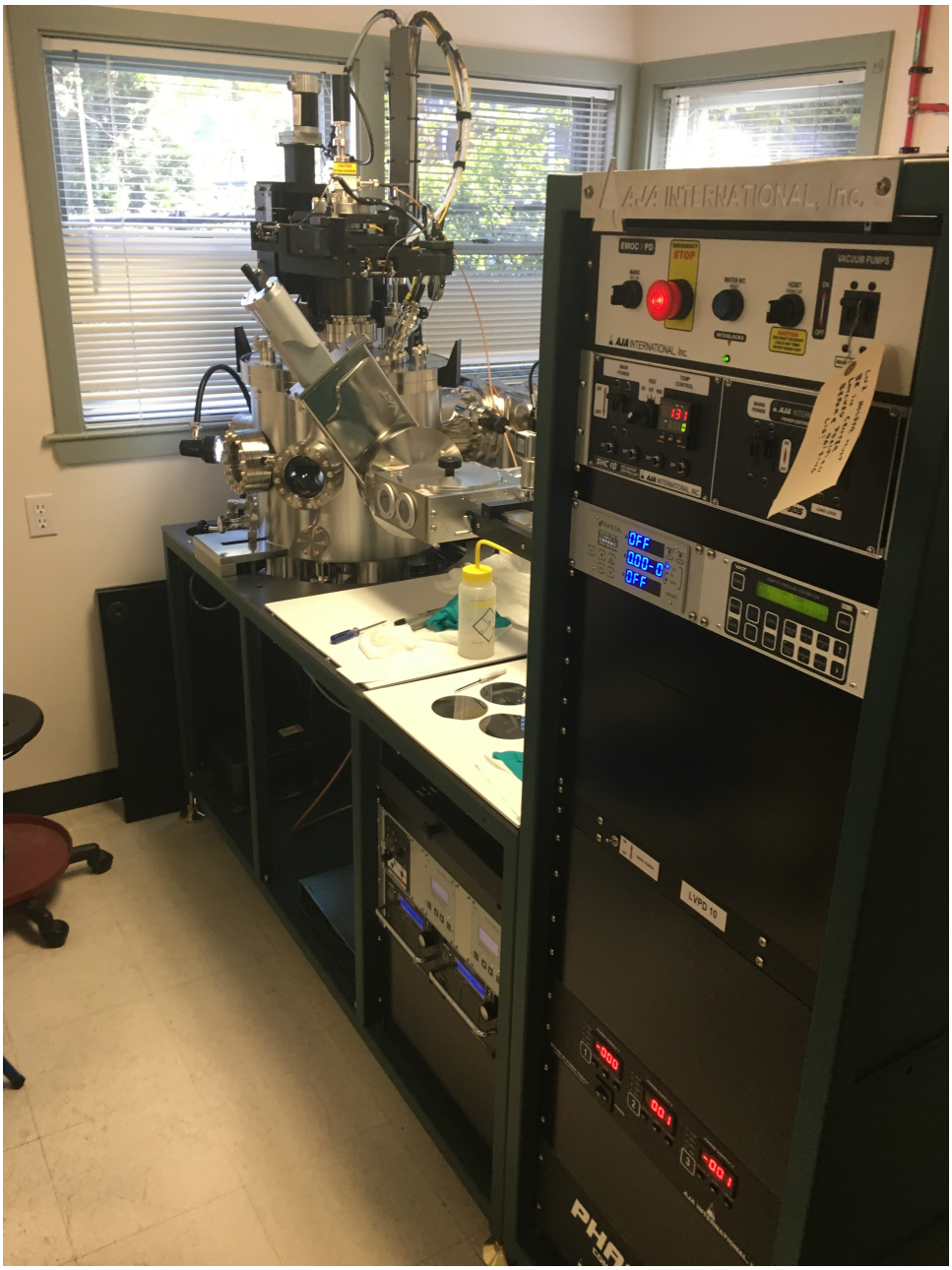

Figure A.1: Sputter Chamber Overview

2. Powering up the system:

   (a) Ensure that all gas vent and process gas lines are closed (N and Ar, typically)

(b) Ensure that the "Vacuum Pumps" switch on the EMOC power distribution system is "Off"

(c) Move the lever on the large "AJA Sputtering" safety box/switch box next to the fridge to the "On" position

(d) Go to the back of the system and power on the water chiller

  i. Turn the power switch on the back of the device to the "on" position

  ii. Once the system has turned on, press the "Run/Stop" button on the front of the instrument for water to begin flowing.

(e) Go to the front of the instrument

(f) On the top panel of the instrument is the EMOC power distribution system.

  i. Ensure that the "Emergency Stop" button is retracted

  ii. Turn the leftmost "Mains On/Off" switch to "on"

  iii. If the water interlock button is illuminated, ensure that the chiller is on and running and press the button to reset. If the button continues to be illuminated, see Troubleshooting.

  iv. If the chamber is under vacuum below 1 Torr, and you do not need to change targets, flip "Vacuum Pumps" switch to "On" and see "Other".

  v. Otherwise, leave "Vacuum Pumps" switch in "Off" position.

(g) Go to the back of the instrument and locate the water relays labeled 1-5

(h) At this point, they should all have an illuminated green LED beneath the label

(i) Check to ensure that the relays are functioning properly. Complete the following procedure for each of the 5 relays within 15-30 seconds, otherwise the system will shut down:

i. Turn off the flow of water off by closing the valve

ii. Ensure that the green light stops being illuminated – you will likely hear a click from the relay

iii. Turn on the flow of water by opening the valve

iv. If all relays are functioning, continue to the next section

3. Venting and opening the main chamber:

(a) To preserve vent gas, we need to keep the load lock under vacuum during this process. Locate the PD-30S power distribution box immediately beneath the "Vacuum Pumps" switch on the EMOC.

i. Ensure that the manual gate valve between the chamber and load lock is closed

ii. Ensure that the load lock lid is in place

iii. Flip the "Mains Power" switch to the "On" position

iv. Flip the "Vacuum Pumps" switch to the "On" position

v. You will hear the load lock turbo begin to spin up and the mechanical backing pump for the load lock begin to pump down the load lock. The pressure gauge for the load lock will also indicate this

(b) Go to the back of the instrument and turn on the vent gas (N) – **CHECK THIS STEP!!!!**

(c) Ensure that the "Vacuum Pumps" switch on the EMOC is off

(d) Hopefully, the main chamber will have been left under vacuum by the previous user. Check the pressure of the chamber by using the "Inficion" controller on the front panel. If this is less than atmosphere, go to step 5. If this is at atmosphere, go to step 6

(e) **SLOWLY** open the vent valve on the main chamber. You will hear the system as it is venting and can watch the pressure using the Inficion gauge

(f) Once the chamber reaches atmospheric pressure, close the vent valve and the vent gas regulator

(g) Ensure that the substrate RF Bias cable is disconnected from the lid of the chamber

(h) Ensure that the substrate holder/heater is raised up to the marker labeled "venting" using the joystick beneath the laptop.

(i) Rotate the combinatorial mask and QCM to be located in the center of the instrument using the two levers with black plastic on the lid. These are most easily accessed from the rear of the instrument.

(j) Check using the viewing windows that these components are not going to collide with anything when the lid is raised

(k) Remove the metal "T" lock from the hoist to allow the lid to rotate when raised

(l) Check the following before proceeding:

   i. RF Cable unplugged

   ii. Mask & QCM rotated in

   iii. Chamber at ATM

(m) Go to the EMOC panel and turn the "Hoist Up/Down" switch to the "Up" position, and hold until the lid is raised

(n) Feel free to push the lid to the left by touching only the exterior. Do not touch the interior of the main chamber without gloves. Ensure that the lid does not hit the thermal evaporator next to the instrument

4. Cleaning components:

   Please use gloves whenever touching components that will be used in high vacuum. In particular, steps 1, g-i

   (a) Inspect the gun and chimney assembly, shutters, and substrate holder. If you plan to do any sensitive depositions, remove these components and place in plastic bin

   (b) To clean, take pieces over to sandblasting room

   (c) Check the log to ensure that any compromising materials (Zn, Sn, Pb, etc.) have NOT been used in the sandblaster with the current medium. If so, please contact Deryck Stave.

   (d) Sandblast each component until clean

   (e) Remove as much of the blasting medium as possible from the blasted components before returning to the MPL. Remember to lock the door to sandblaster room when finished.

   (f) Remove additional sand using compressed air from each component

   (g) Sonicate components in the following solutions in order: (i) acetone, (ii) isopropanol, (iii) di water

   (h) Dry each component using compressed air

   (i) Wipe each component with a Kimtech wipe with isopropanol and let dry

5. Changing Targets:

   Ask for guidance when changing targets for the first time.

   Some good tips include:

- Ensure that there is good contact between the target and the copper (heatsink) gun components.
- When tightening, ensure that screws are "technician" tight – i.e. $\approx 1/8 - 1/4$ turn past when the screw feels tight on initial tightening
- When replacing shutters, open and close with the Phase2J software to ensure that they are mounted correctly.

6. Pumping down the main chamber:

   (a) Once the chamber is ready to be pumped down, rotate the lid directly over the chamber by only touching the exterior of the lid

   (b) Use a Kimtech wipe with isopropanol to wipe down the main chamber O-ring and Lid to ensure both surfaces are clean and free of debris

   (c) Ensure that the vent valves on the front of the main chamber are closed

   (d) Go to the EMOC panel on the front of the instrument

   (e) Ensure that nothing is between the lid and the main chamber – please announce loudly that you are closing the lid to ensure that any passerby does not get injured during this process

   (f) Turn the "Hoist Up/Down" nob to the "Down" position until the lid is resting completely on the main chamber

   (g) On the "VAT" controller, press and hold the "Local" button to put the gate valve controller on the main chamber turbo in local control mode

   (h) Ensure that the main chamber turbo is fully powered off. If not – see item 3

   (i) Fully open the main chamber turbo gate valve by depressing the "Open" button on the "VAT" controller

(j) Ensure that the vent gas (N) is open for the following procedures – the turbo pumps use the vent gas in the event of a power outage to spin down without harming the pumps.

(k) Flip the "Vacuum Pumps" switch on the EMOC box to the "On" position. You should hear the mechanical backing pump and the turbo start up and begin pumping down the main chamber

(l) The chamber should reach mid 10^{-5} Torr within an hour or so, and mid 10^{-7} Torr if the chamber is left pumping overnight

7. Venting the load lock:

(a) Ensure that the manual gate valve between the main chamber and the load lock is completely closed

(b) Ensure that the vent gas (N) is on

(c) To vent the load lock, flip the "Vacuum Pumps" switch on the PD-30S control box to the "Off" position

(d) You will hear the turbo spin down and vent gas will flow into the load lock. Watch the load lock vacuum gauge to ensure that this process is going smoothly

(e) When the load lock has vented to atmospheric pressure, vent gas will continue to flow into the load lock.

- If you are performing an operation that will take a long time with the load lock vented, please shut off the vent gas (N)

(f) Open the load lock as shown below:

i. Lift the lid by pulling up on the handle such that the part of the lid furthest from you lifts up first.

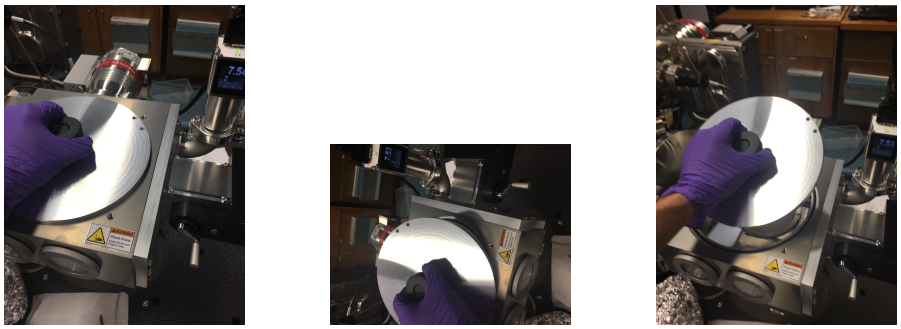

Figure A.2: Load Lock Opening Procedure

ii. Remove the lid as shown

iii. Place the lid on the 3 rubber nubs under the loading arm to prevent scratching

Note: During normal operation, instead of shutting off the vent gas, you can pump the load lock down after removing the substrate holder to mount your samples and vent again to load the substrate holder.

8. Mounting substrates:

   There are two methods of mounting substrates in this system – (1) there is a mounting plate for 4" wafers, and (2) there are clips for securing the substrate. Both systems mechanically secure the substrate to the substrate holder using screws nuts. See illustrations below for details about use each configuration

   (a) 4" Wafer plate

   (b) Mounting clips

9. Pumping load lock (with substrate holder):

   WEAR GLOVES

   (a) Ensure that the load lock is at atmosphere and the load lock lid is removed

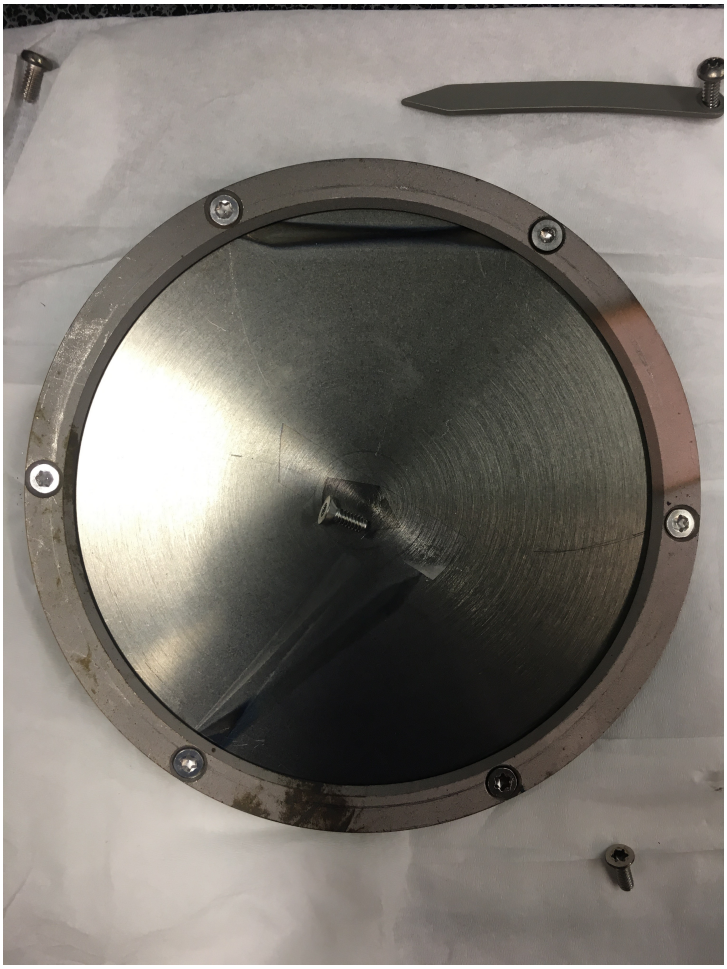

Figure A.3: 4 in diameter wafer substrate holder

(b) Load the substrate holder onto the loading arm as shown below:

i. Ensure that the substrate is facing down

ii. Line up one of the protruding screw heads with the slot on the loading arm. If using clips to secure the substrate, ensure that the screws fixing the clips are not the ones touching the loading arm.

iii. You will see three large "propeller" openings – ensure one of these is pointing directly away from the main chamber

iv. Rotate/wiggle the substrate holder to ensure it is seated securely in the

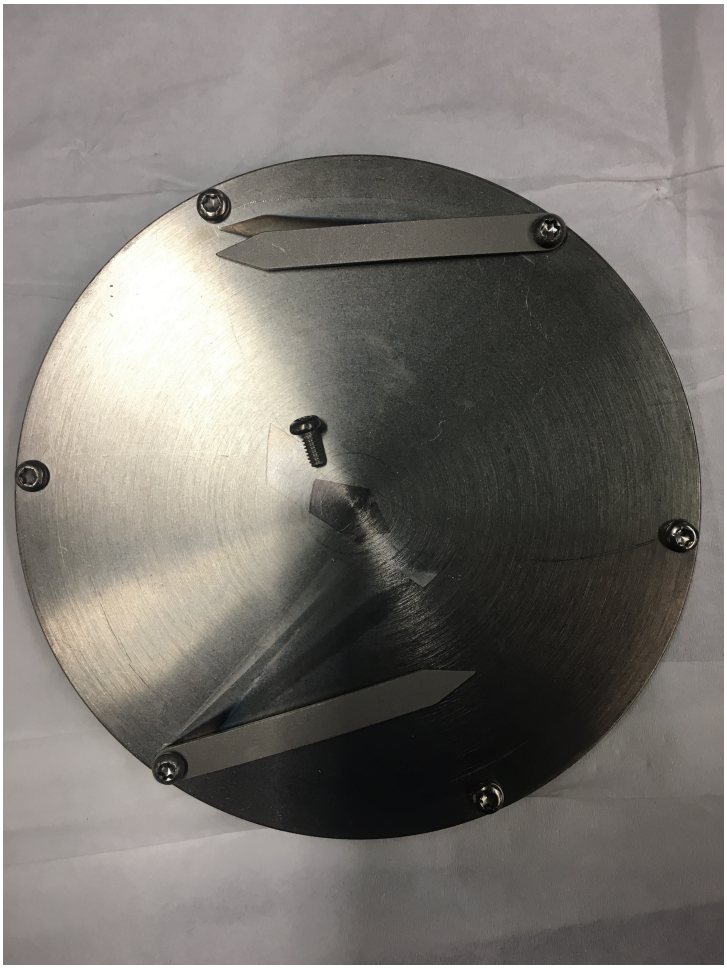

Figure A.4: Clip substrate holder

loading arm

(c) Place the load lock lid on the load lock in the reverse of what is shown in Figure A.2

(d) On the PD-30S control panel, flip the "Vacuum Pumps" switch to the "On" position – you will hear the load lock turbo spin up and see the pressure decrease on the load lock pressure gauge

10. Loading substrates:

(a) Open the Phase2J software and login

(b) Home the stage, and put in position 13

(c) Using the joystick beneath the laptop on the front of the instrument, put the rotation indicator in the "1" position

(d) Open all viewports on the main chamber by rotating out the shutters

(e) Turn on the light to see what you are doing

(f) Ensure that the substrate holder is above the lowest demarcation on the substrate controller/lid

(g) When the load lock reaches pressures in the 10^{-6} Torr and the main chamber is under vacuum, manually open the gate valve between the load lock and the main chamber

- If you experience any resistance, STOP!
- Do not force the gate valve
- Return the valve to the position you found it and seek assistance

(h) While looking through the viewports, **SLOWLY** extend the loading arm with the substrate holder. Again, if you experience any resistance, STOP and seek assistance

(i) Ensure that the rotation indicator is in the "1" position

(j) By moving the joystick up/down, lower the substrate controller/heater until the propeller mechanism is within the substrate holder – this height is noted on the ruler

(k) Using the joystick, **SLOWLY** rotate the substrate controller/heater until the indicator is in the "2" position

(l) If the substrate holder looks secure, raise the controller/heater up about half an inch – enough to clear the loading arm

(m) Rotate the substrate back and forth to ensure that it is in place securely. If not, return the substrate holder to the loading arm and try again

(n) Raise the substrate controller/heater to the desired height for deposition

(o) **SLOWLY** remove the loading arm

(p) **SLOWLY** close the manual gate valve between the main chamber and the load lock

11. Preparing for deposition:

(a) If using rotation, ensure that the toggle switch near the joystick is flipped up and the desired rotational speed is set (50% is normal)

(b) Ensure that the combinatorial mask is in place

(c) Ensure that the QCM is out of the way

(d) Ensure that all components (VAT controller, power supplies) are in remote (analog) control mode

(e) Ensure that the process and vent gas are open

(f) Fire away when ready!

12. Unloading samples:

(a) Ensure that the process has finished

(b) Turn the rotation speed to 0

(c) Put the substrate controller/heater in local mode by flipping the toggle switch above the joystick down

(d) Manually put the rotation to the "2" position

(e) Ensure that the substrate controller/heater is in position 13

(f) Open viewports and turn on light to see what you are doing

(g) Ensure that the substrate height is high enough to allow the loading arm to come beneath it

(h) Ensure that the load lock is under vacuum and the pressure differential is $<10^{-5}$ Torr

(i) **SLOWLY** open the manual gate valve between the load lock and the main chamber

(j) **SLOWLY** insert the loading arm

(k) **SLOWLY** lower the substrate controller/heater, bringing it into contact with the loading arm – you should be able to see one of the protruding screw heads fit into a slot on the loading arm on the right. Play with the rotation (while out of contact with the loading arm) until this fits

(l) When the loading arm is mated with the substrate holder, **SLOWLY** rotate the substrate controller/heater to position "1"

(m) **SLOWLY** raise the substrate controller/heater – this should be separate from the substrate holder, which should be resting on the loading arm. If not, re-connect the substrate holder and substrate controller/heater, raise them up, and repeat the previous steps

(n) When the substrate controller/heater is sufficiently above the loading arm+substrate holder, fully retract the loading arm

(o) Close the manual gate valve between the load lock and main chamber

(p) Vent the load lock

(q) Remove samples – USE GLOVES

13. Shut down procedure:

    This system does not have a "typical" shutdown procedure. The steps below are for a full shutdown of the system, assuming that the next user will not be operating the system for some time. Please communicate with the next user about how they would like the system (i.e. will they need to vent the chamber to change targets? Is it OK to keep the turbo running?) if they plan to use the system right after you.

    (a) Ensure that the vent gas is open

    (b) Ensure that the manual gate valve between the load lock and the main chamber is completely closed

    (c) Out of consideration for the next user, move the QCM and combinatorial mask to the center of the chamber

    (d) On the "VAT" controller on the front of the instrument, put the gate valve controller in "Local" mode

    (e) Completely close the gate valve on the main chamber using the "VAT" controller

    (f) When the gate valve is completely closed, flip both "Vacuum Pumps" switches on the EMOC controller and PD-30S controller to the "Off" position – you will hear both turbos begin to spin down

    (g) If you want to vent the main chamber, slowly open the vent valve on the front of the chamber

    (h) When the load lock is at atmosphere and the main chamber turbo has completely spun down, wait for 5 minutes to ensure that everything is completely off

    (i) Shut off vent gas

(j) Flip "Power Mains" switch next to the "Vacuum Pumps" switches to the "Off" position on the PD-30S box.

(k) Turn the "Mains On/Off" to the off position

(l) Unscrew the RF Bias cable from the top of the instrument to prevent the next user from damaging the cable

(m) Go to the back of the instrument

(n) Turn off the chiller

(o) Flip the switch on the supply box next to the fridge to the "Off" position

14. Clean Up!

(a) When finished using the system, please clean the substrate holder using the procedure in item 5.

(b) If you have used a material that is particularly flaky or have done a long deposition run, please clean the gun, shutter, and chimney assembly.

(c) Tidy up the workspace on the top of the instrument and on the counter opposite the machine.

A.2 Indentation Modulus

In recent discussions with Johann Kappacher and Verena Maier-Kiener, the modulus data presented in Figure 4.5 came into question. The issue with this data was the Poisson ratio used for the indentation modulus calculation (in addition to the depth dependence). For this reason, these data should be taken an upper bound for the actual modulus of the Al-Ni-Ce alloy. While this may affect the image force analysis slightly, it does not greatly affect the interpretation – for instance, if one were to assume a Poisson ratio of

0.33 for the data, the data would look as presented in Figure A.5, and the image force analysis better agrees with a cutoff distance of 1.3-1.4 b from the grain boundary, rather than 1.5 b utilized in Chapter 4.

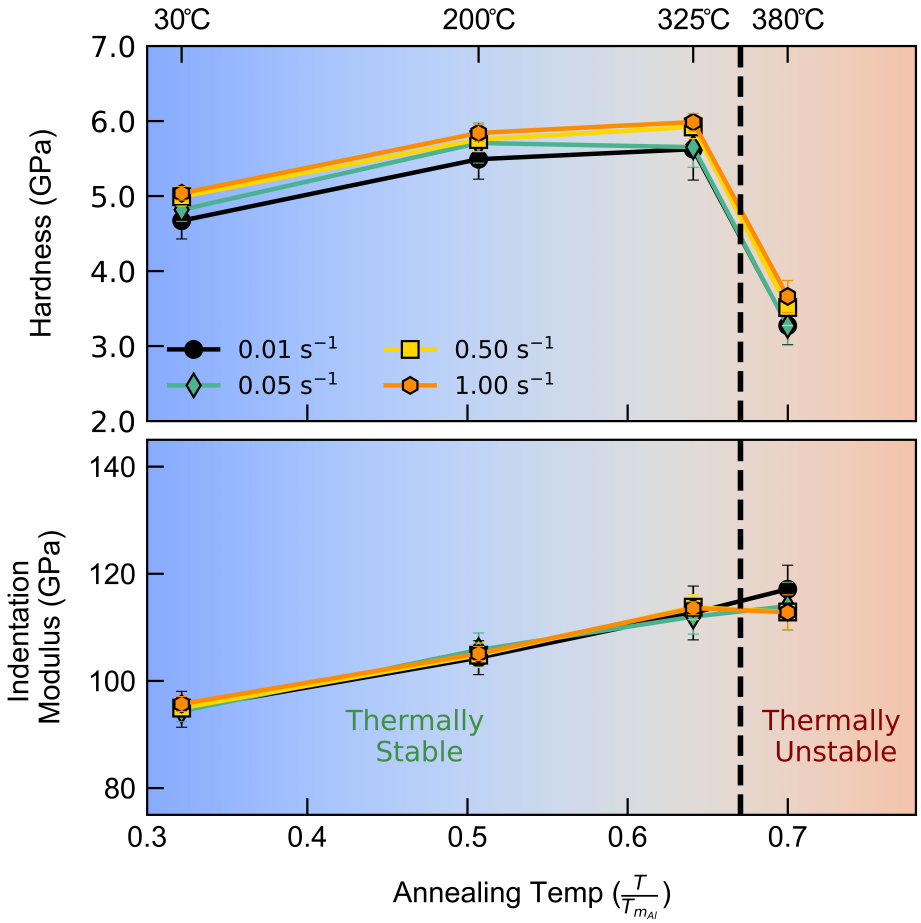

Figure A.5: Indentation hardness and modulus for the Al-Ni-Ce alloy after 1 hour annealing treatments at the noted temperature recalculated with a Poisson ratio of 0.33.

Bibliography

[1] R. Forrester, "History of Metallurgy," *SSRN Electronic Journal*, pp. 1–7, 2016.

[2] R. Tylecote, *A History of Metallurgy*. Maney Publishing, 2nd ed., 2002.

[3] R. Reed, *The superalloys : fundamentals and applications*. Cambridge University Press, 2006.

[4] E. O. Hall, "The Deformation and Ageing of Mild Steel: III Discussion of Results," *Proceedings of the Physical Society. Section B*, vol. 64, pp. 747–753, sep 1951.

[5] D. L. Harrod and R. E. Gold, "Mechanical properties of vanadium and vanadium-base alloys," 2013.

[6] N. J. Petch, "The Cleavage Strength of Polycrystals," *The Journal of the Iron and Steel Institute*, vol. 173(5), pp. 25–28, 1953.

[7] J. Reiser, J. Hoffmann, U. Jäntsch, M. Klimenkov, S. Bonk, C. Bonnekoh, M. Rieth, A. Hoffmann, and T. Mrotzek, "Ductilisation of tungsten (W): On the shift of the brittle-to-ductile transition (BDT) to lower temperatures through cold rolling," *International Journal of Refractory Metals and Hard Materials*, vol. 54, pp. 351–369, jan 2016.

[8] T. J. Rupert and C. A. Schuh, "Sliding wear of nanocrystalline Ni–W: Structural evolution and the apparent breakdown of Archard scaling," *Acta Materialia*, vol. 58, pp. 4137–4148, jul 2010.

[9] V. M. Miller, T. D. Berman, I. J. Beyerlein, and T. M. Pollock, "Prediction of magnesium alloy formability: The role of texture," in *Magnesium Technology*, vol. 2016-Janua, pp. 257–262, Minerals, Metals and Materials Society, 2016.

[10] K. Kumar, H. Van Swygenhoven, and S. Suresh, "Mechanical behavior of nanocrystalline metals and alloys," *Acta Materialia*, vol. 51, pp. 5743–5774, nov 2003.

[11] B. L. Boyce and H. A. Padilla, "Anomalous Fatigue Behavior and Fatigue-Induced Grain Growth in Nanocrystalline Nickel Alloys," *Metallurgical and Materials Transactions A*, vol. 42, pp. 1793–1804, jul 2011.

[12] H. A. Padilla and B. L. Boyce, "A Review of Fatigue Behavior in Nanocrystalline Metals," *Experimental Mechanics*, vol. 50, pp. 5–23, jan 2010.

[13] L. Zhang, C. Lu, and Y. Shibuta, "Shear response of grain boundaries with metastable structures by molecular dynamics simulations," *Modelling and Simulation in Materials Science and Engineering*, vol. 26, p. 035008, apr 2018.

[14] G. Kim, X. Chai, L. Yu, X. Cheng, and D. S. Gianola, "Interplay between grain boundary segregation and electrical resistivity in dilute nanocrystalline Cu alloys," *Scripta Materialia*, vol. 123, pp. 113–117, oct 2016.

[15] A. Tschöpe, R. Birringer, and H. Gleiter, "Calorimetric measurements of the thermal relaxation in nanocrystalline platinum," *Journal of Applied Physics*, vol. 71, pp. 5391–5394, jun 1992.

[16] A. Tschöpe and R. Birringer, "Thermodynamics of nanocrystalline platinum," *Acta Metallurgica Et Materialia*, vol. 41, pp. 2791–2796, sep 1993.

[17] A. Tschöpe and R. Birringer, "On the origin of enhanced specific heat in nanocrystalline platinum," *Philosophical Magazine B: Physics of Condensed Matter; Statistical Mechanics, Electronic, Optical and Magnetic Properties*, vol. 68, no. 2, pp. 223–229, 1993.

[18] H. Gleiter, "Nanocrystalline Materials," in *Advanced Structural and Functional Materials*, pp. 1–37, Berlin, Heidelberg: Springer Berlin Heidelberg, 1991.

[19] M. Meyers, A. Mishra, and D. Benson, "Mechanical properties of nanocrystalline materials," *Progress in Materials Science*, vol. 51, pp. 427–556, may 2006.

[20] Z. C. Cordero, B. E. Knight, and C. A. Schuh, "Six decades of the Hall–Petch effect – a survey of grain-size strengthening studies on pure metals," *International Materials Reviews*, vol. 61, pp. 495–512, nov 2016.

[21] J. R. Trelewicz and C. A. Schuh, "The Hall–Petch breakdown in nanocrystalline metals: A crossover to glass-like deformation," *Acta Materialia*, vol. 55, pp. 5948–5958, oct 2007.

[22] J. P. Hirth and J. Lothe, *Theory of dislocations*. Krieger Publishing Company, 2nd ed., 1982.

[23] J. Hu, Y. N. Shi, X. Sauvage, G. Sha, and K. Lu, "Grain boundary stability governs hardening and softening in extremely fine nanograined metals.," *Science (New York, N.Y.)*, vol. 355, pp. 1292–1296, mar 2017.

[24] M. Legros, B. R. Elliott, M. N. Rittner, J. R. Weertman, and K. J. Hemker, "Microsample tensile testing of nanocrystalline metals," *Philosophical Magazine A*, vol. 80, pp. 1017–1026, may 2000.

[25] H. Rösner, N. Boucharat, J. Markmann, K. A. Padmanabhan, and G. Wilde, "In situ transmission electron microscopic observations of deformation and fracture processes in nanocrystalline palladium and Pd90Au10," *Materials Science and Engineering A*, vol. 525, pp. 102–106, nov 2009.

[26] H. Van Swygenhoven, P. Derlet, and A. Frøseth, "Nucleation and propagation of dislocations in nanocrystalline fcc metals," *Acta Materialia*, vol. 54, pp. 1975–1983, apr 2006.

[27] L. Wang, J. Teng, P. Liu, A. Hirata, E. Ma, Z. Zhang, M. Chen, and X. Han, "Grain rotation mediated by grain boundary dislocations in nanocrystalline platinum," *Nature Communications*, vol. 5, pp. 1–7, jul 2014.

[28] Y. M. Wang and E. Ma, "On the origin of ultrahigh cryogenic strength of nanocrystalline metals," *Applied Physics Letters*, vol. 85, pp. 2750–2752, oct 2004.

[29] Y. M. Wang, A. V. Hamza, and E. Ma, "Temperature-dependent strain rate sensitivity and activation volume of nanocrystalline Ni," *Acta Materialia*, vol. 54, pp. 2715–2726, jun 2006.

[30] M. F. Ashby, "Results and consequences of a recalculation of the frank-read and the orowan stress," *Acta Metallurgica*, vol. 14, pp. 679–681, may 1966.

[31] Thomas H. Courtney, *Mechanical Behavior of Materials*, vol. 1. Long Grove, IL: Waveland Press, Inc, 2nd ed., 2005.

[32] T. J. Rupert, J. C. Trenkle, and C. A. Schuh, "Enhanced solid solution effects on the strength of nanocrystalline alloys," *Acta Materialia*, vol. 59, pp. 1619–1631, feb 2011.

[33] H. Van Swygenhoven and P. M. Derlet, "Grain-boundary sliding in nanocrystalline fcc metals," *Physical Review B*, vol. 64, p. 224105, nov 2001.

[34] Z. Shan, E. A. Stach, J. M. K. Wiezorek, J. A. Knapp, D. M. Follstaedt, and S. X. Mao, "Grain boundary-mediated plasticity in nanocrystalline nickel.," *Science (New York, N.Y.)*, vol. 305, pp. 654–7, jul 2004.

[35] M. Chen, E. Ma, K. J. Hemker, H. Sheng, Y. Wang, and X. Cheng, "Deformation twinning in nanocrystalline aluminum," *Science*, vol. 300, pp. 1275–1277, may 2003.

[36] A. Lund and C. Schuh, "Strength asymmetry in nanocrystalline metals under multiaxial loading," *Acta Materialia*, vol. 53, pp. 3193–3205, jun 2005.

[37] F. Sansoz and J. F. Molinari, "Incidence of atom shuffling on the shear and decohesion behavior of a symmetric tilt grain boundary in copper," *Scripta Materialia*, vol. 50, pp. 1283–1288, may 2004.

[38] R. Schwaiger, B. Moser, M. Dao, N. Chollacoop, and S. Suresh, "Some critical experiments on the strain-rate sensitivity of nanocrystalline nickel," *Acta Materialia*, vol. 51, pp. 5159–5172, oct 2003.

[39] C. Carlton and P. Ferreira, "What is behind the inverse Hall–Petch effect in nanocrystalline materials?," *Acta Materialia*, vol. 55, pp. 3749–3756, jun 2007.

[40] A. C. Lund, T. G. Nieh, and C. A. Schuh, "Tension/compression strength asymmetry in a simulated nanocrystalline metal," *Physical Review B*, vol. 69, p. 012101, jan 2004.

[41] J. Lohmiller, M. Grewer, C. Braun, A. Kobler, C. Kübel, K. Schüler, V. Honkimäki, H. Hahn, O. Kraft, R. Birringer, and P. A. Gruber, "Untangling dislocation and grain boundary mediated plasticity in nanocrystalline nickel," *Acta Materialia*, vol. 65, pp. 295–307, feb 2014.

[42] A. Khalajhedayati and T. J. Rupert, "Emergence of localized plasticity and failure through shear banding during microcompression of a nanocrystalline alloy," *Acta Materialia*, vol. 65, pp. 326–337, feb 2014.

[43] T. J. Rupert, J. R. Trelewicz, and C. A. Schuh, "Grain boundary relaxation strengthening of nanocrystalline Ni–W alloys," *Journal of Materials Research*, vol. 27, pp. 1285–1294, may 2012.

[44] T. J. Rupert and C. A. Schuh, "Mechanically driven grain boundary relaxation: a mechanism for cyclic hardening in nanocrystalline Ni," *Philosophical Magazine Letters*, vol. 92, pp. 20–28, jan 2012.

[45] J. R. Trelewicz and C. A. Schuh, "The Hall–Petch breakdown at high strain rates: Optimizing nanocrystalline grain size for impact applications," *Applied Physics Letters*, vol. 93, p. 171916, oct 2008.

[46] T. J. Rupert, "Strain localization in a nanocrystalline metal: Atomic mechanisms and the effect of testing conditions," *Journal of Applied Physics*, vol. 114, p. 033527, jul 2013.

[47] J. Han, V. Vitek, and D. J. Srolovitz, "Grain-boundary metastability and its statistical properties," *Acta Materialia*, vol. 104, pp. 259–273, feb 2016.

[48] L. Lu, X. Chen, X. Huang, and K. Lu, "Revealing the Maximum Strength in Nanotwinned Copper," *Science*, vol. 323, pp. 607–610, jan 2009.

[49] G. J. Tucker and D. L. McDowell, "Non-equilibrium grain boundary structure and inelastic deformation using atomistic simulations," *International Journal of Plasticity*, vol. 27, pp. 841–857, jun 2011.

[50] O. Renk, A. Hohenwarter, K. Eder, K. Kormout, J. Cairney, and R. Pippan, "Increasing the strength of nanocrystalline steels by annealing: Is segregation necessary?," *Scripta Materialia*, vol. 95, pp. 27–30, jan 2015.

[51] N. Combe, F. Mompiou, and M. Legros, "Disconnections kinks and competing modes in shear-coupled grain boundary migration," *PHYSICAL REVIEW B*, vol. 93, p. 24109, 2016.

[52] N. Combe, F. Mompiou, and M. Legros, "Shear-coupled grain-boundary migration dependence on normal strain/stress," *PHYSICAL REVIEW MATERIALS*, vol. 1, p. 33605, 2017.

[53] D. Gianola, D. Warner, J. Molinari, and K. Hemker, "Increased strain rate sensitivity due to stress-coupled grain growth in nanocrystalline Al," *Scripta Materialia*, vol. 55, pp. 649–652, oct 2006.

[54] J. Han, S. L. Thomas, and D. J. Srolovitz, "Grain-boundary kinetics: A unified approach," *Progress in Materials Science*, vol. 98, pp. 386–476, oct 2018.

[55] A. Rajabzadeh, F. Mompiou, S. Lartigue-Korinek, N. Combe, M. Legros, and D. Molodov, "The role of disconnections in deformation-coupled grain boundary migration," *Acta Materialia*, vol. 77, pp. 223–235, sep 2014.

[56] S. L. Thomas, K. Chen, J. Han, P. K. Purohit, and D. J. Srolovitz, "Reconciling grain growth and shear-coupled grain boundary migration," *Nature Communications*, vol. 8, pp. 1–12, dec 2017.

[57] S. L. Thomas, C. Wei, J. Han, Y. Xiang, and D. J. Srolovitz, "Disconnection description of triple-junction motion," *Proceedings of the National Academy of Sciences of the United States of America*, vol. 116, pp. 8756–8765, apr 2019.

[58] K. Chen, J. Han, X. Pan, and D. J. Srolovitz, "The grain boundary mobility tensor," *Proceedings of the National Academy of Sciences of the United States of America*, vol. 117, pp. 4533–4538, mar 2020.

[59] T. Frolov, W. Setyawan, R. J. Kurtz, J. Marian, A. R. Oganov, R. E. Rudd, and Q. Zhu, "Grain boundary phases in bcc metals," *Nanoscale*, vol. 10, pp. 8253–8268, may 2018.

[60] T. Frolov, Q. Zhu, T. Oppelstrup, J. Marian, and R. E. Rudd, "Structures and transitions in bcc tungsten grain boundaries and their role in the absorption of point defects," *Acta Materialia*, vol. 159, pp. 123–134, oct 2018.

[61] P. M. Derlet, H. Van Swygenhoven†, and A. Hasnaoui, "Atomistic simulation of dislocation emission in nanosized grain boundaries," *Philosophical Magazine*, vol. 83, pp. 3569–3575, oct 2003.

[62] M. Grewer and R. Birringer, "Shear shuffling governs plastic flow in nanocrystalline metals: An analysis of thermal activation parameters," *PHYSICAL REVIEW B*, vol. 89, p. 184108, 2014.

[63] H. Van Swygenhoven, P. M. Derlet, and A. Hasnaoui, "Atomic mechanism for dislocation emission from nanosized grain boundaries," *Physical Review B - Condensed Matter and Materials Physics*, vol. 66, pp. 1–8, jun 2002.

[64] H. Van Swygenhoven, P. M. Derlet, and A. G. Frøseth, "Stacking fault energies and slip in nanocrystalline metals," *Nature Materials*, vol. 3, pp. 399–403, jun 2004.

[65] T. Meiners, T. Frolov, R. E. Rudd, G. Dehm, and C. H. Liebscher, "Observations of grain-boundary phase transformations in an elemental metal," *Nature*, vol. 579, pp. 375–378, mar 2020.

[66] T. Frolov, D. L. Olmsted, M. Asta, and Y. Mishin, "Structural phase transformations in metallic grain boundaries," *Nature Communications*, vol. 4, p. 1899, oct 2013.

[67] N. Vo, J. Schäfer, R. Averback, K. Albe, Y. Ashkenazy, and P. Bellon, "Reaching theoretical strengths in nanocrystalline Cu by grain boundary doping," *Scripta Materialia*, vol. 65, pp. 660–663, oct 2011.

[68] T. J. Rupert, "Solid solution strengthening and softening due to collective nanocrystalline deformation physics," *Scripta Materialia*, vol. 81, pp. 44–47, jun 2014.

[69] N. Q. Vo, R. S. Averback, P. Bellon, and A. Caro, "Limits of hardness at the nanoscale: Molecular dynamics simulations," *Physical Review B*, vol. 78, p. 241402, dec 2008.

[70] L. Zhang, J. Han, Y. Xiang, and D. J. Srolovitz, "Equation of Motion for a Grain Boundary," *Physical Review Letters*, vol. 119, no. 24, pp. 1–5, 2017.

[71] M.-R. He, P. J. Felfer, S. Dasgupta, S. K. Samudrala, P. J. Malone, G. Feng, K. J. Hemker, J. M. Cairney, and D. S. Gianola, "Understanding the mechanical behavior of nanocrystalline Al–O thin films with complex microstructures," *Acta Materialia*, vol. 77, pp. 269–283, sep 2014.

[72] M.-R. He, S. K. Samudrala, G. Kim, P. J. Felfer, A. J. Breen, J. M. Cairney, and D. S. Gianola, "Linking stress-driven microstructural evolution in nanocrystalline aluminium with grain boundary doping of oxygen," *Nature Communications*, vol. 7, p. 11225, apr 2016.

[73] A. Khalajhedayati, Z. Pan, and T. J. Rupert, "Manipulating the interfacial structure of nanomaterials to achieve a unique combination of strength and ductility," *Nature Communications*, vol. 7, p. 10802, feb 2016.

[74] O. K. Donaldson and T. J. Rupert, "Amorphous Intergranular Films Enable the Creation of Bulk Nanocrystalline Cu-Zr with Full Density," apr 2019.

[75] A. Khalajhedayati and T. J. Rupert, "High-Temperature Stability and Grain Boundary Complexion Formation in a Nanocrystalline Cu-Zr Alloy," *JOM*, vol. 67, pp. 2788–2801, dec 2015.

[76] V. Turlo and T. J. Rupert, "Grain boundary complexions and the strength of nanocrystalline metals: Dislocation emission and propagation," *Acta Materialia*, vol. 151, pp. 100–111, jun 2018.

[77] T. G. Nieh and J. Wadsworth, "Hall-petch relation in nanocrystalline solids," *Scripta Metallurgica et Materiala*, vol. 25, pp. 955–958, apr 1991.

[78] C. A. Schuh and A. C. Lund, "Atomistic basis for the plastic yield criterion of metallic glass," jun 2003.

[79] A. Inoue, "Stabilization of metallic supercooled liquid and bulk amorphous alloys," *Acta Materialia*, vol. 48, pp. 279–306, jan 2000.

[80] M. Ashby and A. Greer, "Metallic glasses as structural materials," *Scripta Materialia*, vol. 54, pp. 321–326, feb 2006.

[81] C. A. Schuh, T. C. Hufnagel, and U. Ramamurty, "Mechanical behavior of amorphous alloys," *Acta Materialia*, vol. 55, no. 12, pp. 4067–4109, 2007.

[82] A. Inoue and H. Kimura, "Fabrications and mechanical properties of bulk amorphous, nanocrystalline, nanoquasicrystalline alloys in aluminum-based system," *Journal of Light Metals*, vol. 1, pp. 31–41, feb 2001.

[83] M. E. McHenry, M. A. Willard, and D. E. Laughlin, "Amorphous and nanocrystalline materials for applications as soft magnets," oct 1999.

[84] H. Zhang, D. J. Srolovitz, J. F. Douglas, and J. A. Warren, "Grain boundaries exhibit the dynamics of glass-forming liquids.," *Proceedings of the National Academy of Sciences of the United States of America*, vol. 106, pp. 7735–40, may 2009.

[85] T. Brink and K. Albe, "From metallic glasses to nanocrystals: Molecular dynamics simulations on the crossover from glass-like to grain-boundary-mediated deformation behaviour," *Acta Materialia*, vol. 156, pp. 205–214, sep 2018.

[86] J. A. Brown and N. M. Ghoniem, "Structure and motion of junctions between coherent and incoherent twin boundaries in copper," *Acta Materialia*, vol. 57, pp. 4454–4462, sep 2009.

[87] Y. Sun, A. Concustell, and A. L. Greer, "Thermomechanical processing of metallic glasses: extending the range of the glassy state," *Nature Reviews Materials*, vol. 1, p. 16039, sep 2016.

[88] Y. K. Huang, A. A. Menovsky, and F. R. de Boer, "Calorimetric analysis of the grain growth in nanocrystalline copper samples," *Nanostructured Materials*, vol. 2, pp. 587–595, nov 1993.

[89] A. Tschöpe and R. Birringer, "Thermodynamics of nanocrystalline platinum," *Acta Metallurgica et Materialia*, vol. 41, pp. 2791–2796, sep 1993.

[90] M. J. Demkowicz and A. S. Argon, "Liquidlike atomic environments act as plasticity carriers in amorphous silicon," *Physical Review B - Condensed Matter and Materials Physics*, vol. 72, p. 245205, dec 2005.

[91] D. Magagnosc, G. Kumar, J. Schroers, P. Felfer, J. Cairney, and D. Gianola, "Effect of ion irradiation on tensile ductility, strength and fictive temperature in metallic glass nanowires," *Acta Materialia*, vol. 74, pp. 165–182, aug 2014.

[92] G. Kumar, D. Rector, R. Conner, and J. Schroers, "Embrittlement of Zr-based bulk metallic glasses," *Acta Materialia*, vol. 57, pp. 3572–3583, jul 2009.

[93] H. B. Ke, P. Wen, H. L. Peng, W. H. Wang, and A. L. Greer, "Homogeneous deformation of metallic glass at room temperature reveals large dilatation," *Scripta Materialia*, vol. 64, pp. 966–969, may 2011.

[94] W. Dmowski, Y. Yokoyama, A. Chuang, Y. Ren, M. Umemoto, K. Tsuchiya, A. Inoue, and T. Egami, "Structural rejuvenation in a bulk metallic glass induced by severe plastic deformation," *Acta Materialia*, vol. 58, pp. 429–438, jan 2010.

[95] S. V. Ketov, Y. H. Sun, S. Nachum, Z. Lu, A. Checchi, A. R. Beraldin, H. Y. Bai, W. H. Wang, D. V. Louzguine-Luzgin, M. A. Carpenter, and A. L. Greer, "Rejuvenation of metallic glasses by non-affine thermal strain," *Nature*, vol. 524, pp. 200–203, aug 2015.

[96] D. J. Magagnosc, R. Ehrbar, G. Kumar, M. R. He, J. Schroers, and D. S. Gianola, "Tunable Tensile Ductility in Metallic Glasses," *Scientific Reports*, vol. 3, p. 1096, dec 2013.

[97] D. J. Magagnosc, G. Feng, L. Yu, X. Cheng, and D. S. Gianola, "Isochemical control over structural state and mechanical properties in Pd-based metallic glass by sputter deposition at elevated temperatures," *APL Materials*, vol. 4, p. 086104, aug 2016.

[98] M. Utz, P. G. Debenedetti, and F. H. Stillinger, "Atomistic Simulation of Aging and Rejuvenation in Glasses," *Physical Review Letters*, vol. 84, pp. 1471–1474, feb 2000.

[99] C. Packard, E. Homer, N. Al-Aqeeli, and C. Schuh, "Cyclic hardening of metallic glasses under Hertzian contacts: Experiments and STZ dynamics simulations," *Philosophical Magazine*, vol. 90, pp. 1373–1390, mar 2010.

[100] B. Fan, G. X. Ge, C. H. Jiang, G. H. Wang, and J. G. Wan, "Structure and magnetic properties of icosahedral PdxAg13-x (x = 0-13) clusters," *Scientific Reports*, vol. 7, pp. 1–12, dec 2017.

[101] Y. Fan, T. Iwashita, and T. Egami, "How thermally activated deformation starts in metallic glass," *Nature Communications*, vol. 5, pp. 1–7, sep 2014.

[102] S. Sastry, P. G. Debenedetti, and F. H. Stillinger, "Signatures of distinct dynamical regimes in the energy landscape of a glass-forming liquid," *Nature*, vol. 393, pp. 554–557, jun 1998.

[103] F. H. Stillinger, "A Topographic View of Supercooled Liquids and Glass Formation," *Science*, vol. 267, pp. 1935–1939, mar 1995.

[104] V. Gertsman and R. Birringer, "On the room-temperature grain growth in nanocrystalline copper," *Scripta Metallurgica et Materialia*, vol. 30, pp. 577–581, mar 1994.

[105] M. Ames, J. Markmann, R. Karos, A. Michels, A. Tschöpe, and R. Birringer, "Unraveling the nature of room temperature grain growth in nanocrystalline materials," *Acta Materialia*, vol. 56, pp. 4255–4266, oct 2008.

[106] B. Günther, A. Kumpmann, and H. D. Kunze, "Secondary recrystallization effects in nanostructured elemental metals," *Scripta Metallurgica et Materiala*, vol. 27, pp. 833–838, oct 1992.

[107] J. Weissmüller, "Alloy effects in nanostructures," *Nanostructured Materials*, vol. 3, pp. 261–272, jan 1993.

[108] J. W. Cahn and J. E. Hilliard, "On the equilibrium segregation at a grain boundary," mar 1959.

[109] A. Miedema, R. Boom, and F. De Boer, "On the heat of formation of solid alloys," *Journal of the Less Common Metals*, vol. 41, pp. 283–298, jul 1975.

[110] A. R. Miedema, F. R. De Boer, and P. F. De Chatel, "Empirical description of the role of electronegativity in alloy formation," *Journal of Physics F: Metal Physics*, vol. 3, no. 8, pp. 1558–1576, 1973.

[111] A. R. Miedema, F. R. De Boer, and R. Boom, "Predicting heat effects in alloys," *Physica B+C*, vol. 103, pp. 67–81, jan 1981.

[112] A. K. Niessen, F. R. de Boer, R. Boom, P. F. de Châtel, W. C. Mattens, and A. R. Miedema, "Model predictions for the enthalpy of formation of transition metal alloys II," *Calphad*, vol. 7, pp. 51–70, jan 1983.

[113] T. Chookajorn, H. A. Murdoch, and C. A. Schuh, "Design of Stable Nanocrystalline Alloys," *Science*, vol. 337, pp. 951–954, aug 2012.

[114] K. A. Darling, B. K. VanLeeuwen, C. C. Koch, and R. O. Scattergood, "Thermal stability of nanocrystalline Fe-Zr alloys," *Materials Science and Engineering A*, vol. 527, pp. 3572–3580, jun 2010.

[115] A. J. Detor and C. A. Schuh, "Tailoring and patterning the grain size of nanocrystalline alloys," *Acta Materialia*, vol. 55, pp. 371–379, jan 2007.

[116] H. A. Murdoch and C. A. Schuh, "Estimation of grain boundary segregation enthalpy and its role in stable nanocrystalline alloy design," 2019.

[117] G. Gottstein, D. A. Molodov, and L. S. Shvindlerman, "Grain Boundary Migration in Metals: Recent Developments," *Interface Science*, vol. 6, no. 1/2, pp. 7–22, 1998.

[118] F. J. Humphreys and M. G. Ardakani, "Grain boundary migration and zener pinning in particle-containing copper crystals," *Acta Materialia*, vol. 44, pp. 2717–2727, jul 1996.

[119] C. S. Smith, "Volume 175 - Technical Papers and Discussions - Institute of Metals Division Lecture - Grains, Phases, and Interfaces: An Interpretation of Microstructure (Metals Tech., June 1948, TP 2387)," tech. rep., 1948.

[120] D. Weygand, Y. Bréchet, and J. Lépinoux, "Zener pinning and grain growth: A two-dimensional vertex computer simulation," *Acta Materialia*, vol. 47, no. 3, pp. 961–970, 1999.

[121] E. Botcharova, J. Freudenberger, and L. Schultz, "High thermal stability of mechanically-alloyed nanocrystalline Cu – Nb alloys Dedicated to Professor Eckard Macherauch on the occasion of the 80th anniversary of his birth," vol. 97, 2006.

[122] M. Kapoor, T. Kaub, K. A. Darling, B. L. Boyce, and G. B. Thompson, "An atom probe study on Nb solute partitioning and nanocrystalline grain stabilization in mechanically alloyed Cu-Nb," *Acta Materialia*, vol. 126, pp. 564–575, mar 2017.

[123] K. A. Darling, M. Rajagopalan, M. Komarasamy, M. A. Bhatia, B. C. Hornbuckle, R. S. Mishra, and K. N. Solanki, "Extreme creep resistance in a microstructurally stable nanocrystalline alloy," *Nature*, vol. 537, pp. 378–381, sep 2016.

[124] T. Frolov, K. Darling, L. Kecskes, and Y. Mishin, "Stabilization and strengthening of nanocrystalline copper by alloying with tantalum," *Acta Materialia*, vol. 60, pp. 2158–2168, mar 2012.

[125] J. D. Schuler and T. J. Rupert, "Materials selection rules for amorphous complexion formation in binary metallic alloys," *Acta Materialia*, vol. 140, pp. 196–205, nov 2017.

[126] S. J. Dillon, M. Tang, W. C. Carter, and M. P. Harmer, "Complexion: A new concept for kinetic engineering in materials science," *Acta Materialia*, vol. 55, pp. 6208–6218, oct 2007.

[127] S. V. Divinski, H. Edelhoff, and S. Prokofjev, "Diffusion and segregation of silver in copper 5(310) grain boundary," *PHYSICAL REVIEW B*, vol. 85, p. 144104, 2012.

[128] E. Rabkin, C. Minkwitz, C. H. Herzig, and L. Klinger, "Evidence for structural multiplicity of the $\Sigma = 3$ incoherent twin boundary in cu from grain-boundary diffusion measurements," *Philosophical Magazine Letters*, vol. 79, no. 7, pp. 409–415, 1999.

[129] C. Braun, J. M. Dake, C. E. Krill, and R. Birringer, "Abnormal grain growth mediated by fractal boundary migration at the nanoscale," *Scientific Reports*, vol. 8, p. 1592, dec 2018.

[130] J. M. Dake and C. E. Krill, "Sudden loss of thermal stability in Fe-based nanocrystalline alloys," *Scripta Materialia*, vol. 66, pp. 390–393, mar 2012.

[131] J. E. Darnbrough and P. E. Flewitt, "Growth of abnormal planar faceted grains in nanocrystalline nickel containing impurity sulphur," *Acta Materialia*, vol. 79, pp. 421–433, oct 2014.

[132] G. D. Hibbard, J. L. McCrea, G. Palumbo, K. T. Aust, and U. Erb, "An initial analysis of mechanisms leading to late stage abnormal grain growth in nanocrystalline Ni," *Scripta Materialia*, vol. 47, pp. 83–87, jul 2002.

[133] S. H. Jung, D. Y. Yoon, and S. J. L. Kang, "Mechanism of abnormal grain growth in ultrafine-grained nickel," *Acta Materialia*, vol. 61, pp. 5685–5693, sep 2013.

[134] C. Xiao, R. A. Mirshams, S. H. Whang, and W. M. Yin, "Tensile behavior and fracture in nickel and carbon doped nanocrystalline nickel," *Materials Science and Engineering A*, vol. 301, pp. 35–43, mar 2001.

[135] C. M. Grigorian and T. J. Rupert, "Thick amorphous complexion formation and extreme thermal stability in ternary nanocrystalline Cu-Zr-Hf alloys," *Acta Materialia*, vol. 179, pp. 172–182, oct 2019.

[136] P. R. Cantwell, M. Tang, S. J. Dillon, J. Luo, G. S. Rohrer, and M. P. Harmer, "Grain boundary complexions," *Acta Materialia*, vol. 62, pp. 1–48, jan 2014.

[137] Z. Jian, K. Kuribayashi, and W. Jie, "Solid-liquid Interface Energy of Metals at Melting Point and Undercooled State," Tech. Rep. 4, 2002.

[138] J. Luo, "Stabilization of Nanoscale Quasi-Liquid Interfacial Films in Inorganic Materials: A Review and Critical Assessment," *Critical Reviews in Solid State and Materials Sciences*, vol. 32, pp. 67–109, may 2007.

[139] T. J. Rupert, "The role of complexions in metallic nano-grain stability and deformation," *Current Opinion in Solid State and Materials Science*, vol. 20, pp. 257–267, oct 2016.

[140] A. Khalajhedayati and T. J. Rupert, "Disruption of Thermally-Stable Nanoscale Grain Structures by Strain Localization," *Scientific Reports*, vol. 5, p. 10663, sep 2015.

[141] G. H. Balbus, M. P. Echlin, C. M. Grigorian, T. J. Rupert, T. M. Pollock, and D. S. Gianola, "Femtosecond laser rejuvenation of nanocrystalline metals," *Acta Materialia*, vol. 156, pp. 183–195, sep 2018.

[142] G. H. Balbus, F. Wang, and D. S. Gianola, "Suppression of shear localization in nanocrystalline Al–Ni–Ce via segregation engineering," *Acta Materialia*, vol. 188, pp. 63–78, apr 2020.

[143] Z. Bai, G. H. Balbus, D. S. Gianola, and Y. Fan, "Mapping the kinetic evolution of metastable grain boundaries under non-equilibrium processing," *Acta Materialia*, vol. 200, pp. 328–337, nov 2020.

[144] M. Ohring, *Materials science of thin films : deposition and structure*. Academic Press, 2002.

[145] J. L. Vossen, "Thin Film Processes," *Journal of The Electrochemical Society*, vol. 127, no. 5, p. 213C, 1980.

[146] K. Edalati and Z. Horita, "A review on high-pressure torsion (HPT) from 1935 to 1988," jan 2016.

[147] R. Pippan, "High-Pressure Torsion– Features and Applications," in *Bulk Nanostructured Materials*, pp. 217–233, Weinheim, Germany: Wiley-VCH Verlag GmbH & Co. KGaA, jun 2009.

[148] A. P. Zhilyaev and T. G. Langdon, "Using high-pressure torsion for metal processing: Fundamentals and applications," aug 2008.

[149] A. Hohenwarter, A. Bachmaier, B. Gludovatz, S. Scheriau, and R. Pippan, "Technical parameters affecting grain refinement by high pressure torsion," in *International Journal of Materials Research*, vol. 100, pp. 1653–1661, 2009.

[150] O. Renk, P. Ghosh, and R. Pippan, "Generation of extreme grain aspect ratios in severely deformed tantalum at elevated temperatures," *Scripta Materialia*, vol. 137, pp. 60–63, aug 2017.

[151] O. Renk, A. Hohenwarter, and R. Pippan, "Cyclic Deformation Behavior of a 316L Austenitic Stainless Steel Processed by High Pressure Torsion," *Advanced Engineering Materials*, vol. 14, pp. 948–954, nov 2012.

[152] M. V. Shugaev, C. Wu, O. Armbruster, A. Naghilou, N. Brouwer, D. S. Ivanov, T. J.-Y. Derrien, N. M. Bulgakova, W. Kautek, B. Rethfeld, and L. V. Zhigilei, "Fundamentals of ultrafast laser–material interaction," *MRS Bulletin*, vol. 41, pp. 960–968, dec 2016.

[153] M. P. Echlin, A. Mottura, C. J. Torbet, and T. M. Pollock, "A new TriBeam system for three-dimensional multimodal materials analysis," *Review of Scientific Instruments*, vol. 83, p. 023701, feb 2012.

[154] M. P. Echlin, M. Straw, S. Randolph, J. Filevich, and T. M. Pollock, "The TriBeam system: Femtosecond laser ablation in situ SEM," *Materials Characterization*, vol. 100, pp. 1–12, feb 2015.

[155] S. I. Ashitkov, V. V. Zhakhovsky, N. A. Inogamov, P. S. Komarov, M. B. Agranat, and G. I. Kanel, "The behavior of iron under ultrafast shock loading driven by a femtosecond laser," in *AIP Conference Proceedings*, vol. 1793, p. 100035, AIP Publishing LLC, jan 2017.

[156] B. J. Demaske, V. V. Zhakhovsky, N. A. Inogamov, and I. I. Oleynik, "Ultrashort shock waves in nickel induced by femtosecond laser pulses," *Physical Review B - Condensed Matter and Materials Physics*, vol. 87, p. 054109, feb 2013.

[157] K. Furusawa, K. Takahashi, H. Kumagai, K. Midorikawa, and M. Obara, "Ablation characteristics of Au, Ag, and Cu metals using a femtosecond Ti:sapphire laser," *Applied Physics A: Materials Science & Processing*, vol. 69, pp. S359–S366, dec 1999.

[158] M. Gill-Comeau and L. J. Lewis, "Ultrashort-pulse laser ablation of nanocrystalline aluminum," *Physical Review B*, vol. 84, p. 224110, dec 2011.

[159] S. Marinier and L. J. Lewis, "Femtosecond laser ablation of Cu x Zr 1 x bulk metallic glasses: A molecular dynamics study," *Physical Review B*, vol. 92, p. 184108, nov 2015.

[160] C. Wu, M. S. Christensen, J.-M. Savolainen, P. Balling, and L. V. Zhigilei, "Generation of subsurface voids and a nanocrystalline surface layer in femtosecond laser irradiation of a single-crystal Ag target," *Physical Review B*, vol. 91, p. 035413, jan 2015.

[161] V. V. Zhakhovsky, K. P. Migdal, N. A. Inogamov, and S. I. Anisimov, "MD simulation of steady shock-wave fronts with phase transition in single-crystal iron," in *AIP Conference Proceedings*, vol. 1793, p. 070003, AIP Publishing LLC, jan 2017.

[162] L. V. Zhigilei, Z. Lin, and D. S. Ivanov, "Atomistic Modeling of Short Pulse Laser Ablation of Metals: Connections between Melting, Spallation, and Phase Explosion," *The Journal of Physical Chemistry C*, vol. 113, pp. 11892–11906, jul 2009.

[163] J. M. Liu, "Simple technique for measurements of pulsed Gaussian-beam spot sizes," *Optics Letters*, vol. 7, p. 196, may 1982.

[164] J. Bonse, S. Baudach, J. Krüger, W. Kautek, and M. Lenzner, "Femtosecond laser ablation of silicon–modification thresholds and morphology," *Applied Physics A*, vol. 74, pp. 19–25, jan 2002.

[165] K. L. Johnson, *Contact Mechanics*. Cambridge University Press, 1987.

[166] D. Lorenz, A. Zeckzer, U. Hilpert, P. Grau, H. Johansen, and H. S. Leipner, "Pop-in effect as homogeneous nucleation of dislocations during nanoindentation," *Physical Review B*, vol. 67, p. 172101, may 2003.

[167] V. Maier-Kiener and K. Durst, "Advanced Nanoindentation Testing for Studying Strain-Rate Sensitivity and Activation Volume," *JOM*, vol. 69, pp. 2246–2255, nov 2017.

[168] W. Oliver and G. Pharr, "An improved technique for determining hardness and elastic modulus using load and displacement sensing indentation experiments," *Journal of Materials Research*, vol. 7, pp. 1564–1583, jun 1992.

[169] P. Sudharshan Phani, K. E. Johanns, E. P. George, and G. M. Pharr, "A stochastic model for the size dependence of spherical indentation pop-in," *Journal of Materials Research*, vol. 28, pp. 2728–2739, oct 2013.

[170] R. Saha and W. D. Nix, "Effects of the substrate on the determination of thin film mechanical properties by nanoindentation," *Acta Materialia*, vol. 50, pp. 23–38, jan 2002.

[171] R. W. Armstrong, A. W. Ruff, and H. Shin, "Elastic, plastic and cracking indentation behavior of silicon crystals," *Materials Science and Engineering A*, vol. 209, pp. 91–96, may 1996.

[172] V. Maier, K. Durst, J. Mueller, B. Backes, H. W. Höppel, and M. Göken, "Nanoindentation strain-rate jump tests for determining the local strain-rate sensitivity in nanocrystalline Ni and ultrafine-grained Al," *Journal of Materials Research*, vol. 26, pp. 1421–1430, jun 2011.

[173] H. E. Kissinger, "Variation of Peak Temperature With Heating Rate In Differential Thermal Analysis," Tech. Rep. 4, 1956.

[174] L. C. Chen and F. Spaepen, "Calorimetric evidence for the micro-quasicrystalline structure of 'amorphous' Al/transition metal alloys," tech. rep., 1988.

[175] R. M. Wellen and E. L. Canedo, "On the Kissinger equation and the estimate of activation energies for non-isothermal cold crystallization of PET," *Polymer Testing*, vol. 40, pp. 33–38, dec 2014.

[176] F. de la Pena, T. Ostasevicius, V. Tonaas Fauske, P. Burdet, P. Jokubauskas, M. Nord, M. Sarahan, E. Prestat, D. N. Johnstone, J. Taillon, Jan Caron, T. Furnival, K. E. MacArthur, A. Eljarrat, S. Mazzucco, V. Migunov, T. Aarholt, M. Walls, F. Winkler, G. Donval, B. Martineau, A. Garmannslund, L.-F. Zagonel, and I. Iyengar, "Electron Microscopy (Big and Small) Data Analysis With the Open Source Software Package HyperSpy," *Microscopy and Microanalysis*, vol. 23, pp. 214–215, jul 2017.

[177] P. Juhás, T. Davis, C. L. Farrow, and S. J. Billinge, "PDFgetX3: A rapid and highly automatable program for processing powder diffraction data into total scattering pair distribution functions," *Journal of Applied Crystallography*, vol. 46, pp. 560–566, apr 2013.

[178] A. Peterlongo, A. Miotello, and R. Kelly, "Laser-pulse sputtering of aluminum: Vaporization, boiling, superheating, and gas-dynamic effects," *Physical Review E*, vol. 50, pp. 4716–4727, dec 1994.

[179] M. Sorescu and E. T. Knobbe, "Induced anisotropy and phase transformation in metallic glasses by pulsed-excimer-laser irradiation," *Physical Review B*, vol. 49, pp. 3253–3265, feb 1994.

[180] C.-J. Lin and F. Spaepen, "Nickel-niobium alloys obtained by picosecond pulsed laser quenching," *Acta Metallurgica*, vol. 34, pp. 1367–1375, jul 1986.

[181] B. Rethfeld, K. Sokolowski-Tinten, D. von der Linde, and S. Anisimov, "Timescales in the response of materials to femtosecond laser excitation," *Applied Physics A*, vol. 79, pp. 767–769, sep 2004.

[182] S. Amoruso, R. Bruzzese, M. Vitiello, N. N. Nedialkov, and P. A. Atanasov, "Experimental and theoretical investigations of femtosecond laser ablation of aluminum in vacuum," *Journal of Applied Physics*, vol. 98, p. 044907, aug 2005.

[183] P. B. Johnson and R. W. Christy, "Optical constants of the noble metals," *Physical Review B*, vol. 6, pp. 4370–4379, dec 1972.

[184] R. Querry, Marvin, "OPTICAL CONSTANTS OF MINERALS AND OTHER MATERIALS FROM THE MILLIMETER TO THE ULTRAVIOLET," *CRDEC Report*, 1987.

[185] A. D. Rakić, "Algorithm for the determination of intrinsic optical constants of metal films: application to aluminum," *Applied Optics*, vol. 34, p. 4755, aug 1995.

[186] B. Fultz and H. N. Frase, "Grain boundaries of nanocrystalline materials - Their widths, compositions, and internal structures," *Hyperfine Interactions*, vol. 130, no. 1-4, pp. 81–108, 2000.

[187] J. Sommer and C. Herzig, "Direct determination of grain-boundary and dislocation self-diffusion coefficients in silver from experiments in type-C kinetics," *Journal of Applied Physics*, vol. 72, pp. 2758–2766, oct 1992.

[188] J. R. Trelewicz and C. A. Schuh, "Grain boundary segregation and thermodynamically stable binary nanocrystalline alloys," *Physical Review B*, vol. 79, p. 094112, mar 2009.

[189] K. Durst, B. Backes, and M. Göken, "Indentation size effect in metallic materials: Correcting for the size of the plastic zone," *Scripta Materialia*, vol. 52, pp. 1093–1097, jun 2005.

[190] F. Tang, D. Gianola, M. Moody, K. Hemker, and J. Cairney, "Observations of grain boundary impurities in nanocrystalline Al and their influence on microstructural stability and mechanical behaviour," *Acta Materialia*, vol. 60, pp. 1038–1047, feb 2012.

[191] M. Iyer, V. Gavini, and T. M. Pollock, "Energetics and nucleation of point defects in aluminum under extreme tensile hydrostatic stresses," *Physical Review B*, vol. 89, p. 014108, jan 2014.

[192] T. Y. Tsui, W. C. Oliver, and G. M. Pharr, "Influences of stress on the measurement of mechanical properties using nanoindentation: Part I. Experimental studies in an aluminum alloy," *Journal of Materials Research*, vol. 11, pp. 752–759, mar 1996.

[193] A. Vorobyev, V. Kuzmichev, N. Kokody, P. Kohns, J. Dai, and C. Guo, "Residual thermal effects in Al following single ns- and fs-laser pulse ablation," *Applied Physics A*, vol. 82, pp. 357–362, feb 2006.

[194] A. Y. Vorobyev and C. Guo, "Direct observation of enhanced residual thermal energy coupling to solids in femtosecond laser ablation," *Applied Physics Letters*, vol. 86, p. 011916, jan 2005.

[195] P. G. Callahan, J. C. Stinville, E. R. Yao, M. P. Echlin, M. S. Titus, M. De Graef, D. S. Gianola, and T. M. Pollock, "Transmission scanning electron microscopy: Defect observations and image simulations," *Ultramicroscopy*, vol. 186, pp. 49–61, mar 2018.

[196] M. A. Atwater, H. Bahmanpour, R. O. Scattergood, and C. C. Koch, "The thermal stability of nanocrystalline cartridge brass and the effect of zirconium additions," *Journal of Materials Science*, vol. 48, pp. 220–226, jan 2013.

[197] D. Tabor, *The hardness of metals*. Clarendon Press, 2000.

[198] J. W. Wyrzykowski and M. W. Grabski, "The Hall–Petch relation in aluminium and its dependence on the grain boundary structure," *Philosophical Magazine A*, vol. 53, pp. 505–520, apr 1986.

[199] D. B. Williams and C. B. Carter, *Transmission Electron Microscopy*. Boston, MA: Springer US, 2009.

[200] Y. Olshi and W. D. Klngery, "Self-diffusion of oxygen in single crystal and polycrystalline aluminum oxide," *The Journal of Chemical Physics*, vol. 33, pp. 480–486, aug 1960.

[201] J. Han, V. Vitek, and D. J. Srolovitz, "The grain-boundary structural unit model redux," *Acta Materialia*, vol. 133, pp. 186–199, jul 2017.

[202] H. E. Elsayed-Ali, T. Juhasz, G. O. Smith, and W. E. Bron, "Femtosecond thermoreflectivity and thermotransmissivity of polycrystalline and single-crystalline gold films," *Physical Review B*, vol. 43, pp. 4488–4491, feb 1991.

[203] J. L. Hostetler, A. N. Smith, D. M. Czajkowsky, and P. M. Norris, "Measurement of the electron-phonon coupling factor dependence on film thickness and grain size in Au, Cr, and Al," *Applied Optics*, vol. 38, p. 3614, jun 1999.

[204] C. A. Volkert, A. Donohue, and F. Spaepen, "Effect of sample size on deformation in amorphous metals," *Journal of Applied Physics*, vol. 103, p. 083539, apr 2008.

[205] B. Oberdorfer, D. Setman, E.-M. Steyskal, A. Hohenwarter, W. Sprengel, M. Zehetbauer, R. Pippan, and R. Würschum, "Grain boundary excess volume and defect annealing of copper after high-pressure torsion," *Acta Materialia*, vol. 68, pp. 189–195, apr 2014.

[206] M. Tang, W. C. Carter, and R. M. Cannon, "Grain boundary transitions in binary alloys," *Physical Review Letters*, vol. 97, p. 075502, aug 2006.

[207] E. D. Cubuk, R. J. S. Ivancic, S. S. Schoenholz, D. J. Strickland, A. Basu, Z. S. Davidson, J. Fontaine, J. L. Hor, Y.-R. Huang, Y. Jiang, N. C. Keim, K. D. Koshigan, J. A. Lefever, T. Liu, X.-G. Ma, D. J. Magagnosc, E. Morrow, C. P. Ortiz, J. M. Rieser, A. Shavit, T. Still, Y. Xu, Y. Zhang, K. N. Nordstrom, P. E. Arratia, R. W. Carpick, D. J. Durian, Z. Fakhraai, D. J. Jerolmack, D. Lee, J. Li, R. Riggleman, K. T. Turner, A. G. Yodh, D. S. Gianola, and A. J. Liu, "Structure-property relationships from universal signatures of plasticity in disordered solids.," *Science (New York, N.Y.)*, vol. 358, pp. 1033–1037, nov 2017.

[208] W. Xing, A. R. Kalidindi, D. Amram, and C. A. Schuh, "Solute interaction effects on grain boundary segregation in ternary alloys," *Acta Materialia*, vol. 161, pp. 285–294, dec 2018.

[209] T. Akopyan, N. Belov, E. Naumova, and N. Letyagin, "New in-situ Al matrix composites based on Al-Ni-La eutectic," *Materials Letters*, vol. 245, pp. 110–113, jun 2019.

[210] K. Hono, Y. Zhang, A. Tsai, A. Inoue, and T. Sakurai, "Solute partitioning in partially crystallized Al-Ni-Ce(-Cu) metallic glasses," *Scripta Metallurgica et Materialia*, vol. 32, pp. 191–196, jan 1995.

[211] A. Inoue, K. Nakazato, Y. Kawamura, and T. Masumoto, "The effect of Cu addition on the structure and mechanical properties of AlNiM (M Ce or Nd) amorphous alloys containing nanoscale f.c.c.-Al particles," *Materials Science and Engineering: A*, vol. 179-180, pp. 654–658, may 1994.

[212] A. Inoue, K. Ohtera, and T. Masumoto, "New Amorphous Al-Y, Al-La and Al-Ce Alloys Prepared by Melt Spinning," *Japanese Journal of Applied Physics*, vol. 27, pp. L736–L739, may 1988.

[213] J. Guo and K. Ohtera, "Microstructures and mechanical properties of rapidly solidified high strength Al–Ni based alloys," *Acta Materialia*, vol. 46, pp. 3829–3838, jul 1998.

[214] A. Plotkowski, O. Rios, N. Sridharan, Z. Sims, K. Unocic, R. Ott, R. Dehoff, and S. Babu, "Evaluation of an Al-Ce alloy for laser additive manufacturing," *Acta Materialia*, vol. 126, pp. 507–519, mar 2017.

[215] Y. H. Kim, K. Hiraga, A. Inoue, T. Masumoto, and H. H. Jo, "Crystallization and high mechanical strength of Al-based amorphous alloys," *Materials Transactions, JIM*, vol. 35, no. 5, pp. 293–302, 1994.

[216] A. Tsai, T. Kamiyama, Y. Kawamura, A. Inoue, and T. Masumoto, "Formation and precipitation mechanism of nanoscale Al particles in Al-Ni base amorphous alloys," *Acta Materialia*, vol. 45, pp. 1477–1487, apr 1997.

[217] H. Wang, Z. Li, Z. Chen, and B. Yang, "Thermodynamic Optimization of the Ni-Al-Ce Ternary System," *Journal of Phase Equilibria and Diffusion*, vol. 37, pp. 222–228, apr 2016.

[218] G. Waterloo and H. Jones, "Microstructure and thermal stability of melt-spun Al-Nd and Al-Ce alloy ribbons," *Journal of Materials Science*, vol. 31, no. 9, pp. 2301–2310, 1996.

[219] H. A. Murdoch and C. A. Schuh, "Stability of binary nanocrystalline alloys against grain growth and phase separation," *Acta Materialia*, vol. 61, pp. 2121–2132, apr 2013.

[220] G. Wu, C. Liu, L. Sun, Q. Wang, B. Sun, B. Han, J. J. Kai, J. Luan, C. T. Liu, K. Cao, Y. Lu, L. Cheng, and J. Lu, "Hierarchical nanostructured aluminum alloy with ultrahigh strength and large plasticity," *Nature Communications*, vol. 10, dec 2019.

[221] V. Maier, B. Merle, M. Göken, and K. Durst, "An improved long-term nanoindentation creep testing approach for studying the local deformation processes in nanocrystalline metals at room and elevated temperatures," *Journal of Materials Research*, vol. 28, pp. 1177–1188, may 2013.

[222] O. Renk, V. Maier-Kiener, I. Issa, J. Li, D. Kiener, and R. Pippan, "Anneal hardening and elevated temperature strain rate sensitivity of nanostructured metals: Their relation to intergranular dislocation accommodation," *Acta Materialia*, vol. 165, pp. 409–419, feb 2019.

[223] V. B. Ozdol, C. Gammer, X. G. Jin, P. Ercius, C. Ophus, J. Ciston, and A. M. Minor, "Strain mapping at nanometer resolution using advanced nano-beam electron diffraction," *Applied Physics Letters*, vol. 106, p. 253107, jun 2015.

[224] C. Schuh and T. Nieh, "A survey of instrumented indentation studies on metallic glasses," *Journal of Materials Research*, vol. 19, pp. 46–57, jan 2004.

[225] R. Vaidyanathan, M. Dao, G. Ravichandran, and S. Suresh, "Study of mechanical deformation in bulk metallic glass through instrumented indentation," *Acta Materialia*, vol. 49, pp. 3781–3789, oct 2001.

[226] R. Conner, R. Dandliker, and W. Johnson, "Mechanical properties of tungsten and steel fiber reinforced Zr41.25Ti13.75Cu12.5Ni10Be22.5 metallic glass matrix composites," *Acta Materialia*, vol. 46, pp. 6089–6102, nov 1998.

[227] J. E. Carsley, W. W. Milligan, S. A. Hackney, and E. C. Aifantis, "Glasslike behavior in a nanostructured Fe/Cu alloy," *Metallurgical and Materials Transactions A*, vol. 26, pp. 2479–2481, sep 1995.

[228] F. Meng, K. Tsuchiya, S. Seiichiro, and Y. Yokoyama, "Reversible transition of deformation mode by structural rejuvenation and relaxation in bulk metallic glass," *Applied Physics Letters*, vol. 101, p. 121914, sep 2012.

[229] Y. Tong, T. Iwashita, W. Dmowski, H. Bei, Y. Yokoyama, and T. Egami, "Structural rejuvenation in bulk metallic glasses," *Acta Materialia*, vol. 86, pp. 240–246, mar 2015.

[230] S. C. Pun, W. Wang, A. Khalajhedayati, J. D. Schuler, J. R. Trelewicz, and T. J. Rupert, "Nanocrystalline Al-Mg with extreme strength due to grain boundary doping," *Materials Science and Engineering: A*, vol. 696, pp. 400–406, jun 2017.

[231] R. J. Asaro and S. Suresh, "Mechanistic models for the activation volume and rate sensitivity in metals with nanocrystalline grains and nano-scale twins," *Acta Materialia*, vol. 53, pp. 3369–3382, jul 2005.

[232] C. A. Bronkhorst, S. R. Kalidindi, and L. Anand, "Polycrystalline plasticity and the evolution of crystallographic texture in FCC metals," *Philosophical Transactions of the Royal Society of London. Series A: Physical and Engineering Sciences*, vol. 341, pp. 443–477, dec 1992.

[233] J. Lohmiller, R. Baumbusch, O. Kraft, and P. A. Gruber, "Differentiation of Deformation Modes in Nanocrystalline Pd Films Inferred from Peak Asymmetry Evolution Using In Situ X-Ray Diffraction," *Physical Review Letters*, vol. 110, p. 066101, feb 2013.

[234] J. Weissmüller and J. Markmann, "Deforming Nanocrystalline Metals: New Insights, New Puzzles," *Advanced Engineering Materials*, vol. 7, pp. 202–207, apr 2005.

[235] B. Chen, K. Lutker, S. V. Raju, J. Yan, W. Kanitpanyacharoen, J. Lei, S. Yang, H.-R. Wenk, H.-k. Mao, and Q. Williams, "Texture of Nanocrystalline Nickel: Probing the Lower Size Limit of Dislocation Activity," *Science*, vol. 338, pp. 1448–1451, dec 2012.

[236] X. Zhou, N. Tamura, Z. Mi, J. Lei, J. Yan, L. Zhang, W. Deng, F. Ke, B. Yue, and B. Chen, "Reversal in the Size Dependence of Grain Rotation," *Physical Review Letters*, vol. 118, p. 096101, mar 2017.

[237] P.-L. Larsson, A. Giannakopoulos, E. SÖderlund, D. Rowcliffe, and R. Vestergaard, "Analysis of Berkovich indentation," *International Journal of Solids and Structures*, vol. 33, pp. 221–248, jan 1996.

[238] L. Min, C. Wei-min, L. Nai-gang, and W. Ling-Dong, "A numerical study of indentation using indenters of different geometry," *Journal of Materials Research*, vol. 19, pp. 73–78, jan 2004.

[239] M. Rittner, J. Weertman, and J. Eastman, "Structure-property correlations in nanocrystalline Al-Zr alloy composites," *Acta Materialia*, vol. 44, pp. 1271–1286, apr 1996.

[240] T. Uesugi and K. Higashi, "First-principles studies on lattice constants and local lattice distortions in solid solution aluminum alloys," *Computational Materials Science*, vol. 67, pp. 1–10, feb 2013.

[241] D. Feichtinger, P. M. Derlet, and H. Van Swygenhoven, "Atomistic simulations of spherical indentations in nanocrystalline gold," *Physical Review B*, vol. 67, p. 024113, jan 2003.

[242] G.-J. J. Gao, Y.-J. Wang, and S. Ogata, "Studying the elastic properties of nanocrystalline copper using a model of randomly packed uniform grains," *Computational Materials Science*, vol. 79, pp. 56–62, nov 2013.

[243] X. Chen, T. Richeton, C. Motz, and S. Berbenni, "Elastic fields due to dislocations in anisotropic bi- and tri-materials: Applications to discrete dislocation pile-ups at grain boundaries," *International Journal of Solids and Structures*, vol. 164, pp. 141–156, jun 2019.

[244] ASM International. Handbook Committee., *ASM handbook*.

[245] W. Voigt, "Ueber die Beziehung zwischen den beiden Elasticitätsconstanten isotroper Körper," *Annalen der Physik*, vol. 274, pp. 573–587, jan 1889.

[246] J. Luo, A. Flewitt, S. Spearing, N. Fleck, and W. Milne, "Young's modulus of electroplated Ni thin film for MEMS applications," *Materials Letters*, vol. 58, pp. 2306–2309, jul 2004.

[247] M. Öveçoğlu, M. Doerner, and W. Nix, "Elastic interactions of screw dislocations in thin films on substrates," *Acta Metallurgica*, vol. 35, pp. 2947–2957, dec 1987.

[248] Z. Pan and T. J. Rupert, "Amorphous intergranular films as toughening structural features," *Acta Materialia*, vol. 89, pp. 205–214, may 2015.

[249] K. A. Darling, A. J. Roberts, Y. Mishin, S. N. Mathaudhu, and L. J. Kecskes, "Grain size stabilization of nanocrystalline copper at high temperatures by alloying with tantalum," *Journal of Alloys and Compounds*, vol. 573, pp. 142–150, oct 2013.

[250] A. J. Detor and C. A. Schuh, "Microstructural evolution during the heat treatment of nanocrystalline alloys," *Journal of Materials Research*, vol. 22, pp. 3233–3248, nov 2007.

[251] O. K. Donaldson, K. Hattar, T. Kaub, G. B. Thompson, and J. R. Trelewicz, "Solute stabilization of nanocrystalline tungsten against abnormal grain growth," *J. Mater. Res*, vol. 33, no. 1, 2020.

[252] T.-Y. Huang, A. R. Kalidindi, and C. A. Schuh, "Grain growth and second-phase precipitation in nanocrystalline aluminum-manganese electrodeposits,"

[253] L. Lu, N. R. Tao, L. B. Wang, B. Z. Ding, and K. Lu, "Grain growth and strain release in nanocrystalline copper," *Journal of Applied Physics*, vol. 89, pp. 6408–6414, jun 2001.

[254] H. Natter, M. Schmelzer, and R. Hempelmann, "Nanocrystalline nickel and nickel-copper alloys: Synthesis, characterization, and thermal stability," *Journal of Materials Research*, vol. 13, no. 5, pp. 1186–1197, 1998.

[255] X. Zhou, X. X. Yu, T. Kaub, R. L. Martens, and G. B. Thompson, "Grain Boundary Specific Segregation in Nanocrystalline Fe(Cr)," *Scientific Reports*, vol. 6, pp. 1–14, oct 2016.

[256] J. Eckert, J. C. Holzer, C. E. Krill, and W. L. Johnson, "Mechanically driven alloying and grain size changes in nanocrystalline Fe-Cu powders," *Citation: Journal of Applied Physics*, vol. 73, p. 2794, 1993.

[257] R. shan Lei, M. pu Wang, M. xing Guo, Z. Li, and Q. yi Dong, "Microstructure evolution and thermal stability of nanocrystalline Cu-Nb alloys during heat treatment," *Transactions of Nonferrous Metals Society of China (English Edition)*, vol. 19, pp. 272–276, apr 2009.

[258] S. C. Mehta, D. A. Smith, and U. Erb, "Study of grain growth in electrodeposited nanocrystalline nickel-1.2 wt.% phosphorus alloy," *Materials Science and Engineering A*, vol. 204, pp. 227–232, dec 1995.

[259] V. S. Muthaiah and S. Mula, "Effect of zirconium on thermal stability of nanocrystalline aluminium alloy prepared by mechanical alloying," *Journal of Alloys and Compounds*, vol. 688, pp. 571–580, dec 2016.

[260] M. Mantina, S. L. Shang, Y. Wang, L. Q. Chen, and Z. K. Liu, "3d transition metal impurities in aluminum: A first-principles study," *Physical Review B*, vol. 80, p. 184111, nov 2009.

[261] D. Simonovic and M. H. Sluiter, "Impurity diffusion activation energies in Al from first principles," *Physical Review B - Condensed Matter and Materials Physics*, vol. 79, p. 054304, feb 2009.

[262] K. Song, X. Bian, X. Lv, J. GuO, G. Li, and M. Xie, "Compositional dependence of glass-forming ability, medium-range order, thermal stability and liquid fragility of Al-Ni-Ce-based amorphous alloys," *Materials Science and Engineering A*, vol. 506, pp. 87–93, apr 2009.

[263] X. P. Li, M. Yan, B. J. Yang, J. Q. Wang, G. B. Schaffer, and M. Qian, "Crystallization behaviour and thermal stability of two aluminium-based metallic glass powder materials," *Materials Science and Engineering A*, vol. 530, pp. 432–439, dec 2011.

[264] S. Sohn, Y. Jung, Y. Xie, C. Osuji, J. Schroers, and J. J. Cha, "Nanoscale size effects in crystallization of metallic glass nanorods," *Nature Communications*, vol. 6, pp. 1–6, sep 2015.

[265] V. Turlo and T. J. Rupert, "Linear Complexions: Metastable Phase Formation and Coexistence at Dislocations," *Physical Review Letters*, vol. 122, p. 126102, mar 2019.

[266] M. Wilson and P. A. Madden, "Prepeaks and first sharp diffraction peaks in computer simulations of strong and fragile ionic liquids," *Physical Review Letters*, vol. 72, pp. 3033–3036, may 1994.

[267] H. Y. Hsieh, T. Egami, Y. He, S. J. Poon, and G. J. Shiflet, "Short range ordering in amorphous Al90FexCe10-x," *Journal of Non-Crystalline Solids*, vol. 135, pp. 248–254, nov 1991.

[268] M. Maret, T. Pomme, A. Pasturel, and P. Chieux, "Structure of liquid Al80Ni20 alloy," *Physical Review B*, vol. 42, pp. 1598–1604, jul 1990.

[269] F. Zhang, Y. Sun, Z. Ye, Y. Zhang, C.-Z. Wang, M. I. Mendelev, R. T. Ott, M. J. Kramer, Z.-J. Ding, and K.-M. Ho, "Solute-solute correlations responsible for the prepeak in structure factors of undercooled Al-rich liquids: a molecular dynamics study," *Journal of Physics: Condensed Matter J. Phys.: Condens. Matter*, vol. 27, p. 7, 2015.

[270] L. Hu, X. Bian, W. Wang, J. Zhang, and Y. Jia, "Liquid fragility and characteristic of the structure corresponding to the prepeak of AlNiCe amorphous alloys," *Acta Materialia*, vol. 52, pp. 4773–4781, sep 2004.

[271] Y. E. Kalay, L. S. Chumbley, M. J. Kramer, and I. E. Anderson, "Local structure in marginal glass forming Al-Sm alloy," *Intermetallics*, vol. 18, pp. 1676–1682, aug 2010.

[272] T. Chookajorn and C. A. Schuh, "Thermodynamics of stable nanocrystalline alloys: A Monte Carlo analysis," *Physical Review B*, vol. 89, p. 064102, feb 2014.

[273] A. R. Kalidindi, T. Chookajorn, and C. A. Schuh, "Nanocrystalline Materials at Equilibrium: A Thermodynamic Review," dec 2015.

[274] W. Xing, A. R. Kalidindi, and C. A. Schuh, "Preferred nanocrystalline configurations in ternary and multicomponent alloys," *Scripta Materialia*, vol. 127, pp. 136–140, jan 2017.

[275] A. R. Kalidindi and C. A. Schuh, "A compound unit method for incorporating ordered compounds into lattice models of alloys," *Computational Materials Science*, vol. 118, pp. 172–179, jun 2016.

[276] C. Kittel and D. F. Holcomb, "Introduction to Solid State Physics," *American Journal of Physics*, vol. 35, pp. 547–548, jun 1967.

[277] M. A. Atwater and K. A. Darling, "A Visual Library of Stability in Binary Metallic Systems: The Stabilization of Nanocrystalline Grain Size by Solute Addition: Part 1," tech. rep., 2012.

[278] A. Takeuchi and A. Inoue, "Calculations of Mixing Enthalpy and Mismatch Entropy for Ternary Amorphous Alloys," *Materials Transactions, JIM*, vol. 41, no. 11, pp. 1372–1378, 2000.

[279] A. R. Kalidindi and C. A. Schuh, "Stability criteria for nanocrystalline alloys," *Acta Materialia*, vol. 132, pp. 128–137, jun 2017.

[280] J. L. Hay, W. C. Olive, A. Bolshakov, and G. M. Pharr, "Using the Ratio of Loading Slope and Elastic Stiffness to Predict Pile-Up and Constraint Factor During Indentation," *MRS Proceedings*, vol. 522, p. 101, jan 1998.

[281] L. Ajdelsztajn, B. Jodoin, G. E. Kim, and J. M. Schoenung, "Cold Spray Deposition of Nanocrystalline Aluminum Alloys," *Metallurgical and Materials Transactions A*, vol. 36, no. 3, pp. 657–666, 2005.

[282] H. Choi, S. Lee, J. Park, and D. Bae, "Tensile behavior of bulk nanocrystalline aluminum synthesized by hot extrusion of ball-milled powders," *Scripta Materialia*, vol. 59, pp. 1123–1126, nov 2008.

[283] M. X. Li, S. F. Zhao, Z. Lu, A. Hirata, P. Wen, H. Y. Bai, M. W. Chen, J. Schroers, Y. H. Liu, and W. H. Wang, "High-temperature bulk metallic glasses developed by combinatorial methods," *Nature*, vol. 569, pp. 99–103, may 2019.

[284] J. K. Rana, D. Sivaprahasam, K. Seetharama Raju, and V. Subramanya Sarma, "Microstructure and mechanical properties of nanocrystalline high strength Al–Mg–Si (AA6061) alloy by high energy ball milling and spark plasma sintering," *Materials Science and Engineering: A*, vol. 527, pp. 292–296, dec 2009.

[285] M. Rittner, J. Weertman, J. Eastman, K. Yoder, and D. Stoned, "Mechanical behavior of nanocrystalline aluminum-zirconium," *Materials Science and Engineering: A*, vol. 237, pp. 185–190, sep 1997.

[286] S. Ruan and C. A. Schuh, "Electrodeposited Al–Mn alloys with microcrystalline, nanocrystalline, amorphous and nano-quasicrystalline structures," *Acta Materialia*, vol. 57, pp. 3810–3822, aug 2009.

[287] R. Valiev, N. Enikeev, M. Murashkin, V. Kazykhanov, and X. Sauvage, "On the origin of the extremely high strength of ultrafine-grained Al alloys produced by severe plastic deformation," *Scripta Materialia*, vol. 63, pp. 949–952, nov 2010.

[288] D. Witkin and E. Lavernia, "Synthesis and mechanical behavior of nanostructured materials via cryomilling," *Progress in Materials Science*, vol. 51, pp. 1–60, jan 2006.

[289] A. Yavari, W. Filho, C. Rodrigues, C. Cardoso, and R. Valiev, "Nanostructured bulk Al90Fe5Nd5 prepared by cold consolidation of gas atomised powder using severe plastic deformation," *Scripta Materialia*, vol. 46, pp. 711–716, may 2002.

[290] J. G. Kaufman, *Fire Resistance of Aluminum and Aluminum Alloys*. 2016.

[291] A. B. Pandey, "High temperature aluminum alloys," may 2011.

[292] Z. C. Sims, D. Weiss, S. K. McCall, M. A. McGuire, R. T. Ott, T. Geer, O. Rios, and P. A. E. Turchi, "Cerium-Based, Intermetallic-Strengthened Aluminum Casting Alloy: High-Volume Co-product Development," *JOM*, vol. 68, pp. 1940–1947, jul 2016.

[293] Z. C. Sims, O. R. Rios, D. Weiss, P. E. A. Turchi, A. Perron, J. R. I. Lee, T. T. Li, J. A. Hammons, M. Bagge-Hansen, T. M. Willey, K. An, Y. Chen, A. H. King, and S. K. McCall, "High performance aluminum–cerium alloys for high-temperature applications," *Materials Horizons*, vol. 4, pp. 1070–1078, oct 2017.

[294] W. L. Johnson and K. Samwer, "A Universal Criterion for Plastic Yielding of Metallic Glasses with a (T/Tg)^(2/3) Temperature Dependence," *Physical Review Letters*, vol. 95, p. 195501, nov 2005.

[295] G. J. Shiflet, Y. He, and S. J. Poon, "Mechanical properties of a new class of metallic glasses based on aluminum," *Journal of Applied Physics*, vol. 64, pp. 6863–6865, dec 1988.

[296] G. Mohanty, J. M. Wheeler, R. Raghavan, J. Wehrs, M. Hasegawa, S. Mischler, L. Philippe, and J. Michler, "Elevated temperature, strain rate jump microcompression of nanocrystalline nickel," *Philosophical Magazine*, vol. 95, pp. 1878–1895, jun 2015.

[297] O. D. Sherby and P. E. Armstrong, "Prediction of Activation Energies for Creep and Self-Diffusion from Hot Hardness Data," tech. rep.

[298] J. M. Wheeler, V. Maier, K. Durst, M. Göken, and J. Michler, "Activation parameters for deformation of ultrafine-grained aluminium as determined by indentation strain rate jumps at elevated temperature," *Materials Science and Engineering A*, vol. 585, pp. 108–113, nov 2013.

[299] J. D. Ju, D. Jang, A. Nwankpa, and M. Atzmon, "An atomically quantized hierarchy of shear transformation zones in a metallic glass," *Journal of Applied Physics*, vol. 109, p. 053522, mar 2011.

[300] B. Cheng and J. R. Trelewicz, "Design of crystalline-amorphous nanolaminates using deformation mechanism maps," *Acta Materialia*, vol. 153, pp. 314–326, jul 2018.

[301] A. Stoffers, J. Barthel, C. H. Liebscher, B. Gault, O. Cojocaru-Mirédin, C. Scheu, and D. Raabe, "Correlating Atom Probe Tomography with Atomic-Resolved Scanning Transmission Electron Microscopy: Example of Segregation at Silicon Grain Boundaries," *Microsc. Microanal*, vol. 23, pp. 291–299, 2017.

[302] A. Stoffers, B. Ziebarth, J. Barthel, O. Cojocaru-Mirédin, C. Elsässer, and D. Raabe, "Complex Nanotwin Substructure of an Asymmetric Σ9 Tilt Grain Boundary in a Silicon Polycrystal," 2015.

[303] G. Dehm, M. Rühle, G. Ding, and R. Raj, "Growth and structure of copper thin films deposited on (0001) sapphire by molecular beam epitaxy," *Philosophical Magazine B: Physics of Condensed Matter; Statistical Mechanics, Electronic, Optical and Magnetic Properties*, vol. 71, no. 6, pp. 1111–1124, 1995.

[304] T. Meiners, J. M. Duarte, G. Richter, G. Dehm, and C. H. Liebscher, "Tantalum and zirconium induced structural transitions at complex [111] tilt grain boundaries in copper," *Acta Materialia*, vol. 190, pp. 93–104, may 2020.

[305] E. J. Kirkland, *Advanced Computing in Electron Microscopy*, vol. 40. Boston, MA: Springer US, 2010.

[306] C. Schuh, T. Nieh, and T. Yamasaki, "Hall–Petch breakdown manifested in abrasive wear resistance of nanocrystalline nickel," *Scripta Materialia*, vol. 46, pp. 735–740, may 2002.

[307] J. F. Curry, T. F. Babuska, T. A. Furnish, P. Lu, D. P. Adams, A. B. Kustas, B. L. Nation, M. T. Dugger, M. Chandross, B. G. Clark, B. L. Boyce, C. A. Schuh, and N. Argibay, "Achieving Ultralow Wear with Stable Nanocrystalline Metals," *Advanced Materials*, vol. 30, p. 1802026, aug 2018.

[308] Y. E. Kalay, I. Kalay, J. Hwang, P. M. Voyles, and M. J. Kramer, "Local chemical and topological order in Al-Tb and its role in controlling nanocrystal formation," *Acta Materialia*, vol. 60, pp. 994–1003, feb 2012.

[309] J. J. Maldonis, J. Hwang, and P. M. Voyles, "FEMSIM + HRMC: Simulation of and structural refinement using fluctuation electron microscopy for amorphous materials," *Computer Physics Communications*, vol. 213, pp. 217–222, apr 2017.

[310] P. M. Voyles and D. A. Muller, "Fluctuation microscopy in the STEM," *Ultramicroscopy*, vol. 93, no. 2, pp. 147–159, 2002.